BULGARIAN CHEMICAL COMMUNICATIONS

2020 Volume 52 / Special Issue C

Selected papers presented on the Third International Scientific Conference Alternative Energy Sources, Materials & Technologies AESMT'20, Varna, Bulgaria, June 8 - 9, 2020

Journal of the Chemical Institutes of the Bulgarian Academy of Sciences and of the Union of Chemists in Bulgaria

PREFACE

The Third International Scientific Conference "Alternative Energy Sources, Materials & Technologies AESMT'20" was held between 8th and 9th June 2020 in Varna, Bulgaria. Representatives of 26 countries (Bulgaria, China, Kazakhstan, Turkey, Israel, United Kingdom, Spain, India, Romania, Italy, Serbia, Latvia, Belarus, Poland, Yemen, Cyprus, Denmark, France, Germany, Iran, Ireland, Lithuania, Sweden, USA, Austria, Algeria) sent their works to the conference. Some of the reports (14 works) have been selected and are published after international peer-review in the present Special Issue of the journal "Bulgarian Chemical Communications".

It is our pleasure to be guest editors of the presented articles, which focus on new international scientific results in the field of Alternative Energy Sources, Materials and Technologies (Energy Materials Science, Storages with Phase Change Materials, Shallow Geothermal Energy Applications, Energy Efficiency, Solar Photovoltaic Systems, Low-Carbon Technologies, Mechanical Engineering and Technologies, and Electrical Engineering).

Prof. Aleksandar Georgiev, PhD (European Polytechnic University, Pernik, Bulgaria)

Assoc. Prof. Daniela Dzhonova-Atanasova (Bulgarian Academy of Sciences, Sofia, Bulgaria)

Guest editors of the present Special Issue

Bulgarian Chemical Communications, Volume 52, Special Issue C (pp. 5-11) 2020 DOI: 10.34049/bcc.52.C.0105

Electropolishing of single crystal and polycrystalline aluminum to achieve high quality optical and mechanical surfaces

A. Brusov, G. Orr, M. Azoulay, G. Golan*

Ariel University, Science Park, Ariel 40700, Israel

Electropolishing has found wide application as the final surface treatment of metal products in mechanical engineering and instrumentation, medicine and reflective concentrators for PV cells. It was found that electropolishing (EP) not only reduces the surface roughness and changes its appearance, but improves many operational characteristics as well, such as corrosion resistance, endurance, tensile strength, and many others, and also changes the physicochemical properties, for example, reflectivity, electromagnetic permeability and electronic emission of some ferro-magnetic metals. This fact greatly expands the possibility of using this method in various fields of science and technology. This work is part of a study, examining electro polishing for reducing the crystalline defects adjacent to the surface, thus improving its physical properties, contributing to higher optical efficiency, when used in PV generation and storage devices. Five compositions were examined using different temperature and current density parameters. The polished samples were evaluated using reflectance spectrometry. The solution which was composed of Phosphoric acid - 85%, Acetic acid - 10%, Nitric acid - 5% was found to provide the best results. Another result obtained was that reflectance increased as the current density increased up to 25 A/dm^2. Further increasing the current density resulted in deterioration of the surface and reduced reflectance. It was shown that careful lapping and polishing followed by electropolishing using the suggested solution may consist of an adequate treatment for preparing reflective concentrators for PV cells.

Keywords: Electropolishing, single crystal, aluminium, reflectance spectroscopy

INTRODUCTION

Electropolishing (EP) is a process of leveling a metal surface by anodic dissolution and is used to improve the surface quality of metals in addition to mechanical grinding and polishing. EP is a specific type of electrolysis that involves a direct electric current passing through an electrolyte in an electrolytic cell [1-2]. During machining (cutting, grinding) of a metal, the material structure adjacent to the surface is deformed. In this layer there is a distortion of the crystal structure, concentration of stresses, inclusion of foreign materials, defects, which adversely affect the properties of the material. In thin samples, where the damaged layers contribute more to the physical properties of the material compared to the undamaged volume, the effect is pronounced. It is impossible to eliminate this layer mechanically. Etching is also not acceptable, since it is accompanied by uneven dissolution of the metal and often leads to its hydrogenation. EP is the most effective way to remove the thickness-regulated damaged metal layer and the formation of a new surface layer, devoid of these disadvantages.

EP has a number of advantages compared to mechanical polishing: short process times, low-cost equipment and consumables, versatility, and the ability to machine small parts and parts of complex shapes. EP has worked well for soft metals such as aluminum [3]. In addition to a well-polished surface, it enhances the materials characteristics - increases endurance, long-term strength, fatigue resistance, elastic limit, electromagnetic properties, corrosion resistance and reduced friction coefficient [4-7]. The study of the optical characteristics of soft metal samples puts forward stringent requirements for the preparation of their surface. EP has been demonstrated to be the preferred and successful method to obtain the required optical surface [8-9]. Successful removal of the damaged surface layer is associated with improvement of the optical, electromagnetic, and some other physical properties of the material. The classical theories of the EP process is based on the forming of a viscous liquid layer. In the process of EP, the transition of a metal into a solution occurs under conditions of partial passivity, which is associated with the formation of a viscous liquid layer at the liquid-metal interface which results from the reaction between the metal and the electrolyte. This high resistance layer provides non uniform resistance paths with the ridges created during the mechanical preparation providing lower resistance resulting in higher currents through them. The higher currents lead to faster dissolution of the ridges and smoothing of rough surface, which gradually acquires a wavy relief. Hryniewicz [10] extending Hoar's work [11]

* To whom all correspondence should be sent:
gadygolan@gmail.com

concludes that the oxide film created on the anode surface supplemented by oxygen introduced by water decomposition is the only factor in the electropolishing process. According to this model the metal is dissolved by tunneling the metal ions via dislocation sites and vacancies of the oxide. As the thickness of the oxide on the ridges is lower, they dissolve faster. The effect is a decrease in scattered light and an increase in specular reflection of light, which manifests itself in the appearance of a shine on the metal surface.

The electropolishing method is used to prepare samples for studying the microstructure of metals by electron microscopy [12] and transmission electron microscopy [12,13]. Revealing grain boundaries on high-purity aluminum presents a challenge at times only to be solved using the EP method. In practice, the use of this method requires adjusting process parameters depending on the electrolyte, material, and taking into account the size and shape of the sample. The EP process parameters that need to be adjusted include: current density, temperature, time, electrolyte composition and such additional factors as the method of fastening parts, the material of the cathode and suspension, the method of isolating the suspension device, the geometric shape and ratio of the anode and cathode area, and much more, therefore, for solving a specific research problem, it is necessary to conduct a series of experiments finding the optimal process parameters. In this study we have examined the process for removing the damaged layer, analyzing the surface layer damage using x-ray and specular reflection.

EXPERIMENTAL PROCEDURES

Materials and methods

Tests were conducted on four types of samples available from different sources. The first type with dimensions of 30x10x0.3 mm was obtained from aluminum tape with a minimum purity of 99.99%.

The second and third samples consisted of commercially available aluminum for sputtering targets with a minimum purity of 99.99%, the second with dimensions of 10 × 12 mm and a thickness of 2 mm, the third with 20 x 10 mm and a thickness of 3 mm. Samples were prepared using electrical discharge machining. The fourth sample was cut from a single crystal of aluminum grown in our laboratory, prepared as a 3 mm thick disk. Sample dimensions were of no significance and were based on available material or comfort. In a non traditional manner, samples no. 1 and 4 were cut using a 0.3 mm thick diamond cut-off wheel. The first sample was not lapped since it was manufactured with semi optical surfaces. Random scratches were present on its surfaces. The second and third samples were ground and lapped using abrasive paper according to the following protocol: #600, #1000, #1200, # 2500, #4000 grits, on a polishing/lapping machine. We followed four cleaning protocols depending on the fabrication stage and the state of the sample. Using the first protocol, samples were cleaned by immersing the sample into acetone for 3 minutes in order to degrease it. This was followed by washing the sample in distilled water and drying it using warm air. If deeper cleaning was needed, the second protocol consisted of the samples immersed for 10 minutes in a 10% solution of acetone and water in an ultrasonic cleaner, after which they were washed with running water, followed by washing the samples in ethanol and distilled water. The process was completed by drying the samples with warm air. The third protocol was reserved for samples after the EP process. Samples were washed in ethanol, followed by distilled water, and dried in warm air. For film removal we developed a fourth protocol in which the sample was immersed in a 10% solution of nitric acid, followed by washing in cold running water, then drying in warm dry air. The schematic of the electropolishing cell is shown in Fig.1. The anode is a sample of aluminum, and plates of various materials (lead, graphite, stainless steel) were used as a cathode. The cathode and anode were immersed in a container with electrolyte; the container was placed on a heating plate with a magnetic stirrer. The electrolyte temperature was measured using a mercury thermometer. Voltage was applied to the electrodes using a high current regulated power supply.

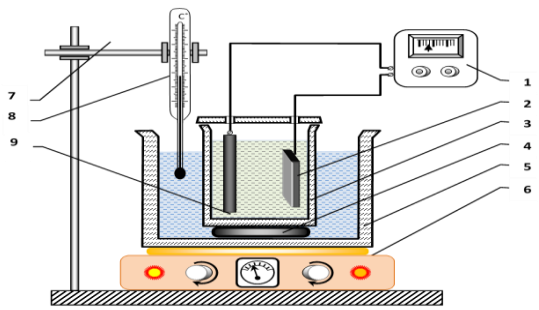

Fig.1. Schematic of the experimental setup: 1. Power supply; 2. Anode (Aluminum sample); 3. Electrolytic bath; 4. Ceramic stand; 5. Water bath; 6. Magnetic plate; 7. Tripod; 8. Thermometer; 9. Cathode

RESULTS AND DISCUSSION

Electrolyte compositions

Various electrolytes were used for EP of aluminum. They can be divided into alkaline and acidic groups.

1. Alkaline electrolytes

From the alkaline group, we chose electrolytes with low toxicity - compositions A and B in Tab.1. The first type of samples were cleaned according to the first protocol, while the other samples were cleaned more thoroughly using the second protocol. The cathode consisted of a 12x30x3 mm graphite plate. The main parameters of the processes are shown in Tab.2.

Table 1. Parameters of electropolishing process in alkaline electrolytes

	Electrolyte composition	Temperature, °C	Current density range, A/dm^2	Voltage range, V	Time, min
A	Sodium Phosphate 5-10% Soda ash 15-30% Water-60-80%	85-90	3-6	4-10	1-5
B	Sodium phosphate - 320-350 g/l Sodium carbonate - 230-250 g/l Water - 450- 400 g/l	80-85	2-6	5-20	0-20

Table 2. Parameters of EP process in acid electrolytes

N	Electrolyte composition	Temperature, °C	Current density range, A/dm^2	Voltage range, V	Time, min
C	Phosphoric acid H_3PO_4 -45- 55% Sulfuric acid H_2SO_4 – 30-40% Nitric acid - HNO_3 – 5-15 %	100-115	30	10-30	1-2
D	Phosphoric acid H_3PO_4 – 75- 85% Acetic acid CH_3COOH – 10- 20% Nitric acid - HNO_3 - 5%	100	30	10-30	0.5-1
E	Phosphoric acid H_3PO_4 – 35 - 70% Sulfuric acid H_2SO_4 – 15-40% Chromic anhydride CrO_3 - 1 -10% Water – 1ß-15%	60-90	20-50	12-18	2-8

Some experiment failures were: 1 - points of erosion, deep etching at point locations; 2 – An uneven surface finish was obtained. Preferred etching at the contacts with the sample; 3 – significant hydrogen generation at the cathode; 4 - the sample reacts with the electrolyte, process begins before the voltage is turned on.

Some reasons for the failures are as follows: incorrectly selected electrical parameters, incorrect estimates of the cathode and anode areas and / or the distance between them, an unclean surface, poor electrical contact between the part and the sample holder. Following the above described failures, the samples were cleaned according to the second deep cleaning protocol, the design of the sample holder and electrical contact was improved, the cathode area was increased, and an optimal current density was selected from the volt-ampere curves for each process.

Subject to the above conditions, we received a satisfactory result: defects and scratches left after lapping were removed. Fig.2 illustrates the microstructure of the aluminum surface before EP (Fig.2a) and after (Fig.2b) at x100 magnification. The polishing quality of samples from pure aluminum and single crystals is higher than that of aluminum alloy. The advantages of this method are simplicity, speed and low toxicity. The disadvantages include insufficient improvement of the surface quality, very high process speed complicating its control.

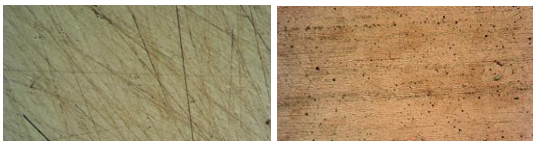

(a) (b)

Fig.2. Optical micrograph at x 100 magnification of (a) unpolished aluminum surface; (b) polished aluminum surface after EP in alkaline electrolyte

2. Acidic electrolytes

In practice, acid based electrolytes are more common than alkaline ones. Their advantages

include: obtaining better reflective surface properties, increased ability to smooth the microrelief and increase roughness by 2-3 grades, the possibility of increasing the efficiency of the process due to the introduction of inhibitors and other additives. The disadvantage of these electrolytes is the high toxicity of the reagents. For aluminum and its alloys, electrolytes based on phosphoric, sulfuric and chromic acids or with chromium anhydride instead of chromic acid are widely used, as well as electrolytes from a mixture of phosphoric acid with nitric, acetic or sulfuric acid. The ratio of their components (mass fraction) fluctuates over a fairly wide range. In experiments, the influence of various proportions of components on the quality of electro-polishing was investigated. The compositions of the studied acidic electrolytes and the parameters of the processes are shown in Tab.2. For example, a mixture of phosphoric and sulfuric acids with their maximum concentration of compositions (C and E) leads to the appearance of a dull film consisting of phosphate salts. This film disappears when the concentration of chromic anhydride increases from 1% (electrolyte E) and nitric acid from 5% (composition C). An increase in the chromic anhydride content is accompanied by an increase in the gloss of the metal surface. An increase in chromic anhydride above 11% leads to surface etching. The optimum sulfuric acid content is 26-30%. In each group of electrolytes, the optimal ratio of components and process parameters were determined. They are shown in Tab.3.

Table 3. Parameters of Electropolishing process

Electro-lyte	Sample type	Current density range, A/dm^2	Voltage range, V	Tempera-ture,°C	Time, min	Cathode/ Anode	Mixing speed RPM	Examples
A	1 2 3	5 10 20	10	80 85 90 95	0.5 1 2 3 4	1:1 1:2 1:5	0 50 100 150 200	**Sample1,2:** Sodium Phosphate-10g, Soda ash - 22,5g, Water –100ml. Temperature - 90°C; Time - 2 min; Current density range – 5 A·dm^{-2}; Voltage – 6 -9 V; Mixing speed- 2-3. **Sample 3:** Temperature - 85°C; Time - 1 min; Current density range -8 A·dm^{-2}, other parameters are same
B	1 3	5 10 30	10-30	80 85	5 10 15	1:1 1:5	50 100	**Sample1:** Sodium Phosphate-350g/l Sodium carbonate - 250g/l, Water–400g/l. Temperature - 85°C; Time -5 min; Current density range 6-9A·dm^{-2} Voltage – 6 -9 V; Mixing speed- 2-3. **Sample 3:** Temperature - 80°C; Time - 8 min; Current density range – 15 A·dm^{-2}, other parameters are same
C	1 2 3	25 30	10	90 100 115	1 2 3 4	1:1 1:5	100 150 200	Electrolyte: Phosphoric acid 50%, Sulfuric acid - 40%, Nitric acid-10%; Temperature - 105° C; Time - 2 min; Current density range – 30A·dm^{-2}; Voltage – 12-15 V; Mixing speed- 4. **Sample 3:** Time - 1 min, the other parameters similar to the previous selection
D	1 2 3	25 30 35 40		90 95 100	0.5 1 2	1:2 1:5	100 150 200	Electrolyte: Phosphoric acid- 85%, Acetic acid - 10%, Nitric acid-5%; Temperature - 100° C; Time - 2 min; Current density range – 30A·dm^{-2}; Voltage – 12-15 V; Mixing speed- 4.
E	1	20 30 40 50	12-15	60 70 80 90	2 4 6 8	1:5	100 150 200 250	Electrolyte: Phosphoric acid- 45%, Acetic acid-35%, chromic anhydride-5%, water - 15%; Temperature - 70° C; Time - 3 min; Current density range – 25A·dm^{-2}; Voltage – 12-15 V; Mixing speed- 4.

Processing parameters

1. Current density

For each one of the electrolytes, the current-voltage relations were measured. An example of such a curve is illustrated in Fig.3. Both alkaline and acids display curves which are similar in form. The horizontal section of the curve between 4 and 10 volts corresponds to the process of stabilization of the passivating layer and diffusion of anions through the passive layer, that is, in this interval, the polishing process takes place.

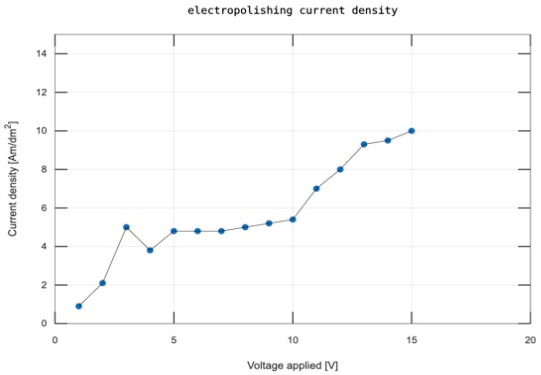

Fig.3. Electropolishing current density –voltage curve in alkaline phosphate electrolytes for aluminum sample (type 1)

2. Temperature

Different authors recommend different optimal temperatures for the same electrolyte compositions [14, 15]. To find out the influence of the temperature, samples of the third type were processed in electrolyte A in the temperature range 80–100°C in increments of 5°C; other process parameters were the same. The quality of processing was evaluated visually by the presence of gloss and a comparison of changes in surface topography (the presence of scratches, and pits) using a microscope at a magnification of x100 times. The amount of metal removed was evaluated by weighing the sample on an analytical balance. There is a noticeable increase in surface gloss with the increase of temperature up to 95°C, increasing it to 100°C a decrease in brightness is observed. At the same time the temperature increase in the above range does not have a noticeable effect on the metal removal rate or surface relief. To reduce the generation of hydrogen on the cathode surface, its surface was tripled.

3. Mixing speed of the solution

To uniformly heat the electrolyte and improve the separation of gas bubbles from the surfaces of the electrodes, we applied forced convection using a magnetic stirrer. The processes was carried out without stirring, with a low speed, medium, high and maximum. Acceptable results were obtained when the rotational velocity of the 5 cm magnet was in the range of 120 to approximately 250 rpm. Without mixing and with a low mixing speed of the electrolyte, an increase in the number of dot patterns on the surface is observed. This can be explained by the fact that the diffusion of matter from the surface of the anode is difficult and the electrolyte near the sample overheats. A very high speed leads to displacement of the sample relative to the cathode and to the deterioration of the contact of the sample holder and the sample.

The ratio of the surface areas of the anode and cathode and other additional process characteristics. EP was carried out with different volumes of electrolyte, with cathodes of various materials (stainless steel, lead, graphite), and with different ratios of the areas of the cathode and anode (1: 1; 2: 1; 5: 1). The best results were obtained by keeping the ratio of the cathode to the anode at 5: 1, with graphite or lead as the cathode material. Furthermore, the solution volume should be at least 300 ml for parts with a surface area of up to 1 cm 2 and 400 ml for parts with a surface area of 6 cm2, the distance between the anode to the cathode should be at least 5 cm, and from the sample to the walls and the bottom of the bath should be at least 3.5 cm.

Electrochemical etching

Our studies have shown the possibility of developing electrolytes in which it is possible to conduct simultaneous electropolishing and electro-etching of aluminum to produce a thin oxide layer on it. The thickness of this layer is minimal, which is necessary to achieve surface gloss (high reflectivity), but at the same time sufficient to obtain adsorption staining. The basis of such an electrolyte is a mixture of sulfuric, phosphoric and acetic acids. For aluminum with a high degree of purity, good results are obtained in an aqueous solution of sodium orthophosphate and sodium carbonate (Fig.4).

RESULTS

As one of the primary goals in the current work is reflective concentrators for PV, it is natural to examine the reflectance in the UV-VIS-IR range.

The measurement system consisted of a reflectance spectrometer with Deuterium and Tungsten Halogen lamps as sources. Calibration was conducted using a gold calibration standard thus limiting the spectral range of the measurement to 600-1600nm. Its strength is the standards inertness and stability compared to aluminum or silver standards resulting in improved measurement repeatability. Fig.5 compares the reflectance of the various compositions in the tested range. From the figure it is apparent that in this research, composition D was superior to the other compositions. The chosen current density and temperature were found to be optimal in most cases.

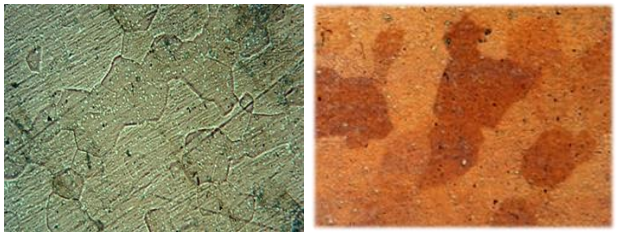

(a) (b)

Fig.4. Microstructures of aluminum after electrolytic etching: a - alkaline electrolyte, b - acidic electrolyte, magnification 100 x

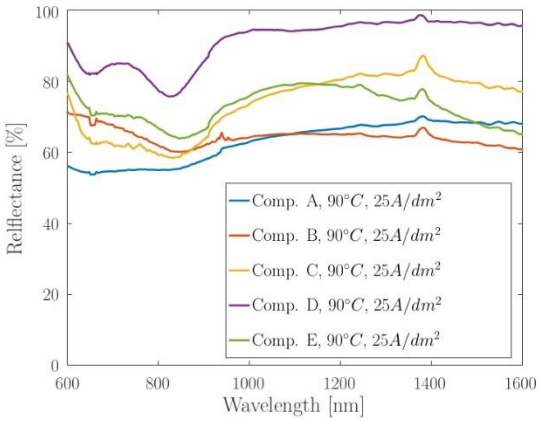

Fig.5. A comparison of the reflectance of the various polishing solutions

Fig.6 illustrates reflectance measurements of polished crystal samples at several current densities.

It can be seen from the plots that best results were obtained at 25 A/dm^2. Increasing the current from 5 A/dm^2 up to 25 A/dm^2 displays an increase in reflectance in the formentioned spectral range. Increasing the current density above 25 A/dm^2 displays reduced reflectance and visual deterioration of the surface. Adelkhani et al. [16] reached similar conclusions though demonstrated lower reflectance at the lower and higher currents. The difference probably stems from the preliminary processing, i.e. multi stage mechanical lapping and polishing.

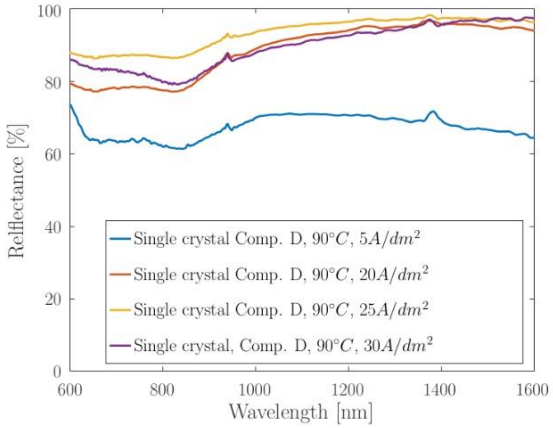

Fig.6. Reflectance measurements of crystals polished using composition D at current densities of 5A/dm^2, 20 A/dm^2, 25 A/dm^2, and 30 A/dm^2

CONCLUSIONS

• Electropolishing of aluminum is effective for obtaining a high quality surface and eliminating machining defects. The best result of electropolishing of an aluminum surface in terms of its quality, as well as the duration and complexity of the process is provided by a combination of preliminary mechanical grinding and polishing followed by EP in an acid electrolyte composition: Phosphoric acid - 85%, Acetic acid - 10%, Nitric acid - 5% (mode D)

• We managed to obtain a polished surface of good quality due to the correct choice of all factors affecting the EP process, such as pretreatment of the metal surface, orientation of the workpiece in the electrolyzer, choice of cathode material, distance between electrodes, process time, solution circulation rate, anode area ratio, and cathode, bath age. This was confirmed using spectral reflectance analysis.

• The tested electrolytes, especially acidic ones, have a narrow range of current density, at which the polishing process takes place. This limits the ability to control the process: removal of material to a given depth and obtaining specified roughness parameters.

• The uniformity of surface treatment is strongly influenced by the design and material of the suspension, the ratio of the anode to cathode surface areas and the location of the sample in the cell. In our experiments, the optimal suspension

material is aluminum and the anode-to-cathode area ratio is 1: 5.

• The use of electrochemical etching to determine the structure of pure aluminum gives good results. This is an effective and simple method, since the process is carried out in the same electrolyzer and with the same electrolytes as the EP. For high purity aluminum, good results are obtained in an aqueous solution of sodium orthophosphate and sodium carbonate.

This work was conducted as part of a larger project trying to improve the aluminum surfaces physical properties in storage devices. As this article is limited in scope, in a following article we will demonstrate the improved results obtained in aluminum single crystals prior and after being processed using the various EP methods discussed in this article. As shall be demonstrated in future articles, X-ray analysis indicates that there is a considerable improvement after treating the surface using the above methods.

REFERENCES

[1] D. Landolt.Fundamental aspects of electropolishing. *Electrochim. Acta*, **32**, 1–11 (1987).

[2] W. Han and F. Fang. Fundamental aspects and recent developments in electropolishing. *International Journal of Machine Tools and Manufacture*, **139**, 1-23 (2019).

[3] Vander Voort, F. George Metallography, principles and practice. The Materials Information Sociaty. New York: McGraw-Hill, 489, 2007.

[4] M. Inman, E. Taylor, A. Lozano-Morales and L. Zardiackas: in Medical Device Materials VI. *Proc. from the Materials and Processes for Medical Devices Conference*, MPMD Minneapolis, ASM International (2011).

[5] C.Wagner. Contribution to the theory of Electropolishing. *I. Electrochem. Soc.*, **101**, 225-228 (1954).

[6] M. Datta and D. Landolt. Fundamental aspects and applications of electrochemical microfabrication, *Electrochim. Acta*, **45** (2000).

[7] Controlled texturing of Aluminum sheet for solav energy applications. *Advances in Material Physics and Chemistry*, **5**, 458-466 (2015).

[8] Leksina I. Z. Optical properties and electronic characteristics of niobium and its alloy with titanium. *Proceedings of the FILI*, **72**, 150, (1974).

[9] K. Shanks, S. Senthilarasu and T. K. Mallick. Optics for concentrating photovoltaics: Trends, limits and opportunities for materials and design. *Renewable and Sustainable Energy Reiews*, **60**, 394-407 (2016).

[10] R. Rokicki and T. Hryniewciz. Enhanced oxidation – dissolution theory of electropolishing. *Transaction of the institute of metal finishing*, **90**, 188-196 (2012).

[11] T. P. Hoar, J. A. S Mowat. The Electropolishing of Nicker in Urea-Ammonium Chloride Melts. J. *Electrodepositor's Tech. Soc.*, **26**(7) (1950).

[12] C. Lyman, D. Newbuy, J. Goldstein, D. Williams, A. Romin, J. Amstrong, P. Echlin, C. Fiori, D. Joy, E. Lifshin, K. P. Peters. Scanning Electron, X-Ray Microanalysis and Analytic Electron Microscope, A Laboratory Workbook, Springer, 1990.

[13] J. Ayache, L.Beaunier, J. Boumendil, G. Ehret and D. Laub: 'Sample preparation handbook for transmission electron microscopy: techniques', Vol.2; New York, Springer Science & Business Media, 2010.

[14] H. Tomlinson. An electro-polishing technique for the preparation of metal specimens for transmission electron microscopy. *Philos. Magazine*, **3**, 867–871, (1958).

[15] G. Yang, B. Wang, K. Tawfiq, H. Wei, S. Zhou, G. Chen G. Electropolishing of surfaces: theory and applications. *Surface Engineering*, DOI 10, (2016).

[16] H. Adelhani, S. Nasoodi, A. H. Jafari. A study of the morphology and optical properties of electropolished aluminum in the VIS-IR region. *Int. J. of Electrochemical Science*, **4**, 238-246 (2000).

Bulgarian Chemical Communications, Volume 52, Special Issue C (pp. 12-19) 2020 DOI: 10.34049/bcc.52.C.0018

Numerical investigation of combustion process behind bluff bodies during separation

A. M. Dostiyarov[1], D. R. Umyshev[2*], Zh. S. Duissenbek[1], I. K. Iliev[3], H. I. Beloev[3], S. Ph. Ozhikenova[1]

[1]*Almaty University of Power Engineering and Telecommunications, Almaty, Kazakhstan*
[2*]*Kazakh National Research Technical University, 22a Satpaev str, Almaty, Kazakhstan*
[3]*University of Ruse, Department of Thermotechnics, Hydraulics and Environmental Engineering 7017 Ruse, 8 Studentska Str., Bulgaria*

The article presents the results of numerical simulation of combustion process methane mixture from the group of corner stabilizers, and the corners arranged in two rows, in first row three area, two in the second area. The influence of the distance between the rows of corners on the formation of toxic substances and the formation of swirling currents was studied. The study showed that from the point of view of reducing nitrogen oxides, the optimal distance is 120 mm. The results of modeling the emission of nitrogen oxides showed that the highest concentrations of nitrogen oxides are formed at a distance of 140 mm and a fuel consumption of 0.1 kg/s. for the variants L=80 mm, L=120 mm, L=140 mm, the oxide concentrations at a flow rate of 0.1 kg/s were equal to 10, 60, 109 ppm respectively.

Keywords: v-gutter flameholders, mixing efficiency, recirculation zone, combustion efficiency

INTRODUCTION

In the combustion chamber and the afterburning chambers of gas turbine engines (GTE) of fuel combustion mainly occurs in turbulent trace behind poor-streamlined body stabilizers flame. The process of turbulent combustion depends on the physic-chemical and hydrodynamic parameters of the flow of hot mixture. The influence of these factors, at least, qualitatively manifests itself in the same way as in the case of combustion in a stream with homogeneous and isotropic turbulence, and when burning in a direct-flow combustion chamber.

Specific features of combustion in the trace of poor-streamlined bodies are as follows. As the measurements showed, the turbulence intensity in the isothermal flow changes dramatically along the length of the stabilizer and in the cross sections of the track, reaching 30% or more on the axis near the stabilizer and decreasing to the intensity of turbulence in the incoming flow as it moves away from the stabilizer and at the borders of the track.

In combustion chambers of jet engines and afterburner chambers of gas turbine engines, the combustion process takes place over lattice (group) stabilizers. In this case, the size and configuration of the flares behind each stabilizer depends on the number of stabilizers and their relative positions in the combustion chamber. When the stabilizers are evenly positioned in the same plane (when the distance S between the edges of adjacent stabilizers is the same, and the distance between the wall and the edge of the adjacent stabilizer is S/2), the torch axes are parallel to the pipe axis and the torches have the same measures behind each stabilizer of the same size and geometric shape.

The study of combustion processes for bluff bodies devoted quite a lot of work. For example, in [1, 2], the influence of installing bluff bodies in a niche on the completeness of hydrogen fuel combustion is considered. The results showed that a bluff body is an anchor for the torch, thereby increasing the completeness of combustion. In [3], methods for measuring the combustion of fuel behind bluff bodies were investigated. Famous works [5, 6] for the study of hydrogen combustion for different types of poor-streamlined bodies. The results showed that the application increased the poor breakdown limit by 2.4 times when using a pyramidal body. Study of the process of detonation gas using [7] showed that poor-streamlined body is the source of the increase in the rate of combustion. Studies are being conducted on the effect of bluff bodies on the flow of liquid in separators [8]. Study of the effect of poor-streamlined bodies on the border of poor failures [9-11, 14] showed that poor-streamlined ones largely significantly expand the boundaries of stable combustion.

The analysis of modern methods and structures of the recirculation zones makes it possible to analyze and put the basic requirements for them. According to [15, 16], modern combustion chambers of gas turbines must meet the following

* To whom all correspondence should be sent:
umishev_d@mail.ru

criteria:

• high coefficient of completeness of fuel combustion; modern combustion chambers should have ηc = 98 ÷ 99%;

• small hydraulic pressure losses;

• high heat intensity of the working volume;

• small temperature non-uniformity of temperatures at the outlet of the compressor station, to ensure reliable operation of the turbine;

• fast and reliable start. Stable operation over the entire load range;

• durability of structures, high reliability;

• absence of smoke, carbon deposits and toxic substances.

The analysis of different methods and principles of burning microflare devices showed the features of microflame burning, which can be as close as possible to the requirements for the combustion chambers presented above. Microflare burning is a type of zone combustion [27].

An analysis of the main causes of the formation of nitrogen oxides in various devices and the prospects for the development of energy showed that traditional methods of burning fuel do not provide the required parameters. Improving the efficiency of fuel combustion can be obtained by using microflare burning [28].

Despite the limited amount of experimental data on the use of microflare burning in combustion chambers, various authors [1-10] noted the following positive qualities of this method: low pressure losses of gas, reduced structural dimensions, reduced unevenness of the temperature field at the outlet of the combustion chambers, low yield of nitrogen oxides with products combustion, reduced radiation loss [26-27].

Still known from the mid-twentieth century [16], microflare burning technology began to attract the attention of scientists relatively recently. Currently, there are several main directions of microflare burning, but all have one thing in common - this is the “spreading" of the torch along the front and volume of combustion [17].

According to [18], reduction of NOx emissions can be achieved by conducting a combustion process with an excess of primary air αI> 1.6 1.8, while ensuring intensification of mixture formation in the front of the combustion chambers. The fulfillment of such requirements makes it possible to reduce the local maximum temperatures in the combustion zone and bring them closer to the average flame temperature and significantly reduce the burnup time of the fuel.

Such principles were implemented on gas turbine units GT-25-700-II, GT-700-12M, GT-50-800. The studies were carried out both with the original combustion chambers and with the modified ones, which makes it possible to visually see the results.

Alstom combustion chambers are known that use multi-burner devices. The company uses burners under the brand name EV and AEV. Emissions of gas turbine NOx using these burners do not exceed 15 ppm. If in the gas turbine engine ABB GT10 (23 MW) there were only 18 burners, then ABB GT13E (> 150 MW) has 72 burners installed in two circular rows.

General Electric LM6000 is a known gas turbine burner. The combustion chambers produced by this company is made in the form of two rings. In the outer two rings there are 60 nozzles, in the inner ring 15. This arrangement of the rings facilitates operation under partial load. 75 nozzles are connected by 30 stems with pre-mixing devices. LM6000-PD turbines have NOx emissions close to 25 ppm, at a power of 50 MW.

Widely known is the DLE technology. In the DLE system, a “premixed lean mixture” of fuel and air is burned, which produces little NOx and CO. In the system of “pre-mixing the lean mixture”, the formation of CO remains relatively low until approaching the conditions of flame failure due to the “lean” mixture. In this system, NOx and CO concentrations are controlled by maintaining the gas-to-air ratio and flame temperature in a narrow range where stable combustion is maintained at low emission levels.

Interesting NASA work on the study of multi-burner devices is presented in [19]. Conventionally, the 120-modular annular combustion chambers designed for Pratt-Whitney engines can conditionally be classified as microflare. Each module consists of a mixer, swirl and stabilizer. Tests of this combustion chamber showed that the small length of flares provided by a sufficiently high degree of preliminary and secondary mixing reduces the formation of nitrogen oxides. When testing the chamber, the NOx concentration was two times lower than conventional chambers.

At the Kiev Polytechnic Institute on the proposal of V.A. Khristich created the original design of a gas burner with separate gas and air supply, which ensures high intensity of the processes of mixture formation and combustion and has the property of self-regulation of the composition of the burning mixture with variable excesses of air [19-24].

The peculiarity of such a burner is that it, with a separate supply of gas and air, provides the same short and transparent torch as the preliminary burners.

Front-end devices operating on the principle of a "perforated front" have one significant drawback - perforations of the front-end device lead to an increase in pressure loss. There are also a number of questions about front cooling and the use of expensive heat-resistant materials and metals.

A known method of burning fuels in the fuel-air mixture, which applied the principle of perforated front [24]. The authors propose using a bulk matrix in the combustion chambers, but mix fuel assemblies in relative proportions before it.

At the exit from the matrix, a flame is maintained in the surface combustion mode with a laminar flow of fuel assemblies and at temperatures in the range of 1200–1500 K. The front-mounted device itself consists of a housing with a fuel supply system and an outlet for combustion products. Inside the combustion chambers case there is a matrix made of heat-resistant material permeable to fuel assemblies. The volumetric matrix is made with cavities that are connected to the outlet for the output of combustion products. This design is aimed at lowering the combustion temperature, as well as at reducing temperature unevenness at the outlet of the compressor station.

The relative low temperature of the flame burning near the matrix allows one to reduce the formation of a significant part of thermal nitrogen, as well as solve the problem of cooling. The design of the chamber itself is also simplified due to the absence of a flame tube and a cooling and dilution system. The decrease in metal consumption leads to an increase in the service life of the structure.

Another closest analogue to the "perforated front" can be a multi-chamber tube-type gas burner [25]. The tubular type gas burner consists of an outer and inner case, which are isolated from each other, nozzles for supplying gas and air. Also, gas burners consists air and gas chambers, end inner and outer walls, between which there are air tubes with gas holes on the side walls, the last of which made in the form of a distribution plate with holes for supplying gas.

There are known developments of multi-burner front devices for combustion chambers of gas turbines [25-26] which contain a front conical wall in which there is a burner section consisting of a central conical sleeve and a peripheral honeycomb frame, which are connected to the ends of the holes on the front conical wall, and seven burners, one of which is mounted in the central conical sleeve, and the rest, consisting of a gas pipe, two flat perforated walls, air tubes and end plates between them, are installed in the honeycombs of the frame. The use of this burner improves the reliability and simplification of the manufacturing technology of the front-end compressor unit, reduces the emission of toxic nitrogen oxides (NOx) and carbon monoxide (CO), ensures high efficiency of the compressor unit in a gas turbine in a wide range of oxidant excess changes.

This front-mounted device allows you to work in a wide range of changes in the excess of oxidizing agent, and provides a minimum level of thermal shocks when starting a gas turbine, a homogeneous aerodynamic and thermal structure of the duct at the entrance to the turbine blade apparatus, and minimal aerodynamic and thermal resistance of a gas turbine compressor unit.

The operation of the front-end device based on turbine profiles is as follows. The air flow in cooperation with a system of fan-shaped fuel jets formed by the atomizer is supplied to the combustion zone together with the fuel, resulting in a well-mixed combustible mixture. Drops of fuel, in contact with the hot walls of the pipe, evaporate and enter the internal cavities of the profiled blades of the register in a mixture with air [6].

Analyzing in general the results of an experimental study of the combustion process behind a system of profiles, it should be noted that the operating conditions of the profile grating in some cases turned out to be close to the operating conditions of a real combustion chambers transport gas turbine engine, primarily in terms of temperature and speed conditions of the incoming air. In addition, a number of the most developed profile options demonstrated reliable operation in a wide range of changes in the coefficient of excess air -1.5 ÷ 25 and higher [23].

The material of the blades used in the microflames is a heat-resistant high-alloy alloy. Naturally, the choice of material for microflame blades for fuel combustion should be determined.

Numerical methods are known for studying various bluff bodies [31-33]. In [31-33], a numerical simulation of the combustion of hydrogen and traditional fuel behind corner stabilizers and other non-streamlined ones was carried out. Studies have shown that they are optimal from the point of view of flame stabilization, and also that numerical simulation can effectively simulate combustion processes behind them.

In previous works of the authors, the following have been studied:

- angle of v-gutters [27];
- length of v-gutter walls [28];
- presence of wall perforations [29];
- fuel supply method [29].

At present, power units with HRSG installations with fuel afterburning are rapidly developing. Accodring to [19, 20]. For this, v-gutter flameholders are the most optimal. However, to date, no studies have been conducted on the effect of different locations of v-gutter, in particular, separation (echeloning) [12]. Based on this, the authors conducted studies of the effect of separation on the formation of toxic substances.

GENERAL DATA ABOUT THE MODELING PROCESS

Fig.1 shows General views of the simulated v-gutter stabilizers.

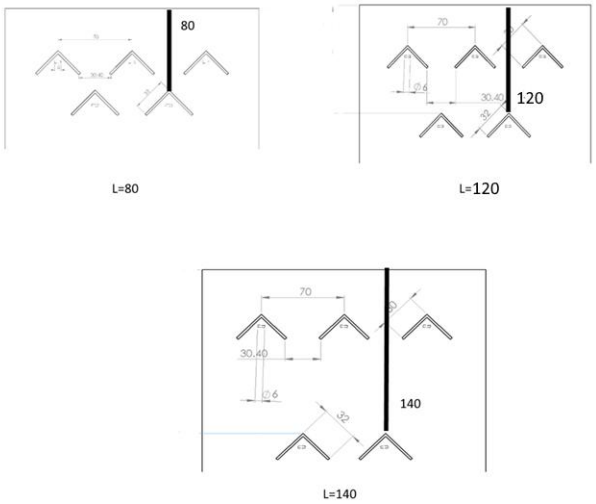

Fig.1. Options for installing v-gutter stabilizers

Tab.1 shows the initial modeling conditions. In the simulation, the airflow was constant and equal to 10 m/s.

Table 1. Iinitial modeling conditions

Airflow through the nozzles	Air speed (taken according to the experimental setup)	Initial temperature of the oxidizer (air)/fuel,	Number of elements in the simulated area
kg/h	m/s	K	-
36	10	300	1 135 456

Fig.2 shows a simulated area consisting of an air source 1, corner stabilizers 2 with a fuel distribution system-nozzles 3, and an output area 4.

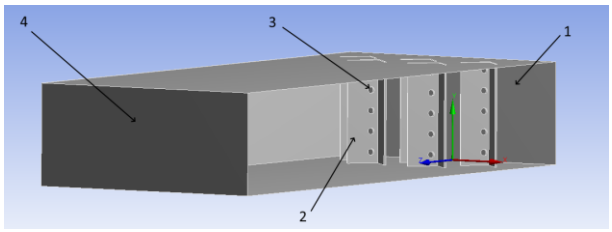

Fig.2. Isometric view of the modeling area.

Fig.3 shows a model grid in which the top part is made with a large number of elements compared to the rest of the parts. This is due to the fact that the flow and reactions have a strict z-axis orientation.

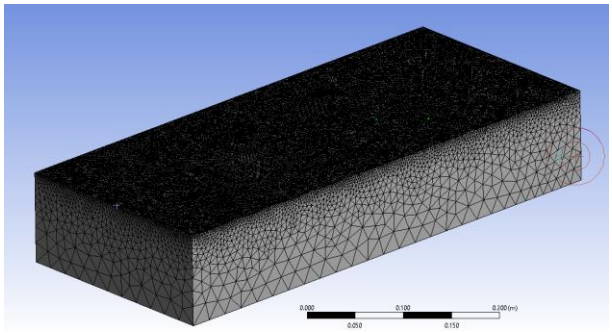

Fig.3. Mesh of the model

The simulation used the k-ε realizable turbulence model, which according to [12] is the most optimal solution. The grid consisted of 1,135,456 elements. Elements with dimensions of 7 mm were used for the mesh. The main part of the grid was on a plane parallel to the combustion process. Fuel was supplied through holes 3, through a flat wall.

The mathematical model developed in [30] was used to validate the experimental results, presented as follows

Continuity equation:

$$\frac{\partial p}{\partial t}+\frac{\partial (pu_i)}{\partial x_i}=0$$

Momentum equation:

$$\frac{\partial (\rho u_i u_j)}{\partial x_j}=-\frac{\partial (p)}{\partial x_i}+\frac{\partial \tau_{ij}}{\partial x_j}$$

Energy equation:

$$\frac{\partial (\rho u_i h)}{\partial x_i}=\frac{\partial}{\partial x_i}\left(\lambda_f \frac{\partial T}{\partial x_i}\right)+\sum_j\left[\frac{\partial}{x_i}(D_{j,m}\rho h_j \frac{\partial Y_j}{\partial x_j})\right]+q$$

Where h the total enthalpy of mixture gas is, h_i is the enthalpy of component j^{th} , λ_f is the thermal conductivity of the fluid, and q is heat of reaction.

State of ideal gas:

$$p = \rho RT \sum_{s=1}^{Ng} \frac{Y_s}{M_s}$$

Model validation

To check the validity of the simulation, the authors compared the results obtained with previous works [27-29] in which this model was used. The model was validated in the following way: for the current model used in this study, v-gutter flamehoderls were placed as in the article [29]. The comparison results are shown in Tab.2. The difference between model and experimental results are 6%, which we consider as sufficient.

Table 2. Model validation

Experimental results [29]	Numerical results results [29]	Numerical results results (current)
Outlet temperature, T_{out}, K	Outlet temperature, T_{out}, K	Outlet temperature, T_{out}, K
783	723	735

RESULTS AND DISCUSSION

The temperature contours. Fig.4 shows temperature contours for different fuel consumption.

As can be seen from the figure, the combustion starts in the region between the v-gutter stabilizers. Moreover, the reduced fuel consumption leads to more complete combustion due to the optimum ratio of fuel/air in the combustion zone. Despite the fact that burning is taking place in the area of maximum turbulence between the v-gutter fins, the maximum temperature achieved in the tail of the torch, it features significantly in the fuel consumption of 0.03 kg/s.

The minimum distance between the v-gutters of 80 mm, provides a uniform flame, due to the" throwing " of the torch to the nearest. In other options, especially at L=140 mm, it is noticeable that combustion occurs independently, and the reverse part of the area is subjected to thermal stress from the hot gases burning in the corners of the first row.

With a significant increase in fuel consumption, it is noticeable that the flame does not burn up, due to the high concentration of fuel and high flow rate from the fuel distribution nozzles. This is obviously undesirable, in view of the large underburning of fuel and according its much more consumption.

It is also noticeable that in the inner part of the area the temperature is not so high, compared to the tailed part, however with increasing distance the combustion starts in the region between the corners, that on the one hand indicates a high completeness of combustion gases, because gases will burn in the zone of recirculation, on the other hand, it imposes certain requirements to heat resistance of materials from which to make the corners.

If to consider the scheme of the combustion chamber, inside of which is installed in the same plane stabilizers of the same shape and size, it will become apparent that regardless of the diameter of the chamber and the number of installed stabilizers in it, the whole process of fuel combustion is essentially determined only by the laws of burnout in the plane of symmetry between two adjacent fins and between the wall and the adjacent stabilizer. Therefore, the two stabilizers can be considered as the main element of the combustion chamber and the combustion between these stabilizers can be extended to the combustion chamber of any size with any number of stabilizers.

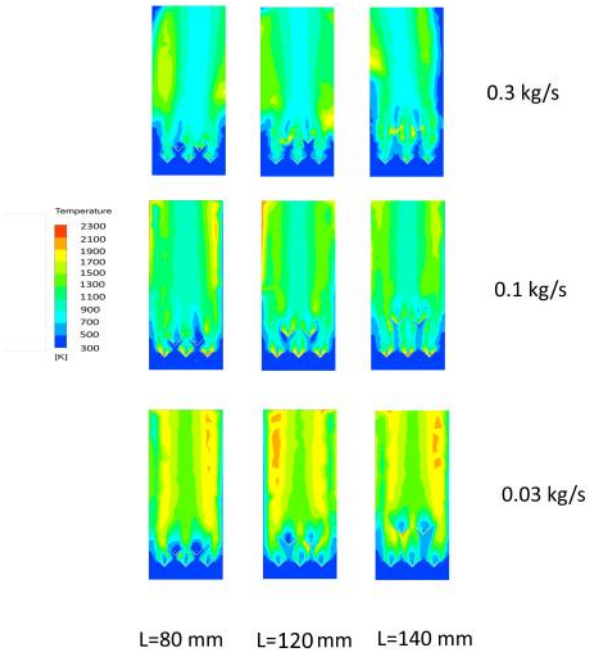

Fig.4. Temperature Contours at different distances

The swirling flow in Fig.5 shows the contours of swirling currents depending on the distance and

fuel consumption. As can be seen from the figure, an increase in fuel consumption leads to significant swirls around the corner stabilizers. However, taking into account the NO_x and temperature dependencies (Figs.6, 7), we can say that despite the high swirling flows, the concentration of nitrogen oxides is small due to the large underburning of the fuel, which occurs due to insufficient mixing of the fuel with air.

The highest concentrations of nitrogen oxides are observed at a fuel consumption of 0.03 kg/s, which is explained by the fuel / air ratio close to stoichiometric. It is known that the formation of nitrogen oxides is mainly influenced by the temperature in the combustion zone, the efficiency of mixing fuel with air and the residence time of gases in the zone of high temperatures. Given that most of the time spent gases have on the fuel consumption of 0.3 kg/s, then we can conclude that the most influential factor is the temperature in the combustion zone. And as you know, it is the maximum in the stoichiometric ratio of fuel/air.

The mutual influence of flares affects not only that the conditions of thermal expansion change and their shape is deformed by the flow, but also that the turbulent characteristics of the flow along the length and cross sections of the combustion chamber change. Obviously, the smaller the distance between the stabilizers, the same length will be above the common level of intensity of turbulence in the gap between the stabilizers and the higher bodyscroll combustion of the fuel in this interval. During combustion behind a grid of stabilizers increases the flow rate gradients along the cross sections of the pipe, which cause additional turbulence of the flow, and this also leads to an increase in the combustion rate.

Suggested, of course, true only in the case that the combustion in the interval between the two adjacent stabilizers do not depend on the total number of stabilizers installed in the camera, or the mutual influence they are small and can be ignored. The characteristic change in the intensity of turbulence of each stabilizer with the maximum intensity on the track axis seems to create two barriers that prevent the penetration of speed pulsations generated behind other stabilizers into the space between the two adjacent stabilizers under consideration and, therefore, the influence of other stabilizers in this respect should be negligible.

But an increase in the number of stabilizers will lead to an increase in heat generation and at the same air flow rate the average flow rate along the length of the combustion chamber will increase; in addition, the thermal expansion conditions will change.

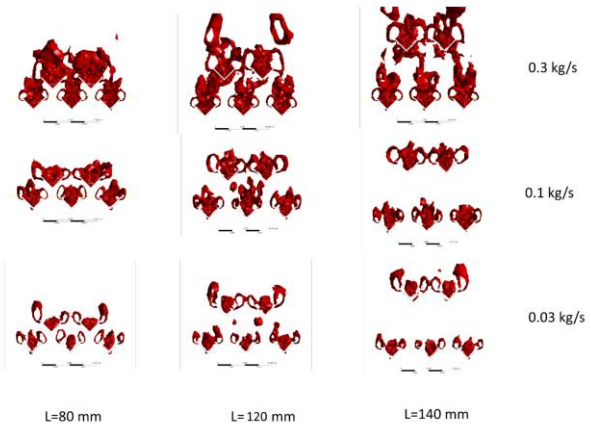

Fig.5. Spin of the flow depending on the distance and fuel consumption

NOX CONCENTRATIONS AND TEMPERATURES

Fig.6 shows the dependence of the concentration of nitrogen oxides on fuel consumption at different distances. As can be seen from the figure, the maximum concentrations are reached at a fuel consumption of 0.03 kg/s, as already noted above, since the fuel/air ratio is close to the stoichiometric one. The minimum concentrations are reached at a fuel consumption of 0.3 kg/s, due to the large amount of underburning fuel [13].

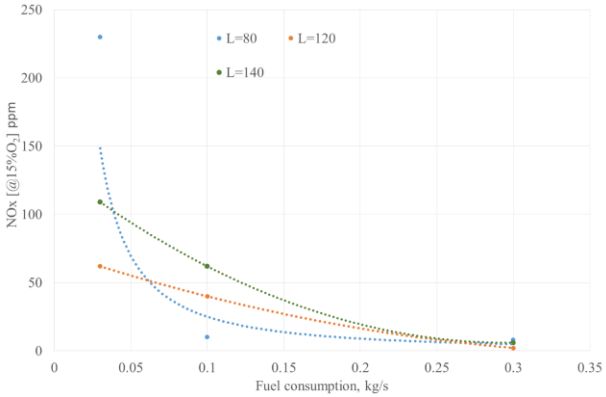

Fig.6. Concentrations of nitrogen oxides at the exit from the simulation zone

Fig.7 shows the dependence of the temperature at the output section of the simulation area on the fuel consumption and the distance between the corners. The temperature data corresponds to the nitrogen oxide data, and the maximum temperature corresponds to the minimum fuel consumption.

As can be seen from the figure, the temperature levels are approximately equal, but there is a

significant difference in nitrogen oxides, this is due to the time spent by high-temperature gases in the combustion zone.

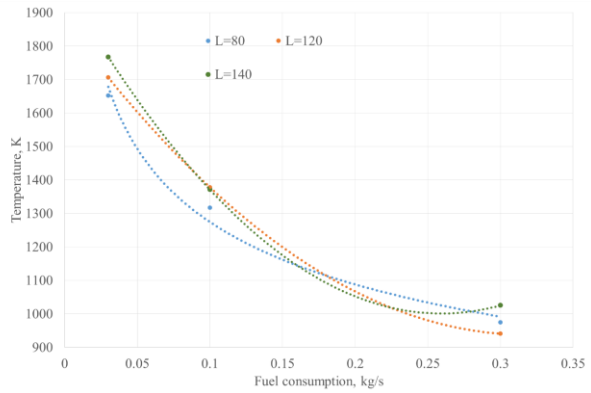

Fig.7. Temperature of exhaust gases at the exit from the simulation zone

CONCLUSIONS

The study shows that the angle of the v-gutter stabilizers are an effective way of stabilizing the combustion at relatively low concentrations of harmful substances. From the simulation, we can conclude that from the point of view of harmful substances and flame stabilization, it is best to use rows of corners with a distance of 100 mm. The highest concentrations of nitrogen oxides are formed at a distance of 140 mm and a fuel consumption of 0.1 kg/s. For variants L=80 mm, L=120 mm, and L=140 mm, the oxide concentrations at a flow rate of 0.1 kg/s were equal to 10, 60, and 109 ppm respectively.

REFERENCES

[1] Zheng Zhang, Kun Wu, Richard Yuen, Wei Yao, Jian Wang. Numerical investigation on the performance of bluff body augmented micro cavity-combustor. *International Journal of Hydrogen Energy*, (2020), in press.

[2] Zheng Zhang, Kun Wu, Wei Yao, Richard Yuen, Jian Wang. Enhancement of combustion performance in a microchannel: Synergistic effects of bluff-body and cavity. *Fuel*, **265** (2020)

[3] Jianfeng Pan, Chenxin Zhang, Zhenhua Pan, Di Wu, Yuejin Zhu, Qingbo Lu, Yi Zhang. Investigation on the effect of bluff body ball on the combustion characteristics for methane/oxygen in micro combustor. *Energy*, **190** (2020)

[4] Yunfei Yan, Ziqiang He, Qingyun Xu, Li Zhang, Lixian Li, Zhongqing Yang, Jingyu Ran. Numerical study on premixed hydrogen/air combustion characteristics in micro–combustor with slits on both sides of the bluff body. *International Journal of Hydrogen Energy*, **44 (3)**, 1998-2012 (2019).

[5] Yunfei Yan, Hongyu Yan, Li Zhang, Lixian Li, Junchen Zhu, Zhien Zhang. Numerical investigation on combustion characteristics of methane/air in a micro-combustor with a regular triangular pyramid bluff body. *International Journal of Hydrogen Energy*, Volume **43**, (15), 7581-7590 (2018).

[6] Lu-Qing Wang, Hong-Hao Ma, Zhao-Wu Shen, Jun Pan. Effects of bluff bodies on the propagation behaviours of gaseous detonation. *Combustion and Flame*, **201**, 118-128 (2019).

[7] Nabil Kharoua, Lyes Khezzar, Mohamed Alshehhi. The interaction of confined swirling flow with a conical bluff body: Numerical simulation. *Chemical Engineering Research and Design*, **136,** 207-218 (2018).

[8] Anthony J. Morales, Ian M. Lasky, Marissa K. Geikie, Christian A. Engelmann, Kareem A. Ahmed,Mechanisms of flame extinction and lean blowout of bluff body stabilized flames. *Combustion and Flame*, Volume **203**, 31-45 (2019).

[9] Juntian Niu, Jingyu Ran, Liya Li, Xuesen Du, Ruirui Wang, Mingchu Ran. Effects of trapezoidal bluff bodies on blow out limit of methane/air combustion in a micro-channel. *Applied Thermal Engineering*, **95**, 454-461 (2016).

[10] Harun Yilmaz. Investigation of combustion and emission performance of a micro combustor: Effects of bluff body insertion and oxygen enriched combustion conditions. *International Journal of Hydrogen Energy*, **44 (**47), 25985-25999 (2019).

[11] S.V. Tsanev, V.D. Burov, A.N. Remezov. Gas-turbine and combined-cycle plants of thermal power plants. - M.: Publishing House of MPEI, (2002) (in Russian)

[12] ANSYS FLUENT 12.0 Theory Guide: «ANSYS» http://ansys.com (2009).

[13] B. Ongar, I. K. Iliev, V. Nikolić and A. Milašinović. The study and the mechanism of nitrogen oxides' formation in combustion of fossil fuels. *Facta Universitatis, Series: Mechanical Engineering* **16 (**2), 273–283 (2018).

[14] Pchelkin Yu.M. Combustion chambers of gas turbine engines, Engineering Publishing House, 1984, (in Russian).

[15] A. M. Dostiyarov, A.G. Userov, T.B. Maysutov. Analysis of studies on emissions of toxic components of gas compressor units of type GTK-10-4 under operating conditions at the Makat compressor station at Atyrau UMG. *International Scientific and Practical Conference Energy, Telecommunications and Higher Education in Modern Conditions*, Almaty (2006).

[16] A. G. Tumanovsky. Some ways to reduce the concentration of nitrogen oxides in the combustion chambers of gas turbines. *Thermal Engineering*, **6,** 30-33 (1973).

[17] L. B. Davis, S. H. Black. GE Power Systems Schenectady, *General Electric Development Brochure. GER-3568G. New York; USA* (2008).

[18] A. S. Isserlin, Gas-burners, Nedra Publishing House, 1966.

[19] V. A. Khristich. About ways to reduce NOx emissions during the combustion of fuels with high and variable excess air, in: The formation of nitrogen oxides in combustion processes and ways to reduce their emission into the atmosphere, Naukova Dumka Publishing house, 33-37 (1979).

[20] V. A. Khristich, G. N. Lyubchik, L. S. Butovsky. On the discharge characteristics of the recirculation zone behind the corner stabilizer, *Bulletin of the KPI, ser. Heat power engineering* **8**, 27-30 (1971).

[21] P. M. Canilo. Numerical modeling of the formation of toxic substances in a gas turbine combustion chamber. *Institute of Mechanical Engineering of the Academy of Sciences of the Ukrainian SSR* **194**, 43 (1984).

[22] A. G. Tumanovsky, A. V. Sudarev, V. A. Mayev. Combustion of liquid fuel in counter-swirling jets of the GTU annular combustion chamber. *Thermal Engineering* **3**, 37-42, (1986).

[23] A. G. Tumanovsky, M. N. Gutnik, K. Yu. Sokolov. Reducing emissions of carbon monoxide and hydrocarbons at starting and variable modes of energy gas turbines when burning liquid and gaseous fuels. *Electric stations* **6**, 2-6, (1991).

[24] A. G. Tumanovsky, M. N. Gutnik, K. Yu. Sokolov. Low-toxic combustion chambers for energy gas turbines. *Thermal Engineering* **3**, 48-52 (1997).

[25] A. V. Sudarev. Development, research of optimal ways to intensify the working process and their implementation in the design of combustion chambers of stationary gas turbines. Doctoral thesis, USSR: MTU, 1980.

[26] M. M. Brevdo, Yu. I. Zakharov, V. A. Maev, A. M. Ponkratov, A. V. Sudarev. Operation results of microtorch annular combustion chambers of gas turbine units with a capacity of 25 MW at compressor stations of gas pipelines *Abstracts of the All-Union Scientific Conference, Moscow*, (1987).

[27] D. R. Umyshev, A. M. Dostiyarov, M. E. Tumanov, Qiuwang Wang. Experimental investigation of v-gutter flameholders. *Thermal science*, **21,** 1011-1019 (2017).

[28] D. R. Umyshev, A. M. Dostiyarov, G. M. Tuytebayeva. Experimental investigation of the management of NOx emissions and their dependence on different types of fuel supply. *Espacios*, **38,** 17 (2017).

[29] D. R. Umyshev, A. M. Dostiyarov, G. M. Tyutebayeva, A. K. Yamanbekova, B. T. Bakhtyar, Jordan Hristov. Effects of different fuel supply types on flame stabilization and nox emissions behind group of v-gutter flame holders: experimental and numerical study. *Thermal science*, **24,** 1A, 379-391 (2020).

[30] Bikram, R. et al.. Effects of Free Stream Flow Turbulence on Blow-Off Characteristics of Bluff-Body Stabilized Premixed Flames. *Combustion and Flame*, **190**, 302-316 (2018).

[31] Linhong Li, Aiwu Fan. A numerical study on non-premixed H2/air flame stability in a micro-combustor with a slotted bluff-body. *International Journal of Hydrogen Energy*, In press, 2020.

[32] Fulei Xu, Yunfei Yan, Ziqiang He, Zhongqing Yang, Li Zhang. Numerical study on the influence of controllable flow ratio on combustion characteristics of a controllable central slotted bluff body and cavity combined micro combustor. *International Journal of Hydrogen Energy*, In press, (2020).

[33] Sudhir Chandra Murmu, Suvanjan Bhattacharyya, Himadri Chattopadhyay, Ranjib Biswas. Analysis of heat transfer around bluff bodies with variable inlet turbulent intensity: A numerical simulation. *International Communications in Heat and Mass Transfer*, **117**, 104779, (2020).

Bulgarian Chemical Communications, Volume 52, Special Issue C (pp. 20-25) 2020 DOI: 10.34049/bcc.52.C.0029

Chemically Activated N-doped Hydrochar flakes and Char for energy applications

A. Plavniece[1,2*], G. Dobele[1], A. Volperts[1], A. Zhurinsh[1], K. Kaare[3], I. Kruusenberg[3], J. Locs[4]

[1] *Latvian State Institute of Wood Chemistry, Riga, Latvia*
[2] *Riga Technical University, Faculty of Material Science and Applied Chemistry, Riga, Latvia*
[3] *National Institute of Chemical Physics and Biophysics, Akadeemia tee 23, Tallinn, Estonia*
[4] *Rudolfs Cimdins Riga Biomaterials Innovations and Development Centre of RTU, Institute of General Chemical Engineering, Faculty of Materials Science and Applied Chemistry, Riga Technical University, Riga, Latvia*

Hydrochar and wood char are two differently obtained forms of carbon which variate in structure. Hydrothermal carbonization for hydrochar and traditional carbonization for wood char, followed by alkali activation and nitrogen doping with DCDA was used to obtain carbon materials. Material porosity, structure and composition were studied, as well as their application as cathodes for oxygen reduction in fuel cells using rotation disc electrode. It is shown that Activated N-doped Hydrochar, as well as Chemically Activated N-doped Wood char, have demonstrated promising electrochemical behaviour.

Keywords: wood, hydrothermal treatment, activated carbon, porous structure, fuel cells

INTRODUCTION

Nowadays production of activated carbon (AC) is one of the ways to obtain commercial products with added value. Activated carbon is used in methane and hydrogen storage, air purification, decaffeination, gold purification, metal extraction, water purification, medicine, sewage treatment, air filters in gas masks and respirators, filters in compressed air, teeth whitening, and many other applications. There are a number of properties which make AC an invaluable material for electrochemical applications since it is stable in various media, has a highly developed specific surface, sufficient electric conductivity and can be produced at a relatively low cost.

It is known that it is practically impossible to obtain highly porous carbon materials with the developed nanoporous structure without alkali activation. Before activation thermal or hydrothermal treatment is used to obtain char. Hydrothermal carbonization (HTC) is a pressurized treatment in liquid media where biomass is converted into solid carbon-rich materials at relatively low temperatures under autogenous pressures [1]. Basically, HTC is a thermo-chemical conversion technique which uses subcritical water or solvent for the conversion of wet or dry biomass into carbonaceous products [2]. Carbon-rich products, which are also referred to as hydrochar, are obtained by a series of reactions such as hydrolysis, dehydration, decarboxylation, demethanation, and aromatization [3].

HTC temperature is dependent on the type of starting materials and its decomposition temperature, typically using a range of 150 - 350^{o}C [4]. The hydrochar exhibits distinct characteristics, including sphere-like morphology and core-shell chemical structure with a hydrophobic nucleus and hydrophilic shell, with high oxygenated functional group (OFG) content which makes it an effective precursor for the production of chemically activated carbon. The HTC process offers several advantages over conventional dry-thermal pre-treatments like slow-pyrolysis in terms of improvements in the process performances and economic efficiency, especially its ability to process wet feedstock without pre-drying requirement. Char produced from both processes exhibits significantly different physicochemical properties that affect their potential applications [5]. Electrochemical properties of carbon materials depend on the ratio of basal planes and edge structures, and in general, are defined by the surface concentration of structural defects. According to this, the highest catalytic activity should be exhibited by the less-ordered activated carbons [6]. AC has highly dispersed structure and their specific surface can reach more than 2000 m^2 g^{-1}. Another important feature of biomass-based AC is the presence of micropores with a characteristic size of less than 2 nm. Also, AC has various surface oxygen groups which are being formed in the process of carbons synthesis and activation [7].

One of the advantages of carbon materials lies in the vast possibilities of their modification, which leads to new areas of application. For example,

* To whom all correspondence should be sent:
ance.plavniece@inbox.lv

introduction of various heteroatoms into the carbon matrix makes them more active for the electrocatalytic processes like the reduction of molecular oxygen [8] and electropositive metals [9], oxidation of volatile hydrides and organic compounds [10], [11], etc. Among the various heteroatoms (N, B, P, S), nitrogen has significant advantages for the modification of graphene-like materials since nitrogen and carbon has similar atomic sizes and can form a strong covalent bond. Theoretical studies [12] demonstrated that nitrogen can be viewed as an n-type donor for transferring electrons to carbon atoms. Application of N-doped carbon materials as catalysts of oxygen reduction in fuel cells for the transformation of chemical energy into electricity is another actual and prospective approach for the use of carbon materials. Fuel cells attract attention due to their high efficiency [13], independence from the power grid and longer operation times comparing to accumulators [14]. Alkali fuel cells are among the most effective devices for the generation of electricity as their efficiency reaches 70%. It is one of the most developed technologies which has been used from the 60s by NASA for Apollo and Space Shuttle programs [15].

Despite the considerable research efforts toward the increase of performance, efficiency and durability of fuel cells, there still is no successful upscale commercialization [16], [17]. Development of new non-platinum catalysts is one of the crucial problems for the widespread application of fuel cells. Besides price considerations, platinum or other precious materials containing catalysts are prone to catalyst poisoning and have rather poor stability [18], [19]. Thus it is highly important to develop cheap, non-platinum catalysts with the same electrochemical activity and higher stability [14].

The aim of this work was to synthesize activated carbons using wood charcoal and hydrochar as precursors, dope them with nitrogen to obtain electrochemical catalysts and study them in oxygen reduction reactions for fuel cells.

MATERIALS AND METHODS

Hydrochar (HTC) was produced from birch wood chips: 300g of dry wood chips were dispersed in 4l of distilled water, followed by its transfer into a stainless steel autoclave (Parr). The HTC reactor was heated to the target temperature and time. After the target time was reached reactor was cooled to room temperature, the solid product was collected by filtration and followed by drying at 105°C. In this study, the temperature was controlled at 250°C while the reaction times were set at 4h.

Hydrochar and wood char (SIA "Fille", Latvia) (AWC), were refined in a planetary mill, fraction ~$5x10^{-6}$ m. Activated carbons (AC) were obtained using a chemical activation method with NaOH. Activation process is described in details elsewhere [7], [20].

Nitrogen was introduced into activated samples using dicyandiamide (DCDA) solution in dimethylformamide with mass ratio of carbon material/DCDA 1:20. Doping was performed at 800°C for 1 hour in an argon atmosphere. For AWC additional heat treatment was used [21].
Porous characteristics were determined from nitrogen adsorption isotherms using Nova 4200e instrument (Quantachrome, USA).

The elementary composition was evaluated using the Vario Macro CHNSO device (Elementar, Germany).

X-ray diffraction (XRD) data were collected on a PANalytical X'Pert Pro diffractometer (Malvern Panalytical Ltd, UK). Cu Kα1 radiation was used, time per step was 50s, step size 0.050º2Θ, irradiated length 7 mm. X'Pert Highscore software and PDF-2 database were used for phase identification.

Scanning electronic microscopy (SEM) was performed using the Vega device (Tescan, Czech Republic).

The electrochemical measurements were performed with a standard three-electrode system using the rotating disk electrode (RDE) method. Saturated calomel electrode was used as a reference electrode and Pt foil was used as a counter electrode. Glassy carbon disk (GC-20SS, Tokai Carbon) with a geometric area of 0.2 cm^2 was used as a working electrode. The catalyst ink with a concentration of 4 mg mL^{-1} in isopropanol was prepared by using 0.25 % of AS-04 OH^- ionomer (Tokuyama Corp., Japan), followed by sonication for 1h. The electrodes were evenly covered with the catalyst material by drop coating with 20 µl of previously prepared catalyst ink. After coating the electrodes were dried in the oven at 60 ºC. Pine AFMSRCE (Pine, USA) rotator and speed controlling unit was used for the RDE

measurements. The software used for controlling the experiments was Nova 2.1.2 (Metrohm Autolab P.V., The Netherlands) and the potential was applied with a potentiostat/galvanostat Autolab PGSTAT 128N (Metrohm Autolab P.V., The Netherlands). Measurements were performed in 0.1 M KOH solution at room temperature (23ºC) at rotation rate of 1900 rpm. Electrode preparation, electrochemical and fuel cell testing has been discussed in more detail by S. Ratso *et al.* [22], [23].

RESULTS AND DISCUSSION

Carbon materials on the base of wood and its treatment residues, synthesized using NaOH activation, have demonstrated prospective properties when applied for electrochemical purposes, specifically as electrodes in supercapacitor [24–26]. In this study, the alkali activation method was used for the synthesis of activated carbons on the base hydrochar and wood char with consequent nitrogen doping.

Yields and elemental composition of all the materials under study are presented in Tab.1.

Table 1. Yield and elemental composition of wood char (Carbonizate), hydrochar (HTC), and AC based on wood char (AWC and AWC-N) and hydrochar (AHTC and AHTC-N) pre and post nitrogen doping

Sample	Yield*	N	C	H	O
	%	%	%	%	%
Alder wood	-	0.24	49.31	5.08	45.37
Carbonizate	35	0.78	82.54	1.94	14.53
AWC	11	0.7	93.8	0.62	4.75
AWC-N	-	4.92	91.53	0.82	2.73
HTC	49	0.17	69.92	4.12	25.79
AHTC	9	1.42	91.31	1.36	6.91
AHTC-N	-	5.31	90.05	1.81	2.55

*All yields are calculated from raw materials

The yield of HTC is considerably higher than that of wood char (Carbonizate) – 49 vs 35% respectively. At the same time, HTC contains notably less carbon, only 69.92 vs 82.54% and more oxygen, 25.79 vs 14.53%. These factors are important from the standpoint of activated carbon production and can influence the feasibility of the process taking into account concepts of biorefinery. Activated carbons prepared from both precursors have remarkably similar high carbon content. In the case of AC synthesized from HTC (AHTC) a higher oxygen and nitrogen contents are observed, which can be among the number of factors influencing higher N content in the doped sample (AWC-N and AHTC-N, respectively). Nitrogen doping does not lead to mass losses.

Morphology of the samples under study was evaluated using SEM (Fig.1). It can be seen that for HTC and AHTC (Fig.1 A and B) the distinct stratified structure consisting of layers of AHTC is formed in the process of activation. For the carbonizate and AWC, the structure does not change in the process of activation, however, the size and the shape of particles alters: their size diminishes and the edges become more rigid and pronounced (Fig.1 B and C).

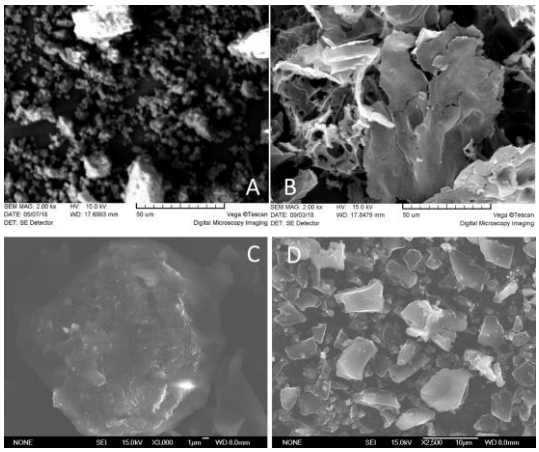

Fig.1. SEM images of hydrochar (HTC) (A), AC based on hydrochar (AHTC) (B), wood char (carbonizate) (C) and AC based on wood char (AWC) (D).

Table 2. Comparison of the porous structure of wood char (Carbonizate), hydrochar (HTC), and N-doped AC based on wood char (AWC-N) and hydrochar (AHTC-N)

Sample	Specific surface area (BET)	Total pore volume	Micropores volume (DR)	Mesopore volume
	$m^2\ g^{-1}$	$mm^3\ g^{-1}$	$mm^3\ g^{-1}$	$mm^3\ g^{-1}$
Carbonizate	6.91	72.24	35.14	37.10
AWC-N	2205	1157	767	390
HTC	4.22	11.33	1.15	10.18
AHTC-N	2853	1906	874	1032

Wood char and HTC have low porosity. AWC-N and AHTC-N demonstrate the high efficiency of alkali activation with specific surface areas 2205 and 2853 $m^2\ g^{-1}$ according to BET theory and total pore volumes 1157 and 1906 $m^2\ g^{-1}$, respectively. As described in the previous article comparing doped and non-doped samples specific area and total pore volume insignificantly decrease [27].

Comparing AWC-N and AHTC-N, the mesopore volume increases from 390 mm^3 g-1 to 1032 mm^3 g-1 and the micropore volume is similar for both materials, 767 and 874, respectively. The input of micropores into the total pore volume in the case of AHTC-N is less than half, which points at the mesoporous nature of this material. Micropore volume was calculated using the Dubinin-Radushkevich theory (DR) [28].

X-ray diffraction (XRD), generally considered the "ideal" technique for the structural characterization of materials, not only allows the structures of different carbon allotropes and polytypes to be distinguished from each other but also enables the degree to which the structure of a given carbon form departs from the ideal graphite structure to be determined [29]. Anything that changes interatomic distances, temperature, substitutional doping and stress will be reflected by a change in peak positions (Fig.2).

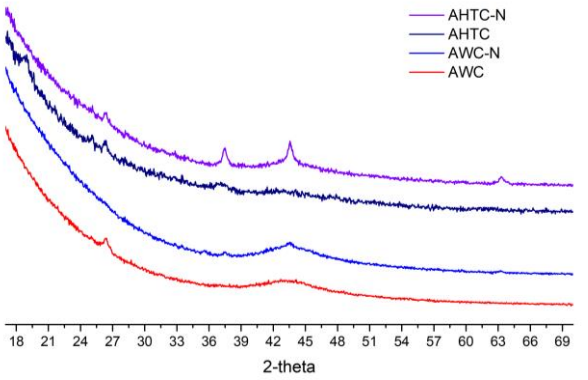

Fig.2. X-ray diffraction patterns of AC based on wood char (AWC), and hydrochar (AHTC), nitrogen-doped AC based on wood char (AWC-N) and hydrochar (AHTC-N)

All diffraction profiles exhibit two prominent broad bands centred around 2θ = 26 and 43°, which are currently mentioned as associated with the diffraction of the 002 and 100/101 planes, respectively, with 43° being sharper in the case of doped carbons, especially prominent for AHTC-N. The peak at around 64° belongs to (103) crystal plane, reflections assigned to graphite [30], it likely appears due to the higher temperature treatment (800°C) during the doping process. These are characteristic of typical graphitic structure and are associated with the crystallite height and width, they become more prominent with the treatment of carbonaceous materials at the higher temperatures [31].

Rotating disc electrode technique is widely applied to study the oxygen reduction mechanisms at the cathode for fuel cells [32]. Fig.3. illustrates catalyst polarization curves of the electrodes made from samples under study comparing to commercial 20% Pt/C-electrode and multiwall carbon nanotubes (MWCNT). To evaluate the ORR (oxygen reduction reaction) activity of a catalyst material, the onset potential is an important criterion, which for both biomass-derived nitrogen-doped wood-based carbons is approximately at -0.09 V vs SCE. It should be noted that AWC shows good results only after additional heat treatment. Despite increasing the rotation rate, the onset potential remained the same indicating at least short-term stability of the catalyst.

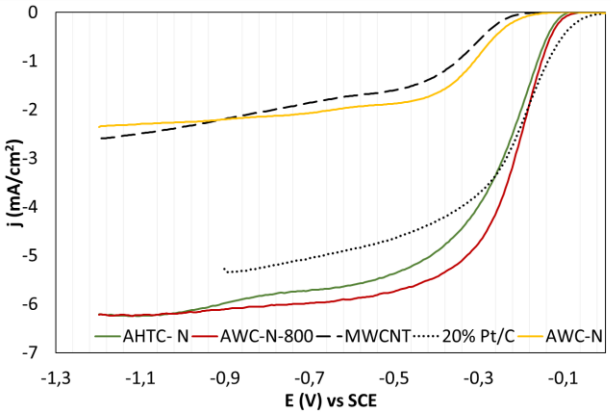

Fig.3. Comparison of RDE results for nitrogen-doped AC based on wood char (AWC-N and AWC-N-800 without and with additional thermal treatment) and hydrochar (AHTC-N), multiwall carbon nanotubes (MWCNT), and commercial 20% Pt/C catalyst in O_2 saturated 0.1 M KOH (v =10 mV/s, ω=1900 rpm)

The onset potential and half-wave potential for both N-doped wood-based catalysts are much more positive compared to multiwall carbon nanotubes (MWCNT) which are often used as electrode material in various types of fuel cells [33], [34].

CONCLUSIONS

Two methods, namely carbonization and hydrothermal treatment are compared for the synthesis of the nitrogen-doped activated carbons. Carbons porosity, structure and composition were studied and revealed differences in their structure.

Carbons porosity, structure and composition were studied and revealed differences in their structure. It is shown, that hydrothermal treatment promotes the development of mesoporosity in the materials. It is demonstrated that both pretreatment methods allow obtaining of nanporous carbons, and hytrothermal method leads to development of the higher mesoporosity. Doping with DCDA (nitrogen content 4-5%) leads decrease of oxygen in the samples and negligible alterations in the porous structure.

Both nitrogen-doped activated biomass-based catalysts were tested using rotation disc electrode for application as cathodes for oxygen reduction in fuel cells. An onset potential of -0.09 V vs SCE and a half-wave potential of -0.16-0.18 V vs SCE in an alkaline medium, along with excellent stability, are making them promising alternatives to state-of-art precious-metal-based catalysts and excellent catalyst carrier for many different applications. The superiority of the wood-derived catalysts is demonstrated with even similar oxygen reduction reaction activity comparable to the commercial 20% Pt/C catalyst in 0.1 M KOH solution. It is demonstrated that the most active catalyst was obtained in sequence of hydrothermal pretreatment, alkali activation and nitrogen doping. To reach the same catalytic properties for the materials obtained in the course of conventional carbonization, activation and nitrogen doping the additional thermal treatment was required.

Taking into account biorefinery and green chemistry concepts hydrothermal treatment offers another promising approach for the synthesis of novel highly efficient and ecologically friendly catalysts.

ACKNOWLEDGEMENTS

The study was supported by LZP-2018/1-0194 project “Nanostructured Nitrogenated Carbon Materials as Promoters in Energy Harvesting and Storage Technologies (NN-CARMA)”, Riga Technical University's Doctoral Grant programme and Latvian State Institute Of Wood Chemistry Grant “Biobased catalysts for biorefining”.

REFERENCES

[1] K. Fakkaew, T. Koottatep, and C. Polprasert, “Faecal sludge treatment and utilization by hydrothermal carbonization,” *J. Environ. Manage.*,**216**, 421–426 (2018).

[2] Z. Liu, F.-S. Zhang, J. Wu. Characterization and application of chars produced from pinewood pyrolysis and hydrothermal treatment. *Fuel*, **89**, (2), 510–514 (2010).

[3] G. K. Parshetti, S. Kent Hoekman, R. Balasubramanian. Chemical, structural and combustion characteristics of carbonaceous products obtained by hydrothermal carbonization of palm empty fruit bunches. *Bioresour. Technol.*, **135**, 683–689 (2013).

[4] M. Sevilla, A. B. Fuertes, and R. Mokaya. High density hydrogen storage in superactivated carbons from hydrothermally carbonized renewable organic materials. *Energy Environ. Sci.*, **4** (4), 1400 (2011).

[5] H. S. Kambo, A. Dutta. A comparative review of biochar and hydrochar in terms of production, physico-chemical properties and applications. *Renew. Sustain. Energy Rev.*, **45**, 359–378 (2015).

[6] S. L. Candelaria et al. Nanostructured carbon for energy storage and conversion. *Nano Energy*, **1**, 195–220 (2012).

[7] G. Dobele, T. Dizhbite, M. V. V. Gil, A. Volperts, T. A. Centeno. Production of nanoporous carbons from wood processing wastes and their use in supercapacitors and CO2 capture. *Biomass and Bioenergy*, **46**, 145–154 (2012).

[8] V. V. Strelko, V. S. Kuts, P. A. Thrower. On the mechanism of possible influence of heteroatoms of nitrogen, boron and phosphorus in a carbon matrix on the catalytic activity of carbons in electron transfer reactions. *Carbon*, **38** (10), 1499–1503 (2000).

[9] V. V. Strelko, Selektivnaâ sorbciâ i kataliz : na aktivnyh uglâh i neorganičeskih ionitah. Kiyv: Naukova Dumka, 2008.

[10] A. Bagreev, J. Angel Menendez, I. Dukhno, Y. Tarasenko, T. J. Bandosz. Bituminous coal-based activated carbons modified with nitrogen as adsorbents of hydrogen sulfide. *Carbon N. Y.*, **42**, (3), 469–476 (2004).

[11] S. V. Mikhalovsky, Y. P. Zaitsev. Catalytic properties of activated carbons I. Gas-phase oxidation of hydrogen sulphide. *Carbon N. Y.*, **35**, (9), 1367–1374 (1997).

[12] S. U. Lee, R. V. Belosludov, H. Mizuseki, Y. Kawazoe. Designing nanogadgetry for nanoelectronic devices with nitrogen-doped capped carbon nanotubes. *Small*, **5** (15), 1769–1775, (2009).

[13] F. Barbir, T. Gómez. Efficiency and economics of proton exchange membrane (PEM) fuel cells. *Int.*

J. Hydrogen Energy, **22** (10–11), 1027–1037 (1997).
[14]O. Gröger, H. A. Gasteiger, J.-P. Suchsland, "Review—Electromobility: Batteries or Fuel Cells?. *J. Electrochem. Soc.*, **162**, (14), 2605–2622 (2015).
[15]M. C. Williams. Fuel Cells. *Fuel Cells Technol. Fuel Process.*, 11–27 (2011).
[16]M. K. Debe, Electrocatalyst approaches and challenges for automotive fuel cells. *Nature*, **486**, (7401), 43–51 (2012).
[17]Y. M. Volfkovich, V. E. Sosenkin, and V. S. Bagotsky, "Structural and wetting properties of fuel cell components," J. Power Sources, vol. 195, no. 17, pp. 5429–5441, Sep. 2010.
[18]V. S. Bagotzky, N. V. Osetrova, A. M. Skundin. Fuel Cells: State-of-the-Art and Major Scientific and Engineering Problems. *Russ. J. Electrochem*., **39** (9), 919–934 (2003).
[19]X. Cheng et al. A review of PEM hydrogen fuel cell contamination: Impacts, mechanisms, and mitigation. *J. Power Sources*, **165** (2), 739–756 (2007).
[20]G. Dobele, D. Vervikishko, A. Volperts, N. Bogdanovich, E. Shkolnikov. Characterization of the pore structure of nanoporous activated carbons produced from wood waste. *Holzforschung*, **67** (5), 587–594 (2013).
[21]K. Kaare et al. Highly active wood-derived nitrogen-doped carbon catalyst for the oxygen reduction reaction. *ACS Omega*, **5** (37), 23578–23587 (2020).
[22]S. Ratso et al. Highly active nitrogen-doped few-layer graphene/carbon nanotube composite electrocatalyst for oxygen reduction reaction in alkaline media. *Carbon N. Y.*, **73**, 361–370 (2014).
[23]S. Ratso, I. Kruusenberg, U. Joost, R. Saar, K. Tammeveski. Enhanced oxygen reduction reaction activity of nitrogen-doped graphene/multi-walled carbon nanotube catalysts in alkaline media. *Int. J. Hydrogen Energy*, **41** (47), 22510–22519 (2016).
[24]G. Dobele et al. Wood-based activated carbons for supercapacitors with organic electrolyte. *Holzforschung*, **69** (6), 777–784 (2015).
[25]A. Volperts, G. Dobele, D. Vervikishko, and E. Shkolnikov. Nanoporous wood based carbon materials for supercapacitors electrodes, 2014.
[26]G. Dobele, A. Volperts, A. Plavniece, A. Zhurinsh, I. Kruusenberg. Wood-based nitrogen doped activated carbons for fuel cells. 18–21.
[27]A. Volperts et al. Biomass based activated carbons for fuel cells. *Renew. Energy*, **141** (2019).
[28]R. C. Bansal and M. Goyal, Activated carbon adsorption. Taylor & Francis, 2005.
[29]E. J. Bottani and J. M. D. Tascón, Adsorption by carbons. Elsevier, 2008.
[30]J. C. Arrebola, A. Caballero, L. Hernán, J. Morales. Graphitized carbons of variable morphology and crystallinity: A comparative study of their performance in lithium cells. *J. Electrochem. Soc.*, **156** (12) (2009).
[31]H. Aso, K. Matsuoka, A. Sharma, A. Tomita. Structural analysis of PVC and PFA carbons prepared at 500-1000°C based on elemental composition, XRD, and HRTEM. *Carbon N. Y.*, **42** (14), 2963–2973 (2004).
[32]S.-J. Lee, S.-I. Pyun, S.-K. Lee, S.-J. L. Kang. Fundamentals of Rotating Disc and Ring-Disc Electrode Techniques and their Applications to Study of the Oxygen Reduction Mechanism at Pt/C Electrode for Fuel Cells. *Isr. J. Chem*., **48**, (3–4), 215–228 (2008).
[33]N. Thepsuparungsikul, N. Phonthamachai, H. Y. Ng. Multi-walled carbon nanotubes as electrode material for microbial fuel cells. *Water Sci. Technol.* **65** (7), 1208–1214 (2012).
[34]C. Luo, H. Xie, Q. Wang, G. Luo, C. Liu. A Review of the Application and Performance of Carbon Nanotubes in Fuel Cells. *J. Nanomater.*, 1–10 (2015).

Bulgarian Chemical Communications, Volume 52, Special Issue C (pp. 26-31) 2020 DOI: 10.34049/bcc.52.C.0048

Reduction harmful emissions at the pulverized fuel combustion in the furnace chamber

A. S. Askarova [1,3], P. Safarik[2], S. A. Bolegenova [1,3], V.Yu. Maximov[1], S. A. Bolegenova [3], A.O. Nugymanova[1*], R. K. Manatbayev[1], Zh.K. Shortanbayeva[1]

[1]Al-Farabi Kazakh National University, Dept. of Physics and Technology, 71a, Al-Farabi ave, 050040 Almaty, Kazakhstan

[2] Czech Technical University in Prague, Faculty of Mechanical Engineering, 166 07 Praha 6, Czech Republic

[3] Scientific Research Institute of Experimental and Theoretical Physics, Tole bi 96 a, 050012, Almaty, Kazakhstan

The basic characteristics of heat and mass transfer processes in the furnace chamber of the BKZ-75 boiler of the Shakhtinskaya thermal power plant (Kazakhstan) using numerical methods were studied during a forced partial stop of the supply of coal dust through burners. Two methods were studied: 1– a direct-flow method of supplying air mixtures: two direct-flow burners are working and two are in emergency mode; 2 – vortex method of supplying air mixtures: two vortex burners with a swirl angle of the air mixture flow and their inclination to the center of symmetry of the boiler by 30 degrees and two are in emergency mode. The numerical experiments allowed to obtain the temperature fields and concentration of carbon monoxides CO, nitrogen dioxide NO_2 throughout the entire volume of the combustion chamber and conduct a comparative analysis for the two investigated emergency mode. It can be concluded that in the case of a forced partial stop of the supply of coal dust, the use of the vortex method of supplying air mixtures improves heat and mass transfer processes and allows minimizing emissions of harmful substances.

Keywords: numerical modeling, thermal power station, combustion, off-design performance, coal, carbon monoxides, nitrogen dioxide

INTRODUCTION

Coal in Kazakhstan has several advantages: low sulphur content, high volatile content, on a dry ash less mass and low price, because the coal is mined in open cast mainly. It is characterized by its low rating due to the high ash content in its composition (more than 40%) [1-9]. As a result, the use of such fuel in the power system leads to problems in flame stabilization and combustion in general, in slagging of convective heating surfaces (furnace walls) and air pollution from fly ash, carbon monoxide, nitrogen oxides and other combustion products. Using low-grade coals increases the consumption of fuel oil or natural gas used to melt the boiler, pick up and stabilize the burning of the dust torch, and the environmental situation worsens [10-15].

In this work, a computer package of applications of Florean [16-23] applied programs was used as a basis for the conduct of computational experiments on thermal transfer processes using 3D modeling in the combustion chamber of the thermal power plant. Studies have been conducted to determine the effect of a forced partial stop of the supply of coal dust through the burner devices on the main characteristics of the combustion chamber of the BKZ-75 boiler of the Shakhtinskaya thermal power plant (TPP, Kazakhstan) [24-29].

* To whom all correspondence should be sent:
nugymanova.aizhana@gmail.com

INITIAL DATA FOR COMPUTATIONAL EXPERIMENTS

The BKZ-75 boiler of the Shakhtinskaya TPP (Kazakhstan) was chosen as the object of the study. The boiler is equipped with four pulverized coal burners which installed in two on the front and back walls in one tier. A more detailed description of the boiler's combustion chamber, mathematical model, solution method, application software package was given in previously published articles and included in the list of references [30-40]. The boiler burns the dust of Karaganda ordinary coal, with an ash content of 35.1%, a yield of volatile 22% and a calorific value of 18.55 MJ/kg.

For carrying out of computing experiments the geometry of investigated object according to the real scheme (Fig.1).The finite difference grid has steps along the X, Y, Z axes of: 59×32×67, which is 138 355 control volumes. Two modes of fuel supply were investigated: a direct-flow method of delivering the air mixture, when two direct-flow burners are working, two are in emergency mode and a vortex method of delivering the air mixture - two vortex burners with an angle of swirl of the air mixture and their inclination to the boiler symmetry center by 30 degrees; two are in emergency mode.

Fig.1 shows the design of the burners of the furnace chamber of the boiler BKZ-75 in **emergency mode** (off burners are marked in red).

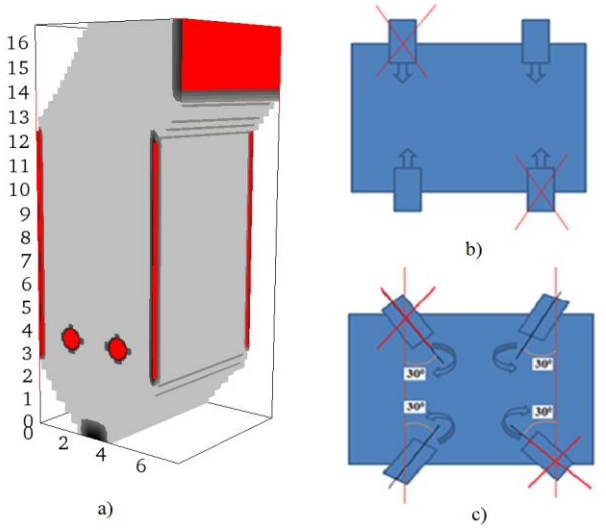

Fig.1. General view (a) and designs of the burners of the furnace chamber of the BKZ-75 boiler in emergency mode: (b) direct-flow method of supplying air mixture; (c) vortex method of supplying air mixture

MATHEMATICAL MODEL OF THE PROBLEM

In the present work, the physical, mathematical, and chemical models have been used for investigating the heat and mass transfer in high-temperature media. These models include the system of three-dimensional Navier-Stokes equations and the heat and mass transfer equations with allowance for source terms, which are determined by the process chemical kinetics, nonlinear effects of thermal radiation, interfacial interaction as well as by many stages of chemical reactions.

The governing equations employed for the solution of the posed problem:

- the mass conservation law (the continuity equation);
- the momentum conservation law (the Navier–Stokes equation);
- the energy conservation law (the first law of thermodynamics);
- the conservation law for the mixture components.

In this article the employed governing equations in the generalized form as follows:

$$\frac{\partial(\rho\phi)}{\partial t} = -\frac{\partial(\rho u_1\phi)}{\partial x_1} - \frac{\partial(\rho u_2\phi)}{\partial x_2} - \frac{\partial(\rho u_3\phi)}{\partial x_3} + \frac{\partial}{\partial x_1}\left[\Gamma_\phi \frac{\partial\phi}{\partial x_1}\right] + \frac{\partial}{\partial x_2}\left[\Gamma_\phi \frac{\partial\phi}{\partial x_2}\right] + \frac{\partial}{\partial x_3}\left[\Gamma_\phi \frac{\partial\phi}{\partial x_3}\right] + S_\phi \quad (1)$$

where ϕ is the transport variable, S_ϕ is the source term determined by the chemical kinetics of the process, nonlinear effects of thermal radiation, interfacial interaction as well as by the multi-stage character of chemical reactions.

RESULTS AND DISCUSSION

Fig.2 shows three-dimensional temperature distributions characterizing the thermal behavior of the pulverized-coal flow in the combustion chamber for the two studied modes of supply of air mixture (direct-flow and vortex). Compared to using the direct-flow method of supplying the air mixture, the average temperature of the furnace chamber of the BKZ-75 boiler during the vortex method of supplying the air mixture increases both the central section 991.6°C. This is due to the vortex nature of the flow, providing maximum convective transport and an increase in the residence time of coal particles in the furnace chamber of the BKZ-75 boiler.

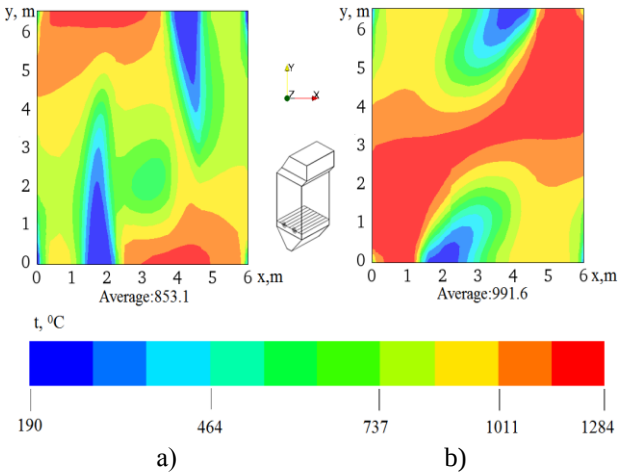

Fig.2. Distribution of the temperature in in the burner section (z=4) of the combustion chamber of the boiler BKZ-75 during emergency mode: a) direct-flow method of supplying air mixture; b) the vortex method of supplying air mixture

Fig.3 presents a comparative analysis of the distribution of the average temperature along the height of the combustion chamber for the two studied modes. We observe an increase in the zone of maximum temperatures (curve 1) with the vortex method of supplying the air mixture (curve 2). The temperature at the outlet of the combustion chamber in this case is less than with the direct-flow method of supplying the air mixture and its value is 836^0C versus 847^0C. The temperature at the outlet of the combustion chamber (base version) is confirmed by experimental data at TPPs and

theoretical value calculated by the method of CBTI (Central Boiler-and-Turbine Institute) for direct-flow supplying of air mixture [41-42].

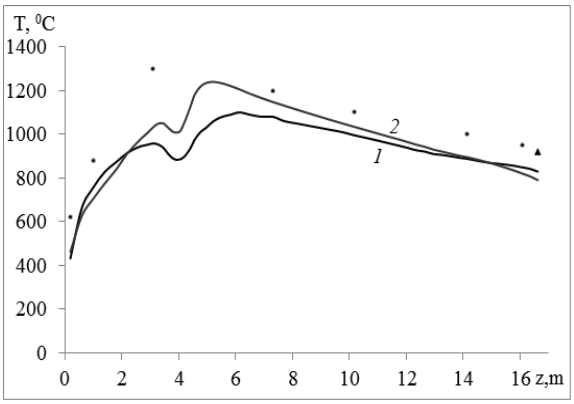

Fig.3. Distribution of the temperature T along the height of the combustion chamber of the BKZ-75 boiler in emergency mode:1- direct-flow method of supplying air mixture; 2- vortex method of supplying air mixture; ● experimental data at TPPs [41]; ▲- is theoretical values obtained by the method of thermal calculation[42]

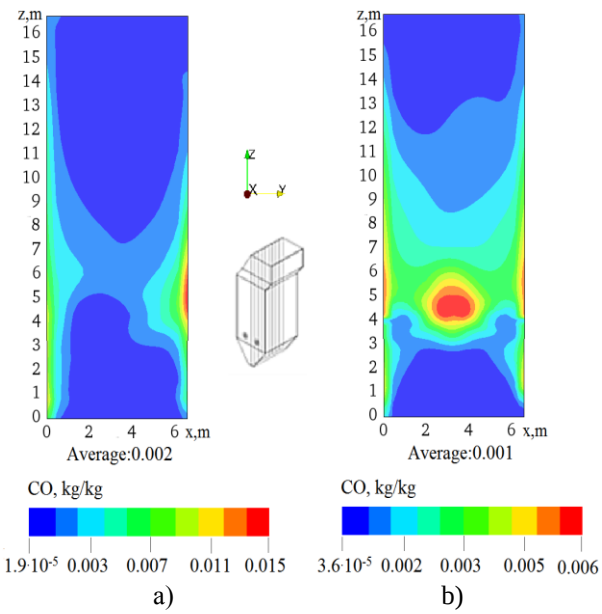

Fig.4. Distribution of carbon monoxide CO in the central sections (x=3) of the furnace chamber of the boiler BKZ-75 in emergency mode:a) direct-flow method of supplying air mixture; b) the vortex method of supplying air mixture

Fig.4 illustrates the distribution of carbon monoxide CO in central section of the combustion chamber of the BKZ-75 boiler. An analysis of the figure shows that with a direct-flow method of supplying an air mixture, the average values of the concentration of carbon monoxide CO in the central longitudinal sections (x=3) are 0.002 kg/kg, while with a vortex method of supplying an air mixture, the minimum average values of the concentration of carbon monoxide CO are observed – 0.001 kg/kg. It can be noted that the maximum values of the concentration of carbon monoxide CO are observed in the region where the burner devices are located, and at the outlet from the combustion chamber its concentration decreases. The concentration of carbon monoxide CO at the outlet of the combustion chamber is $5.2 \cdot 10^{-4}$ kg/kg for direct-flow method of supplying air mixture, and $3.4 \cdot 10^{-4}$ kg/kg for the vortex method of supplying the mixture. This is confirmed by Fig.5, which shows the curves of the distribution of the concentration of carbon monoxide CO over the height of the combustion chamber of the BKZ-75 boiler for the two studied cases.

Fig.5 illustrates the distribution of concentrations carbon monoxide CO in different sections of the combustion chamber of the BKZ-75 boiler.

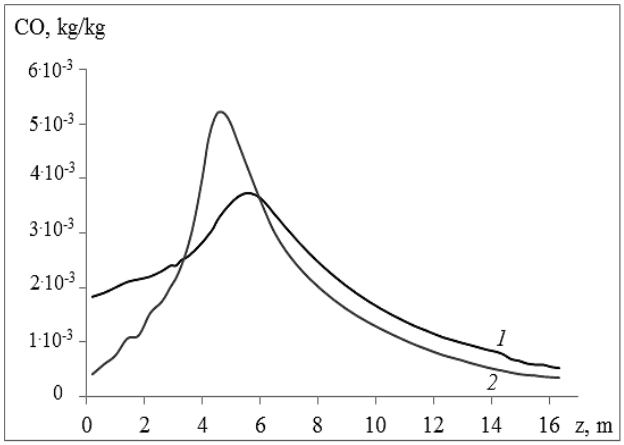

Fig.5. Distribution of the concentration of carbon monoxide CO along the height of the combustion chamber of the BKZ-75 boiler in emergency mode:1- direct-flow method of supplying air mixture; 2- vortex method of supplying air mixture

The concentration distributions of nitrogen dioxide NO_2 in central sections of the combustion chamber are shown in Fig.6. An analysis of these figures shows that the main gas formation of nitrogen dioxide NO_2 occurs in the area of propagation of flows from the burners. Intensive mixing of fuel and oxidizing agent created by turbulent flows of injected aerosol mixtures near the burners, as well as the high temperature in the torch core, create favorable conditions for the formation of nitrogen dioxides. In this area, the concentration of nitrogen dioxide NO_2 reaches its average values is equal to 791 mg/nm^3 with a

direct-flow method of supplying air mixture, and 852 mg/nm^3 with a vortex method of delivering an air mixture.

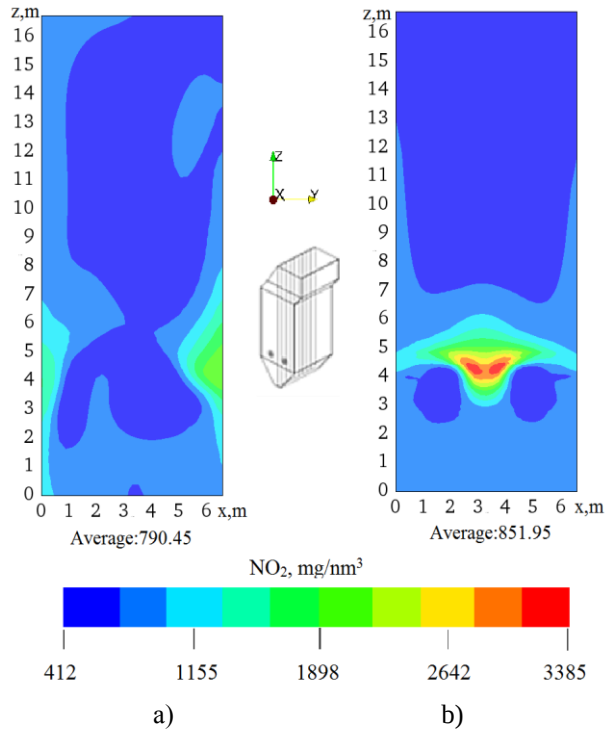

Fig. 6. Distribution of nitrogen dioxide NO_2 in the central sections (x=3) of the furnace chamber of the boiler BKZ-75 in emergency mode:a) direct-flow method of supplying air mixture; b) the vortex method of supplying air mixture

Fig.7 shows a graph of distribution of nitrogen dioxide NO_2 along the height of the combustion chamber of the BKZ-75 boiler in emergency mode for the two studied modes of supply of air mixture (direct-flow and vortex).

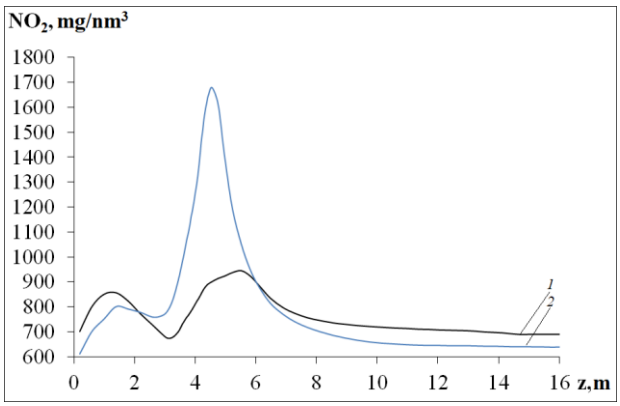

Fig.7. Distribution of nitrogen dioxide NO_2 along the height of the combustion chamber of the BKZ-75 boiler in emergency mode:1- direct-flow method of supplying air mixture; 2- vortex method of supplying air mixture

We see that the use of the vortex method of supplying air mixture leads to a decrease in the total concentration of nitrogen dioxide NO_2 at the outlet from the furnace space and amounts to 638 mg/Nm^3 (curve 1), and for the direct-flow method of supplying air mixture 688 mg/Nm^3 (curve 2).

CONCLUSIONS

The results of computational experiments are presented: temperature fields T, concentration fields of carbon oxides CO and nitrogen dioxide NO_2 over the entire volume of the combustion chamber and their comparative analysis for the two studied modes of supply of air mixture (direct-flow and vortex). Based on the results of studies on **emergency mode** of burner devices, the following conclusions can be drawn:

- The use of vortex burners in the combustion chambers of coal-fired TPPs can significantly optimize the combustion process of low-grade high-ash coals and significantly reduce emissions of harmful substances (NO_2 and CO) into the environment.
- The vortex method of supplying air mixture into the burner devices of the combustion chamber leads to a decrease in temperature T, the concentration of carbon oxides CO and nitrogen oxides NO at the outlet of the combustion chamber.
- At the outlet carbon monoxide CO and nitrogen dioxide NO_2 concentrations are less than the maximum permissible concentration (MPC) accepted in Kazakhstan. Thus, we can conclude that the vortex method of supplying air mixtures in the combustion chambers of energy boilers significantly improves the environmental performance of thermal power plants.

ACKNOWLEDGEMENTS

This work has been supported financially by the Ministry of Education and Science of the Republic of Kazakhstan No.AP09261161 and No.AP08857288.

REFERENCES

[1] H. Muller, R. Leithner Combustion of low-rank coals in furnaces of Kazakhstan coal-firing power plants. *VDI Berichte*, 497-502 (2007).

[2] M. Beketayeva, Z. Gabitova, A. Bekmukhamet Control harmful emissions concentration into the atmosphere of megacities of Kazakhstan Republic. *International conference on Future Information Engineering, Beijing, Peoples China*, **10**, 252-258 (2014). DOI: 10.1016/j.ieri.2014.09.085.

[3] M.T. Beketayeva, S.A. Bolegenova, et al. Computational method for investigation of solid fuel combustion in combustion chambers of a heat power plant. *High Temperature*, **53**(5), 751-757 (2015).

[4] Sh. Ospanova, S. Bolegenova, A. Ergalieva 3D modeling of heat and mass transfer during combustion of solid fuel in BKZ-420-140-7C combustion chamber of Kazakhstan. *Journal of Applied Fluid Mechanics*, **9**(12), 699-709 (2016). DOI:10.18869/acadpub.jafm.68.225.22881.

[5] S.A. Bolegenova, A.B. Syzdykov Investigation of the different Reynolds numbers influence on the atomization and combustion processes of liquid fuel. *Bulgarian Chemical Communications*, **50,** 68-77 (2018).

[6] A.S. Askarova, et al. Processes of heat and mass transfer in furnace chambers with combustion of thermochemically activated fuel. *Thermophysics and Aeromechanics*, **26**(6), 925-937, (2019).

[7] V.Maximov, S.A. Bolegenova, M.T. Beketayeva Numerical experimenting of combustion in the real boiler of CHP. *International J. of Mechanics*, **7**(13), 343-352 (2013).

[8] Z. Gabitova, A. Yergaliyeva, Zh. Shortanbayeva Simulation of the aerodynamics and combustion of a turbulent pulverized-coal flame. *Proc. of 4th International Conference on Mathematics and Computers in Sciences and in Industry (MCSI 2017). Corfu Island, Greece*, 92-97 (2017).

[9] A. Georgiev, Zh.T. Baizhuma, A.O. Nugymanova The use of a new "clean" technology for burning low-grade coal in on boilers of Kazakhstan TPPs. *Bulgarian Chemical Communications*, **50**, 53-60 (2018).

[10] S.A. Bolegenova, S. Ospanova, Z. Gabitova Investigation of turbulence characteristics of burning process of the solid fuel in BKZ 420 combustion chamber. *WSEAS Transactions on Heat and Mass Transfe*r, **9**, 39-50 (2014).

[11] S. Bolegenova, et al. Numerical modeling of burning pulverized coal in the combustion chamber of the boiler PK 39. *News of the national academy of sciences of the Republic of Kazakhstan-series physico-mathematical*, **2**(312), 58-63 (2017).

[12] M. Buchmann, A. Askarowa Structure of the flame of fluidized-bed burners and combustion processes of high-ash coal. *Proceedings of 18th Dutch-German Conference on Flames, VDI Berichte*, **1313,** 241-244 (1997).

[13] P. Safarik, V. Maximov Investigation of heat and mass transfer processes in the combustion chamber of industrial power plant boiler. Part 2. Distribution of concentrations of O_2, CO, CO_2, NO. *J. Applied and Computational Mechanics*, **12,** 127-138 (2018).

[14] R. Manatbayev, N. Mazhrenova 3D modelling of heat and mass transfer processes during the combustion of liquid fuel, *Bulgarian Chemical Communications*, **48,** 229-235 (2016).

[15] A.S.Askarova, Z.K. Shortanbayeva On the effect of the temperature boundary conditions on the walls for the processes of heat and mass transfer. *International J. Mechanics*. **10**, 349–355 (2016).

[16] R. Leithner, H. Muller, A.Askarova CFD code FLOREAN for industrial boilers simulations. *WSEAS Transactions on Heat and Mass Transfer*, **4**(4), 98-107 (2009).

[17] S.A. Bolegenova, E.I. Heierle CFD study of harmful substances production in coal-fired power plant of Kazakhstan. *Bulgarian chemical communications*, **48,** 260-265 (2016).

[18] A.S.Askarova, Yu.V.Maximov 3D-modelling of Kazakhstan low-grade coal burning in power boilers of thermal power plant with application of plasma gasification and stabilization technologies. J. *of Physics: Conference Series*, **1261-1**, 12-22 (2019) DOI:10.1088/1742-6596/1261/1/012022.

[19] V.E. Messerle, I.V. E.I. Karpenko, Optimization of the combustion of power station coals using plasma technologies. *J. Thermal Engineering*, **51**(6), 488-493 (2004).

[20] R. Leithner, A. Nugymanova Computational modeling of heat and mass transfer processes in combustion chamber at power plant of Kazakhstan. *MATEC Web of Conferences*, **76**, 06001. (2016).

[21] Z.Gabitova, S. Ospanova Using 3D modeling technology for investigation of conventional combustion mode of BKZ-420-140-7C combustion chamber. *J. of Engineering and Applied Sciences*, **9**(1), 24-28 (2014). DOI: 10.3923/jeasci.2014.24.28.

[22] V.E. Messerle, A.S. Askarova, A.B. Ustimenko Reduction of noxious substance emissions at the pulverized fuel combustion in the combustor of the BKZ-160 boiler of the Almaty heat electro power station using the "Overfire Air" technology. *Thermophysics and Aeromechanics*, **23**(1), 125-134 (2016). https://doi.org/10.1134/S0869864316010133.

[23] V. E. Messerle, V. Yu. Maksimov, A.B. Ustimenko et al. Numerical simulation of the coal combustion process initiated by a plasma source. *Thermophysics and Aeromechanics*, **21**(6), 747-754 (2014).

[24] A.S. Askarova, P. Safarik, M.T. Beketayeva Modern computing experiments on pulverized coal combustion processes in boiler furnaces. *News of the national academy of sciences of the Republic of Kazakhstan-series Physico-mathematical*, **6**(322), 5-14 (2018).

[25] R.K. Manatbayev, Sh.S Ospanova, V.Yu.Maximov, The computational study of heat and mass transfer processes at combustion of pulverized Kazakh coal in real conditions of

energy objects. *Bulgarian Chemical Communications*, **50,** 61-67 (2018).

[26] A. Askarova, P. Safarik 3D computer simulation of heat and mass transfer processes to improve the energy efficiency of combustion chambers. *Bulgarian Chemical Communications*, **51**(F), 11-18 (2019).

[27] P. Safarik, V.Yu. Maximov, S.A. Bolegenova 3D modeling of combustion thermochemical activated fuel. *News of the national academy of sciences of the Republic of Kazakhstan-series physico-mathematical*, **2**(324), 9-16 (2019).

[28] A.S. Askarova, S.A. Bolegenova, M.T. Beketayeva Modeling of heat mass transfer in high-temperature reacting flows with combustion. *J. High Temperature*, **56**(5), 738-743 (2018).

[29] P. Safarik, S.Bolegenova, A.Nugymanova Simulation of low-grade coal combustion in real chambers of energy objects. *J. Acta Polytechnica*, **59**(2), 98-108 (2019). DOI:10.14311/AP.2019.59.0098.

[30] A.S. Askarova, et al. Numerical research of aerodynamic characteristics of combustion chamber BKZ-75 mining thermal power station. *Procedia Engineering*, **42,** 1250-1259 (2012). DOI:10.1016/j.proeng.2012.07.507.

[31] P. Safarik, A.S. Askarova, et al. 3-D modeling of the aerodynamics and heat transfer process during the combustion of solid fuel in a swirl furnace. *J. Acta Polytechnica*, **59**(6), 543-553 (2019).

[32] P. Safarik, V.Y. Maximov, A. Nugymanova, et al. 3D modeling of heat transfer processes in the combustion chamber boiler of thermal power plant. *News of the national academy of sciences of the Republic of Kazakhstan-series physico-mathematical*, **6**(328), 5-13 (2019).

[33] P. Safarik, S.A. Bolegenova, et al. Optimization of the solid fuel combustion process in combustion chambers in order to reduce harmful emissions. *News of the national academy of sciences of the Republic of Kazakhstan-series physico-mathematical*, **6**(328), 34-42 (2019).

[34] A.S. Askarova, S.A. Bolegenova, V.Y. Maximov, et al. Mathematical simulation of pulverized coal in combustion chamber. Procedia Engineering, **42,** 1150-1156 (2012). DOI:10.1016/j.proeng.2012.07.507.

[35] S.A. Bolegenova, Z. Gabitova Three-dimensional modeling of heat and mass transfer during combustion of low-grade Karaganda coal.22nd International Congress of Chemical and Process Engineering. *CHISA 2016 and 19th Conference on Process Integration, Modelling and Optimization for Energy Saving and Pollution Reduction, Press 2016*, 1102, (2016).

[36] M.T. Beketayeva A.S. Askarova, S.A. Bolegenova 3D modeling of the aerodynamics and heat transfer in the combustion chamber of the BKZ-75 boiler of the Shakhtinsk cogeneration plant. *Thermophysics and Aeromechanics*, **26-2,** 295-311 (2019).

[37] M.T. Beketayeva, S.A. Bolegenova, et al. Influence of boundary conditions to heat and mass transfer processes. *International J. of Mechanics*, **10**, 320-325 (2016).

[38] S. Bolegenova, A.E. Boranbayeva Mathematical modeling of heat and mass transfer in the presence of physical chemical processes. *Bulgarian Chemical Communications*, **48**(E2), 272-277 (2016).

[39] Bedikhan K., Application of 3D modelling for solving the problem of combustion coal-dust flame. *Bulgarian Chemical Communications*, **48**(E2), 236-241 (2016).

[40] P. Safarik, A. Yergalieva Numerical investigation of heat and mass transfer processes in the combustion chamber of industrial power plant boiler. Part 1 flow field, temperature distribution, chemical energy distribution. *Applied and Computational Mechanics*, **11**(2), 115-128, (2017).

[41] B.K. Alijarov, and M.B. Alijarova Combustion of Kazakh coals in thermal power stations and large-power boiler houses. Almaty, 2012.

[42] Thermal calculation of boilers (normative method). Publishing House AOOT "NCPO Central Boiler-and-Turbine Institute", 1998.

Bulgarian Chemical Communications, Volume 52, Special Issue C (pp. 32-39) 2020 DOI: 10.34049/bcc.52.C.0111

Analysis of the energy recovery possibilities of energy from scrap tire

D. P. Chakyrova*, A. T. Andreev, N. O. Doseva

Technical University of Varna, Dept. of Thermal Engineering,1 Studentska Str, 9010 Varna, Bulgaria

The analysis of waste polymers as a source of energy is the main goal of this study. A novelty in the research is the development of a methodology for evaluating the productivity and energy efficiency of both new and existing pyrolysis systems in order to be optimize them. Two of the processes of thermochemical conversion are considered: direct combustion and pyrolysis, are compared to choose the most efficient, both economically and environmentally. This requires an assessment of their properties, which define them as fuel. The analyzes were performed with the help of literature data: for ultimate analysis of waste polymers; for analytical models of yields of pyrolysis products of waste polymers; the composition of the produced biogas; analytical dependences for determination of Heating Value (HV) of waste polymers and products of their pyrolysis; models for determining the heat of pyrolysis. The process of treatment of waste polymers by pyrolysis was investigated experimentally and a gas analysis of the obtained pyrolysis gas was performed to compare with the predicted results of the analytical calculations. An ultimate and quantitative analysis of both the raw material used and the obtained products was made. the total amount of heat used in the process was measured. The results show that the energy obtained can ensure the application of the pyrolysis process, and the residual energy can be used for other purposes.

Keywords: pyrolysis, waste tires, biomass, gas and liquid products, biogas

INTRODUCTION

The world is currently facing to significant problems, such as fossil fuel shortages and environmental pollution. The problems are constantly exacerbated due to the growing population and, accordingly, the increasing energy consumption per capita. These data can be seen in the annual report of the British Petroleum (BP Statistical Review of World Energy), showing the trends in global energy consumption.

In order to overcome the problems, more and more attention is paid to renewable energy sources, which bring economic and social benefits.

Large quantities of polymers are produced and obtained naturally worldwide, with the production and consumption are constantly increasing every year. Despite their valuable qualities, many out-of-date polymers are ones of the main polluters of the environment.

Most of them are not biodegradable, they are resistant to moisture, chemicals, sunlight and microorganisms. Dumped in landfills, their "life" continues and if stored improperly, fires and infectious diseases can occur. The impact of this waste on the environment can be minimized by recycling or using it as energy.

The pyrolysis process finds application in the treatment of solid organic waste, such as waste automotive tires, plastics, biomass, animal waste and solid waste from wastewater treatment plants.

* To whom all correspondence should be sent:
chakyrova_d@tu-varna.bg

By heating in an oxygen-free environment, they decompose to give solid, liquid and gaseous products which have applications as fuels or raw materials for the chemical industry.

In recent decades, both the processing and the use of waste polymers as fuel in various industries, in households and in transport have increased. The reason for this is Directive 2009/28/EU on renewable energy, which establishes a comprehend-sive policy for the production and promotion of energy from renewable sources and requires the EU to meet at least 20% of it‘s total energy needs with energy from renewable sources by 2020.

The main purpose of this article is to analyze waste polymers as an energy source. This requires an assessment of their properties, which define them as a fuel.

In order to determine the energy potential of waste polymers, it is necessary to establish their energy value. Heating value is often used as an indicator of the energy contained in waste.

There are two main aspects related to the use of waste polymers as fuel: (1) expanding and improving the basic knowledge about their composition and properties and (2) the application of this knowledge to the most modern and environmentally safe use. Numerous studies have been conducted worldwide and extensive data have been obtained on the waste polymers themselves and their transformation products, which have intensified over the last two decades. These results provide a solid basis as an initial database that can be used to characterize and subsequently classify and sustainably operate this waste [1, 16, 25].

Waste polymers can be defined as a material that consists mainly of carbon, hydrogen, oxygen, nitrogen and smaller parts of inorganic substances.

In the literature and practice [1, 2, 4, 13, 22] the following methods are known for the treatment of waste polymers for their further utilization, by converting them into liquid, gaseous and solid fuels, which is carried out in two main ways: biochemical (fermentation) and thermochemical (pyrolysis, gasification, esterification and direct incineration).

Three types of secondary fuels are produced from waste polymers:

- Liquid (ethanol, biodiesel, methanol, vegetable oil and pyrolysis oil);
- Gaseous (biogas (CH_4, CO_2), industrial gas (CO, H_2, CH_4, CO_2, H_2), synthetic gas (CO, H_2), natural gas substitute (CH_4));
- Solid (coal, purified biomass).

The utilization of waste polymers, in the aspect of this study, is for the purpose of obtaining heat to be put back into the process and obtaining fuels for use in other processes. In this sense, the present study considers only thermochemical treatments, comparing them in order to choose the most efficient of them, both economically and environmentally. The aim of the study is to create a methodology for evaluating the productivity and energy efficiency of both new and existing pyrolysis systems in order to be optimize them. We have no evidence that other researchers conducted similar studies.

The authors of [17, 18] determine that the amount of gases obtained in the pyrolysis process is sufficient to realize the process without additional energy sources. As a rule, this kind of gas has a heating value of about 13-15 MJ/m^3.

The study shows that many researchers study the processes of obtaining volatile substances from various solid materials, such as solid fuels, polymers, industrial waste, agricultural waste and wastewater treatment plants. The interest in the processes of gasification and pyrolysis in recent years is very high and this is justified from an environmental, economic and social point of view.

This study analyzes the properties of the waste polymers and the products of it‘s processing into secondary fuels, which characterize them as fuels. For this purpose were used literature data such as: proximate and ultimate analysis of waste polymers; for the analytical models of the yields of the products of their pyrolysis; for the composition of the obtained pyrolysis gas; for analytical dependences for determination of High HV (HHV) or Low HV (LHV) of the waste polymers and the products of their pyrolysis.

The process of processing the waste polymers by pyrolysis was experimentally studied, and a gas analysis of the obtained pyrolyzed gas was performed in order to compare the predicted results of the analytical calculations. Samples for elemental qualitative and quantitative composition are given in the Microanalytical Laboratory for "Elemental Analysis" at the Institute of Organic Chemistry With Center of Phytochemistry – Bulgarian Academy of Sciences.

MATERIALS, METHODS AND DATA USED

Analytical investigation of thermochemical conversion of waste polymers and it‘s products

1. **Models for determining the yields of individual products**

The creation of a model and its comparison with similar ones by other authors is aimed at using the process parameters as independent variables. The following models are known in the literature.

The authors of [14] have established the proportions of char and gases, products of pyrolysis, as well as the ratios of some of them as a function of temperature. Particle size, heating rate, and reactor size have limited influence on these empirical relationships.

$$Y_{ch,F} = 0.106 + 2.43 \cdot \exp(-0.66 \cdot 10^{-2} \cdot T) \quad (1)$$

$$Y_{H_2,F} \approx Y_{H,F};\ Y_{CO,F} \approx Y_{O,F}\frac{28}{16}; \quad (2)$$

$$Y_{CH_4,F} = -2.18 \cdot 10^{-4} + 0.146 \cdot Y_{CO,F}; \quad (3)$$

$$\frac{Y_{H_2,F}}{Y_{CO_2,F}} = 3 \cdot 10^{-4} + \frac{0.0429}{1+\left(\frac{T}{632}\right)^{-7.23}}. \quad (4)$$

After using the statistical method Box-Behnken design (BBD) to process the results of a test study of pyrolysis of organic materials in argon field empirical relationships were obtained between the amount of pyrolysis oil and the process parameters, as well as between the obtained solid residue and the process parameters [20].

$$\begin{aligned} Y_1 = {} & 107.70125 + 0.59689 \cdot X_T + 0.043345 \cdot X_P - \\ & -6.06250 \cdot X_N - 1.607 \cdot 10^{-4} \cdot X_T \cdot X_P + \\ & +1.125 \cdot 10^{-5} \cdot X_T \cdot X_N + 1.4333 \cdot 10^{-4} \cdot X_P \cdot X_N - \\ & -6.96412 \cdot 10^{-5} \cdot X_T^2 - 3.415 \cdot 10^{-5} \cdot X_P^2 - \\ & -1.28472 \cdot X_N^2 \end{aligned} \quad (5)$$

$$Y_2 = 144.2165 - 0.3277 \cdot X_T - 0.04226 \cdot X_P + \\ +0.035275 \cdot X_N + 1.15 \cdot 10^{-4} \cdot X_T \cdot X_P + \\ +5.8333 \cdot 10^{-6} \cdot X_T \cdot X_N - 8.33333 \cdot 10^{-5} \cdot X_P \cdot \\ \cdot X_N + 3.79575 \cdot 10^{-4} \cdot X_T^2 + 1.473 \cdot 10^{-4} \cdot X_P^2 - \\ -1.43611 \cdot 10^{-4} \cdot X_N^2 \quad (6)$$

The authors of [23] propose empirical dependences for calculating the share of bio-char and the H/C ratio as a function of the process parameters: T_{py}, HR and RT. The dependencies are different for different materials. For straw there are types:

$$Yb(\%) = 89.29 - 0.131 \cdot T_{py} - 0.622 \cdot HR - \\ -0.587 \cdot RT - 0.001 \cdot T_{py} \cdot HR - \\ -0.001 \cdot T_{py} \cdot RT \qquad R2 = 0.929 \quad (7)$$

2. Modeling of the heating value

The raw material (waste polymers)

There is a standard defining the approach for experimental determination of the upper heat capacity of solid biofuels - BDS EN ISO 18125: 2017. The cited standard can be successfully applied to waste polymers. An alternative to experimental measurements is the approximate estimation of the upper heating value of waste polymers by means of analytical dependences. Similar models are available in the literature, some of which indicate a relationship between the upper heating value of dry fuel, Q_{HHV}, and its chemical composition, others - between Q_{HHV} and fixed carbon, volatiles and ash content [22]. The influence of the ash content and humidity of the biomass is negative.

$$Q_{HHV,Dry} = 0.341 \cdot C + 1.323 \cdot H - 0.12 \cdot O - \\ -0.12 \cdot N + 0.68 \cdot S - 0.015 \cdot ASH, \ [\text{MJ/kg}] \quad (8)$$

Note: The elemental composition in Eq.(8) is related to the working mass of the fuel.

$$Q_{HHV,Dry} = 0.1559 \cdot VM + 0.3536 \cdot FC - \\ -0.0078 \cdot ASH, \ [\text{MJ/kg}] \quad (9)$$

The third group of dependencies gives the connection between Q_{HHV} and the content of lignin, L, in the fuel, and the fourth group of dependences - between the upper heating value and the structural composition of the biomass (the content of lignin, cellulose and hemicellulose) [19].

$$Q_{HHV,Dry} = 0.0979 \cdot L + 16.292, \ [MJ/kg] \quad (10)$$

$$Q_{HHV,Dry} = 0.1739 \cdot Ce + 0.2663 \cdot L + \\ +0.3219 \cdot E, \quad [MJ/kg] \quad (11)$$

In the case of wet raw material the heat obtained from the combustion of 1 kg of fuel is due only to the share of dry biomass, ie. (1- W_{wb}). Then [22]:

$$Q_{HHV} = (1 - W_{wb}) \cdot Q_{HHV,Dry}, \ [MJ/kg] \quad (12)$$

On the other hand, the expression for the lower heating value of waste polymers, taking into account its operating humidity, yields the form [22]:

$$Q_{LHV} = (1 - W_{wb}) \cdot Q_{HHV,Dry} - \\ -2.447 \cdot \left[W_{wb} + 9 \cdot (1 - W_{wb}) \cdot H\right], \ [MJ/kg] \quad (13)$$

In the present study, the dependencies with data from ultimate analysis for waste tires are used, due to the lack of data from proximate analysis of the same.

On the products

The heating value, according to [24] of solid and liquid fuels is determined by:

$$Q_{LHV} = 339.39 \cdot C + 1257 \cdot H - 108.94 \cdot \\ \cdot (S - O) - 25.14 \cdot (9 \cdot H - W_{wb}), \ [\text{kJ/kg}] \quad (14)$$

The heating value of gaseous fuels is determined, according to [24], by:

$$Q_{LHV} = 0.127 \cdot CO + 0.108 \cdot H_2 + \\ +0.358 \cdot CH_4, \ [\text{MJ/Nm}^3] \quad (15)$$

3. Energy balance models

The analysis of the energy balance of the pyrolysis processes was made using the scheme of Fig.1 [1].

Compare combustion reactions, most gasification reactions are endothermic.

For this reason, heat must be supplied to the gasifier in order to carry out these reactions at the planned temperature. The amount of external heat supplied to the gasifier depends on the heat demand of the endothermic reactions, as well as on the gasification temperature.

The total heat balance, according to Fig.1 [1] is:

- incoming energy:

$$A \cdot Cp_a \cdot T_0 + F \cdot Cp_f \cdot T_0 + W \cdot H_0 + \\ +F \cdot Q_{HHV} + Q_{ext} \quad (16)$$

- energy of the outgoing streams:

$$(C_{CO}\cdot V_{CO}+C_{CO_2}\cdot V_{CO_2}+C_{CH_4}\cdot V_{CH_4}+ +C_{H_2}\cdot V_{H_2}+C_{O_2}\cdot V_{O_2}+C_{N_2}\cdot V_{N_2})\cdot T_g+ +\left(1-X_g\right)\cdot W\cdot H_g+P_c\cdot q_c+Q_{gasif}+ +Q_{loss}+Q_{product} \quad (17)$$

According to authors of [24]:

$$Q_{LHV}^{raw}+Q_{pyr}=g_{gas}\cdot Q_{LHV}^{gas}+Q_{phh}^{gas}+ +g_{char}\cdot Q_{LHV}^{char}+Q_{phh}^{char} \quad (18)$$

$$Q_{phh}^{gas}=c_{gas}\cdot g_{gas}\cdot\left(t_{pyr}-t_0\right)+ +c_{steam}\cdot g_{steam}\cdot\left(t_{pyr}-t_0\right)+r\cdot g_{steam} \quad (19)$$

$$Q_{phh}^{char}=c_{char}\cdot g_{char}\cdot\left(t_{pyr}-t_0\right) \quad (20)$$

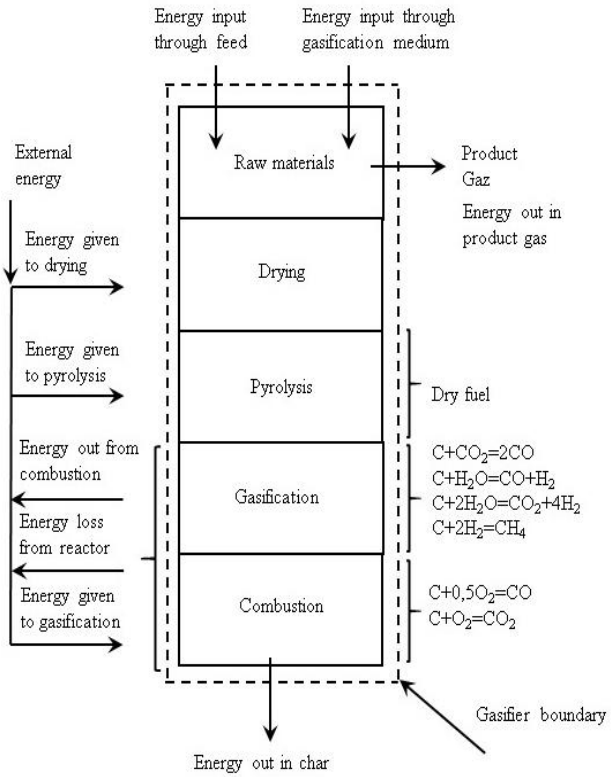

Fig.1. Energy balance of a pyrolysis reactor [1]

According to authors of [21], the heat required for pyrolysis is calculated by:

$$Q_{pyr}=\Delta H_S+\Delta H_r \quad (21)$$

$$\Delta H_S=\dot{m}_{tire}\cdot\left(\int_{T_0}^{T_{reac}} c_{p,tire}dT\right) \quad (22)$$

$$\Delta H_r=\dot{m}_{tire}\cdot(553-3142\cdot\mu_{char}) \quad (23)$$

In the present study, a methodology for determining the energy balance based on experimental studies has been used. The obtained results are compared with those calculated by the analytical models, proposed by other authors.

Experimental investigation of thermochemical conversion of waste polymers and it's products

The laboratory system is shown in Fig.2. Thermometers have been installed to measure the temperature at various points in the system, as well as taking samples to determine the composition and concentration.

Experiments were performed in which different waste tires were subjected to pyrolysis.

A discrete amount of feedstock is placed in the pyrolysis reactor and heated. The vapors obtained from the decomposition of the raw material are cooled in a heat exchanger and some of them condense. The liquid product is collected in a tank, and the non-condensed gases leave the system by passing through a hydraulic seal, which does not allow atmospheric air to enter the system.

The waste rubber that undergoes pyrolysis has a known qualitative and quantitative composition. The experiment was performed at a predetermined temperature in the reactor. The amount of pyrolysis oil obtained and solid residue after completion of the experiment are taken into account. The products are analyzed to determine their elemental, qualitative and quantitative composition.

The pyrolysis gas obtained is also analyzed. Its composition is determined by a gas analyzer, and the quantity is determined by weight, based on the material balance. The consumption of cooling water by a rotameter and the inlet and outlet temperature of the heat exchanger are also taken into account. The energy imported into the system is also taken into account for the needs of the energy balance. It is accepted that the process proceeds until the moment when gas is no longer released from the reactor. The pyrolysis oil obtained from the experiments was further subjected to distillation.

RESULTS AND DISCUSSIONS

An experiment was performed in which two types of waste raw materials were subjected to pyrolysis. Waste car tire (Model-1) and waste tire from the conveyor belt (Model-2).

In the pyrolysis reactor is maintained at a temperature of about 300/400/500 ^{0}C under stationary conditions. Under these conditions, gaseous, liquid and solid products are obtained. In the course of the experiment, the amount of liquid obtained, the energy consumed to maintain the operating conditions in the pyrolysis reactor, the

flow rate of the cooling water are monitored and the time for which the process takes place is taken into account.

The resulting pyrolysis oil was further subjected to atmospheric distillation and divided into fractions with different boiling points.

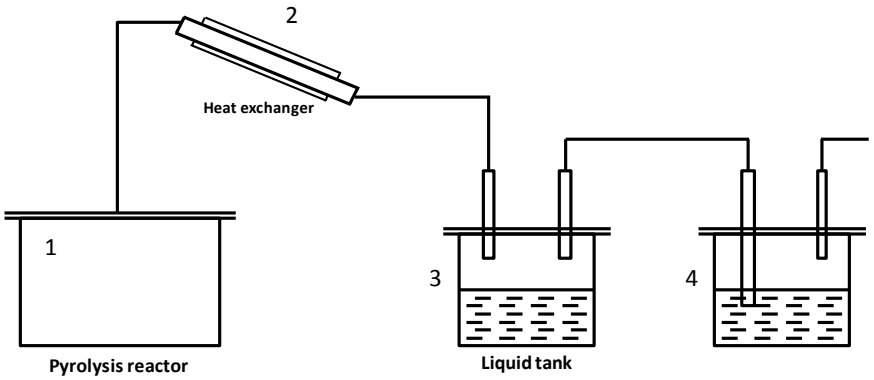

Fig.2. Principal scheme of the experimental system: 1 – Pyrolisys reactor; 2 – Heat exchanger; 3 – Liquid tank, 4 reservoir - hydraulic shutter

The results are presented in Tab.1.

Table 1. Yields of the obtained products at different temperatures

Raw	Temp.	Char	Oil	Gas
	^{0}C	wt%	wt%	wt%
Scrap tire	300	45	45	10
Model-1	400	30	62	8
	500	30	62	8
Scrap tire	300	41	48	11
Model-2	500	32	56	12

The reason for the observed differences in the amount of products obtained is that at low temperatures, the process proceeds to an equilibrium state, which stops the decomposition of the polymer compounds and the production of hydrocarbons with a shorter chain. This coincides with the published results of Thermogravimetric Analysis (TGA) of many researchers [5] and does not contradict the accepted models describing the process [3, 5, 9, 7].

It can be seen that the amount of liquid obtained at 400 ° C and 500 ° C is the same, but the liquids differ in their fractional composition.

In this experiment, the raw material (waste rubber model-1) and the pyrolysis products - pyrolysis gas, pyrolysis oil and solid carbon residue, were subjected to additional analyzes.

Samples for elemental qualitative and quantitative composition are given in the Microanalytical Laboratory for "Elemental Analysis" at the Institute of Organic Chemistry With Center of Phytochemistry – Bulgarian Academy of Sciences.

The pyrolysis gas obtained is also analyzed by a gas analyzer to give a qualitative and quantitative composition of the main gases contained therein.

The results are presented in Tab.2, Tab.3, Tab.4 and Tab.5.

Table 2. Elemental qualitative and quantitative composition

Component	Scrap Tire	Char	Oil	Gas
	mass%	mass%	mass%	mass%
C	85.08	90.48	87.00	72.40
H	9.76	3.68	10.00	13.00
N	2.93	2.71	2.00	11.00
S	0.97	2.84	0.00	0.00
O	1.26	0.29	1.00	3.67

Table 3. Qualitative and quantitative composition of pyrolysis gas

Component	H_2	CO	CO_2	NO	NO_2	CH_4	C_6H_6
mass%	2.08	34.20	27.48	6.63	15.89	12.66	1.06

Table 4. Heat of combustion of raw materials and pyrolysis products

Parameter	Units	Scrap Tire	Char	Oil	Gas
Specific heat, Cp	kJ/kg.K	9.348	5.843	10.848	1.382
LHV	kJ/kg	37 656	13 882	40 752	34 811

Table 5. Comparative data from the conducted tests

Temp.	Method of heating	Time	Fuel	Energy	Primary energy
ºC		min	g	kWh/kg raw	kWh/kg raw
300	Propane-butane	43	64,50	8.90	9.73
300	electricity (induction heating)	26	-	6.20	18.60
400	Propane-butane	35	52.53	7.30	8.03
500	Propane-butane	35	58.33	8.10	8.91

A comparison of the obtained experimental data with those published by other researchers is made. The comparison is presented in Tab.6 and Tab.7.

Table 6. Quantitative comparison of experimentally obtained products by pyrolysis

Autor	Temp.	Char	Oil	Gas
	ºC	wt%	wt%	wt%
Williams, [6]	300-720	35	55	10
Chang, [12]	200-600	14-28	28-42	30-53
Berrueco, [11]	400-700	47-63	30-43	4-11
Barbooti, [7]	400-460	32.5	51	16.6
González, [10]	350-700	37-40	55	4-11
This paper Model-1	300	45	45	10
This paper Model-1	400	30	62	8
This paper Model-1	500	30	62	8
This paper Model-2	300	41	48	11
This paper Model-2	400	36	50	14
This paper Model-2	500	32	56	12

Table 7. Ultimate analysis of waste tires

Autor	C	H	O	N	S	Inorganic residue
	%	%	%	%	%	%
Williams, [8]	85.8	8.0	0.4	1.0	2.3	2.4
Barbooti, [7]	83.8	7.6	0.4	1.4	3.1	3.7
Wang, [15]	81.2	7.2	0.5	1.6	2.1	7.4
Berrueco, [11]	88.5	6.6	0.4	1.6	3.0	-
González, [10]	86.7	8.1	0.4	1.4	1.3	2.9
This paper	85.1	9.8	2.9	1.0	1.3	-

A comparison of the results shows that the researchers worked in a very wide temperature range in the reactor. An exception is the study of [7], where the temperature in the pyrolysis reactor is maintained at 400-460 °C. It can be seen that the quantity of the obtained pyrolysis products is the same, but there are no published data on the elemental qualitative and quantitative composition of the raw material. If the same raw material is subjected to a pyrolysis process under the same conditions, the same amounts of pyrolysis products will be obtained. This is proven by the experiments that are the subject of this study.

In order to make any correct comparison of the pyrolysis process, it is necessary that the experiments be carried out in narrow temperature ranges and, if possible, under stationary conditions. The abrupt and prolonged change in the conditions disturbs the stationarity and leads to a change in the quantity of the products obtained, and the generation of losses, which in an experimental system cannot always be registered.

A very important condition for making a correct comparison is the requirement to know the composition of the raw material that is subjected to pyrolysis.

Regression analysis was performed with the experimental data. The target function shows the amount of product obtained from the pyrolysis process under different conditions (independent variables). The independent variables involved in the model are the temperature at which the process takes place in the pyrolysis reactor (x_1) and the heating rate (x_2).

Equation (24) describes how much pyrolysis gas is produced depending on the temperature in the reactor and the heating rate.

$$y_1 = 74.75 - 0.34 \cdot x_1 + 0.0004 \cdot x_1^2 + \\ +0.16 \cdot x_2 \quad R^2 = 0.99 \tag{24}$$

The influence of the heating rate and the maintained temperature in the pyrolysis reactor on the amount of pyrolysis oil obtained is given by equation (25).

$$y_2 = -58.50 + 0.51 \cdot x_1 - 0.00056 \cdot x_1^2 + \\ +0.0018 \cdot x_2^2 \quad R^2 = 0.99 \tag{25}$$

How the heating rate and the maintained temperature in the pyrolysis reactor affect the obtained carbon residue is given by equation (26).

$$y_3 = 80.65 - 0.13 \cdot x_1 - 0.34 \cdot x_2 + \\ +0.00014 \cdot x_2^2 \quad R^2 = 0.99 \tag{26}$$

Tab.8 presents the results for product yields from the experiment and compares with the

predicted values calculated from the described models in the literature.

Table 8. Yields of pyrolysis products

Temp.	Heating rate	Pyrolysis products: char predic.	char exp.	oil predic.	oil exp.	gas predic.	gas exp.
ºC	ºC/min	wt%	wt%	wt%	wt%	wt%	wt%
300	27.5	45.00	44.15	45.00	33.15	10.00	22.70
400	62.5	30.00	27.94	62.00	41.20	8.00	30.86
500	59.3	30.00	19.56	62.00	50.80	8.00	29.64

In the Tab.9 and Tab.10 are present the results of the calculations of the calorific value of the raw material and the products of pyrolysis and are compared with the results of the experiment.

Table 9. Low Heating Value for solid and liquid materials

Material	C	H	O	N	S	LHV Predict.	LHV Exper.
	%	%	%	%	%	kJ/kg	kJ/kg
Scrap tire	85.08	9.76	1.26	0.93	0.97	38 904	37 656
Char	90.48	3.68	0.29	2.71	2.84	34 779	34 811
Oil	87.00	10.00	1.00	2.00	0.00	39 725	40 752

Table 10. Low Heating Value for pyrolysis gas

CO	CH_4	H_2	C_6H_6	LHV Predict.	LHV Exper.
mass%	mass%	mass%	mass%	kJ/kg	kJ/kg
34.20	12.66	2.08	1.06	9 712	13 882

The main problem in compiling the energy balance of the pyrolysis process is the determination of the heat required for the realization of the gasification process. Different authors offer different approaches. In the Tab.11 are present the results of the experiment and are compared with the analytical calculations of the models presented with equations (16) – (23).

Table 11. External addition heat

Temp.	External addition heat: Predicted (from eq. 16-20)	Experimental
°C	kWh/kg raw	kWh/kg raw
300	1.569	8.900
400	2.067	7.300
500	2.565	8.100

According to the author of [1], the calculation of the heat required to carry out the endothermic reactions of Fig.1 is 1,683 kWh / kg raw, which is comparable to the values obtained from the calculation according to equations (16) – (23). The larger values of the experiment are due to environmental losses and unused in the process heat from incomplete combustion.

The analysis of the results in Tabs.9 to 11 shows that the heat obtained from the combustion of 1 kg of waste tires is 37 656 kJ. The heat obtained from the combustion of the pyrolysis products per 1 kg of waste tires is 36 820 kJ. Including the costs of endothermic gasification reactions, it is clear that it is more cost-effective to burn waste tires directly. From the point of view of ecology and environmental pollution, however, pyrolysis is a more gentle technology for obtaining energy from waste polymers, which has become increasingly important in recent years.

The results also show that the energy of the pyrolysis products is 10.23 kWh/kg raw, the energy required for the pyrolysis process, minimizing losses, is about 3 kWh/kg raw. It can be seen that the profit from 1 kg of raw material is about 6 kWh.

CONCLUSIONS

The conducted experiments show that the speed of the pyrolysis process strongly depends on the maintained temperature in the reactor. The quantities of the obtained pyrolysis products also depend on it.

The raw materials that undergo pyrolysis are diverse and have characteristic properties and their elemental qualitative and quantitative composition affects the quantity of pyrolysis products. This has been proven by experiments conducted under the same conditions with different types of raw material.

Subjected to atmospheric distillation, pyrolysis oil is divided into four main fractions, which are very close to the fractions obtained by atmospheric distillation of oil. This allows the treatment of waste polymers by pyrolysis to find its place in large oil refineries, where the efficiency of the process can be improved by utilizing waste heat from other industries.

The comparison of experimental results and obtaining significant conclusions from them for the pyrolysis process is correct, in cases when the experiments are carried out in stationary conditions and narrow limits of the observed process parameters.

The results of the conducted experiments and the performed analytical calculations are coordinated with those of other authors, published in literature sources.

Energy analysis has led to the conclusion that the energy contained in waste polymers can be utilized preferably by pyrolysis, which is a environmentally friendly technology.

NOMENCLATURE

Y - mass ratio, kg / kg fuel;

T, T_{reac}, t_{pyr}, X_T, T_{py}, x_1 – temperature in the reactor, °C;

X_P – pressure in the reactor, Pa;

X_N, RT - residence time of products in the reactor, min;

Y_1, y_2 – mass ratio of pyrolysis oil, kg/kg fuel;

Y_2, μ_{char}, y_3 - mass ratio of char, kg/kg fuel;

y_1, - mass ratio of pyrolysis gas, kg/kg fuel;

HR, x_2 - heating rate (°C/min);

VM - volatile substances, kg/kg daf fuel;

FC - fixed carbon, kg /kg daf fuel;

Q_{HHV} - high heating value, MJ/kg;

Q_{LHV} - low heating value, MJ/kg;

Ce - mass ratio of cellulose and hemicellulose, mass %db;

L - lignin, mass %db;

E - proportion of extracts, mass %db;

W_{wb} - working humidity, kg/kg wet mass;

C, O, H, N, S and ASH - mass fraction of carbon, oxygen, hydrogen, nitrogen, sulfur and ash in the fuel on a dry basis (db), kg/kg fuel;

A, W, F - the amount of air, of steam needed to gasify, fuel to produce 1 Nm^3 of product gas, kg;

C_i - the volumetric specific heat of the gas species, i, at temperature Tg, kJ/(m^3.K);

V_i, the volume of the gas species, i, m^3;

Tg - gasifier exit temperature,°C;

T_0 - reference temperature, °C;

P_c - the quantity of char produced, kg/kg fuel;

Q_{gasif} , Q_{pyr} - the net heat of the reaction, kJ;

Q_{loss} - total heat loss, kJ;

q_c - heating value of the char, kJ/kg;

(1-X_g)W - the net amount of steam remaining in the product gas of the gasification, kg;

H_0, H_g – enthalpies of steam at the reference and the gasifier exit temperatures, kJ/kg;

$Q_{product}$ -the energy in the product gas, kJ;

Q_{ext} - external heat addition, of product gas to the system, kJ;

c– mass specific heat of gas, steam and char, kJ/(kg.K);

g - and the mass ratio of gas, steam and char, kg;

Q_{phh} – physical heat of gas and char, kJ/kg;

r - the water vaporization heat, kJ/kg;

t_0 – initial fuel temperature, °C;

ΔH_S – the sensible heat for the temperature rise of biomass to the reaction temperature, kJ/kg;

ΔH_r - the heat of reaction, kJ/kg;

$\dot{m}_{tire}$ - tire flow rate, kg/s.

Subscripts

F – dry ash free (daf) fuel.

REFERENCES

[1] P. Basu. Biomass Gasification and Pyrolysis: Practical Design and Theory, Elsevier, US, 2010.

[2] A. Broido, M. Evett, G. C. Hodges. Combution and Flame, **24** (1975).

[3] C. Chen, Y. Jin, J. Yan, Y. Chi. *J. of Zhejiang Univ.-SCI. A*, **11** (2010).

[4] A. Demirbas. *J. Anal. Appl. Pyrolysis*, **72** (2004).

[5] C. Di Blasi. *Chem. Eng. Sci.*, **51** (1996).

[6] P. T. Williams, S. Besler. *Fuel* **74** (1995).

[7] M. M. Barbooti, Th. J. Mohamed, A. A. Hussain, F. O. Abas. *J. of Anal. and Appl. Pyr.*, **72** (2004).

[8] Paul T. Williams, S. Besler, D. T. Taylor. *Fuel*, **69**, (1990).

[9] M. Juma, Z. Koreňová, J. Markoš, J. Annus, Ľ. Jelemenský. *Petroleum & Coal* **48** (1) (2006).

[10] J. F. González, J. M. Encinar, J. L. Canito, J. J. Rodríguez. *J. of Anal. and Appl. Pyr.*, **1** (2001).

[11] C. Berrueco, E. Esperanza, F.J. Mastral, J. Ceamanos, P. Garc ´a-Bacaicoa. *J. Anal. Appl. Pyrolysis*, **73**, (2005).

[12] Y.-M. Chang. *Conserv. & Recycling*, **17** (1996).

[13] L. Fagbemi, L. Khezami, R. Capart. *Appl. Energy* **69** (2001).

[14] D. Neves, H. Thunman, A. Matos, L. Tarelho, A. Gómez-Barea. *Progress in Energy and Combustion Science* **37** (2011).

[15] S. Wang, X. Guo, K. Wang, Z. Luo. *J. Anal. Appl. Pyrolysis* **91** (2011).

[16] S. V. Vassilev, D. Baxter, L. K. Andersen, C. G. Vassileva. *Fuel* **89** (2010).

[17] H.J.Park, JI Dong, JK Jeon, YK Park, KS Yoo, SS.Kim, J.Kim, S.Kim. *J.Chem. Eng.* **143** (2008).

[18] O. Onay and O. M. Kockar. *J. Renew. Eng.*, **28**, 2417-2433 (2003).

[19] A. Acar and A. Ayanoglu. *Energy Education Science and Technology Part A*: *Energy Science and Research*, **28** (2012).

[20] Z. Chen, B. Niu, L. Zhang, Z. Xu. *J. of Hazardous Mat.*, **342** (2018).

[21] K. Atsonios, K. D. Panopoulos, A.V. Bridgwater, Em. Kakaras. *Int. J. of Thermod.*, **18** (4) (2015).

[22] UNEP Technologies for Converting Waste Agricultural Biomass to Energy, *United Nations Environmental Programme*, Osaka, 2013.

[23] I. S. dos Reis Almeida. https://pdfs.semanticscholar.org/f1dc/e092e8278088ce5b6a6c2a9339d573ecba75.pdf.

[24] Suhockij A. B., Secondary energy resources. Unconventional and renewable energy sources, Minsk, 2012, 9 78-985-530-137-1.

[25] T. P. Wampler. Applied pyrolysis handbook. Boca Raton: CRC Press/Taylor & Francis, 2007.

Bulgarian Chemical Communications, Volume 52, Special Issue C (pp. 40-45) 2020 DOI: 10.34049/bcc.52.C.0047

Sintering BFO targets for RF sputtering

G. Orr, A. Goryachev, G. Golan*

Ariel University, Science Park, Ariel 40700, Israel

Ceramic $BiFeO_3$ samples were prepared by rapid sintering at $880^{\circ}C$. Two compositions were examined. A 56/44 Bi_2O_3/Fe_2O_3 mole% composition and a $56Bi_2O_3$ $44Fe_2O_3$ + 6.5*wt*% *NaCl* composition. The samples were heat treated at different times up to 8 minutes and the phase content was examined as a function of the time using XRD measurements and analysis. It was demonstrated that using both compositions, maximum $BiFeO_3$ phase content is obtained after 3.5 minutes. In the former approximately 50% of the material transformed to $BiFeO_3$ while in the latter 98.5%.

Keywords: BFO, sputtering, photovoltaic, multiferroic

INTRODUCTION

BFO has regained much interest in recent years due to its multiferroic nature [1]. It is one of the few known materials which simultaneously possess both ferroelectric and ferromagnetic ordering at room temperature. It has promising applications in photovoltaics, and due to the magneto-electric coupling between the electric and magnetic polarization providing for new device design. As such, the material shows much promise in realizing spintronic devices, sensors and multistate memory devices [1, 2]. It has been demonstrated [3] that impurities will result in additional phases, the more common and stable ones being the $Bi_2Fe_4O_9$ (mullite) and $Bi_{25}FeO_{40}$ (sillenite) with a relatively short lived phase of $BiFeO_3$ (BFO). Of the two variants ($BiFeO_3$, $Bi_2Fe_4O_9$) much work has been done in sintering ceramics composed of the variety of phases with the aim of obtaining materials which are composed mostly of $BiFeO_3$ nano crystallites. This is required for fabricating experimental devices based on deposition of thin films such as spintronics based components and sensors. $BiFeO_3$ sintered ceramic disks may be used as targets for the thin film deposition process. While all three phases appear at different ratios within the sintered material, we can expect that those phases with the greater change in Gibbs energy will be more stable. Based on experimental work, Phapale et al. [4] evaluated the heat capacity and derived the standard Gibbs energy of formation for the above compounds from room temperature up to $640^{\circ}C$. Selbach et. al. expanded this work demonstrating that at the temperature range of 447~$767^{\circ}C$ Gibbs energy of formation of $BiFeO_3$ is a metastable compound which would be the first to nucleate but would eventually transform into $Bi_2Fe_4O_9$ and $Bi_{25}FeO_{40}$. But above $767^{\circ}C$ increasing to the proximity of the peritectic temperature at $930^{\circ}C$, or below it is a stable compound. Carvalho et. al. [5] using sol-gel combustion to create ceramic samples of $BiFeO_3$ have also demonstrated similar results to Selbach's work. They further demonstrate that at a temperature of $600^{\circ}C$ the $BiFeO_3$ transforms into the more stable mullite phase $Bi_2Fe_4O_9$ over many hours. This is the reasoning behind the short period heating and rapid cooling techniques for obtaining BFO ceramics [6, 7, 8]. Using ultra-pure starting materials Lu et. al. [3] tested the stability as a function of the crucible type (gold or aluminium oxide) and the process from which the compound was synthesized. The processes consisted of solid-state reaction of the starting materials without reducing parasitic phases using HNO_3, solid state reaction of the materials followed by parasitic phase reduction and crushed crystals. Composition stability was tested at $850^{\circ}C$ for 24 and 48 hours and $855^{\circ}C$ for 24 hours. Both temperatures are above $767^{\circ}C$ so we should expect them to form the more stable $BiFeO_3$ phase. After 48 hours at $850^{\circ}C$ both the phase reduced (alumina crucible) and the crushed crystal (gold crucible) did not decompose, while after 24 hours 44% of the non reduced compound decomposed. At $855^{\circ}C$ after 24 hours, 7% of the crushed crystals in gold crucible, 26% of the parasitic phase reduced in gold crucible, and 87% of the parasitic phase reduced in alumina crucible decomposed. Evidently, and as expected at $850^{\circ}C$ BFO is the stable phase, at the same temperature the material without parasitic phase reduction decomposed considerably. The important point to consider is that the HNO_3 treatment dissolves every compound but the BFO and the $Bi_2Fe_4O_9$, thus without such a treatment, some phase

* To whom all correspondence should be sent:
gadygo@ariel.ac.il

impurities and not necessarily only the sillenite phase exist resulting in an increased decomposition. At $855^{\circ}C$ the volatility of bismuth comes into play. Lu claims it is a phase transformation, but we doubt it, as no one has observed a phase transformation at that temperature, and that includes the DSC (Differential scanning calorimetry) results that they present in the mentioned article. It is more likely a compositional change due to bismuth evaporation. Considering the parasitic reduced phase in the alumina crucible, something totally different is happening. According to the published phase diagrams [9, 10, 11, 3] we should not expect the mullite phase unless we exceed $930^{\circ}C$ or if we suffer from considerable evaporation of bismuth. Hence, we are drawn to suspect that the existence of the mullite phase in areas which it is not a favourable phase is indicative of impurities.

In order to test this assumption, we will compare a Bi_2O_3 saturated composition against the same Bi_2O_3 saturated composition but with $NaCl$ as an impurity.

EXPERIMENTAL

Material synthesis and sintering

The starting materials for the samples which were sintered are based on what was found to be the optimal composition by Bush et. al and Gabbasova et. al [12] for growing BFO macroscopic crystals from the melt. Analytical grade chemicals were selected, Bi_2O_3 (Merck 99.99% typ.), Fe_2O_3 (Alfa Aesar 99.9%) and NaCl (Merck 99.99%). The melt composition is 75.6 weight% Bi_2O_3, 17.9 weight% Fe_2O_3, and 6.5 weight% NaCl. Disregarding the NaCl that provides the sodium as a spectator ion, this translates to 56 mole% Bi_2O_3 and 44 mole% Fe_2O_3. We regard the above material as the material with controlled impurities, finding that the mentioned 6.5 weight% consists of the optimal impurity composition for obtaining the highest BFO content after sintering. This was compared to results obtained with a composition of 78.85 weight% Bi_2O_3 and 21.15 weight% Fe_2O_3, considered the material without controlled impurities. It gives ample room for study without the system shifting into a different phase system during the study due to mass loss. A recent article [13] illustrates this mass loss using DTA/TGA curves stating that above 400◦C and up to 800◦C approximately 2.5% Bi evaporation occurs. This corresponds to approximately a 1 mole% decrease in Bi content. Based on [3] we can assume that at 855◦C it increases to 7 mole% over a period of 24 hours. As shall be seen, the above compositions will assist us in evaluating dynamics and evolution of the different compounds in the sintered samples. The constituents were mixed and milled, followed by calcination at 800◦C for 4 hours in alumina crucibles. The furnace was heated at a rate of 100 degrees per hour with the material inside until it reached the target temperature. After 4 hours of calcination it was cooled to room temperature at a rate of 100 degrees per hour. The calcinated material was ground for 2 hours using a ball grinder and sieved through a 50µm mesh. Approximately 0.6g was pressed uniaxially into 12.7 mm disks with a pressure of approximately 100MPa. Pressed disks were inserted into a muffle furnace set at 880◦C for a certain period of time set in minutes and were extracted followed by quenching in air.

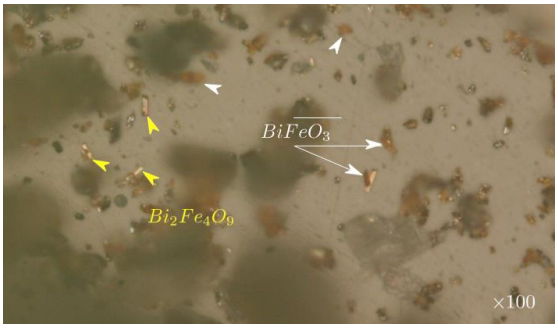

Fig.1. Fragments of crushed material after calcination prior to grinding. Much of the material has crystallized into its distinguishable phases

Evaluation of the calcined materials

The resulting calcined materials and sintered samples were recorded visually using a metallurgical microscope, followed by XRD and SEM analysis. The XRD measurements were conducted on a Rigaku SmartLab using the SmartLab Studio II software for analysis. One of the most important aspects for comprehending the optical microscope images is the ability to distinguish the morphology of at least one of the phases. As we shall see from the XRD analysis, the three obtained crystalline phases important to us, are $BiFeO_3$, $Bi_2Fe_4O_9$ and $Bi_{25}FeO_{40}$. Based on the Gibbs energy of formation [14] during the initial stages of nucleation, and for a relatively short time a metastable $BiFeO_3$ compound prevails over the $Bi_2Fe_4O_9$ and the $Bi_{25}FeO_{40}$. It means as well, that the metastable compound will prevail at a lower temperature range. In the longer time span we expect the more stable compounds as are described by the Bi_2O_3 Fe_2O_9 phase system. For

the 56/44 mole% Bi/Fe composition we expect either BFO or sillenite. We begin by analysing the compounds after calcination. Fig.1 illustrates an x100 optical microscope image of fragments of crushed calcinated material before grinding.

The figure illustrates that during the calcination process some of the constituents may be separated for analysis. In the example illustrated in the figure, two phases are distinguishable, the metallic color orthorhombic $Bi_2Fe_4O_9$ and the orange tinted brown rhombohedral $BiFeO_3$. Crystal phases developed due to the calcination process were analysed by crushing some of the calcinated compounds rinsing them in HNO_3 and washing them in water. This procedure dissolved all the different phases but the $Bi_2Fe_4O_9$ and $BiFeO_3$. The two remaining crystals were manually separated and were analysed with XRD.

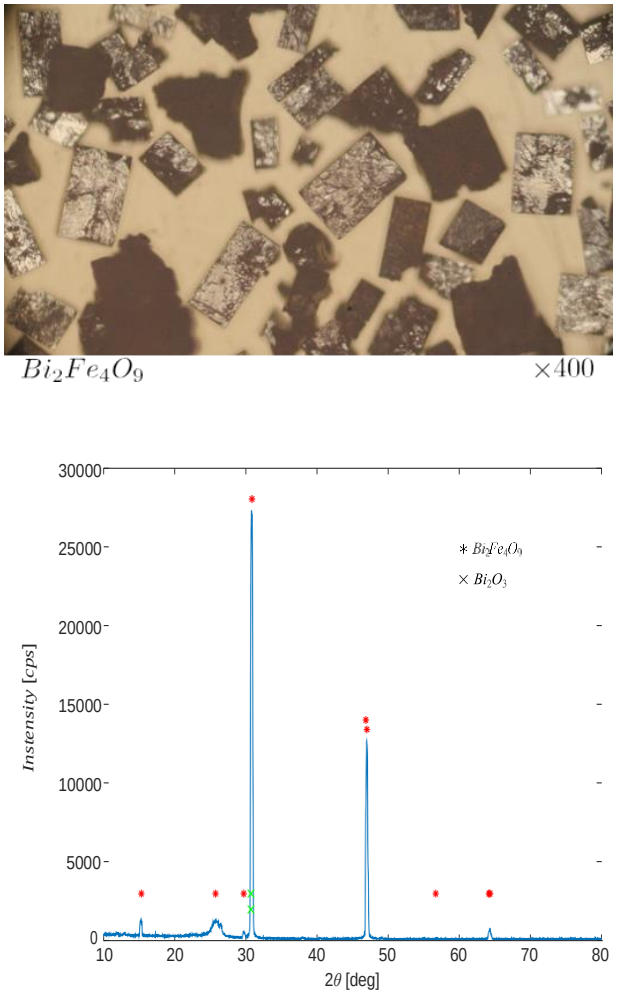

Fig.2. *$Bi_2Fe_4O_9$* crystals extracted from the calcinated material with its XRD profile

Fig.2 illustrates an example of separated $Bi_2Fe_4O_9$ crystals.

For the above example using split pseudo-Voigt fitting of the diffraction peaks and fitting the peaks with the ICDD database. The lattice parameters were measured to be $a = 7.9947\mathring{A}$; $b = 8.4599\mathring{A}$; $c = 5.9254\mathring{A}$.

We now compare the crystallized compositions of the two synthesized materials (with Bi_2O_3; *NaCl* flux and Bi_2O_3 flux) after calcination and grinding. Fig.3 illustrates the ground material with 6.5 weight% *NaCl*.

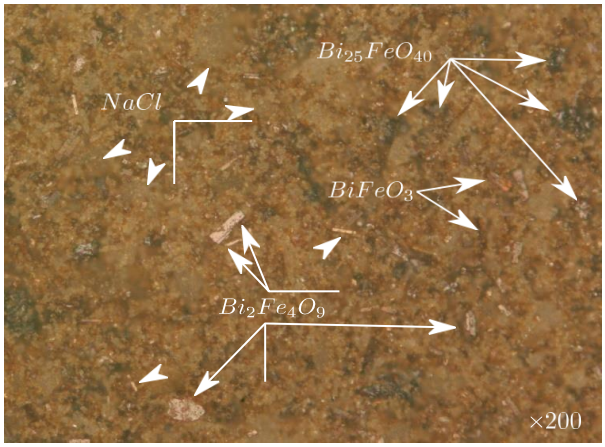

Fig.3. An optical microscope image of the synthesized and ground material with 6.5 *weight*% *NaCl* prior to sintering. An example of the various phases that can be observed is pointed using arrows

X-ray diffraction measurements of the ground material with NaCl in the flux show the following weight fraction of the crystalline phases (Tab.1).

Table 1. Weight fraction of crystalline phases in calcinated BFO *Bi_2O_3*; *NaCl* based flux

Compound	Weight fraction [%]	a [Å]	b [Å]	c [Å]	α [°]	β [°]	γ [°]
$Bi_2Fe_4O_9$	27.4	7.96623	8.434444	5.99638	90.000	90.000	90.000
$Bi_{22}Fe_2O_{36}$	26.3	10.13167	10.13167	10.13167	90.000	90.000	90.000
$Bi_{25}FeO_{40}$	24.4	10.15868	10.15868	10.15868	90.000	90.000	90.000
$BiFeO_3$	14.6	5.63427	5.63427	13.78349	90.000	90.000	120.000
α-$BiFeO_3$	7.3	5.62267	5.62936	5.62796	59.330	59.330	59.330

As we can expect, we see that the prevailing phases are the mullite (27.4%) and sillenite (24.4%). An additional, less commonly reported compound $Bi_{22}Fe_2O_{36}$, was observed as well. This compound was suggested by Mel'Nikova et al. [15] who developed a method of determining the composition of sillenites using XRD data. Murakami [16] working on $BaTiO_3$ $BiFeO_3$ compounds, reports detecting the compound but does not dwell on the subject. We assume that it is one of the metastable phases which is attained due

to the existence of the sodium ions, acting as spectator ions. A smaller fraction (14.6%) of rhombohedral $BiFeO_3$ phase exists with an additional 7.3% (2:1 ratio) of the triclinic (P1) α $BiFeO_3$. The α $BiFeO_3$ results obtained, corresponds with the lattice parameters reported by Wang et al. [17]. It is interesting to notice that even though the NaCl did not react with the material displaying obvious segregation it was found to be in an amorphous state.

Fig.4 displays an optical microscope image of the second calcinated and ground Bi_2O_3 based flux.

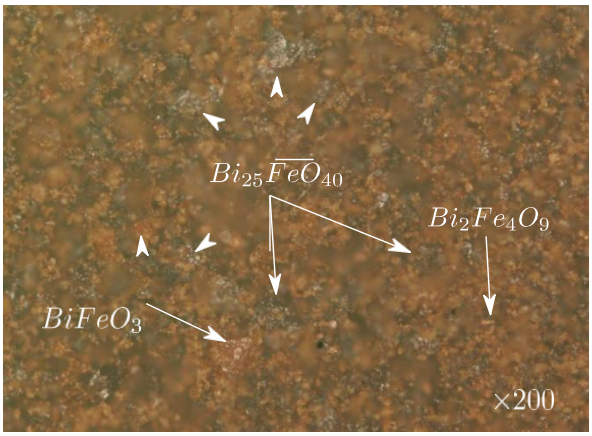

Fig.4. Optical microscope image of the calcinated and ground Bi_2O_3 based flux

While the orthorhombic mullite structure is hardly observed in the figure, one can easily notice the considerable increase in the metallic grey areas signifying the sillenite compound. Tab.2 displays the weight fraction of the crystalline phases of the calcinated flux materials that do not include the sodium chloride.

Table 2. Weight fraction of crystalline phases in calcinated BFO flux materials without sodium chloride

Compound	Weight fraction [%]	a [Å]	b [Å]	c [Å]	α [°]	β [°]	γ [°]
$Bi_{25}FeO_{40}$	68.9	10.15600	10.15600	10.15600	90.000	90.000	90.000
$BiFeO_3$	25.7	5.57801	5.57801	13.86400	90.000	90.000	120.00
$Bi_2Fe_4O_9$	5.39	7.97971	8.43282	6.00463	90.000	90.000	90.000

Tab.2 shows a similar percentage of mullite to the material in which the parasitic phases were not reduced (Lu [3]). In this molar ratio we do expect the sillenite to be much more abundant as it is one of the two stable phases.

Sintering

Prior to sintering and in order to test the stable phases, the materials were placed for 16 hours at $600^{\circ}C$ thus increasing the stable phases at that temperature range, i.e. - the mullite and sillenite phases. The reaction trend gives us a better indication which are the stable phases. As the various articles using rapid sintering [6, 7, 8] reported placing the pressed disks within the furnace between 400 and 450 seconds, the samples were placed in the furnace up to 8 minutes and then rapidly cooled by extracting them from the furnace and letting them cool on a piece of ceramic at room temperature. Fig.5 illustrates the results obtained from the 56/44 mole% Bi_2O_3 Fe_2O_3 solid state compounds based on XRD measurements.

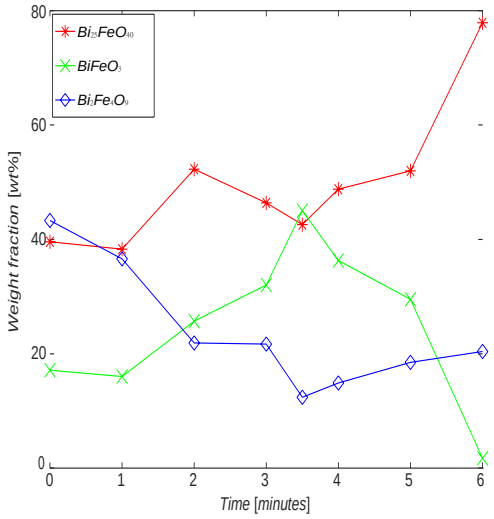

Fig.5. Weight fraction of the different compounds resulting from the solid-state reaction of the quenched disks at $880^{\circ}C$ based on the reaction time

At this specific Bi_2O_3/Fe_2O_3 ratio, the two expected phases that are known to coexist are the BFO phase and the sillenite phase. The results show that up to approximately 3.5 minutes the $BiFeO_3$ phase increased to about 50% at the expense of both the $Bi_{25}FeO_{40}$ and $Bi_2Fe_4O_9$ phases, after which it experiences a fast decline to undetectable levels. After 3.5 minutes while the BFO decomposes the level of the mullite increases slightly and the sillenite becomes the dominant stable phase. This does not correspond with the accepted phase diagram and hints that some impurities from the crucible may have altered the composition or that at $880^{\circ}C$ $Bi_{25}FeO_{40}$ is the dominant phase.

We repeated the process described above, with the Bi_2O_3 Fe_2O_3 NaCl composition. The weight fraction of the different compounds obtained by the system as a function of time is described in Fig.6.

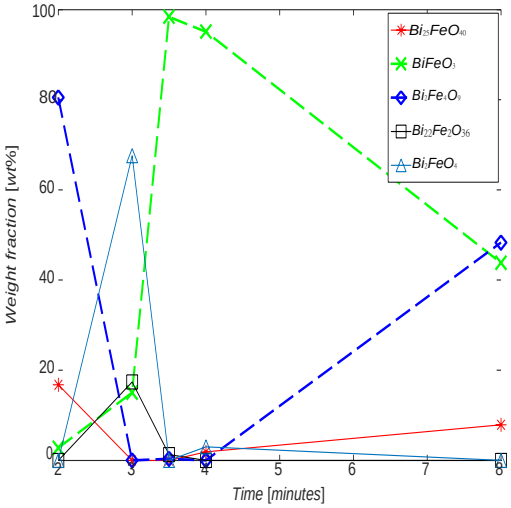

Fig.6. Weight fraction of the different compounds obtained by the $56Bi_2O_3{\cdot}44Fe_2O_3$ + 6.5*wt*% *NaCl* composition heated and quenched disks at 880°*C* based on the reaction time.

Fig.6 demonstrates the process in which the NaCl (Melting point 801◦C) slowly, dissolves the constituents and between 3-4 minutes suppressing the mullite and sillenite phases while the BiFeO3 temporarily dominates. At this composition, the material is beyond the peritectic which for longer periods will result in a liquid + $Bi_2Fe_4O_9$ similar to the transition, for the 56/44 mole% composition above 934◦C.

DISSCUSION

Based on the accepted phase diagram [18, 9, 10, 11, 3], and Gibbs energy of formation [14], during the synthesis of materials and solid state reactions above 767◦C the $Bi_2Fe_4O_9$ phase, should not be a stable phase. This is true as long as the Bi_2O_3/Fe_2O_3 molar ratio is above 1:2. Contrary to what has just been stated, experience has shown that for long enough periods of time the mullite phase does form as a stable phase. As a result, rapid heating and cooling techniques are a common practice for obtaining a high weight fraction of BFO ceramics. Lu et. al. have shown that for highly controlled compositions in gold crucibles at a temperature of 850◦C, BFO is the prevalent stable phase. Given impurities it will slowly decompose to other phases primarily to mullite. At temperatures above 855◦C even the highly controlled compositions tend to decompose over a long period of time. This has to be taken into account if one attempts to grow bulk crystals even for highly controlled environments, one is limited below 850◦C for bulk BFO crystal growth. As the goal of this work was sintering targets for sputtering machines, we were interested in BFO phase stability and the adequate sintering time during the sintering process. We compared a 56:44 mole% Bi_2O_3-Fe_2O_3 composition to a $56Bi_2O_3{\cdot}44Fe_2O_3$ + 6.5wt% NaCl composition. We demonstrated that at 880◦C after 3.5 minutes in the composition which does not include NaCl only approximately 50% of the material has transformed into BFO. At the same time using the composition that includes NaCl as a flux, 98.5% of the material was in the BFO phase totally suppressing any other phase. Further work is being carried out in order to increase the BFO content for at least 99.98% obtaining the required grade for RF sputtering purposes. The importance of this finding is that it is relatively simple to remove the NaCl from the sintered disk. This is done by rinsing the disk in water. One drawback of this method is that it leaves the disk with pitting and cavities.

CONCLUSIONS

In this article a simple method for rapid sintering of BFO targets for RF sputtering purposes is demonstrated. The targets are significant for applications in photovoltaic, memory and sensor design based on BFO, mullite or a combination of both phases as discussed in [19]. A 56/44 Bi2O3/Fe2O3 + 6.5wt% NaCl composition was shown to give superior results in rapid sintering of targets compared to the same composion without the NaCl. It is important to note that the NaCl did not form new phases or compounds but provides the sodium as a spectator ion. After the sintering process, the NaCl was extracted from the target by rinsing in water. We note that the suggested experimental setting is providing a good preliminary BFO composition. However, the concentration should be further increased in order to employ it as a BFO sputtering target.

REFERENCES

[1] Nicola A Spaldin, Sang-Wook Cheong, and Ramamoorthy Ramesh. Multiferroics: Past, present, and future. *Physics Today*, **63**(10), 38 (2010).

[2] Gustau Catalan, James F Scott. Physics and applications of bismuth ferrite. *Advanced materials*, **21**(24), 2463–2485 (2009).

[3] J Lu, LJ Qiao, PZ Fu, YC Wu. Phase equilibrium of Bi2O3–Fe2O3 pseudo-binary system and growth of BiFeO3 single crystal. *Journal of crystal growth*, **318**(1), 936–941 (2011).

[4] S Phapale, R Mishra, D Das. Standard enthalpy of formation and heat capacity of compounds in the

pseudo-binary Bi2O3–Fe2O3 system. *Journal of nuclear materials*, 373(1- 3), 137–141 (2008).

[5] TT Carvalho and PB Tavares. Synthesis and thermodynamic stability of multiferroic BiFeO3. *Materials Letters*, **62**(24), 3984–3986 (2008).

[6] JAHAR L MUKHERJEE, FRANKLIN FY WANG. Kinetics of solid-state reaction of Bi2O3 and Fe2O3. *Journal of the American Ceramic Society*, **54**(1), 31–34 (1971).

[7] YP Wang, L Zhou, MF Zhang, XY Chen, J-M Liu, and ZG Liu. Room-temperature satu- rated ferroelectric polarization in BiFeO3 ceramics synthesized by rapid liquid phase sintering. *Applied Physics Letters*, **84**(10), 1731–1733 (2004).

[8] MS Awan and AS Bhatti. Synthesis and multiferroic properties of BFO ceramics by melt-phase sintering. *Journal of materials engineering and performance*, **20**(2), 283–288 (2011).

[9] EI Speranskaya, VM Skorikov, E Ya Rode, VA Terekhova. The phase diagram of the system bismuth oxide-ferric oxide. *Bulletin of the Academy of Sciences of the USSR, Division of chemical science*, **14**(5), 873–874 (1965).

[10] A Maitre, M Francois, and JC Gachon. Experimental study of the Bi2O3-Fe2O3 pseudo-binary system. *Journal of Phase Equilibria and Diffusion*, **25**(1), 59–67 (2004).

[11] R Palai, RS Katiyar, Hans Schmid, Paul Tissot, SJ Clark, Jv Robertson, SAT Redfern, GA Catalan, JF Scott. β phase and γ- β metal-insulator transition in multiferroic $BiFeO_3$. *Physical Review B*, **77**(1), 014110 (2008).

[12] ZV Gabbasova, MD Kuzm´ in, AK Zvezdin, IS Dubenko, VA Murashov, DN Rakov, IB Krynetsky. Bi(1-x)R(x)FeO3(R= rare earth): a family of novel magnetoelectrics. *Physics Letters A*, **158**(9), 491-498 (1991).

[13] Piyush Sharma, PK Diwan, OP Pandey. Impact of environment on the kinetics involved in the solid-state synthesis of bismuth ferrite. *Materials Chemistry and Physics*, **233**, 171–179 (2019).

[14] Sverre M Selbach, Mari-Ann Einarsrud, Tor Grande. On the thermodynamic stability of BiFeO3. *Chemistry of Materials*, **21**(1), 169–173 (2009).

[15] TI Mel'nikova, GM Kuz'micheva, NB Bolotina, NV Sadovskaya. Development of methods of X-ray diffraction analysis for determining the composition and structure of sillenite-family crystals. *Crystallography Reports*, **59**(2), 155–159 (2014).

[16] Shunsuke Murakami. BaTiO3-BiFeO3 based lead-free ceramics for actuator applications. PhD thesis, University of Sheffield, 2018.

[17] Hui Wang, Chengxu Yang, Jun Lu, Meimei Wu, Jie Su, Kuo Li, Junrong Zhang, Guobao Li, Tounan Jin, Takashi Kamiyama, et al. On the structure of α-BiFeO3. *Inorganic chemistry*, **52**(5), 2388–2392 (2013).

[18] Hideo Koizumi, Nobukazu Niizeki, and Takuro Ikeda. An X-ray study on Bi2O3-Fe2O3system. *Japanese Journal of Applied Physics*, **3**(8), 495–496 (1964).

[19] A.S. Poghossian, H.V. Abovian, P.B. Avakian, S.H. Mkrtchian, V.M. Haroutunia. Bismuth ferrites: New materials for semiconductor gas sensors. *Sensors and Actuators B*: *Chemical*, **4**(3), 545-549 (1991).

Bulgarian Chemical Communications, Volume 52, Special Issue C (pp. 46-52) 2020 DOI: 10.34049/bcc.52.C.0102

An integrated approach for improvement of the efficiency of the photovoltaic system by using cogeneration

I. S. Stoyanov[1], T. B. Iliev[2*]

[1]*"Angel Kanchev" University of Ruse, Department of Electric Power Engineering, 8 Studentska Str, 7017 Ruse, Bulgaria*

[1]*"Angel Kanchev" University of Ruse, Department of Telecommunications, 8 Studentska Str, 7017 Ruse, Bulgaria*

The present study explores the possibility of increasing the efficiency of a stand-alone photovoltaic system through cogeneration - simultaneous production of electricity and low-temperature water heating. Optimal operation means to achieve the best performance of the photovoltaic system, with certain limitations, and the optimal will be what provides the best condition of the system. The extreme value of a certain accepted quality assessment functional plays the role of an optimality criterion. It has been found that improving the performance of the photovoltaic system can be achieved by finding the optimum between the production of electricity, water heating and solar radiation, which ensures the highest efficiency of the system. An experimental installation has been developed and the results of the study of the photovoltaic system with cogeneration has been shown. The results of this study confirm the feasibility of the proposed solution for the production of electricity and heat energy for water heating.

Keywords: Solar energy, Photovoltaic system, Cogeneration, Optimal operation, Efficiency.

INTRODUCTION

A number of types of photovoltaic system (PVS) exist. It is known that the electric power produced by the photovoltaic system (PVS) depends on a number of factors such as the new solar radiation, climatic weather (clear or cloudy day), ambient temperature, angle of inclination, temperature of the modules and others. All of them have a significant impact on the effectiveness of PVS. Depending on their weight on the work of PVS, the factors can be grouped into:

1) Seasonal: For example, the annual season. They determine the seasonal cycle of change.

2) With Random modification: They are essential for the efficiency of photovoltaic modules. The most important of these is the type of day. If the day is clear, then the expected amount of electricity received from the photovoltaic module will be the largest. Random factors with relatively less but constant importance are the area and type of the photovoltaic module, the location of the photovoltaic installation and others.

3) Periodical: The time of day.

All of these are presumptive established effects can be classified as uncontrollable factors, as the power obtained from the photovoltaic module changes over time under their influence [18].

The efforts of many researchers are aimed at improving the performance of PVS. In this regard, new materials, technological and technical solutions are being developed to increase the efficiency of solar energy conversion. These efforts can be summarized in two large groups - the creation of new semiconductor materials, in which the conversion of solar energy directly into electricity is as efficient as possible through the combined production (cogeneration) of another type of energy [7, 8]. The purpose of all these solutions is to reduce the required area of photovoltaics by increasing the density of solar energy flux.

The main problem of direct conversion is the relatively low efficiency - between (10 -15) %. The rest of the solar energy that reaches the panels is converted into heat. In order to solve this problem, the multi-junction solar cells are being proposed, also, new types of solar cells are being created and more [11]. The rest of the solar energy that falls on the photovoltaic panels is converted into heat.

Another way to make better use of solar energy in PVS is through the combined production (cogeneration) of another type of energy [15]. A photovoltaic system with cogeneration allows for the simultaneous production of electricity and other energy. It is known that in the process of their work photovoltaics heat up. On the other hand, heating the photovoltaic panels further reduces their efficiency by 0.4 - 0.5% for every 1 °C at Standard Test Conditions (STC) - 1000 W/m² solar radiation level, 25 °C cell temperature and A.M. 1.5 air mass rate. Therefore, it is essential for photovoltaic modules to

* To whom all correspondence should be sent:
tiliev@uni-ruse.bg

operate at conditions as close as possible to STC to obtain higher energy yields and better efficiency.

All this is a prerequisite for the combined production of energy from photovoltaic modules through the simultaneous production of electricity and heat.

A photovoltaic-thermal system (PVTS) consists of a PV panel and a thermal collector installed on the rear surface of the panel [4]. This makes it possible for the part of the solar radiation alighted on the surface of the photovoltaic panel to be converted into electrical power and heat [9, 19, 20].

In the literature, a number of authors have published their studies in the field of PVTS. In [6, 10, 19, 20] are suggested different profiles of thermal collectors. In [1] it was found that electrical, thermal and overall efficiencies reached 12.65%, 56.73%, and 85% respectively. A possible approach to cool it down through oiling tubes to the PV panel was presented in [17]. In [5] the energy and energy efficiencies of PVT air collector with monofacial solar cells and for the bifacial PVT were established.

The analysis of all this shows that the technical solutions are aimed at the joint development of electricity and heat (cogeneration) by solving the problem of cooling photovoltaic panels and at the same time improving the energy efficiency of PVS.

The purpose of this paper is to determine the optimal operating mode of a photovoltaic system using cogeneration for producing electricity and thermal energy.

The aim of this article is to study the efficiency of a stand-alone photovoltaic system through cogeneration - simultaneous production of electricity and low-temperature water heating.

MATHEMATICAL MODEL FOR THE OPTIMAL OPERATION

Optimal operation means to achieve the best performance of the photovoltaic system. Having in mind some limitations, the optimal would be what provides the best system state. Extreme value of an adopted function for quality assessment acts as a criterion for optimality [12, 13, 14]. The task is to find and maintain some extreme (maximum or minimum). In doing so, it comes down to determining the differential equation or the transfer function.

The solution of the considered problem can be reduced to minimizing the Hamilton function H [λ, x, y, t], written about a nonstationary system [2]:

$$\dot{x}(t) = A(t).x(t) + B(t).u(t). \quad (1)$$

If the minimum condition of the function H [λ, x, y, t] is applied with respect to the control u (t). This is equivalent to the condition for a minimum of $u(t) \in Q$ and at all points of continuity of the control of the function Λ [λ, x, y, t]:

$$min\,\Lambda[\lambda,x,u,t] = min\left\{\frac{dV[x(t),t]}{dt} + H[\lambda,x,u,t]\right\} = 0. \quad (2)$$

where: $V[x(t),t]$ is the Lyapunov function [16].

For each object, a certain relationship can be established between the relative yield *q* and the control effects u_j, $j=1...r$:

$$q = \sum_{j=1}^{j=r} \nu_j |u_j(t)|, (\nu_j > 0), \quad (3)$$

where: $\nu_j, j = 1...r$ are the coefficients of proportionality.

The total amount of energy produced in the interval [t_0, t_f] can be expressed by a functional of the form:

$$Q = \int_{t_0}^{t_f} \sum_{j=1}^{j=r} \nu_j.[u_j(t)]dt., \quad (4)$$

while minimizing the functional (4), the process time

$$T = t_f - t_0, \quad (5)$$

is not less than the minimum possible T^*. This time corresponds to the optimal speed process, i.e. $T \geq T^*$.

The control vector is assumed to be constrained as follows:

$$|u_j(t)| \leq 1; j = 1,...,z. \quad (6)$$

Therefore, the managed system is of the form:

$$\dot{x}(t) = A.x(t) + B.u(t). \quad (7)$$

If the matrix A has eigenvalues with negative real parts, then the controlled object is stable. The free motion *x(t)* at $t \to \infty$ can be determined from the initial state $x(t_0) = x \neq 0$ to the origin of the coordinates $x(t_j) = x^j = 0$ for the control vector *u(t)* = 0:

$$\lim_{t\to\infty} x(t) = e^{t.A}; x = 0 \quad (8)$$

Therefore, if the transition time is set $T_j = t_j - t$ (at negative eigenvalues of A) the trivial solution

will be obtained $u^*(t)=0; T_j=\infty$. n doing so, the end time of the transition will be fixed:

$$t_j - t_0 = T_j \geq T^*, \tag{9}$$

where: T^* is the duration of an optimal speed process.

Record the Hamilton function for system (7):

$$H[x(t),p(t),u(t)] = \\ = \sum_{j=1}^{r} \left|u_j(t)\right| + \langle A.x(t),p(t)\rangle + \langle B.u(t),p(t)\rangle. \tag{10}$$

The condition for optimality is expressed by the relation:

$$\sum_{j=1}^{r} \left|u_j^*(t)\right| + \left\langle A.x^*(t),p^*(t)\right\rangle + \left\langle u^*(t),B^T p^*(t)\right\rangle \\ \leq \sum_{j=1}^{r} \left|u_j(t)\right| + \left\langle A.x(t),p^*(t)\right\rangle + \left\langle u(t),B^T p^*(t)\right\rangle, \tag{11}$$

where: $t \in \lfloor 0,T_j \rfloor$ is performed for each admissible control u (t) bounded by (6).

Inequality (11) is equivalent to the following relation:

$$\sum_{j=1}^{r} \left|u_j(t)\right| + \left\langle u^*(t),B^T p^*(t)\right\rangle \\ \leq \sum_{j=1}^{r} \left|u_j(t)\right| + \left\langle u(t),B^T p^*(t)\right\rangle. \tag{12}$$

or

$$\sum_{j=1}^{r} \left|u_j(t)\right| + \sum_{j=1}^{r} u_j^*(t)\left\{\sum_{j=1}^{n} b_{ij}.p_j^*(t)\right\} \\ \leq \sum_{j=1}^{r} \left|u_j(t)\right| + \sum_{j=1}^{r} u_j(t)\left\{\sum_{j=1}^{n} b_{ij}.p_j^*(t)\right\}. \tag{13}$$

Switching functions are entered

$$\nu_j^*(t) = \sum_{j=1}^{n} b_{ij}.p_i^*(t); (j=1,...,r), \tag{14}$$

where $p_i^*(t); (i=1,...,n)$ are the solutions of (7).

Therefore, inequality (13) can be written in a more compact form:

$$\sum_{j=1}^{r} \left\{\left|u_j^*(t)\right| + u_j^*(t).\nu_j^*(t)\right\} \\ \leq \sum_{j=1}^{r} \left\{\left|u_j(t)\right| + u_j(t).\nu_j^*(t)\right\}. \tag{15}$$

The last inequality means that the function

$$H_m[u(t)] = \sum_{j=1}^{r} \left\{|u_j(t)| + u_j(t).\nu_j^*(t)\right\} \tag{16}$$

takes an absolute minimum at

$$u(t) = u^*(t); j=1,...,r);$$

$$H_m[u(t)] = \\ u(r)\in\Omega \\ = \sum_{j=1}^{r} \min_{|u_j(t)\leq 1|} \left\{\left|u_j(t)\right| + u_j(t).\nu_j^*(t)\right\}, \tag{17}$$

that is:

$$\min_{u(t)\in\Omega} H_m[u(t)] = \\ = \sum_{j=1}^{r} \min_{|u_j(t)\leq 1|} \left\{u_j(t).\left[signu_j(t) + \nu_j^*(t)\right]\right\} \tag{18}$$

$$= \begin{Bmatrix} \sum_{j=1}^{r}\left[1-\left|\nu_j^*(t)\right|\right] & npu & \left|\nu_j^*>1\right| \\ 0 & npu & \left|\nu_j^*<1\right| \end{Bmatrix}$$

A sufficient condition for the normality of the problem is the performance for each *j=1,2,…,r* of:

$$det\left[G_j^T A^T\right] \neq 0, \quad (j=1,2,...,r), \tag{19}$$

where:

$$G_j = \left[b_j : Ab_j : ... : A^{n-1}b_j\right]. \tag{20}$$

If the task is degenerated, it is necessary to optimize the operation of the system, i.e. for some equation i.e. for some j = 1,2,…, r, the equality should be in force:

$$det\left[G_j^T, A^T\right] = 0. \tag{21}$$

If the task is normal, this corresponds to the optimal operating mode.

RESULTS

Fig.1 shows the block diagram of the investigated autonomous PVT system. It consists of a photovoltaic panel PV1 without forced cooling, a cogeneration photovoltaic panel PV2 with water cooling, a charging controller; storage tank for cold and hot water; rechargeable battery, inverter and load, and the specialized measuring device NI USB-6008. It has 8 analog inputs, two analog outputs and 12 digital channels.

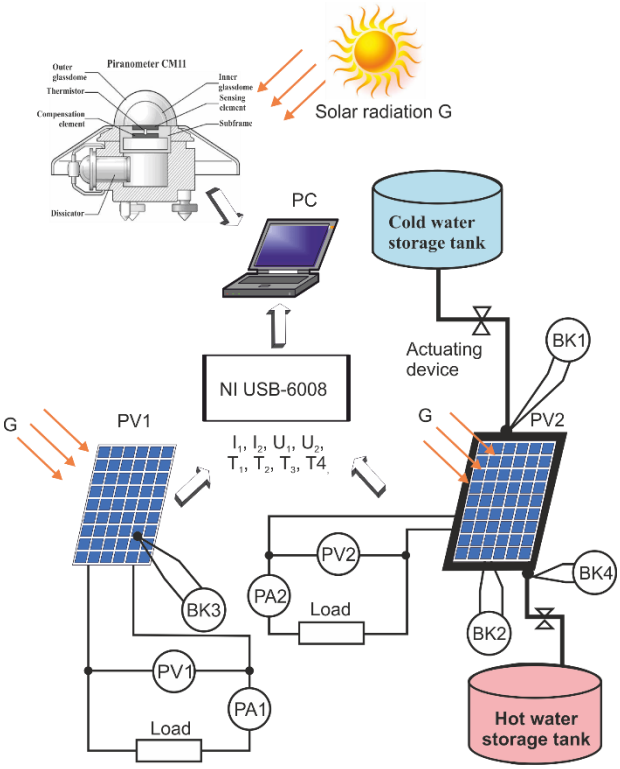

a

b

Fig.1. Layout (a) and the photo (b) of the investigated PV cogeneration system

Using the ammeters PA, the voltmeters PV and the temperature sensors BK, the magnitude of the current Ii, the voltage Ui, and the temperature Ti of the photovoltaic modules at constant load Load = const. are recorded, respectively.

The registered values are supplied in a suitable form and levels to the analogues in the input of the device NI USB-6008 in the range from -1 to + 10V. From it the data is transferred via USB cable in real time to a personal computer, for storage, processing and analysis.

The research of the solar radiation was performed with the help of a specialized measuring system of the company Kipp & Zonen B.V. It consists of a pyranometer CM11 and an integrating unit - Integrator. This instrument measures global solar radiation. The pyranometer has the spectral response of between 335 and 2200 nm. The integrated unit offers the possibility to directly in W,m^2 , or integrally in kJ, measure the intensity of direct and diffuse solar radiation. Through a standard communication serial interface (RS232) the processed signal from Integrator is fed to a personal computer.

With the help of specialized software, the obtained information about the intensity of solar radiation is visualized, stored and processed (Fig.2).

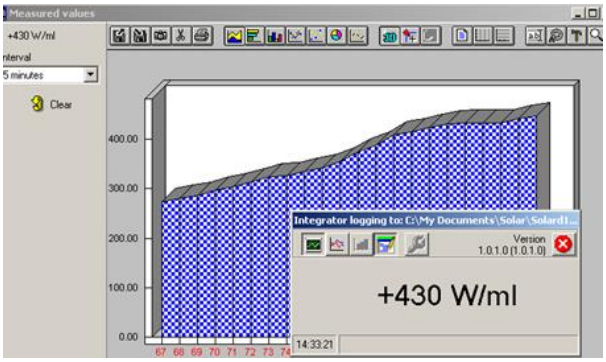

Fig.2. Working window of the software program Integrator [3]

The incident solar radiation on the surface of photovoltaic modules is the primary source of electricity production, but at the same time the modules are heated to a certain temperature. The two modules are mounted on a common stand and are oriented at the same angle to the Sun. On one of modules on the back is a tightly attached heat exchanger made of a spirally wound tube. Water is used as a heat carrier. The heat transfer from the photovoltaic module to the water is done through thermal conductivity and convection.

The heat flow (Q_t) can be determined by the expression:

$$Q_t = \Delta t.V.\rho.c.(T_2 - T_1), Wh \quad (22)$$

where:

Δt - interval of time in which the heat exchange was performed, h;

V – mass flow, l/h;

ρ – specific density, kg/l;

c - specific heat capacity of water (c = 4186,8 kJ/(kg. ºC);

T_1, T_2 are respectively the temperature of the water inlet and outlet, ºC.

The amount of heat that is released by the module and absorbed by the water can be determined by the calorimetric equation

$$Q = m.c(T_2 - T_1) \quad (23)$$

where:

m is the water mass, kg.

The heat transfer depends on the type and speed of the fluid, the area and the material of the heat exchanger. The speed of the fluid through the heat exchanger can be regulated by means of two taps mounted at the outlet of the cold tank and at the inlet of the hot tank by means of an actuating device.

The power P of the photovoltaic module increases with increasing solar radiation G and decreases with increasing temperature T.

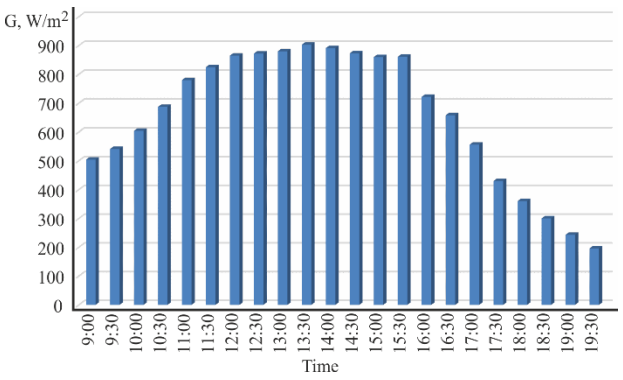

Fig.3. Dynamics of solar radiation G, W/m^2

The electrical efficiency η_{el} of the photovoltaic panel can be determined using the expression

$$\eta_{el} = \frac{P_{mp}}{G.A} \quad (24)$$

where:

P_{mp} – maximum power generated by the panel, W;

G – solar radiation, W/m^2;

A – area of the panel, m^2.

By differentiating (24) with respect to temperature, it is obtained

$$\frac{\eta_{el}}{dT} = \frac{1}{G.A}\left(I_{mp}\frac{U_{mp}}{dT} + U_{mp}\frac{I_{mp}}{dT}\right). \quad (25)$$

Therefore, the dependence on the electrical efficiency of the panel is valid:

$$\eta_{el} = \eta_{ref}\left(1 - \beta\left(T - T_{ref}\right)\right), \quad (26)$$

where:

η_{ref} – efficiency of cell at reference temperature;

β – cell's temperature coefficient, K^{-1};

T – module temperature, °C.

T_{ref} – reference temperature, °C.

On the Figs.3, 4 and 5 are presented obtained results.

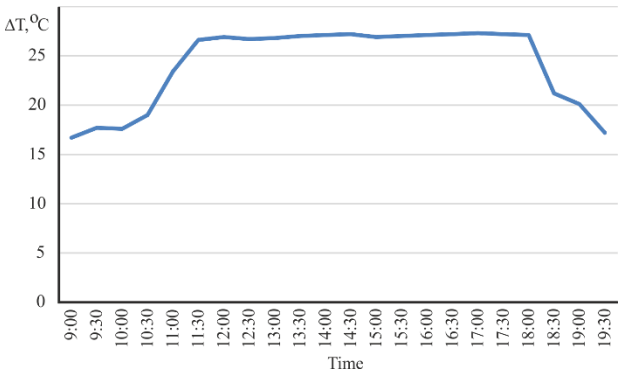

Fig.4. Temperature difference ΔT between PV1 and PV2, ºC

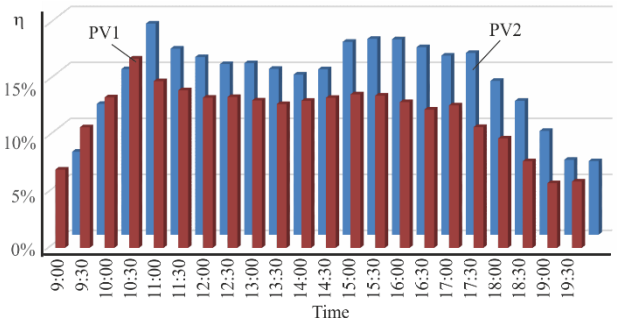

Fig.5. Efficiency dynamics η of PV_1 and PV_2

The analysis of the obtained dependences shows that the nature of the change in the intensity of the solar radiation during the sunny days is similar (see Fig.3). The minimal differences observed in size depend on the optical properties of the atmosphere. The change in function of astronomical time is parabolic, corresponding to the azimuth of the sun. The maximum intensity of solar radiation is observed in the middle of the day.

The positive effect of cogeneration is visualized in Figs.4 and 5. As a result of the heat exchange, the temperature of the photovoltaic panel with water cooling is almost constant, while the temperature of

the other increases gradually with increasing solar radiation. The temperature of PV2 is from 20 to 24 ºC lower than PV1, with the largest difference observed during the hours with maximum levels of solar radiation. The resulting dependence has a trapezoidal shape and the horizontal section corresponds to the time range in which a PV system can be fully used for the production of electricity and heat. As a result of heat transfer, the water temperature rises by about 12.6 ºC.

Due to the cooling the generated current and voltage from PV2 are higher than those from PV1, respectively the electric power produced is higher. In addition, due to the relatively constant temperature of PV2 it is expected to have less heat load, and hence increase of service life.

The analysis of the dynamics of the efficiency η of PV1 and PV2 shows that the photovoltaic panel with cogeneration PV2 always has a higher efficiency compared to PV1. The efficiency of PV2 in electricity production is up to 30% higher than in the case of conventional air cooling, and the overall efficiency of the autonomous photovoltaic system increases from 12% to 14.1%. The thermal efficiency is 4,8% and the total efficiency of the investigated PV cogeneration system is up to 19%.

CONCLUSIONS

An approach is proposed to optimize the operation of a photovoltaic system by using cogeneration and increasing efficiency by achieving a balance between electricity and heat production.

An experimental system has been developed to study the operation of the PVT system. The obtained results prove the efficiency and feasibility of the proposed solution. The use of a heat exchanger reduces the heat load of the photovoltaic module, increases the generated electric power and low-temperature water heating.

The proposed approach is suitable for application in stand-alone photovoltaic systems, for combined production of electricity and heat and can be used in agricultural areas and remote sites where there are no centralized energy sources. It has been established that cogeneration makes it possible to increase the energy efficiency of photovoltaic systems.

REFERENCES

[1] Abdullatif A., Mohammed K. and Saifalddeen A. The hybrid Photovoltaic-Thermal double-pass solar system for drying applications. *IOP Conference Series: Materials Science and Engineering*, **765** (2020), 012024 IOP Publishing, doi:10.1088/1757-899X/765/1/012024.

[2] Baldiotti, M.C. & Fresneda, Rodrigo & Molina, C. A Hamiltonian approach to Thermodynamics. *Annals of Physics*, **373** (2016), 10.1016/j.aop.2016.07.004.

[3] CM11 Pyranometer. www.kippzonen.com.

[4] Dean, Jesse, McNutt, Peter, Lisell, Lars, Burch, Jay, Jones, Dennis, and Heinicke, David. Photovoltaic-Thermal New Technology Demonstration. United States: NREL, 2015, p 43., Web. doi:10.2172/1170335.

[5] Fudholi, A., Mustapha, M., Taslim, I., Aliyah, F., Koto, A. G., & Sopian, K. (2019). Photovoltaic thermal (PVT) air collector with monofacial and bifacial solar cells: A review. *International Journal of Power Electronics and Drive Systems*, **10** (4), 2021-2028. doi:10.11591/ijpeds.v10.i4.2021-2028.

[6] Govind N. Kulkarni, Shireesh B. Kedare, Santanu Bandyopadhyay, Optimization of solar water heating systems through water replenishment, *Energy Conversion and Management*, **50** (3), 837-846 (2009) ISSN 0196-8904, https://doi.org/10.1016/j.enconman.2008.09.019.

[7] Joe-Air J., T. Huang, Y. Hsiao, Ch. Chen. Maximum Power Tracking for Photovoltaic Power Systems. Tamkang *Journal of Science and Engineering*, **8** (2), 147-153 (2005).

[8] Kulkarni G., Sh. B. Kedare, S. Bandyopadhyay. Optimization of solar water heating systems through water replenishment. *Energy Conversion and Management*, **50** (3), 837-846 (2009), https://doi.org/10.1016/j.enconman.2008.09.019.

[9] Mangesh S. Thakare, G. S. Krishna Priya, Prakash Chandra Ghosh, Santanu Bandyopadhyay. Optimization of photovoltaic–thermal (PVT) based cogeneration system through water replenishment profile, *Solar Energy*, **133**, 512-523, (2016), ISSN 0038-092X, https://doi.org/10.1016/j.solener.2016.04.037.(http://www.sciencedirect.com/science/article/pii/S0038092X16300706).

[10] Mangesh, S., G. Priya, P. Ghosh, S, Bandyopadhyay. Optimization of photovoltaic–thermal (PVT) based cogeneration systemthrough water replenishment profile. *Solar Energy*, **133**, 512-523 (2016).

[11] Marti A., A. Luque. Next Generation Photovoltaics: High Efficiency through Full Spectrum Utilization. CRC Press, p. 136, 2003.

[12] Matanov N., A. Zahov, Remote Electricity Metering Systems. 2019 11th Electrical Engineering Faculty Conference (BulEF), Varna, Bulgaria, 1-6, 2019, doi: 10.1109/BulEF48056.2019.9030800.

[13] Matanov N., S. Dimitrova, Operating Modes Optimization of the Capacitor Banks in Electrical Power Systems. *10th Electrical Engineering Faculty Conference (BulEF), Sozopol, Bulgaria*, 1-3, 2018, doi: 10.1109/BULEF.2018.8646938.

[14] Rachev, S., Stefanov, D., Dimitrov, L., Koeva, D. Evaluation of Electric Power Losses of an Induction Motor Driving a Compact Electric Vehicle at Change of Parameters and Loads," 2019 *Electric Vehicles International Conference (EV), Bucharest, Romania*, 1-5, (2019), doi: 10.1109/EV.2019.8893057

[15] Ramos A., Maria Anna Chatzopoulou, Ilaria Guarracino, James Freeman, Christos N. Markides. Hybrid photovoltaic-thermal solar systems for combined heating, cooling and power provision in the urban environment. *Energy Conversion and Management*, **150**, 838-850 (2017).

[16] W. Lei and Q. Li. Online Power Control Based on Lyapunov Optimization Framework for Decode-and-Forward Relay Systems With Energy Harvesting. *IEEE Access*, **7**,71335-71349 (2019), doi: 10.1109/ACCESS.2019.2919968.

[17] Yousefnejad, R., Atabaki, N. and Chiao, M.. An algorithm for designing a cooling system for photovoltaic panels. *Solar Energy*, **194**, 450-460 (2019).

[18] Zlatov, N., Iliev, I., Terziev, A., Kamburova, V. Influence of climatic data and degradation factor on the efficiency of the photovoltaic modules. *15th International Workshop on Research and Education in Mechatronics (REM), El Gouna*, 1-5 (2014) doi: 10.1109/REM.2014.6920447

[19] Zondag H. A., D. W. de Vries, W.G.J. van Helden, R. J. C. van Zolingen, A. A. van Steenhoven. The thermal and electrical yield of a PV-thermal collector. *Solar Energy*, **72** (2), 113-128 (2002) ISSN 0038-092X, https://doi.org/10.1016/S0038-092X(01)00094-9. (http://www.sciencedirect.com/science/article/pii/S0038092X01000949)

[20] Zondag H. A., D.W. de Vries, W.G.J. van Helden, R.J.C. van Zolingen, A.A. van Steenhoven. The yield of different combined PV-thermal collector designs, *Solar Energy*, **74** (3), 253-269 (2003), ISSN0038-092X, https://doi.org/10.1016/S0038-092X(03)00121-X. (http://www.sciencedirect.com/science/article/pii/S0038092X0300121X).

Bulgarian Chemical Communications, Volume 52, Special Issue C (pp. 53-64) 2020 DOI: 10.34049/bcc.52.C.0009

A review of phase change material based thermal energy accumulators in small-scale solar thermal dryers

J. Patel[1], J. Andharia[1], A. Georgiev[2,3], D. Dzhonova[2*], S. Maiti[1], T. Petrova[2], K. Stefanova[2], I. Trayanov[2], S. Panyovska[2]

[1]*CSIR-Central Salt & Marine Chemicals Research Institute, Gijubhai Badheka Marg, Bhavnagar364002, Gujarat, India*

[2] *Institute of Chemical Engineering at the Bulgarian Academy of Sciences, Acad. G. Bonchev Str. Bl.103, Sofia 1113, Bulgaria*

[3]*Technical University of Sofia, Plovdiv Branch, Dept. of Mechanics,25 Tsanko Diustabanov Str, 4000 Plovdiv, Bulgaria*

Solar thermal energy is usually of intermittent and dynamic character and the possibility to use it during non-sunshine periods is one of the current interest of researchers. Phase change materials as thermal energy accumulators are attractive because of their high storage density and ability to release thermal energy at a constant temperature corresponding to the phase transition temperature.

This paper reviews the recent state-of-the-art small-scale solar thermal dryers integrated with phase change material as energy accumulators. This is an intensive field of investigation for more than 30 years with importance for the agriculture and the food industry, especially in hot climate. A variety of commercial small-scale solar dryers are offered as a low-cost, zero-energy solution for small farmers. And yet, there are no commercial systems using latent thermal storage because at the present level of development this unit will increase unacceptably the price of the system. The solution needs a very simple design, accessible materials and optimal conditions for operation.

The aim of the present work is on the basis of the recent developments to identify the requirements for this new solution. Among the great number of designs, devices and materials, it compares the most cost and energy effective solar dryer systems with thermal storage. At the same time it makes an overview of the methods for theoretical evaluation and prediction, which are used to design and assess them. The resulting conclusions from the collected and compared information will serve as prerequisites for a novel solution of a cost-effective thermal energy storage for a small-scale solar dryer, which will lead to improved efficiency of the drying process due to controlled temperature and longer operation time. This information might serve also in the development of the wider field of thermal energy storage, which is an important part of the technologies of renewable and waste energy conversion.

Keywords: Solar energy, thermal energy accumulator, solar dryer, latent heat, phase change, energy efficiency, exergy efficiency, computational fluid dynamics

INTRODUCTION

The continuing increase in energy demand in the world creates deficiencies globally. That is why the efforts in science and technology are directed towards more effective utilization of renewable energy sources. The objectives are higher yields of product per device and lower ecological risk combined with lower cost of the devices.

Solar energy is one of the most prospective sources of renewable energy. Its intermittent nature is a drawback which can be overcome to some extent by thermal energy storage (TES) for heat supply during the non-sunshine hours. A thermal energy accumulator, integrated with a solar dryer, diminishes the fluctuation in the inlet temperature and supplies heat flow near constant temperature.

The constant temperature regulation helps to prevent the degradation of product quality. The effect on the environment is reducing harmful emissions in the atmosphere.

Solar energy can be stored by thermal, electrical, chemical, and mechanical methods, [1]. TES includes three principles of heat accumulation, by using sensible heat, latent heat and chemical heat (Fig.1). Typical examples of each principle are presented in the figure.

The rock bed is the most common material for sensible storage used in solar dryer systems. Drying of peanuts was investigated [2] using solar energy stored in a rock bed. The drying time ranged from 22 to 25 h reducing the moisture content to the safe storage moisture level of 20% with an air flow rate of 4.9 m^3/s.

* To whom all correspondence should be sent:
dzhonova@bas.bg

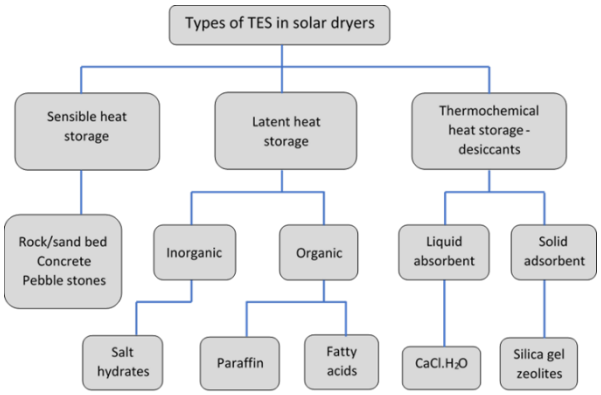

Fig.1. Types of TES integrated in solar dryer systems

It should be noted that the high energy storage density of the phase change material (PCM) is an advantage, but does not guarantee higher efficiency of the system. Surprising is the conclusion in [3] that using sensible heat storage with pebble stones is more advantageous for drying process compared to latent heat storage (LHS) with paraffin wax, with regard to performance and cost. The study presented experiments for comparison of two systems for heat storage in a solar air dryer. One of the systems was a packed bed of pebble stones and the other was paraffin wax with a melting temperature of 55-60°C, placed in heat resistant bags. One and the same quantity of 500 kg of each material was used to dry 10 kg of 5 mm thick lemon slices. The drying process lasted an average of 6.23 h (paraffin) and 6.27 h (pebble stones). The total discharge time of the two systems was 7 h on average. The presented data demonstrate the importance of the design of the LHS. The advantage of the PCM can be wasted because of hindered air flow and poor heat transfer provided by the bags containing the PCM.

The chemical heat storage is characterized by the highest energy storage density of the material, but this technology is less mature than the previous two in respect to commercialization. It uses reversible reactions which involve absorption and release of heat. In solar dryers, an example of this technology is liquid or solid desiccant material used for reducing the humidity of the drying air in off-sunshine hours.

Intensive research is carried out recently on LHS with paraffin in combination with a solar dryer. A variety of solar dryers for different food and agricultural products are suggested, tested, modified and simulated. The wide interest in these systems is due to the increasing need for preservation of food at low energy consumption with high quality of the product. One modern trend is drying of medicinal plants [4]. The heat is stored when paraffin changes its phase from solid to liquid and the heat is released at a constant temperature when paraffin cools down and solidifies again. The phase change temperature of paraffin corresponds to the drying temperature range appropriate for most of the food products to retain their valuable components.

The low thermal conductivity of paraffin is still a problem for its worldwide application and further research and development is carried out in this regard [5].

The aim of the present review is to reveal the current level of development of LHS in solar air dryers, which is an area offering many engineering solutions, experimental data and mathematical approaches for prediction and evaluation of the systems. The particular task is on the basis of the collected and compared solutions and data on LHS with a focus on paraffin as PCM to evaluate the perspectives for cost and energy-efficient design of LHS for solar dryers of small capacity (for households and small producers). The increasing of the costs of the dryer, when integrating a thermal energy accumulator, with the currently available constructions and materials, still hinders commercialization. The present overview is a step towards solving this problem, by identifying the most important conditions which will ensure a cost and energy-efficient system. It points out the characteristics of TES, proper for integration with a small-scale solar dryer, designed as a low-cost zero-energy system.

SMALL-SCALE SYSTEMS FOR SOLAR AIR DRYING WITH PARAFFIN

Conditions for successful solar drying

The drying temperature range of 40ºC to 60ºC is found to be sufficient for most of the food products to retain their flavor, aroma, texture and nutrition values. Therefore, the minimum melting temperature of the PCM should be 5–10ºC higher than the desired temperature of the heat transfer fluid (HTF) [6]. The good design of a solar dryer has to ensure the continuously stable temperature of the drying air in the order of 10–25ºC above the ambient temperature [7]. This is necessary to avoid the dried object from re-absorbing the moisture during the night, when in absence of solar energy, the air temperature drops and its humidity increases. Initial and final moisture content and maximum allowable temperature for drying of some crops are summarized in [8]. Literature review of solar drying of some medicinal plants and herbs is presented in [9]. It reveals the conditions for good quality of these heat sensitive products.

The focus of the present work is on the integration of a solar dryer with latent TES to prevent the interruption of the drying process at night. The development of a latent heat TES system involves the understanding of three essential subjects [10]: kind of phase change materials, containers' material and form of HEs.

Waxes were distinguished [1] among other LHS materials due to their availability in a wide temperature range.

Paraffin as phase change material

Paraffins are tabulated in [10] with their number of carbon atoms (from 14 to 34) and categorized as more or less promising according to their characteristics. Paraffin consists of a mixture of n-alkanes CH_3-(CH_2)-CH_3 into which the crystallization of the (CH_3) - chain is responsible for a large amount of energy absorption [10]. The melting point and heat of fusion increase with molecular weight. The latent heat of fusion of paraffin varies from nearly 170 kJ/kg to 270 kJ/kg with the temperature of phase change between 5°C to 76°C [10] which makes them suitable for solar applications. Paraffin as PCM is characterized in [10] with its advantages: it is safe, reliable, predictable, less expensive and non-corrosive; and disadvantages: low thermal conductivity, possible non-compatibility with the plastic container and moderate flammability. The following recent studies on paraffin wax in solar air dryers show the important preferred characteristics for that application.

Five paraffin waxes and a wood resin were compared [11] by studying their thermo-physical properties. The investigation aimed at selection of a PCM, for its potential use as a TES in a solar dryer. The selected paraffin had maximum density of 932.9 kg/m^3 in liquid state, and maximum latent heat of fusion and solidification 383.87 kJ/(kg K) and 320.26 kJ/(kg K), respectively. The selected PCM was used in the flat plate collector (FPC) of the solar dryer to identify the thermal zones and to validate its capability as a thermal storage. The maximum temperature achieved at outlet of the FPC was 50°C. It was found that after 18:00, the average temperature of the collector chamber with the selected paraffin was found to be 23.5% higher than that without using PCM.

In [12] paraffin with melting point 45-48°C was found more suitable compared to paraffin with melting point 68-70°C for application in fish drying with maximum temperature at the inlet of up to 75°C. The use of PCM to control the temperature inside the chamber was an important aspect as fish could not sustain a temperature of more than 62°C.

Thermal conductivity enhancement of paraffin

Multiple techniques are used to increase the charging/ discharging rate of paraffin by increasing its thermal conductivity. They include dispersion of high conductivity particles in the PCM [13, 4], using extended surfaces, and porous material embedded in the PCM. As a result the effective thermal conductivity of the PCM can be increased up to five times leading to higher rate of the heat transfer [14].

1. Additives

Novel materials were categorized in [15] for preparation of high performance PCM as 3D, 2D, 1D and 0D additives. Examples of these groups of additives used with paraffin are: graphene– nickel foam, graphite and metal foams (3D); expanded perlite, kaolin, expanded graphite (2D lamellar structure); graphite fiber (1D); and graphite-based nano-particles, nano-Al_2O_3 (0D). Improvement of 2 to over 10 times of the thermal conductivity of paraffin wax by additives is reported in [15].

2. Encapsulation of paraffin

The main advantages of PCM encapsulation are providing large heat transfer area, reduction of the material reactivity towards the outside environment and controlling the changes in volume of the storage materials as phase change occurs [16]. Based on size, the PCM encapsulation is classified into nano (0–1000nm), micro (0–1000 μm), and macro (above 1mm) encapsulation. The cheapest containers used for macro-encapsulation are tin cans and plastic bags or bottles. Typical shapes of containers for PCM are discussed in a review [17] with an emphasis on the type of the geometric configuration and orientation of the container. The shapes include spherical, rectangular, cylindrical (both horizontal and vertical) and annular containers. It was concluded there that increasing the height/width ratio of the container of the same volume decreases the time for the melting process due to the stronger buoyancy effect. Usually the material of the shell is plastic or metal (copper, aluminum and steel) when higher heat transfer rates are desirable.

Results in [18] had shown that a rectangular container needed nearly half of the melting time of a cylindrical container with the same volume and heat transfer area. The duration of the heat discharge increased with increasing PCM container diameter in the order of sphere, cylinder, plate and tube [19].

3. Extended surfaces

Experimental measurements and theoretical predictions for different fin heights and thicknesses [20, 21] showed that the use of fins enhanced significantly the heat transfer rate in and out of the element containing the PCM.

Paraffin wax was investigated [22] (phase change temperature 35–54°C, heat of fusion 196.05 kJ/kg) in a solar dryer for sweet potato coins. The TES tank was a cylindrical acrylic vessel, where HTF flowed in a tube with 18 copper fins (Fig.2). It was found that melting was dominated by heat conduction followed by free convection; charging time decreased with the increase in the inlet air temperature and air velocity.

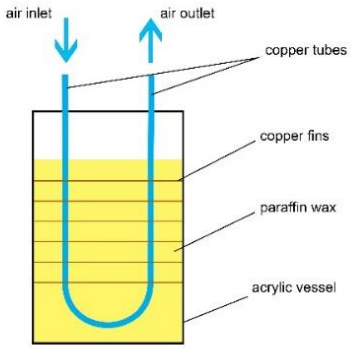

Fig.2. A scheme of a TES vessel with fins [22]

The discharging time of the LHS at an air velocity of 1 m/s was 180 min, while it was 165 min at an inlet velocity of 2 m/s. The results indicated that the air velocity did not affect much the discharging time since heat conduction was dominant during solidification.

PCM-BASED THERMAL ENERGY ACCUMULATORS IN SMALL-SCALE SOLAR THERMAL DRYERS

For solar dryers with integrated thermal energy accumulators the classification of [8] can be adopted as follows (Fig.3).

The development of a solar air drying system with paraffin includes solving several essential problems leading to energy and cost efficiency of the system: location and volume occupied by PCM; intensification of heat transfer between PCM and HTF; low energy consumption and heat loss in the systems.

It was shown [23] that the flow rate of the drying air had a significant effect on the performance of the system.

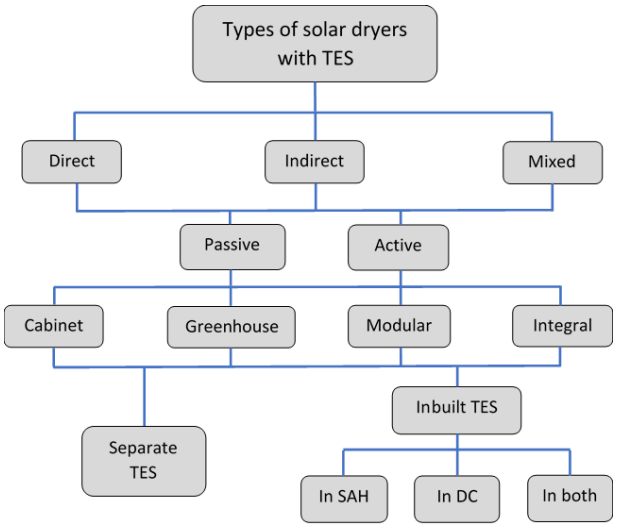

Fig.3. Types of solar dryer system with TES

The heated air for drying can be driven by buoyancy forces, or a fan, or both. Natural convection solar dryers are suitable for the rural sector and remote areas as they do not require external energy source. But it is generally agreed that well designed forced-convection distributed solar dryers are more effective and more controllable than the natural circulation types. The following dependences have been observed: the higher the mass flow rates, the higher the efficiency of the collector; the electrical energy of the fan increases with the increase in the mass flow rate of air; the effect of leakages increases with the increase in the air flow rate. The usage of forced convection in the drying system can reduce the drying time tree times and can decrease by 50% the necessary collector area [24]. Fans may be powered with utility electricity, if it is available, or with a solar photovoltaic panel.

The types of TES with PCM and their possible location in solar dryers are shown in Fig.4.

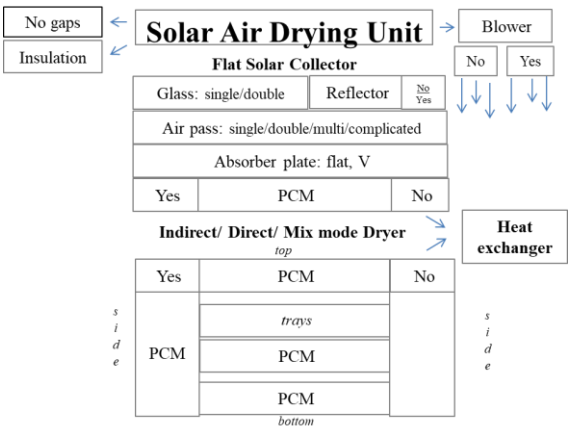

Fig.4. Solar air drying unit and possible location of PCM

A thermal energy accumulator can be integrated in the dryer system as a *separate unit*, connected outside the solar air heater (SAH) or *inbuilt* in the SAH or in the drying chamber (DC) (at the top, bottom, side walls), Fig.4.

The PCM can fill part of the volume of the unit, or can be encapsulated in containers with different form, size and material, arranged or dumped in a packed bed.

Separate TES unit with PCM

In [25] the performance of a PCM-based solar dryer is analyzed for drying black turmeric. The DC is of a mixed-mode type with hot air entering from one side and a glass top cover allowing the direct sun radiation to pass into it. Paraffin wax is used as PCM. The TES system is a shell-and-tube heat exchanger (HE) and the paraffin wax (35 kg) is placed in the shell side (Fig.5). The air from the collector passes through the tubes made of copper; one tube at the center and the other nine tubes at the periphery.

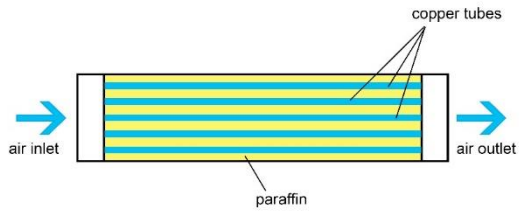

Fig.5. Shell-and-tube TES [25]

Results obtained for a solar dryer with PCM where compared to open sun drying and there was 60.7 % saving of time. The discharging of paraffin wax maintained the temperature 4-5 ^{0}C higher than the ambient temperature for 6 hours after sunset.

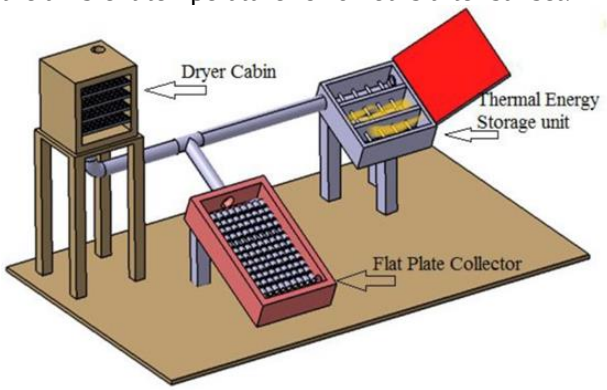

Fig.6. Solar air dryer with a separate TES unit [26]

The performance enhancement of a solar air dryer with a FPC was focused in [26], Fig.6. The FPC provided outlet air temperature up to 100°C at natural convection mode during sunshine hours, when the TES was disconnected from the system. Direct solar radiation was incident on the TES unit during the charging period. At off-sunshine hours the solar TES was connected to the dryer cabin and the FPC was disconnected. A fan was located at the base of the dryer cabin to maintain the air flow at night. The TES unit consisted of an absorber plate, a reflective mirror, and heat pipes with fins as a vapor-liquid phase change device, dipped in paraffin wax as PCM, Fig.6. The efficiency decreased with the increase in air velocity. The increase in temperature gradient led to an increase in the efficiency.

Inbuilt thermal energy accumulator in the SAH and/or the DC

The most common solution for integration of the thermal energy accumulator in the SAH is to place the PCM in the volume under the absorber plate. This construction (Fig.7) was adopted in the study [27]. Part of the heat from the solar radiation heated the air for the drying process and the rest of it charged the PCM. These two processes were separated in two solar air collectors. The solar energy accumulator in [27] comprised a PCM cavity (with dimensions 2.04 m x 1.04 m and total volume of 0.33 m^3,) with insulator and a cover glass. Experiments were conducted in no-load conditions (without material for drying) to evaluate the charging and the discharging characteristics of the latent heat unit. The daily energy efficiency of the solar energy accumulator reached 33.9%, while the daily exergy efficiency reached 8.5%.

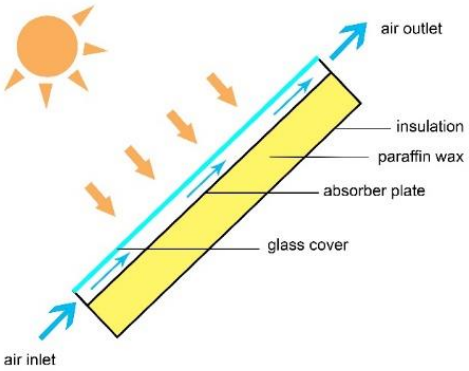

Fig.7. PCM placed below the absorber plate of the SAH [27]

The solar dryer of 0.7 m^3 with 60 kg of paraffin wax kept the relative humidity inside the DC of 0.768 m^3 between 17 and 34.5% lower than the ambient relative humidity and maintained the DC temperature 4-16 °C higher than the ambient temperature all the night.

The absorber plate shape factor (the ratio of the total collector area to the absorber area normal to the solar radiation) is one of the most important parameters in the design of a SAH. The increase in

the total absorber area intensifies the heat transfer to the air flow, but leads to an increase in the pressure drop, therefore increase in the power consumption [28]. There is an optimal range of the shape factor for maximal efficiency.

A widely employed configuration is a double-pass SAH, where the air flows over and under the absorber plate. An experimental investigation [29] was carried out on an asymmetric double-pass air heater containing paraffin macro-encapsulated in rectangular or cylindrical metallic containers (Fig.8).

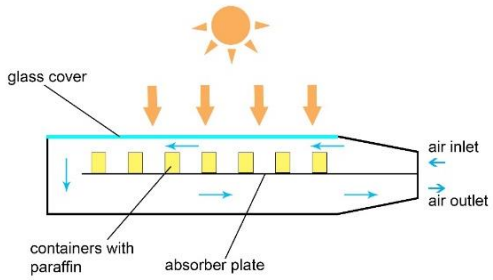

Fig.8. Double-pass SAH with containers with paraffin [29]

It was found [30] that the poor thermal conductivity of PCM had negligible effect on the heat transfer due to high surface convective resistance provided by the air in a packed bed storage unit.

A solar air HE was studied [31] with paraffin wax encapsulated in aluminum cans filled with 5% w/w aluminum wool (Fig.9), which doubled the thermal conductivity of the paraffin wax.

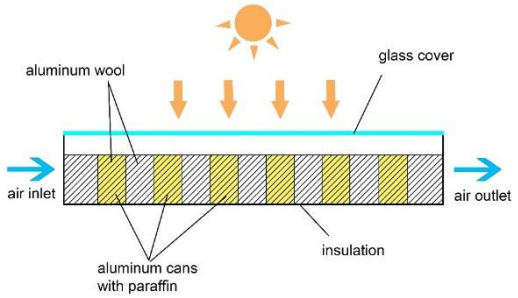

Fig.9. Paraffin wax in aluminum containers inside the SAH with aluminum wool inside and outside the containers [31]

The usage of aluminum wool outside the PCM containers reduced the conductive resistance of air and increased the HE efficiency in charging stage from 46.8% to 48.9% and in discharging stage from 64.4% to 80%.

An example of LHS inbuilt in the DC is shown in [12]. The PCM is placed in boxes inside the DC in a fish dryer (Fig.10). 3 boxes of 3 kg paraffin are placed at the three sides of the DC.

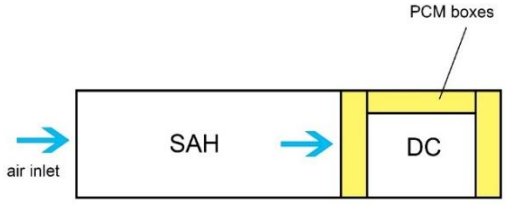

Fig.10. Boxes with PCM in the DC [12] - top view

PREDICTION OF THERMAL BEHAVIOR AND EFFICIENCY ESTIMATION OF A SOLAR DRYER WITH PCM

A variety of mathematical models are employed in order to compare storage systems and to optimize their design. They predict the thermal behavior of the systems and calculate their efficiency. Two types of models are distinguished [32], based on the first law of thermodynamics (FLT) and the second law of thermodynamics (SLT). An overview of the first type models, FLT, in [10] shows different analytical and numerical techniques to solve the energy equation at the moving solid–liquid interface (Stefan problem) of the PCM [33]. The difficulty with the moving interface is avoided by the enthalpy method [10]. It assumes a mushy zone between the two phases and introduces the total volumetric enthalpy as the sum of sensible heat and latent heat of the PCM. The energy conservation for the phase change process is expressed in terms of that enthalpy. This approach is widely exploited in the Computational Fluid Dynamics (CFD) models.

Energy analysis

The energy analysis of a system with a thermal energy accumulator is based on the FLT. It calculates the energy efficiency, denoted also as first-law efficiency.

The energy analysis presumes that energy efficiency η_I is defined as the ratio of the output energy E_{out} to the input energy E_{in}, part of which is lost as energy loss, E_{loss}

$$E_{in} = E_{out} + E_{loss} \quad (1)$$

$$\eta_I = \frac{E_{out}}{E_{in}} = \frac{E_{in} - E_{loss}}{E_{in}} \quad (2)$$

Energy efficiency equations, used by different authors for the constituent units in solar dryer systems with PCM storage are listed below.

1. SAH efficiency

The SAH efficiency is defined as a ratio of the heat flow rate extracted by the SAH to the solar radiation incident on the absorber surface.

$$\eta_{SAH} = \frac{\dot{Q}_{sah}}{A_{abs}\, I_{SAH}}, \quad (3)$$

where, $(\dot{Q}_{SAH})$ [W], is the heat flow rate, extracted by the SAH and can be calculated [27, 34] as:

$$\dot{Q}_{SAH} = \dot{m}_{SAH}\, c_{p,SAH}\, (T_{SAH,o} - T_{SAH,i}) \quad (4)$$

2. Stored/ recovered thermal energy

The amount of energy stored inside the PCM during charging cycle Q_{ch} [J],

$$Q_{ch} = m_{PCM}[c_{PCM,s}\,(T_{PCM,F} - T_{PCM,i\_ch}) + L + + c_{PCM,l}\,(T_{PCM,f\_ch} - T_{PCM,F})]\,. \quad (5)$$

Similarly, the amount of energy recovered from the PCM during discharging cycle Q_{dis} [J]

$$Q_{dis} = m_{PCM}\,[c_{PCM,l}\,(T_{PCM,i\_dis} - T_{PCM,F}) + L + +c_{PCM,s}\,(T_{PCM,F} - T_{PCM,f\_dis})]. \quad (6)$$

3. Efficiency of the PCM modules

The efficiency of the PCM modules is calculated by the ratio of the thermal energy extracted in discharging cycle to the thermal energy stored in charging cycle for a specific period of time [35, 36].

$$\eta_{PCM} = \frac{Q_{dis}}{Q_{ch}} \quad (7)$$

4. Efficiency of the solar drying system at natural convection of air through the SAHs without PCM modules

The system efficiency is the ratio of the thermal energy used to evaporate the moisture from the sample to the global solar radiation incident on the absorber surface of the SAHs [37].

$$\eta_{sys,1} = \frac{\int_0^{t_{end}} m_e\, h_{fg}\, dt}{\int_0^{t_{end}} I_{SAH}\, A_{abs}\, dt} \quad (8)$$

5. Efficiency of the solar drying system at forced convection of air through the SAHs without PCM modules

The system efficiency is the ratio of the thermal energy used to evaporate the moisture from the sample to the sum of the global solar radiation incident on the absorber surface and the energy consumed by the fan [37].

$$\eta_{sys,2} = \frac{\int_0^{t_{end}} m_e\, h_{fg}\, dt}{\int_0^{t_{end}} I_{SAH}\, A_{abs}\, dt + \int_0^{t_{end}} P_{fan}\, dt} \quad (9)$$

6. Efficiency of the solar drying system at forced convection of air through the SAHs with n PCM modules

The system efficiency is the ratio of the thermal energy used to evaporate the moisture from the product plus the thermal energy stored in the modules to the sum of the global solar radiation incident on the absorber surface and the energy consumed by the fan

$$\eta_{sys,3} = \frac{\int_0^{t_{end}} m_e\, h_{fg}\, dt + \sum_o^n \int_0^{t_{end}} Q_{ch}\, dt}{\int_0^{t_{end}} I_{SAH}\, A_{abs}\, dt + \int_0^{t_{end}} P_{fan}\, dt}\,. \quad (10)$$

Exergy analysis

The second-law models are introduced as a more correct approach to find the potential for improvement of the thermodynamic behavior of the TES [32]. According to them, not energy is important, but the thermodynamic availability of this energy. Unlike first-law energy analysis, they take into account the loss of energy because of irreversibility of the process. They formulate second-law efficiency based on entropy number [38] or exergy analysis.

Exergy is the maximum amount of work which can be produced by a system or a flow of matter till the system or the flow comes to equilibrium with a reference environment [39].

Second-law efficiency η_{II} [40] can be expressed as the ratio of the exergy output Ex_{out} to the exergy input Ex_{in}.

$$\eta_{II} = \frac{Ex_{out}}{Ex_{in}} = \frac{Ex_{in} - Ex_{loss} - Ex_{des}}{Ex_{in}} \quad (11)$$

Ex_{des} is the exergy destruction due to the irreversibility of the process, Ex_{loss} is the exergy lost to the environment.

The exergy analysis in [37] of the units of a solar dryer with PCM uses the following equations taken from literature:

1. Exergy analysis of the SAH

The exergy analysis employs the steady flow exergy equation expressed as follows [41]:

$$\dot{E}x = \dot{m}_a \left\{c_{pa}(T - T_r) - T_r \left[c_{pa} ln\left(\frac{T}{T_r}\right) - -R\, ln\left(\frac{P}{P_r}\right)\right]\right\} \quad (12)$$

The exergy efficiency of the SAH $\eta_{Ex,SAH}$ is expressed as the ratio between the exergy received by the working fluid (air) $\dot{E}x_{re,air}$ to the exergy inflow $\dot{E}x_{in,SAH}$

$$\eta_{Ex,SAH} = \frac{\dot{E}x_{re,air}}{\dot{E}x_{in,SAH}}, \quad (13)$$

where the exergy inflow into the air heater is expressed as

$$\dot{E}x_{in,SAH} = \left[1 - \frac{T_r}{T_{sun}}\right]\dot{Q}_{in}, \quad (14)$$

T_{sun} denotes the apparent sun temperature and it is assumed to be 4500 K, T_r - reference temperature of the ambient, $\dot{Q}_{in} = \alpha\tau' I A_{SAH}$ is the energy input to the solar heater. $\dot{E}x_{re,air}$ is expressed using the steady flow exergy equation (Eq.12):

$$\dot{E}x_{re,air} = \dot{m}_a c_{pa}\left[\left(T_{o,SAH} - T_{i,SAH}\right) - T_r \ln\left(\frac{T_{o,SAH}}{T_{i,SAH}}\right)\right] \quad (15)$$

2. Exergy analysis of energy storage

The exergy efficiency of energy storage is the ratio of the net exergy recovered from the energy storage during the discharging period Ex_{dis} to the net exergy input to the storage during the charging period Ex_{ch}

$$\eta_{Ex,es} = \frac{Ex_{dis}}{Ex_{ch}} \quad (16)$$

$$Ex_{ch} = \int_0^t \dot{m}_a c_{pa}\left[\left(T_{i,es} - T_{o,es}\right) - -T_r \ln\left(\frac{T_{i,es}}{T_{o,es}}\right)\right] dt \quad (17)$$

$$Ex_{dis} = \int_0^t \dot{m}_a c_{pa}\left[\left(T_{o,es} - T_{i,es}\right) - -T_r \ln\left(\frac{T_{o,es}}{T_{i,es}}\right)\right] dt. \quad (18)$$

3. Exergy analysis of the DC

The exergy efficiency of the DC, $\eta_{Ex,d}$, is defined as the ratio of the exergy outflow $\dot{E}x_{od}$ to the exergy inflow $\dot{E}x_{id}$ of the DC

$$\eta_{Ex,d} = \frac{\dot{E}x_{od}}{\dot{E}x_{id}} \quad (19)$$

$$\dot{E}x_{id} = \dot{m}_{da} c_{pa}\left[\left(T_{id} - T_r\right) - T_r \ln\left(\frac{T_{id}}{T_r}\right)\right] \quad (20)$$

$$\dot{E}x_{od} = \dot{m}_{da} c_{pa}\left[\left(T_{od} - T_r\right) - T_r \ln\left(\frac{T_{od}}{T_r}\right)\right]. \quad (21)$$

Examples of efficiency evaluation of solar dryers with PCM

The article [37] presents performance studies of a forced convection solar dryer of chili, integrated with a shell-and-tube TES unit, based on paraffin wax. The performance of each component of the drying system was evaluated in terms of energy and exergy efficiency. The average instantaneous heat input and heat recovered during the charging and discharging processes of the energy storage were in the range of 105–130 W and 89–116 W, respectively. The net heat input and heat recovered varied from 2.5 MJ to 3.2 MJ and from 1.2 MJ to 1.5 MJ, respectively. The average energy efficiency or the percentage of the energy recovered (Eq.7) was in the range of 43.6–49.8%. No heat energy was retrieved from the storage after 18:00 h as the air coming out of the storage at the temperature below 36 ºC was not much effective for drying the chili. The drying time was reduced by 55% of the drying time in open sun drying. The TES provided an extended drying time of 2 h after sunset and the overall efficiency of the drying system was 10.8%. The net exergy input and recovered were in the range of 0.2–0.3 MJ, and 0.04–0.05 MJ, respectively. The overall exergy efficiency ranged from 18.3% to 20.5%.

Pebble stones and paraffin wax (as TES) were used in drying of lemon slices [3] Considering that the drying time increased with increasing the product amount, it was concluded that maximum 11.3 kg of lemon slices could be dried with each of the energy storage systems. As a result of the experimental studies, the average energy efficiencies were obtained as 68.2% and 68.55% for pebble stones and paraffin, respectively. When the systems were evaluated economically, it was observed that the TES based on pebble stones had a 10.47% lower initial investment cost compared to the TES based on paraffin. Pebble stone unit price used in the system was $ 0.0725/kg. The unit price of paraffin wax used in the PCM system was $ 2.483/kg. Moreover, paraffin wax loses its ability to store energy since its properties deteriorate after a certain period of time (approximately 4 years) and should be replaced.

CFD predictions of thermal behavior of solar dryers with PCM

CFD is a useful tool in designing drying systems. The commercial numerical packages for CFD most often used to improve the performance of a solar dryer with TES are COMSOL Multiphysics, ANSYS CFX, Fluent, FORTRAN and OpenFOAM [42]. CFD reveals a detailed picture of flow velocity

and temperature and humidity distribution pattern inside the units of the solar dryer.

A low-temperature latent heat TES device was studied [43] for drying of agricultural products in an indirect-type solar dryer. A 2D geometry was created. It had an inner copper tube and outer plastic tube assembly. The air flowed into the copper tube and the PCM was in the outer plastic tube. Transient simulations were conducted by ANSYS Fluent 2015 to capture the velocity, temperature, melting and solidification fractions.

The enthalpy-porosity model of phase change is employed in ANSYS Fluent. It adopts the following equations for describing the processes in charging/discharging of the PCM:

Continuity equation:

$$\frac{\partial \rho}{\partial t} + \nabla(\rho \boldsymbol{v}) = 0. \quad (22)$$

Momentum equation:

$$\frac{\partial}{\partial t}(\rho \boldsymbol{v}) + \nabla(\rho \boldsymbol{v}\boldsymbol{v}) = -\nabla p + \nabla \boldsymbol{\tau} + \rho \boldsymbol{g} + \boldsymbol{S}, \quad (23)$$

where $\boldsymbol{v}$ is the velocity vector, p is the static pressure, $\boldsymbol{\tau}$ is the stress tensor and $\rho\boldsymbol{g}$ and $\boldsymbol{S}$ are the vectors of gravitational and external body forces.

The momentum sink due to the reduced porosity in the mushy zone takes the following form:

$$\boldsymbol{S} = \frac{(1-\beta)^2}{(\beta^3+\varepsilon)} A_{mush} \boldsymbol{v}, \quad (24)$$

where β is the liquid volume fraction, ε is a small number (0.0001) to prevent division by zero, A_{mush} $=10^5$ is the mushy zone constant.

Energy equation:

$$\frac{\partial}{\partial t}(\rho H) + \nabla(\rho \boldsymbol{v} H) = \nabla(k \nabla T). \quad (25)$$

The enthalpy H consists of sensible enthalpy h and latent heat ΔH

$$H = h + \Delta H, \quad (26)$$

where $h = h_r + \int_{T_r}^{T} c_p dT$, $\Delta H = \beta L$.

The latent heat content can vary between 0 for solid and L for liquid. The liquid volume fraction can be defined as:

$$\beta = 0 \text{ if } T < T_s$$
$$\beta = 1 \text{ if } T > T_l$$
$$\beta = \frac{T - T_s}{T_l - T_s} \text{ if } T_s < T < T_l,$$

where T_s and T_l are solidus and liquidus temperatures respectively.

The CFD simulations of the TES in [43] were run from 8.00 am to 10.00 pm. The inlet air temperature was gradually increased and reached a maximum value of 349 K at 2.00 pm. The model helped to analyze the potential of PCM to store excess solar energy and to estimate the temperature distribution in radial direction of the TES device.

Different configurations of a solar dryer integrated with thermal storage medium were analyzed in [44] by means of a CFD software to study temperature and humidity distributions in the system. Paraffin wax was used as PCM. It was assumed that at the inlet the temperature was 303.00 K, the pressure was 101325.00 Pa and the air velocity was 1.2 m/s. Maximum fluid temperature of 346.56 K was obtained at the chimney of the solar dryer. The results of the study showed that maximum temperature loss occurred due to the metallic components of the solar air dryer, where suitable insulation material should be used.

A 2D numerical study was conducted in [45] (by ANSYS Fluent) for a TES device of an indirect type solar dryer. Two cases were considered: Case-I without fins and Case-II with fins. The TES dimensions of both cases were the same. Fin dimensions were 0.5 mm tip diameter, 5 mm length 14.86 mm fin spacing. Paraffin wax was used as a PCM material for both cases. CFD simulations were carried out for four air velocity conditions (1m/s, 2m/s, 3m/s, 4m/s). It was found that both cases worked best with an air velocity of 1 m/s compared to higher air flow velocities. Higher air flow velocity did not exercise much impact on the DC temperature compared to lower velocity. Also, lower air flow velocity maintained the uniformity of drying over a longer period of time. At the same time, higher air flow velocity carried more moisture from the food product, so the drying time could be reduced. Melting fraction was higher in Case-II compared to Case-I as the fins transferred more heat to the PCM. For all the velocities considered in this work, the heat gained by the air was higher for Case-II compared to Case-I. The maximum heat gained by the air for Case–II was 55.2% more in comparison to Case–I at an air velocity of 1 m/s.

CONCLUSIONS

The rate of drying depends on various parameters such as solar radiation, ambient temperature, air flow velocity, relative humidity, initial moisture content, wind speed, type of goods, absorptivity and mass of product per unit exposed area. The conditions for heat transfer in the units of the solar dryer with paraffin (containers' materials and surface area, insulation, desiccants, air flow rate and velocity, arrangement of the grids for the drying material, etc.) which lead to good results of the drying process are considered in order to determine the important performance characteristics of a successful simplified small-size solar dryer with paraffin.

The main requirements in the design of a thermal energy accumulator are:

- Continuously stable temperature of the drying air at least 10-25°C above the ambient temperature. This is necessary to avoid the dried object to re-absorb the moisture during night, when the air temperature drops and its humidity increases.

- Choice of proper PCM according to the drying regime; the minimum melting temperature of the PCM should be of 5–10 ºC higher than the desired temperature of the HTF.

- Minimal heat loss by effective thermal insulation.

- Intensive heat transfer (measures for reduction of air convective resistance and enhancement of thermal conductivity of PCM.)

- Metal lamellae structures are a good solution for increasing paraffin thermal conductivity more than 2 times.

- Macro-encapsulation is recommended for providing large heat transfer area, reduction of the paraffin reactivity towards environment and controlling the changes as phase change occurs. Increasing the height/width ratio of the container for the same volume decreases the time for the melting process due to the stronger buoyancy effect. Usually the material of the shell is plastic or metal (copper, aluminum and steel) when higher heat transfer rates are desirable.

- Metal fins enhance significantly the heat transfer rate in and out of the element containing the PCM.

- The thermal storage should not create additional pressure drop, especially in natural convection units. It can also serve as an obstacle to the air flow that increases the heat transfer area and enhances the air flow conditions, by creating turbulence and eliminating stagnant zones.

- The second-law models are a more informative approach to find the potential for improvement of the thermodynamic behavior of the thermal energy accumulator, since they evaluate the thermodynamic availability of energy.

- CFD simulation of the TES is useful for analyzing the potential of PCM to store excess solar energy during sunshine hours and to release the same at night. It enables to compare different device configurations by revealing the picture of temperature, humidity and velocity distribution.

ACKNOWLEDGMENTS

This work is supported by the National Science Fund, Bulgaria, Contract No KP-06-INDIA/11/02.09.2019 and the Department of Science and Technology, India (DST/INT/P-04/2019).

NOMENCLATURE

A - area, m^2;
c_p - specific heat, J/(kg K);
$c_{p,SAH}$ - average specific heat of air between $T_{SAH,i}$ and $T_{SAH,o}$, J/(kg K);
$c_{PCM,s}$- average specific heat of solid PCM, J/(kgK);
$c_{PCM,l}$ - average specific heat of liquid PCM, J/(kg K);
Ex - exergy, J;
$\dot{E}x$ - exergy flow rate, W;
$\boldsymbol{g}$ - gravitational acceleration vector, m/s^2;
h - sensible enthalpy, J/kg;
H_{FG} - latent heat of vaporization, J/kg;
H - enthalpy, J/kg;
ΔH - latent heat, J/kg;
I - solar intensity, W/m^2;
k - thermal conductivity, W/(mK);
L - heat of fusion per unit mass, J/kg;
m - mass, kg;
$\dot{m}$ - mass flow rate, kg/s;
p - static pressure, Pa;
P_{fan} - power consumption of fan, W;
Q - thermal energy, J;
$\dot{Q}$ - heat flow rate, W;
R - gas constant, J/(kgK);
t - time, s;
T - temperature, K;
$\boldsymbol{v}$ - velocity vector, m/s;

Greek letters

α - absorptivity;
η - thermal efficiency;
β - liquid volume fraction;
Δ- difference;
μ - dynamic viscosity, Pa.s;
ρ - density, kg/m^3;
$\boldsymbol{\tau}$ - stress tensor, Pa;
τ' – transmissivity.

Subscripts

a - air;
abs - absorber;
ch - charging;
d – dryer;
dis - discharging;
des - destruction;
e - evaporated moisture;
es - energy storage;
f - fluid;
f_ch - final in charging;
f_dis - final in discharging;

F - fusion;
i - inlet;
i_ch - initial in charging;
i_dis - initial in discharging;
in - input;
l - liquid;
o - outlet;
out - output;
PCM - phase change material;
r- reference;
re - received;
s - solid;
SA - solar accumulator;
sys - drying system;
SAH - solar air heater.

Abbreviations

CFD - computational fluid dynamics;
DC - drying chamber;
FLT - first law of thermodynamics;
FPC - flat plate collector;
HE - heat exchanger;
HTF - heat transfer fluid;
LHS - latent heat storage
PCM - phase change material;
SAH - solar air heater;
SLT - second law of thermodynamics;
TES - thermal energy storage.

REFERENCES

[1] L. M. Bal, S. Satya, S. N. Naik. Solar dryer with thermal energy storage systems for drying agricultural food products: A review. *Renewable and Sustainable Energy Reviews*, **14**(8), 2298-2314 (2010).

[2] J. L. Butler, J. M. Troeger. Drying peanuts using solar energy stored in a rockbed. Agricultural energy vol. I, solar energy, selected papers and abstracts. ASAE Publication, St Joseph, Michigan; 1980.

[3] H. Atalay. Assessment of energy and cost analysis of packed bed and phase change material thermal energy storage system for the solar assisted drying process. *Solar Energy*, 198, 124-138 (2020).

[4] S. M. Shalaby, M. A. Bek, A. A. El-Sebaii. Solar dryers with PCM as energy storage medium: A review. *Renewable and Sustainable Energy Reviews*, 33, 110-116 (2014).

[5] M. Mofijur, T. M. I. Mahlia, A. S. Silitonga, H. C. Ong, M. Silakhori, M. H. Hasan, S. M. Rahman. Phase change materials (PCM) for solar energy usages and storage: an overview. *Energies*, **12**(16), 3167 (2019).

[6] G. A. Lane. Solar Heat Storage: Latent Heat Materials, - Vol. I: Background and scientific principles, USA, Boca Raton, Florida: CRC Press, 1983.

[7] S. Aboul-Enein, A.A. El-Sebaii, M.R.I. Ramadan, H. G. El-Gohary. Parametric study of a solar air heater with and without thermal storage for solar drying applications, Renewable Energy, **21** (3–4), 505-522 (2000).

[8] A. Sharma, C. R. Chen, N. V. Lan. Solar-energy drying systems: A review. *Renewable and sustainable energy reviews*, **13**(6-7), 1185-1210 (2009).

[9] A. K. Bhardwaj, R. Chauhan, R. Kumar, M. Sethi, A. Rana. Experimental investigation of an indirect solar dryer integrated with phase change material for drying valeriana jatamansi (medicinal herb). *Case studies in thermal engineering*, 10, 302-314 (2017).

[10] A. Sharma, V. V. Tyagi, C. R. Chen, D. Buddhi. Review on thermal energy storage with phase change materials and applications. Renewable and Sustainable energy reviews, **13**(2), 318-345 (2009).

[11] O. A. Babar, V. K. Arora, P. K. Nema. Selection of phase change material for solar thermal storage application: a comparative study. *Journal of the Brazilian Society of Mechanical Sciences and Engineering*, **41**(9), 355 (2019).

[12] V. M. Swami, A. T. Autee, T. R. Anil. Experimental analysis of solar fish dryer using phase change material. *Journal of Energy Storage*, 20, 310-315 (2018).

[13] R. Singh, S. Sadeghi, B. Shabani. Thermal conductivity enhancement of phase change materials for low-temperature thermal energy storage applications. *Energies*, **12**(1), 75 (2019).

[14] H. Ettouney, H. El-Dessouky, E. Al-Kandari. Heat transfer characteristics during melting and solidification of phase change energy storage process. *Industrial & engineering chemistry research*, **43**(17), 5350-5357 (2004).

[15] S. Wu, Ting Yan, Zihan Kuai, Weiguo Pan. Thermal conductivity enhancement on phase change materials for thermal energy storage: A review *Energy Storage Materials* 25, 251–295 (2020)

[16] M. M. Farid, A. M. Khudhair, S. A. K. Razack, S. Al-Hallaj. A review on phase change energy storage: materials and applications. *Energy conversion and management*, **45**(9-10), 1597-1615 (2004).

[17] N. S.Dhaidan, J. M. Khodadadi. Melting and convection of phase change materials in different shape containers: A review. *Renewable and Sustainable Energy Reviews*, 43, 449-477 (2015).

[18] B. Zivkovic, I. Fujii. An analysis of isothermal phase change of phase change material within rectangular and cylindrical containers. *Solar energy*, 70(1), 51-61 (2001).

[19] J. Wei , Y. Kawaguchi, S. Hirano, H. Takeuchi,. Study on a PCM heat storage system for rapid heat

supply. *Applied thermal engineering*, **25**(17-18), 2903-2920 (2005).

[20] K. A. R. Ismail, C. L. F. Alves, M. S. Modesto,. Numerical and experimental study on the solidification of PCM around a vertical axially finned isothermal cylinder. *Applied Thermal Engineering*, 21(1), 53-77 (2001).

[21] K. A. R. Ismail, F. A. M. Lino. Fins and turbulence promoters for heat transfer enhancement in latent heat storage systems. *Experimental thermal and fluid science*, **35**(6), 1010-1018 (2011).

[22] S. Devahastin, S. Pitaksuriyarat. Use of latent heat storage to conserve energy during drying and its effect on drying kinetics of a food product. *Appl. Therm. Eng.*, 26, 1705–1713 (2006).

[23] T. Pirasaci, D.Y. Goswami. Influence of design on performance of a latent heat storage system for a direct steam generation power plant. *Appl. Energy*, 162, 644–652 (2016).

[24] A. Tiwari. A review on solar drying of agricultural produce. *J Food Process Technol.*, **7**(9) 1-12 (2016).

[25] D. V. N. Lakshmi, P. Muthukumar, A. Layek, P. K. Nayak. Drying kinetics and quality analysis of black turmeric (*Curcuma caesia*) drying in a mixed mode forced convection solar dryer integrated with thermal energy storage. *Renewable Energy*, 120, 23-34 (2018).

[26] V. V. Bhagwat, , S. P. Salve, S. Debnath,. Experimental analysis of a solar dehydration with phase changing material. *AIP Conference Proceedings*, vol. 1998, No. 1, p. 020003 (2018).

[27] A. El Khadraoui, S. Bouadila, S. Kooli, A. Farhat, A. Guizani. Thermal behavior of indirect solar dryer: Nocturnal usage of solar air collector with PCM. *Journal of Cleaner Production*, 148, 37-48 (2017).

[28] H. Benli. Experimentally derived efficiency and exergy analysis of a new solar air heater having different surface shapes. *Renewable Energy*, 50, 58-67 (2013) .

[29] A. K. Raj, M. Srinivas, S. Jayaraj. A cost-effective method to improve the performance of solar air heaters using discrete macro-encapsulated PCM capsules for drying applications. *Applied Thermal Engineering*, 146, 910-920 (2019).

[30] S. Karthikeyan, G. Ravikumar Solomon, V. Kumaresan, R. Velraj, Parametric studies on packed bed storage unit filled with PCM encapsulated spherical containers for low temperature solar air heating application, Energy Conversion and Management 78, 74-80 (2014).

[31] A. Reyes, A. Mahn, F. Vásquez. Mushrooms dehydration in a hybrid-solar dryer, using a phase change material. *Energy Conversion and Management*, 83, 241-248 (2014).

[32] P. Verma, Varun, S.K. Singal. Review of mathematical modeling on latent heat thermal energy storage systems using phase-change material, *Renewable and Sustainable Energy Reviews*, 12 (2008) 999–1031 (2008)

[33] M. Turkyilmazoglu. Stefan problems for moving phase change materials and multiple solutions, *International Journal of Thermal Scienc*es 126 67–73 (2018)

[34] S.M. Shalaby, M.A.Bek, Experiment investigation of a novel indirect solar dryer implementing PCM as energy storage medium, *Energy Conversion and Management* 83 1-8 (2014).

[35] E. T. Toshkov Investigation of a Hybrid System with Ground Source Heat Pump and Solar Collectors, PhD Thesis, Technical University of Sofia, Plovdiv Branch, 2015 (in Bulgarian).

[36] A.G. Georgiev, R. Popov, E.T Toshkov. Investigation of a hybrid system with ground source heat pump and solar collectors: Charging of thermal storages and space heating, *Renewable Energy*, **147**, 2, 2774-2790 (2020)

[37] D. K Rabha, P.Muthukumar, Performance studies on a forced convection solar dryer integrated with a paraffin wax-based latent heat storage system, *Solar energy*, 149, 214-226 (2017).

[38] A. Bejan. Two thermodynamic optima in the design of sensible heat units for energy storage. *J Heat Transfer* 100(4) 708-712 (1978).

[39] K. Taheri, Rainer Gadowa, Andreas Killinger. Exergy analysis as a developed concept of energy efficiency optimized processes: The case of thermal spray processes, *Procedia CIRP* 17 511 – 516 (2014).

[40] D. Kumar, Pinakeswar Mahantaa, Pankaj Kalita, Energy and exergy analysis of a natural convection dryer with and without sensible heat storage medium, *Journal of Energy Storage* 29 101481 (2020).

[41] P. K. Nag. Basic and applied thermodynamics, Tata McGraw-Hill, 2006.

[42] K. Kant, A. Shukla, A. Sharma, A. Kumar, A. Jain. Thermal energy storage based solar drying systems: A review. *Innovative food science & emerging technologies*, 34, 86-99 (2016).

[43] S. Yadav, A. Bhanudas Lingayat, V.P. Chandramohan, V.R.K. Raju. Numerical analysis on thermal energy storage device to improve the drying time of indirect type solar dryer, *Heat and Mass Transfer*, part of Springer Nature 2018, https://doi.org/10.1007/s00231-018-2390-7.

[44] R. T. Ramteke, S. N. Solanki, B. S. Bhosale CFD (Computational fluid dynamics) Analysis of the Solar Dryer Integrated with Thermal Storage Media, J. Agric. Res. Technol., 43 (2) : 401-404 (2018).

[45] S. Yadav, V. P. Chandramohan. Performance comparison of thermal energy storage system for indirect solar dryer with and without finned copper tube, *Sustainable Energy Technologies and Assessments* 37 100609 (2020).

Bulgarian Chemical Communications, Volume 52, Special Issue C (pp.65-71) 2020 DOI: 10.34049/bcc.52.C.0030

Role of the CdS/ZnS core/shell quantum dots in the thin film lead-free perovskite solar cells

M. P. Aleksandrova[1*], G. D. Kolev[1], R.Tomov[1], A. K. Singh[2], K. C. Mohite[3], G.H.Dobrikov[1]

[1]*Technical University of Sofia, Dept. of Microelectronics, 8 Kliment Ohridski Blvd, 1000 Sofia, Bulgaria*
[2]*Govt.V.Y.T.PG. Autonomous College, Dept. of Chemistry, Near Raipur Naka, G.E. Road, Durg, India.*
[3]*University of Pune, Ganeshkhind Rd, Ganeshkhind, Pune, Maharashtra 411007, India*

The performance of the thin film solar cells has been enhanced in recent years by development of new materials broadening the spectral response of the cell and supressing the long wavelength absorption close to the near infrared range. Absorber layers are developed to improve the collection of photo-carriers when perovskites are used as photoelectric converting films. This is due to the easy tuning of the energy levels alignment at the films interface. For the new types of lead-free perovskites, the interaction between sulphide based absorber and the perovskite is not yet investigated. First, the deposition and processing conditions for the perovskite coatings were optimized in terms of crystallization degree and uniform surface. The perovskite films crystal morphology and the crystal growth kinetics were found to be similar like the films' morphology consisting of organic molecules having non-perovskite structure. Optimized perovskite films, containing this absorber with different thickness were applied in combination with lead-free perovskite films. Homogeneous core/shell type CdS/ZnS films with high density were produced. Simple cell construction is proposed, containing ITO/ZnO:Ga_2O_3 front panel electrode, lead-free $CH_3NH_3I_{3-x}Cl_x$ based perovskite and gold back contact. The cells were tested at open circuit conditions at different illumination intensity and different wavelength of the illuminating source. At optimal conditions the fabricated solar cells showed which 1.9% higher conversion efficiency, to the reference cell without absorber. The results demonstrated the applicability of the lead-free perovskite material and the effect of sulphide layers on the solar cell electrical parameters improvement. This is a basic step to further optimization of this technology.

Keywords: sulphide absorber layer, quantum dots, core/shell technology, perovskite photoconductor, lead-free solar cell

INTRODUCTION

In recent years, the Perovskite solar cells have been developed dramatically, due to their low-cost and simple fabrication, especially the hybrid ones, containing organic and inorganic constituents, such as $CH_3NH_3PbI_3$ for example [1]. For ten years the materials science technology has allowed 6 times increase in the power conversion efficiency. In 2018 has been reported about 23.3% produced from devices with size of 1 cm^2 [2].

General formula for perovskite is ABX_3, in which A is monovalent cation, B is divalent cation (i.e., Pb^{2+}/Sn^{2+}/Pd^{2+} etc.) and X is halide ion, it is the base of solar cell. ABX_3 halide perovskite is a photovoltaic material and has shown higher efficiency in solar cell technology compared to cadmium-tellurium material. By deep literature study we observed that electronic configuration of lead (Pb^{2+}) is mainly responsible for photovoltaic behavior of solar cell. Lead based perovskite solar cell still has limited use because many countries have strict regulation for use of heavy metal ions, so research now focused on making lead free perovskite solar cells [3-5].

* To whom all correspondence should be sent:
m_aleksandrova@tu-sofia.bg

Nowadays, the hybrid perovskite solar cells with their electrical and optical parameters are competitive to the well-established thin film technology for photoelectric convertors based on cadmium telluride CdTe and copper indium gallium selenide (CIGS). A lot of researches have been conducted to achieve this goal, related to thin film quality. It seems that the favourable behaviour of these modules is due to the broad absorption of the solar spectrum, because of the presence of lead as a core chemical element in the perovskite material. The new trends worldwide for implementation of environmental friendly materials and technologies, excluding the lead-containing substances have made further development of these solar cells senseless. The focus has been shifted on the synthesis of new, eco-friendly perovskites, in which the lead is replaced by Br, Sb, or I [6].

There are various methods were reported for synthesis of thin film of perovskite solar cell, e.g., sequential deposition, one step, vapour assisted solution process and vapour deposition method [7]. However, spin coating method is one of the best, cost effective and efficient methods [8]. An alternative approach for producing planar perovskite thin films based on combination of RF-sputtering with the solution process route.

Rahul et al., have fabricated a new class of

material ($CH_3NH_3SnCl_3$) to prepare lead free perovskite solar cell by direct deposition method. It is environment friendly and cost effective too [9]. Balakrishna et al. have reported effect of iodide treatment on stability of perovskite solar cell [10]. Li et al. have reported a mini review on lead free and less lead containing perovskite solar cell and possible solution for its stability and photoelectric performance [11]. Nakajima et al. have used computation software using Density functional theory, to study various organic-inorganic materials to find out perfect combination of environment friendly perovskite solar cell and they proposed 51 low toxic double and single halide combinations [12]. Baenstein et al. have replaced lead in halide perovskite and replace it by combination of mono and trivalent cation as a bulk single crystal and a thin layer [13].

Because their natural bandgap is narrower in comparison with those of the hybrid solar cells (mostly in the range 450-550 nm), the conversion efficiency has dropped to 2 %. Some of the important results in the field have been published by Jiang et al. in 2018, who has reported greater efficiency when Cl is incorporated as a light absorber in a complex perovskite $(CH_3NH_3)3Sb_2Cl_xI_{9-x}$ [14]. At present, still many challenges must be overcome before the commercialization of the perovskite solar cells, which hinder their broad application. Appropriate materials and designs still have to be proposed to solve the problem with the low power conversion efficiency, toxicity of some solvents and great sensitivity to radiation out of the visible range make their long-term stability under question.

Adding multilayer absorber film stack into the structure, like CdSe/ZnS, for example, is one of the current approaches of interest to improve the performance of cells due to extension of the absorption ability in a broader wavelength range. Some authors report for insertion of similar films with this function, subjected to annealing for interdiffusion and complex compound achieving such as $CdSe_xTe_{1-x}$, with only partial control over the exact composition [15]. Recently, the core/shell technology has offered a great advantage of no leakage of excited electrons, better energy level alignment with the surrounding coatings, and higher quantum yield [16]. These materials have higher efficiency to absorb solar energy and to convert it into electrical energy.

In this study, we propose to enhance the light conversion ability of a solar cell containing lead-free perovskite material by inserting sulphide based absorbing films of core-shell type. To the best of our knowledge such study has not been conducted and reported in the literature so far. For this purpose, absorber layers with different thicknesses were introduced and the basic characteristics of the cell were measured. The results show that using additional absorption layers can gain the long wavelength absorption, thus increasing the cell performance, while the short wavelength response is not changed. The effect of the ambient environment on the perovskite films was also studied and suitable pre- and post-deposition processing was proposed in order to reduce the degree of random crystallization effect. Secondary benefits from the study are the conclusions that can be made for the wetting ability of the $ZnO:Ga_2O_3$ (GZO) transporting layer from the perovskite ink as a novel concept for front panel filter of the sun heating component decreasing the solar cells' efficiency.

EXPERIMETNAL SECTION

Perovskite photoconductive film was spin coated on glass/ITO (180 nm)/$ZnO:Ga_2O_3$ (GZO, 100 nm) substrates. The glass substrate was cleaned in standard detergent solution incuding ammonia, hydrogen peroxide and distilled water. Indium tin oxide was RF sputtered at sputtering pressure of 10^{-3} Torr and sputtering voltage of 700 V, followed by RF sputtering of $ZnO:Ga_2O_3$ at the same sputtering pressure and sputtering voltage of 850 V. Recently, we found that GZO can serves as efficient front panel transporting layer, supporting the function of the transparent ITO conductor, but at the same time exhibiting optical rejection ability in the near infrared spectrum. It could successfully replace the conventionally used in the perovskites solar cells TiO_2 film, serving only as a transporting layer [17]. Methyl ammonium iodide chloride based perovskite ink was spin coated at 1000 rpm per 30 sec and consequently dried for 10 min at 130 ^oC. Preliminary simulation showed that the optimum layer in terms of suppressing parasitic electrical losses in the cell is 300 nm [18]. Open-source software combining the features of Silvaco and PC1Dmod was used. The basic equations rely on the Boltzmann equations with the assumptions that the two carriers flow independently without scattering, both types charge carriers (positive and negative charges) remain in thermal equilibrium with the surrounding matter (no matter crystalline or non-crystalline), and the energy levels form rigid bands, i.e. not affected by the excitation. The software considers direct-gap and indirect-gap

transitions. The front and rear surface reflections are calculated based on the refractive indices and thicknesses of thin films and the substrate following the Fresnel's equations. The absorption from the substrate obeys the Lamber-Beer law. Considering the hybrid nature of the cell (organic-inorganic) for this case the description of charge transport at hetero-interfaces follows the model of Miller-Abrahams and the recombination processes – the model of Kerr and Cuevas. Top gold electrode with thickness of 120 nm was deposited by DC sputtering. Core/shell CdS/ZnS quantum dots (QDs) were spin-coated from carboxylic acid dispersion at 500 rpm with additional drying at 70^{o}C for 10 min. These films were used as absorbers in the cell structure and they were placed in front of the perovskite films. Variety of CdS/ZnS QDs monolayers were produced by different number of consequent dispersion casting to study the effect of the absorbing layer thickness on the solar cell characteristics. One casting provides ~60 nm thickness of the coating (1 layer = ~ 60 nm; 2 layers = ~120 nm). Schematic drawing of the device structure is shown in Fig.1.

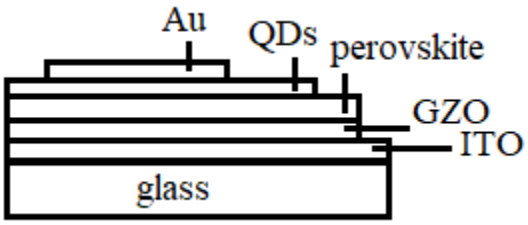

Fig.1. The structure of the proposed lead-free perovskite solar cell

The area of the fabricated samples was 3 cm^2. For the open circuit mode a light source with white spectrum and maximum power of 100 μW/cm^2 was set to avoid a crowd effect in the films, serving as shallow reservoirs for the excited charge carriers. For the closed circuit mode (with load) colour filters were used to pass selectively one of the three basic wavelengths – red, green and blue – for spectral sensitivity study. The thickness of the films was measured by surface profilometer Alpha-step Tencor 100 VEECO. The roughness of the thin film surface is observed by atomic force microscope (AFM) Oxford Instruments MFP-3D. The optical absorption and transmission of the films was measured by using spectrophotometer UV VIS NU-T6PC Zhengzhou Nanbei Instrument. Current-voltage (IV) characteristics of the perovskite thin film solar cells were measured by Agilent 34410A voltmeter and picoamperemeter Keithley 6482 after calibration with a GaAs reference cell. The efficiency of the solar cells was measured by the Thorlabs PDA200C Benchtop Photodiode Amplifier.

RESULTS AND DISCUSSION

The initial experiments related to the spin-coating of the perovskite ink on the transparent electrode showed that the ink distribution is not uniform due to the poor wetting ability of the substrate (Fig.2). Additionally, random crystallization centres were revealed with diameter almost 156 μm worsening further the quality of the coating after exposure the samples to direct contact with the ambient and hard baked at 130 ^{o}C.

Fig.2. Microscopic image of the perovskite coating at the initial deposition of perovskite ink on the glass/ITO/ $ZnO:Ga_2O_3$ substrates

Interesting effect that needs further investigation of its formation mechanism is the crystallization degree dependence on the perovskite coating thickness. It was observed that the films with a thickness in the range 200-250 nm exhibited stronger tendency to form network of local crystalizing centres as compared to the thicker films in the range 500-550 nm (Fig.3) at one and the same ambient conditions. Study of such dependence was recently reported about ultrathin organic molecules containing films with varying thickness in the range of 34-220 nm [19]. The kinetics of the crystallization process showed similar trends, which was ascribed to the non-linear dependence of the crystallization rate with the film thickness, according to the Lauritzen-Hofman growth. It could be assumed that the same model could be fitted in the case of perovskite films.

It was applied pre-deposition treatment with UV light (365 nm), so that the ultraviolet exposure can break the bonds from the surface states of the coating making them dangling. It was previously demonstrated that the approach increased the free energy on the surface and the wetting susceptibility from inks [20]. Additionally, the film growth was conducted in ambient air-free environment and

baked at lower temperature of 100 °C to avoid fast solvent evaporation (Fig.4). Notable improvement of the surface morphology was observed with very few crystallization centres formed.

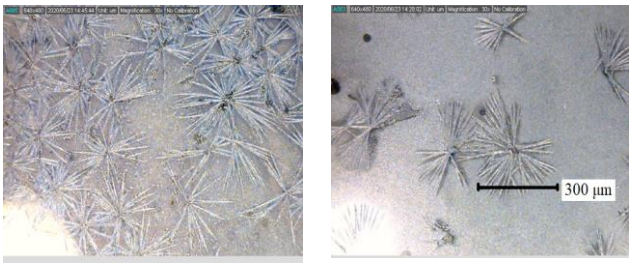

Fig.3. Microscopic image of the perovskite coatings with different thicknesses - 230 nm (left) and 540 nm (right)

Fig.4. Microscopic image of the perovskite coating at the optimized deposition of perovskite ink on the glass/ ITO/ZnO:Ga_2O_3 substrate

The conditions for substrate pre-treatment, spin-coating and drying conditions for the perovskite films deposition and the film crystallization qualitative evaluation were summarized in Tab.1, considering the ultraviolet exposure pre-treatment and the type of ambient (inert or not).

Table 1. Summarized growth conditions for the perovskite films

UV treat.	Spinning	Drying	Crystallization
no	1000 rpm	130°C amb.	Strong
no	2500 rpm	130°C amb.	Much stronger
yes	1000 rpm	130°C inert	Average to low
no	1000 rpm	100°C inert	Average to low
yes	1000 rpm	100°C inert	Low

Fig.5 shows the visible absorption spectra for: perovskite only layer (reference cell); CdS/ZnS core/shell/perovskite layer with 1 layer; CdS/ZnS core/shell/perovskite layer with 2 layers. It was noted that the increase of the core/shell thickness resulted in a shift of the overall absorption spectra to the higher wavelength. Moreover, the absorption of the cells with double core/shift layer is approximately 20 % greater in the long wavelength range than the reference cell. Overall, the light absorption of these absorbing layers is greater, as compared to CdSe, for example. The total absorption shift was approximately 22 nm. Therefore, the thickness of this layer can control the absorption spectrum in terms of broadening, or shortening, causing a peak position to vary.

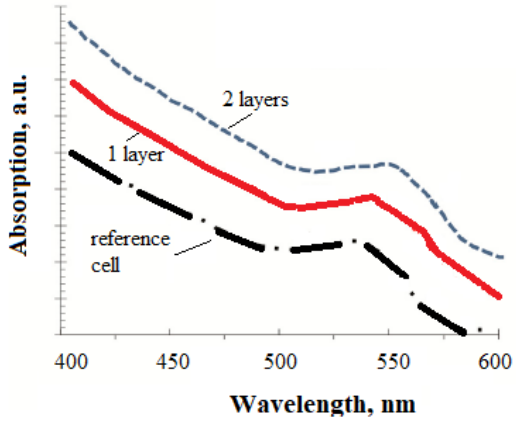

Fig.5. Absorbance spectra of the perovskite films without absorber layer (reference cell) and with different number of CdS/ZnS core/shell layers

The AFM 2-dimensional images (top view) of the perovskite films without absorber layer (reference cell) and with different number of CdS/ZnS core/shell layers are shown in Fig.6, from which the particle distribution and film homogeneity can be visualized.

The surface of the films in all studied cases was found dense and homogenous with roughness of 32 nm, 28 nm and 20 nm, respectively for the perovskite films without absorber layer (Fig.6a), for the single layered CdS/ZnS core/shell (Fig.6b) and for the double layered CdS/ZnS (Fig.6c). Compared with perovskite films only, the surface roughness decreases with the core/shell thickness increases.

The J-V curves corresponding to different CdS/ZnS core/shell films thickness are shown in Fig.7 at white light with radiometric intensity of 0.05 mW/cm^2 without load. Single layer core-shell seems not sufficient to support for longer time the absorption phenomena of the photons. Although at the beginning such conditions exist it is quickly degraded due to the small concentration of light absorbing QDs in one layer. In addition, although the surface roughness of the system perovskite/CdS/ZnS is lower as compared to the

reference cell, it is still not sufficient to guarantee uniform contact and small interface resistance with the electrodes. At higher current densities of ~4 mA/cm^2 this drawback didn't manifest, but as the current density got smaller as the sensitivity to this contact resistance effect got stronger, which imposed application of two-layered structure of the absorber. Similar effect has been observed in [21] for $CdSe_xTe_{1-x}$/CdTe cells, where such behaviour has been also ascribed to the contact resistance, however caused by the multiple thin film interfaces.

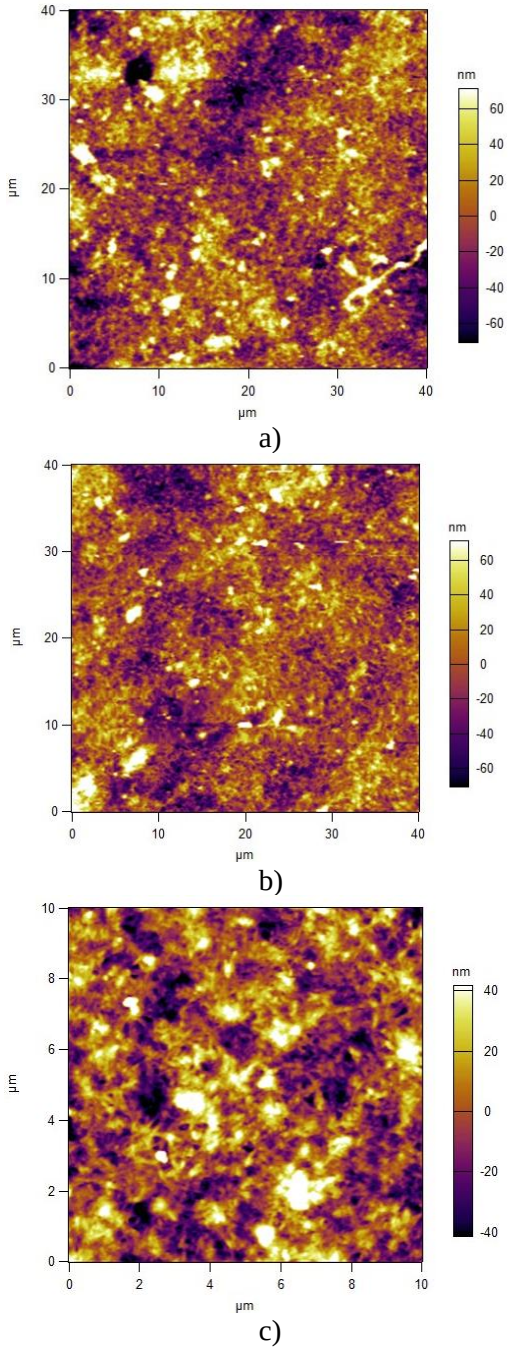

Fig.6. AFM 2D surface morphology of a) perovskite film without absorber layer (reference cell) b)single CdS/ZnS core/shell layer; c)double CdS/ZnS core/shell layer

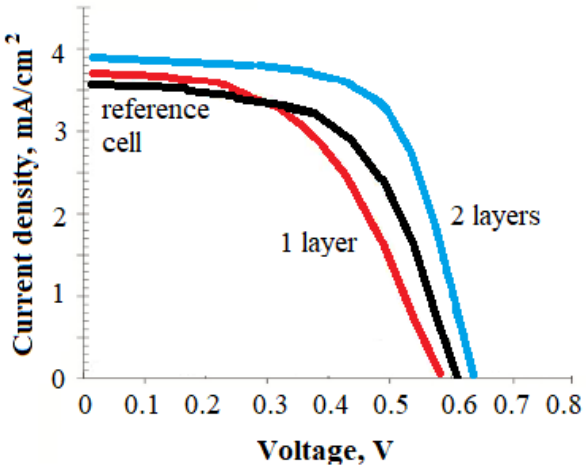

Fig.7. Current-voltage characteristics comparing the light performance of the cells with different core/shell layer thickness against a reference device

The effective band gap of the absorbing layer was calculated, following methodology described elsewhere [22], based on the cut-off edge of the quantum efficiency curve at the long wavelength visible/NIR boundary. According to it, the increase of the thickness of the core/shell layer as compared to the reference, absorber-free cell, resulted in a shift of the cut-off edge toward the longer wavelength without affecting the short wavelength range. It varied from 1.45 eV at zero thickness to 1.42 eV at the optimal thickness.

The device exhibited the best performance at a thickness of the core/shell layer of ~120 nm. The highest efficiency of 16 % was reached with back gold electrode. The maximum current density reached almost 4 mA/cm^2 at 120 nm thickness of the CdS/ZnS (for comparison, for the reference cell, a current about 3.5 mA/cm^2 was measured). Open circuit voltage is also increasing with the CdS/ZnS thickness (from 0.57V to 0.63V), although its change of 60 mV is more insignificant.

The change of the solar cell efficiency at thickness of the core/shell layer of 120 nm, as compared to the reference cell is shown in Fig.8.

In the paper [18] it was demonstrated the double function ability of the absorbing layer - it can function not only as an absorber, but also as a back buffer for balancing the charges path for which the maximum diffusion length was achieved at a thickness of 300 nm (considering the difference in the charge carriers mobility existing in the cell). When it is not used as a buffer (i.e. transporting layer), its thickness should be significantly reduced to avoid contribution of potential defects for the light scattering and optical losses. Thus, some

approximate ratios known from the literature with similarity to the non-perovskite cells were used as a starting point to determine the thickness of the absorber [23]. Higher than the maximal used in this study thickness destroyed the balance in the light penetration against the diffusion coefficient of the charge carriers injected and increased the reflectivity, leading to negative effect of electrical energy drops, because of the worsen collection efficiency (not shown).

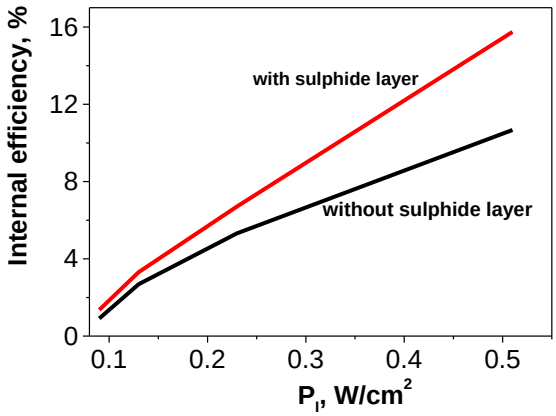

Fig.8. Comparison between the efficiency of the solar cell without and with buffer absorbing layer at white light [18]

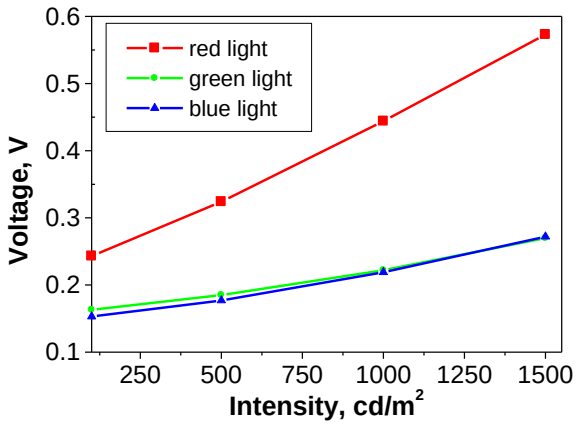

Fig.9. Voltage vs. intensity at different light colours for the optimal solar cell with attached electrical load

Study of the produced voltage's spectral sensitivity of the sell with buffer layer at photometric intensity in the range of 100-1500 cd/m^2, with light-emitting diode (LED) attached as a load, showed the greatest values produced at the red light (Fig.9). It was measured maximum 573 mV at 1500 cd/m^2 and minimum 243 mV at 100 cd/m^2. In contrast, poor sensitivity was demonstrated for green and blue light, with almost twice lower and similar maximum voltages for both wavelengths, varying between 153 mV and 272 mV in the whole range of intensities.

Comparison with the widespread CdS/CdTe based cells showed that the absorption of the present structure near the long-wavelength region is notably increased, indicating that the light absorption range of the absorber in the studied devices is broader. Therefore, the quantum efficiency in this region is expected to be significantly enhanced, which is shown with the corresponding electrical power spectral sensitivity, shown in Fig.10. This is in line with previous report [24] and additionally confirms the results from the absorbance spectra.

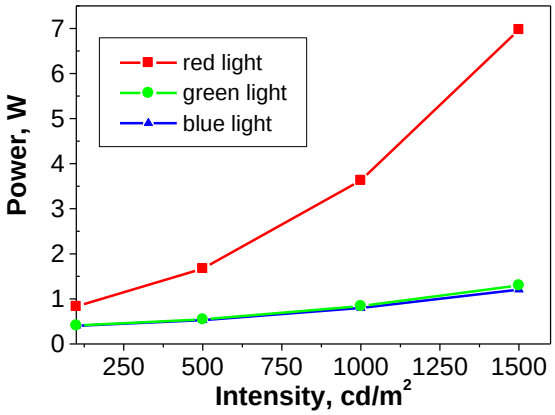

Fig.10. Electrical power vs. intensity at different light colours for the optimal solar cell with attached electrical load

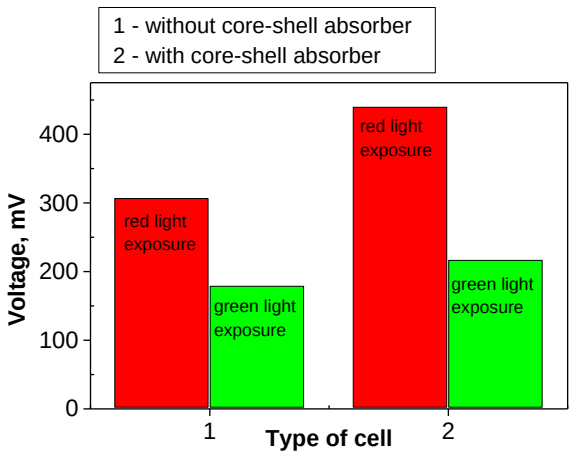

Fig.11. Comparison of the voltages produced from cells with and without core-shell absorber at different wavelengths of the exposure light

The performance of the cell and the influence of the absorber layer can be also estimated by direct comparison between the photogenerated voltage in

open circuit mode for perovskite ink and for core-shell/ink structures at 1000 cd/m^2 (Fig.11).

CONCLUSIONS

In summary, solar cell with perovskite lead-free coatings were prepared and investigated. The perovskite films crystal morphology was found to be similar like the growth kinetics of organic containing molecules with non-perovskite structure. The evolution of the crystallization centres formation and films morphology was followed according to the ambient and processing condition. A double layered core/shell CdS/ZnS material was applied by casting to change the film morphology in the solar cell. With the increase of the layer thickness, the morphology of the film changed noticeable. Improved optic conditions in the long wavelength range can be noted, which affects in a decrease of the bandgap and improved current and voltage generated conditions. As a general conclusion, it can be said that the absorbing core/shell layer with optimized thickness is a crucial part to improve the efficiency of lead-free perovskite solar cells.

As the power is produced on a simple resistive load only as a demonstrator for successful energy transfer to a load, our future work will be related to the power supplying a consumer like battery, backup supercapacitor and integrating circuit for smart photoelectric sensor, and then to determine the work point, fill factor and efficiency of the cell with respect to its size, constructive design and external connection.

ACKNOWLEDGEMENTS

This work has been supported by the joint project for bilateral cooperation in science and technology Bulgaria - India – КП06-India-6.

REFERENCES

[1] Chen Q. et al. *Nano Today*, **10**, 355-396 (2015).
[2] M. Yang et al. *ACS Energy Lett.,* **3**, 322–328 (2018).
[3] Noel N. K. et al. *Energy Environ. Sci.,* **7**, 3061–3068 (2014).
[4] Hao F., Stoumpos C.C., Cao D.H., Chang R.P.H., Kanatzidis M.G.*Nat. Photon*., **8**, 489–494 (2014).
[5] Zhao Z.,et al. *Adv Sci (Weinh)*, **4**, 1700204 (2017).
[6] Zhang Q. et. al. *Sci Technol Adv Mater*, **19**, 425–442, (2018).
[7] Song T. B., Chen Q., Zhou H., Jiang C., Wang H. H., Yang Y., Liu Y., You J., Yang Y. *J. Mat. Chem.*: A, **3**, 9032-9050 (2015).
[8] Rivera C. P., Cambero L. S., Torres M. S., Lima E., Ibarra D.S. *ACS Energy Lett.*, **3**, 2835–2840 (2018).
[9] Rahul P. K., Singh R., Singh V., Singh B., Bhattacharya Z., Khan H. *Mat. Res. Bul*., **97**, 572-577 (2018).
[10] Balakrishna R. G., Kobosko S. M., Kamat P. V. *ACS Energy Lett*., **3**, 2267–2272 (2018).
[11] Li Q., Zhang P., Yao L., Deng L., Ren X., Li Y. *Int. J. Electrochem. Sci*., **12**, 4915-4927 (2017).
[12] Nakajima T., Sawada K., *J. Phys. Chem. Lett*., **8**, 4826–4831 (2017).
[13] Bakenstein Y., Dahl J. C., Huang J., Osowiecki W. T., Swabeck J. K., Chan E. M., Yang P., Alivisatos A. P. Nano Lett. **18**, 3502-3508 (2018).
[14] Jiang F.et. al., J. *Am. Chem. Soc*., **140**, 1019–1027 (2018).
[15] Paudel N. R., Yanfa Y. Current enhancement of CdTe-based solar cells. *IEEE 42nd Photovoltaic Specialist Conference (PVSC)*, 14-19 June 2015, USA (2015).
[16] Amira R. Abou Elhamd, Khaled A. Al-Sallal, Ahmed Hassan. *Energies*, 12, 1058 (2019)..
[17] Aleksandrova M,. Ivanova T., Gesheva K., Strijkova V., Tsanev T., Singh J., Singh A. K. *Mat. Proc*., **2**, 1-4 (2020).
[18] Aleksandrova M. P., Kolev, G. D. Tomov, R., Singh, A. K., Mohite, K. C., Dobrikov, G.H., *Proc. of the 3rd Int. conf. "Alternative Energy Sources, Materials & Technologies (AESMT'20)"*, 8-9 June 2020.
[19] Khairuddin, J. *Phys. Conf. Ser.*, **776**, 012055 (2016).
[20] Aleksandrova M., Kurtev, N. Videkov V. Tzanova S., Schintke S. *Microelectron. Eng*. 145, 112-116 (2015).
[21] Li C., Li Ch, Wang Y., Ren S., Wang H., Wang W., Zhang J., Feng L. *Mat. Sci*. Semicon. Proc., **121**, 105341 (2021).
[22] Naba R. Paudel and Yanfa Yan. *Appl. Phys. Lett*. **105**, 183510 (2014).
[23] Moon Md. M. A., Ali Md. H., Rahman Md. F., Hossain J., Ismail A. B. Md. *Phys. Stat. Sol.*, 217, 1900921 (2020).
[24] Swanson D. E., Sites J. R., Sampath W. S. *Sol. En. Mat. and Solar Cells*., **159**, 389-394 (2017).

Bulgarian Chemical Communications, Volume 52, Special Issue C (pp. 72-78) 2020 DOI: 10.34049/bcc.52.C.0031

Possibilities for the utilization of highly mineralized water in Central Bulgaria as a source of thermal energy, based on the Austria's experience

M. Trayanova[1*], E. Haslinger[2*], S. Wyhlidal[2], P. Kinner[2], R, Atanassova[1], A. Benderev[1]

[1] *Geological Institute, Bulgarian Academy of Sciences, Acad. G. Bonchev St., Block 24, Sofia 1113, Bulgaria*
[2] *Austrian Institute of Technology, Center for Energy. Giefinggasse 6, 1210 Vienna*

The hydrogeological conditions in Northern Bulgaria are determined by the presence of a large artesian basin. It is constituted by several aquifers, which with depth significantly increase their temperature and total dissolved solids. These waters have been used in the past mainly for balneology and heating, but in the recent years their utilization has decreased significantly. One of the reasons for this is the processes of scaling in the wells and associated facilities. Many countries, including Austria, whose geological and hydrogeological conditions are similar to those in Bulgaria, have experience in its implementation. In the artesian basins, in the mountain depressions and in the pre-Alpine basin, high-temperature reservoirs with high total dissolved solids (TDS) are formed, some of which are used as a source of energy. One example is the hydrothermal power plant 'Frutura'at Bierbaum an der Safen in Styria, which began operation in 2016. The geothermal doublet uses water with a temperature of 124.5 °C - the highest temperature so far of all geothermal wells in Austria and with total dissolved solids (TDS) of 78 g/l. This experience could be used in Bulgaria, mainly in the Central parts of Northern Bulgaria, where highly mineralized waters with high temperatures are present. For this purpose, the data on the main artesian aquifers were summarized, with the main focus being on the most water-rich ones – the Upper-Jurassic-Lower-Cretaceous. In order to locate suitable areas for utilization of geothermal energy, their spatial position, temperature and chemical composition are characterized. A regional assessment of the amount of heat energy has been made.

Keywords: hydrogeothermal plants, scaling, corrosion, artesian basin, geothermal resousces Austria, Bulgaria

INTRODUCTION

Thermal waters have widespread, but uneven distribution around the world. They are formed under different conditions and this directly affects their quantities, qualities and utilization. Based on information from 87 countries, a summary of the amount of geothermal energy used in the world is made [1]. The heat energy used in 2020 was 1,326.96 TJ/yr. In the last years the role of renewable energy sources has been increasing also in Bulgaria, but the utilization of the energy potential from thermal waters is still largely untapped. The main interest is directed to the hot waters formed in the fractured hydrothermal systems in Southern Bulgaria. During the joint work on the implementation of the Project "Scaling and corrosion in hydrogeothermal plants and wells in Austria and Bulgaria - a comparison", along with the main tasks, attention was paid to the similarities and differences in the use of geothermal energy.

* To whom all correspondence should be sent:
milat@geology.bas.bg
edith.haslinger@ait.ac.at

The purpose of this study is to identify opportunities for using the experience of Austria in the exploration and operation of highly mineralized waters from aquifers in artesian basins, with respect to similar areas in Northern Bulgaria.

CONDITION AND USE OF GEOTHERMAL ENERGY IN BULGARIA

In Bulgaria, the formation of thermal waters is closely related to the geological-tectonic conditions. Rocks of different origin, lithologic and petrographic composition, ranging from Precambrian to Quaternary, are common on the territory of the country. Although there are different perceptions of the tectonic structure of the country [2, 3, 4, 5, 6], two radically different zones can be distinguished in its territory, predetermining different conditions for the formation of both fresh [7] and thermal waters [8, 9, 10] (Fig.1). The southern part of the country is entirely related to the Alpine-Himalayan orogeny, characterized by tectonic structure, with folded structures, imposed graben depressions, filled with Quaternary and

Pliocene deposits with porous aquifers. Fissured and karst waters with active circulation are predominant. The presence of faults predetermine the formation of fissured water systems. Northern Bulgaria is located on the Moesian platform, which predetermines the formation of a large artesian structure, with storey-arranged aquifers, descending mainly in the north direction. Hydrodynamic, geothermal and hydrochemical patterns are observed with descending of aquifers in depth.

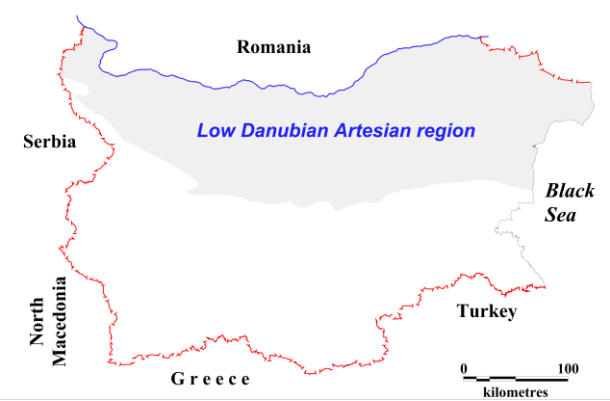

Fig.1. Distribution of the artesian waters in Bulgaria

The different geological-structural and hydrogeological conditions also have an impact on the distribution of the thermal field in the country - an important factor for the formation of thermal waters. According to [11, 12, 13, 14], with a high degree of certainty, one could assume an increase in the temperature at the same depth from north to south direction in Southern Bulgaria, and within the Moesian platform from west to east. Neotectonic activation, which greatly affected the Rhodope Mountains, was apparently related to mantle activity and the arrival of mantle asthenospheric materials from depth within the Earth's crust. This may explain the appearance of a number of anomalous points with heat flux values above 120 mW/m^2 and 440 mW/m^2, mainly due to hydrothermal activity at the mentioned points. In Northern Bulgaria aquifers of considerable thickness and wide area distribution play an important role in the distribution of the thermal field.

The nature of thermal water sources in Northern and Southern Bulgaria is different. In Northern Bulgaria, thermal aquifers are being revealed with a number of boreholes that have been drilled mainly for oil and gas exploration within the reach of the Low-Danube artesian basin. Their depth ranges from several hundred meters to more than 5,000 meters. The temperature of the waters depends on the depth of intersection of the respective aquifer, and in their deepest parts the temperature reaches over 100 °C [15]. Data from the chemical analysis of aquifers in northern Bulgaria have been published by Yovchev and Ryzhova (1962), Monakhova (1964, 1975) [16, 17, 18]. The values of the total dissolved solids (TDS) range from less than 1.0 g/l in the shallower parts of the aquifers to more than 150.0 g/l in their deepest parts.

In southern Bulgaria, thermal waters are attached to fissured-fractured confined groundwater systems. Their drainage is most often done by natural springs, but in the twentieth century a number of boreholes were drilled in the areas around the springs and in areas of supposedly not discharged on surface thermal waters. The depths of the wells are significantly smaller than in Northern Bulgaria, only in some cases they are up to 2000 m. The prevailing water temperatures are up to 60 °C, only in some cases they are above 70 °C. The highest temperature in southern Bulgaria is in Sapareva Banya where water with 103 °C is revealed. Thermal waters are fresh, predominating of those with a TDS below 1 g/l, and only in some cases -2-3 g/l.

The current state of thermal water exploitation in Bulgaria is reviewed by Hristov et al. 2019, Hristov, Gerginov, 2019 [19, 20]. Of all the existing thermal water fields and water sources, 102 are state-owned, the rest are provided for municipal management for a period of 25 years. About 72% of the total resources are with relatively low temperatures - up to 50 ºC on the surface. The flow rates of most exploited water sources vary from 1 l/s to 20 l/s, with a TDS below 1.0 g/l. Thermal waters in Northern Bulgaria with higher TDS are not exploited. Despite the relatively good hydrothermal capacity of 9957 TJ/year (2765,855 MWh), the use of thermal water is still only 25-30% of the total amount of renewable energy. The installed heat output increases from approximately 83.10 MWt in 2014 to 99.37 MWt in 2018.

CONDITION AND USE OF GEOTHERMAL ENERGY IN AUSTRIA

As in Bulgaria, the territory of Austria is characterized by rocks of different age, lithology and petrographic composition, which are in complex relationships with regard to its tectonic conditions [21]. The main regional structure is the Alpine-Himalayan orogeny, which occupies more than 3/4 of the country's territory. This is a typical

folded structure built of various Mesozoic, Paleozoic and older rocks. Pre-mountain lowered sections are usually filled by molasses and flysch complexes. To the north and east, the mountain structures switch into the Vienna and Styrian basins, which are parts of the Middle Danube lowland. Hydrogeologically, three main structures are separated in Austria - the Eastern Alps, the Pre-Alpine basin and the Czech basin [22].

The Eastern Alps are characterized by the spread of fresh fissured and karst waters with intense circulation and good drainage conditions. At times, in some depressions, artesian basins with relatively higher water abundance are formed.

The Pre-Alpine basin is characterized by the presence of distinct smaller artesian basins (Molasse, Vienna, Styrian, Pannonian) with its characteristic storey-arranged aquifers. They are characterized by an increase in temperature and TDS in depth.

The Czech massif is relatively low water-abundant and is characterized by the presence of fissured waters in the weathered zones of the rocks.

As in Bulgaria, two main types of thermal water can be separated in Austria - those attached to fissured water systems (mainly in mountainous regions) and to layered aquifers in the artesian basins (Fig.2). A total of over 210 thermal and thermal mineral water fields have been identified [23].

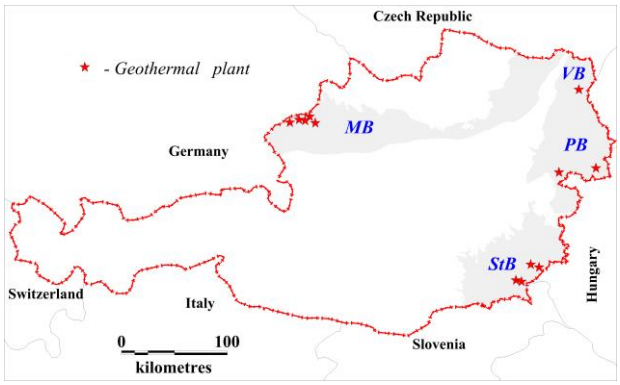

Fig.2. Distribution of artesian waters in Austria (MB - Molasse basin, VB - Vienna basin, PB - Pannonian/Danube basin, StB - Styrian basin)

Three major provinces could be separated:

- Acidic waters, attached to large tectonic disturbances in areas of relatively young magmatism located along the distribution of crystalline rocks and their eastern boundary with the Pre-Alpine basin - most of the known natural springs.

- The second group is mainly hydrocarbon thermal waters in the area of the youngest tectonic movements in the Alps.

- In the artesian basins, in the intermountain depressions and in the pre-alpine basin, highly-temperature and highly mineralized water reservoirs are formed.

In some parts of the Northern Limestone Alps, sodium and sulfate springs, attached to salt and gypsum deposits, are also presented.

Although there is a long tradition in the use of renewable energy in Austria, the share of geothermal heat production is estimated at around 1.6% [24]. Geothermal conditions in Austria are different across the Alpine region, on the one hand, and the main sedimentary basins, on the other. In the eastern part of Austria, increased heat flux densities above 100 mW/m^2 (Pannonian, Styrian basin) can be observed.

Local anomalies in the Molasse and Vienna basins are related to hydrothermal systems of local and regional importance. Inside the alpine orogen, the heat flux density is usually reduced due to the thickening of the Earth's crust. Particularly in the Northern Alps, the long-ranged infiltration systems for meteoric water lead to a further reduction in the heat flux density to below 50 mW/m^2. Natural springs with temperatures up to 46 °C are used for balneological purposes. The thermal waters of the Vienna and Styrian artesian basins are much more widely used.

The exploitation of natural thermal waters has a long tradition in Austria. The waters were used for balneology and recreation mainly. The use of thermal water as an energy source has been increasing since 2014 - in addition to the numerous resorts. Currently, 10 hydrogeothermal power plants are operating in Austria. They are located in the Molasse and Styrian basins, where the most favorable conditions for hydrogeothermal use in terms of heat flow, capacity of water-bearing structures and groundwater chemistry composition are presented. However, the water from these two regions is quite widely exploited and offer limited available resources - around 100 MWth according to Goldbrunner, Goetzl [24].

The exploitation of high mineralization thermal waters in artesian aquifers is associated with the processes of scaling and corrosion of pipes and installations [25, 26, 27, 28, 29, 30]. The water sources used have a temperature in the range of 39 to 115 °C, half of which are above 80 °C and are attached to artesian aquifers, some of which with very high TDS.

HYDROTHERMAL POWER PLANT 'FRUTURA' AT BIERBAUM AN DER SAFEN IN STYRIA

The waters with the highest temperature and mineralization that are used in Austria are those from the hydrothermal power plant 'Frutura' at Bierbaum an der Safen in Styria, which has started exploitation in 2016 (Fig.3). For the heating of greenhouses, a reinjection system of two boreholes was constructed in 2016 [24]. Initially, the boreholes were drilled for oil and gas exploration. The pumping well is 3,300 m deep, revealing the Malm-Valanginian aquifer. It pumps out water at a flow rate of 60 l/s with a temperature of 124.5 °C (the highest temperature so far of all geothermal wells in Austria). The water is Na-Cl type with a TDS of 78 g/l. The reinjection borehole is located at about 1800 m distance and so are the borehole heat exchangers. The currently installed heat output is 15 MWt, which is used for greenhouses. On some parts of the heat exchangers halite is deposited, which is periodically removed.

Pumping well

Reinjection borehole and hydrothermal power plant

Halite scaling on the borehole heat exchangers

Location (Goldbrunner, Goetzl, 2019).

Fig.3. Hydrothermal power plant 'Frutura' at Bierbaum an der Safen in Styria

STATE AND POSSIBILITIES OF USING HYDROTHERMAL ENERGY IN CENTRAL NORTHERN BULGARIA

Conditions for the formation of higher temperature thermal waters exist in northern Bulgaria within the reach of the Lower Danube artesian basin [8, 9, 10]. Water-bearing rock complexes have a wide surface area in horizontal direction and varying lithological composition and stratigraphic vertical range. Several aquifers are formed which are storey-arranged. The basin is characterized by hydrodynamic, hydrochemical and hydrogeothermic zoning, both vertically and horizontally [16]. In the aquifer recharge zones, the waters are fresh, with active water exchange and low temperature. In depth, the temperature gradually increases, the type of their chemical and gas composition changes.

With the largest area distribution and importance is the Upper Jurassic-Lower Cretaceous aquifer. It is attached to a thick carbonate complex, where the rocks, including in depth being cracked and unevenly karstified [31]. In the southern parts, there is a gradual transition of carbonate to flysch sediments, which also changes their collector properties. The aquifer is hardly outcropped on the surface, except for some spots directly or under a thin quaternary cover in the highest, crest parts of the North Bulgarian vault (Northeastern Bulgaria). From there, the carbonate rocks descend in depth in all directions. To the East, towards the Black Sea and south of the North Bulgarian vault- in the Varna Depression, the Upper Jurassic - Lower Cretaceous aquifer descends from its recharge area (in the outcrops in the North Bulgarian vault) to the west and south.

The waters are cold in the recharge zone and increase their temperature up to 30-55 °C along the Black Sea Coast The predominant TDS of thermal waters is in the range of 0.4-0.8 g/l, where only at the Northern Black Sea waters with TDS of 1-4 g/l are present. To the West, as the aquifer descends, the temperature gradually increases, reaching more than 100 °C in the deepest western parts. At the same time, the TDS increases, reaching values of few dozens of g/l.

The object of the present study is the part of the Upper Jurassic-Lower Cretaceous aquifer, located in Central Northern Bulgaria, in the zones where the temperature increases and there would be relatively more potential consumers of geothermal energy.

The area under consideration is about 8000 km^2, with the Iskar River as western; the Danube River as northern; the Yangtara River as eastern; and the tectonic boundary separating the Moesian Platform as southern boundary. The basic information about its the geological, hydrogeological and geothermal conditions was used during the prospecting for oil and gas, summarized in 1983 in the monograph "Geology and oil and gas perspectives of the Moesian Platform in Central North Bulgaria" under the editorship of A. Atanasov and P. Bokov [32].

The predominant thickness of the water-bearing rocks is 700 - 900 m, which in the South increases to 1500 m, and then sharply decreases due to the transition of the rocks from carbonate to flysch facies. The aquifer lies on the Middle-Jurassic aquitard or the Lower-Middle- Jurassic aquifer complex and is covered by the Lower Creatious aquitard complex. The relief at the top of the aquifer (Fig.4) in its north-eastern parts is relatively smooth, but smaller structures with positive and negative character are observed (elevation of its top -700 - -1300 m a.s.l.). In the Southwest, a gradual descending is observed, with a maximum depth of over 3000 m. The horizon is characterized by filtration heterogeneity, with values of conductivity varying from about 40 to over 3000 m^2/d, with a decrease in values with the aquifer descending from the east to the west. The waters of the aquifer are confined and in most cases the water level is below the terrain. The temperature of the waters increases in depth, ranging from below 40° to 100 °C (Fig.4). The geothermal gradient within the aquifer, due to its high water abundance, is low - from 1 to 2°/100 m. Only in the deepest parts of the horizon, where the water exchange is slow, the gradient is above 2.5°/100 m. The aquifer is characterized by slightly salty to salty thermal waters with a tendency to increase in the TDS from north-northeast to south-southwest [33]. The lowest value of TDS is 1.55 g/l and the highest - 22.3 g/l (Fig.5). The hydrogen index is in the range of 6 to 10, with predominant values between 7 and 8. The predominant types of water are chloride-sulphate-sodium-calcium and chloride-sulphate-sodium. In the west, with depth, the water changes into sodium chloride type.

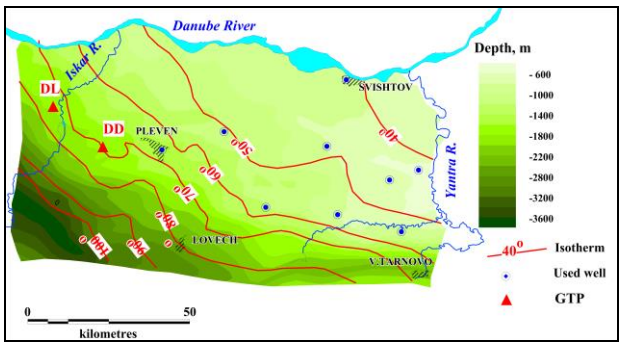

Fig.4. Map of temperatures in depth of the upper part of the Upper Jurassic-Lower Cretaceous aquifer and locations of used in the past boreholes and geothermal plants (GTP): DD - Dolni dabnik, DL – Dolni Lukovit

DISCUSSION

The conducted analysis of the quantities and qualities of thermal waters in Central Northern Bulgaria, as well as their thermal energy, show that there are possibilities for their use in the area. Unfortunately, this potential is hardly utilized.

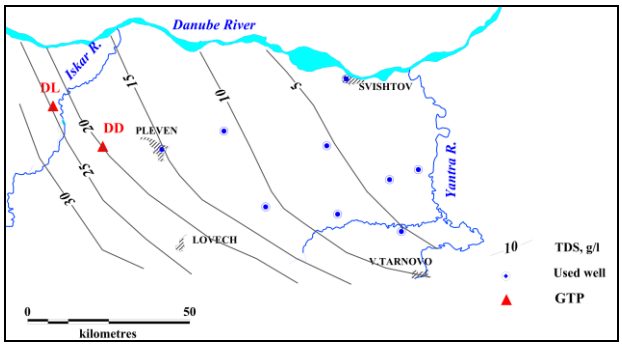

Fig.5. Map of TDS distribution of the Upper Jurassic-Lower Cretaceous aquifer and locations of used in the past boreholes and geothermal plants (GTP): DD - Dolni dabnik, DL – Dolni Lukovit

In the past and at present time for balneology, greenhouses, hygienic needs and heating, only thermal waters from some single wells, located in the eastern, shallower part of the aquifer have been used. Their temperature varies from 44 to 58 °C and have TDS from 2.8 to 12 g/l. In the 1990s, tests in the western part of the aquifer were conducted to evaluate the possibility of using geothermal energy in several sections. Subsequently, two geothermal plants were built, which operated for a short period - from 1987 to 1989. The geothermal plant in Dolni Dabnik was designed in 1986. For this purpose, a pumping well was used, which reveals thermal water with temperatures of 70-71 °C in the Upper Jurassic/ Lower Cretaceous aquifer in the interval 1794 - 2693 m. The re-injection of 8 °C cooled water was carried out in a well, located at a distance of 1750 m, revealing the same aquifer in the range 1808 - 2705 m. A backup injection well at a distance of 1270 m was also planned. The plant was equipped with iron heat exchangers, but it was intended to replace them with titanium. The plant's design capacity was around 30 l/s, but due to the change in its political and economic status during its operation in Bulgaria, which led to a significant decrease in energy consumers. Initially, 8 l/s were used for the heating of administrative buildings, and later its operation was canceled and the buildings and facilities were abandoned. The situation with the other geothermal plant - near the village of Dolni Lukovit is similar. The designed flow rate was 7 l/s, with a temperature drop of 13 °C (from 66 °C to 53°C). At present, the plant is also not fully used and only operates during the colder months for heating of buildings. The distance between the pumping well and the

injection wells was 5 km. In both plants there were problems with scaling.

The examples given above, as well as the experience of Austria, show that the Upper Jurassic/-Lower Cretaceous aquifer in the studied area is promising for the use of geothermal energy. An indicative regional assessment of the aquifer's thermal energy was made, according to the methodologies given by Galabov [34].

At a natural resource of the aquifer of 1380 l/s, with a reduction of the temperature up to 40 °C, the heat output amount is 115 MW_{th} and up to 15 °C - 259 MW_{th}. With the use of re-injection, the energy potential is significantly higher. For its estimation, a representative area around the town of Pleven, with an area of 1600 km^2, was selected. The choice is based, on one hand, that there are potential energy users in the area and, on the other, the suitable geological, hydrogeological and geothermal conditions. In the area under consideration, the upper part of the Upper Jurassic-Lower Cretaceous aquifer is at absolute elevations between -1200 and -2500 m, at an average thickness of about 1000 m, the water level is at an average depth of 120 - 125 m and the conductivity is about 40 m^2/d. The water temperature in the upper part of the horizon is between 60 and 90 °C, and in the lower part with 10-20 °C higher. The TDS is in the range of 10 to 25 g/l. The estimated calculations were conducted at a temperature drop of 30 °C according to the following scheme: 800 thermocouples were evenly located over the area under consideration, with an estimated operating flow rates of each pumping well of 10 l/s with groundwater table decline of about 13 m. The estimated value for the heat capacity is 1000 MW_{th}.

CONCLUSIONS

Although geothermal energy is not being sufficiently utilized in Austria, there are positive trends in its use, including the construction of a number of new hydrogeothermal plants, including in the artesian basins, where significant amounts of high-temperature groundwater bodies are present. Serious studies have focused on the processes that hinder the exploitation of geothermal energy. A review of the hydrogeological and geothermal conditions in Bulgaria shows that Austria's positive experience can be applied, especially in Northern Bulgaria. This is confirmed by the use of thermal and mineral waters in the past. For example, in Central Northern Bulgaria, only about 35-40 l/s of thermal water was used for heating and balneology in the late 1980s, while at present these quantities are minimal, mainly only for hygienic purposes and partially for balneology. Unfortunately, the existing and efficiency proven geothermal power plants at Dolni Dabnik and Dolni Lukovit, have been abandoned. In this respect, it would be useful for the administrative authorities and businesses to be aware of the possibilities of optimal utilization and use of this renewable energy potential.

ACKNOWLEDGEMENTS

The research was carried out in the framework of the bilateral cooperation project between Bulgaria and Austria 01/13/05.10.2017 "Scaling and corrosion in hydrogeothermal plants and wells in Austria and Bulgaria – a comparison", financed by the Austrian Federal Ministry of Science, Research and Economy (BMWFW) and by the Bulgarian Ministry of Education and Science (Scientific Research Fund).

REFERENCES

[1] J. Lund, A. Toth. Direct utilization of geothermal energy 2020 worldwide review. *Geothermics*, ***9*** (2020),*https://doi.org/10.1016/j.geothermics.2020.101915*.

[2] D. Yaranov. Tectonics of Bulgaria. Technics, 1960 (in Bulgarian).

[3] E. Bonchev. Problems of Bulgarian Geoectonics. Technics, 1971 (in Bulgarian).

[4] Y. Yovchev (ed.). Tectonic structure of Bulgaria. Technics, 1971 (in Bulgarian).

[5] C. Dabovski, I. Boyanov, K. Khrischev, T. Nikolov, I. Sapounov, Y. Yanev, I. Zagorchev. Structure and Alpine evolution of Bulgaria. *Geol. Balc*. **32**, (2–4), 9–15 (2002).

[6] I. Zagorchev. Geomorphological zonation of Bulgaria. Principles and state of the art. *Comptes rendus de l'Academie Bulgare des Sciences*, **62**, 8, 981-982 (2009).

[7] H. Antonov, D. Danchev. Groundwater in the Republic Bulgaria. Technika, 1980 (in Bulgarian),

[8] K. Shterev. Mineral waters in Bulgaria, Nauka i izkustvo, 1964 (in Bulgarian).

[9] P. Petrov, S. Martinov, K. Limonadov, Y. Straka. Hydrogeological investigations of mineral waters in Bulgaria. Technika, 1970 (in Bulgarian).

[10] A. Benderev, V. Hristov, K. Bojadgieva, B. Mihailova. Thermal waters in Bulgaria, in: Mineral and thermal waters of southeastern Europe, P. Papic (ed.). Springer Part of the series Environmental Earth Sciences, 47-64 (2016).

[11] T. Velinov. Geothermal field in Bulgaria. *Rev. Bulg. Geol. Soc.*,**47**(1), 1–9 (1986) (in Bulgarian).

[12] T. Dobrev, S. Dimovski, S. Kostianev. Level of study of the geothermal field in Bulgaria and a

metodical approach towards investigating its depth distribution. *Ann. Univ. Mining and Geol*., **47**(1), 251–258 (2004) (in Bulgarian).

[13] R. Radichev, S. Dimovski. A study over the specifics in the distribution of the correlation coefficient between geophysical fields. *Ann. Univ. Mining and Geol.*, **50**(1), 171–177 (2007) (in Bulgarian).

[14] M. Khutorskoy, N. Kostova, A. Benderev, V. Hristov. Heat flow and depth temperatures in the Earth crust of Bulgaria based on numerical modelling. *Rev. Bulg. Geol. Soc.*, **80**(2), 55-62, (2019) (in Bulgarian).

[15] K. Bojadgieva, S. Gasharov. Catalogue of Geothermal Data of Bulgaria. Sofia, GorexPress, 2001 (in Bulgarian).

[16] R. Yovchev, V. Rijova Groudwaters in Northern Bulgaria. GUGOZN, 1962 (in Russian).

[17] L. Monahova. Chemistry and chemical groundwater characterization in oil and natural gas deposits in Northern Bulgaria, *Ann. GUG*, 91-217 (1964) (in Bulgarian).

[18] L. Monahova. Hydrochemical parameters for oil study in Northern Bulgaria. *Bull. Geol. Inst., Ser. Oil and Coal Geolog*, **23**, 83-99 (1975) (in Bulgarian).

[19] V. Hristov, B. Deneva, S. Valchev, A. Benderev. Geothermal Energy Use, Country Update for Bulgaria (2014-2018). *European Geothermal Congress 2019. Den Haag, The Netherlands, 11-14 June 2019,* CUR-05-Bulgaria.pdf (2019).

[20] V. Hristov, P. Gerginov. Mineral water resources in Bulgaria. *Conference Proceedings "Climate, atmosphere and water resources during climate change" Sofia, 14 - 15 Oct. 2019*, 102-115. (2019) (in Bulgarian).

[21] H. Egger, H. Krenmater, G. Manol, A. Matura, A. Novotny, G. Pascher, G. Pestal, J. Pistonic, M. Rockenchaub, W. Schnabel. Geologische Übersichtkarte der Republik, 1999.

[22] H .Schlönlaub, (ed.), Hydrogeologishe Übersichtkarte der Republik Österreich. Geologishe Bundesanstalt, Wien, 2003.

[23] G. Hobiger. et al. Thermal and mineral waters in Österreich. – In: Hydrological Atlas of Austria. Bundesministerium für Land- und Forstwirtschaft, Umwelt und Wasserwirtschaft (BMLFUW), 2005.

[24] J. Goldbrunner, G. Goetzl. Geothermal Energy Use, Country Update for Austria. *European Geothermal Congress 2019 Den Haag, The Netherlands, 11-14 June 2019*, 6 p., CUR-01-Austria.pdf, (2019).

[25] N. Mundhenk, P. Huttenloch, B. Sandjuan, T.Kohl, H. Stenger, R. Zorn. Corrosion and scaling as interrelated phenomena in an operating geothermal power plant. *Corrosion sciences*, **70**, 17-28, (2013).

[26] S. Wyhlidal, E. Haslinger, R. Boch, H. Fröschl, M. Dietzel, A. Leis, R. Knauss, J. Goldbrunner, A. Shirbaz, O. Plank. 2015. Mineralogy, hydro- and isotope chemistry of thermal water and scalings in hydrogeothermal plants and preliminary results of batch experiments. *14th Austrian stable isotope network meeting, Tulln/Donau, 26.-27. Nov.2015*. mineralogy-hydro-and-isotope-chemistry-of-thermal-water-and-scali-2

[27] E. Haslinger. Charakterisierung von thermalen Tiefengrundwässern zur Verhinderung von Ausfällungen und korrosionen bei geothermieanlage. *Forschungs projekt noscale vöbu-forum***, 39**, 22 – 23 (2016).

[28] G. Götzl, E. Haslinger. Scalings in hydrogeothermal plants in Austria. Geothermal ERA-NET, Reports from Joint Activities. *Joint Activity OpERA - Operational issues in Geothermal Energy in Europe, Status and overview*, 12 – 15. 2016

[29] E. Haslinger, J. Goldbrunner, M. Dietzel, A.Leis, R.Boch, R.Knauss, D.Hippler, A.Shirbaz, H.Fröschl, S.Wyhlidal, O.Plank, M.Gold, D.Elster.: Charakterisierung von thermalen Tiefengrundwässern zur Verhinderung von Ausfällungen und Korrosionen bei Geothermieanlagen. *Forschungsprojekt NoScale. Der Geothermiekongress DGK 2016, Essen, 29.11 - 01.12.2016*. DGK Tagungsband 2016.

[30] R. Boch, A. Leis, E. Haslinger, J. Goldbrunner, F . Mittermayr, H. Fröschl, D. Hippler, M. Dietzel. Scale-fragment formation impairing geothermal energy production: Interacting H2S-Corrosion and CaCO3 crystal growth. *Geothermal energy*, 5:4, s40517-017-0062-3, (2017).

[31] I. Stanev. Ancient and contemporary karst in the Upper Jurrasic - Low Cretaceous aquifer in the Northern Bulgaria, Rev. *Bulg. Geol. Soc*., **2**, 241-249 (1970) (in Bulgarian).

[32] A. Atanasov, P. Bokov (ed.). Geology and oil and gas perspectives of the Moesian Platform in Central North Bulgaria. Technics, 1983 (in Bulgarian).

[33] M. Trayanova, S. Kolev, N. Hristov, A. Benderev. Hydrochemical characterization of groundwater in mesozoic aquifers in Central Northern Bulgaria. Procc. *19-th International Multidisciplinary Scientific GeoConference SGEM 2019, 27 June - 7 July, 2019, Albena, Bulgaria*, **19**(1.2), *Hydrogeology, Engineering Geology and Geotechnics*, 305-312 (2019).

[34] M. Galabov, N. Stoyanov. Thermo-hydrodynamics of geothermal fields. Publishing House "Vanyo Nedkov", Sofia, 2011 (in Bulgarian).

Bulgarian Chemical Communications, Volume 52, Special Issue C (pp. 79-84) 2020 DOI: 10.34049/bcc.52.C.0106

Turbulent Flow Pump for CO_2 Capture from Combustion Emissions

N. Shahar[1,2*], S. Zerbib[1], M. Maharizi[1], G. Golan[1*]

[1] *Ariel University, Science Park, Ariel 40700, Israel*
[2]*Livolt Ltd., PO Box 44, Elon Moreh 4483300, Israel*

In this work, we provide detailed experiments describing the behaviour of CO_2 post-combustion capture (PCC) using Monoethanolamine (MEA) solution and integration of a Turbulent Flow Pump (TFP) into the laboratory scale system. We relate the CO_2 concentration in the inlet gas flow, total mixed gas flow rate, and solvent pump speed against the CO_2 capture efficiency. CO_2 capture efficiency computed per mass transfer and thin-film theory to estimate the overall mass transfer coefficient based on the diffusion rate between gas and liquid phases. The use of TFP showed the advantages of saving space and improve process efficiency. The interconnection between studied parameters is analysed via single variable regression models to generate design equations for developing and scale-up of carbon capture systems.

Keywords: MEA, CO_2 capture, amines solvents, absorption, desorption, mass transfer

INTRODUCTION

Sustainable energy systems are a concern for governments throughout the world. As a result, the capture and management of carbon dioxide from combustion systems is a critical element of the environmental policies of many countries [1]. Amine solutions are the most mature method for capturing carbon dioxide from mixed gas streams as part of natural gas sweetening processes [2]. This process is also applicable for the separation of CO_2 from flue gases composed mostly of N_2, CO_2 and H_2O. The use of amine solvents is effective and reliable; however, the process suffers from several drawbacks, including but not limited to high corrosivity, energy consumption, and maintenance costs [3]. In an amine-based CO_2 Post Combustion Capture (PCC) system, where CO_2 captured, compressed, and stored to prevent it from being released to the atmosphere. Aqueous alkanolamine solutions used to absorb the acid gas from the flue gas stream in countercurrent operation and the solvents need to be transported from the absorber outlet back to the inlet and undergo a regenerative heating process to release the acid gas. At present, this process requires large columns to separate CO_2 from the flue gas because the current technology of separation is limited by relatively slow mass transfer of process. Mass transfer coefficient in stirred cells and spray columns have been extensively investigated [4] [5], however the process intensification and improvement of these processes still face immense challenges to reduce in device size. Improving spray system performance was achieved through the integration of a Turbulent Flow Pump (TFP). That integrates the solvent pump in the bottom of the column, such that TFP operation generates turbulence and superior carbon dioxide dissolution vs an in-line pump that might be installed outside of the reactor within the system piping. Integration of TFP in the process may increase the surface area interface between the gas phase and the liquid phase, stirring of the later cancel differences in concentrations which found to be beneficial in spray absorbers [6].

* To whom all correspondence should be sent:
natan@livolt.net
gadygolan@gmail.com

MASS TRANSFER

Absorption and desorption processes refer to the migration of solute from the gas phase to the liquid phase and vice versa [7]. The CO_2 is absorbed and released in certain mass transfer rates that are dependent upon both reaction rate and transport rate of the two phases. Kinetics of reaction is set by the driving force, which can be presented as the difference between the actual CO_2 concentration and the equilibrium concentration ($y^*_{CO_2}$) and is assumed to be fast using lean CO_2 amine solutions. According to film theory [8], resistance to mass transfer occurs in a thin layer of stagnant fluid while the bulk is well mixed. Mass transport through the different layers illustrated on Fig.1. The gaseous CO_2 diffuses from the gas bulk to the interface with relatively high resistance, at the interface CO_2 react with MEA and decreases significantly (dotted line), CO_2 molecules continues to diffuse through the liquid film to the well stirred bulk. An equivalent behaviour of mass transfer is shown in solid line from the interface to

liquid bulk. Fick's law, under the assumption of well stirred reactor and steady state conditions [9], [10], set the column height dependent concentration equation on the interface between two phases.

$$\frac{dY_{CO_2,G}}{dZ} = K_G a_e \cdot \left(\frac{P(y_{CO_2,G} - y^*_{CO_2})}{G_I}\right) \quad (1)$$

where $Y_{CO_2,G}$ is the mole ratio of CO_2 in the gas phase, $P\left(y_{CO_2.G} - y^*_{CO_2}\right)$ is the expression for the mass transfer driving force, shown in diffusing plot on Fig.2, Z is the height of the absorber/stripper column, G_I is the inert gas molar flux and overall gas phase mass transfer coefficient expressed as $K_G a_e$, it includes a combination of diffusion rate on the gas phase, reaction kinetics, and thermodynamics of CO_2 absorption process and can be illustrated as labelled in Fig.1. Due to High solubility of CO_2 in aqueous alkanolamine solutions. gas phase resistance is the preponderant portion of the mass transport in this process, as indicated in Eq.2-30.

$$\frac{1}{K_G} = \frac{1}{k_G} + \frac{m}{k_L} \quad (2)$$

$$\frac{1}{K_G} \approx \frac{1}{k_G} \quad (3)$$

where K_G is the overall gas phase mass transfer coefficient, m/k_L represents the liquid phase resistance, and k_G is the gas mass transfer coefficient.

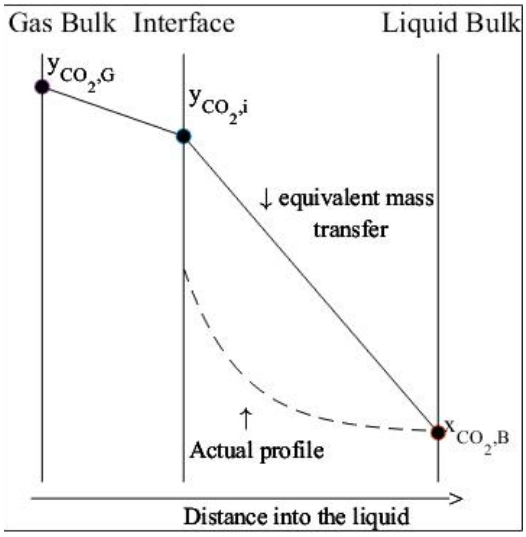

Fig.1. Illustration of CO_2 diffusion from gas phase to liquid *[7].* $y_{CO_2,G}$, $y_{CO_2,i}$, , $y_{CO_2,B}$ are CO_2 concentration in gas phase, interface and liquid bulk respectively

According to Eq.1, to reduce the CO_2 concentration it is needed to increase the total area of the reactor, increasing the overall mass transfer coefficient using improve amine kinetics, increase the driving force and increase in the contact surface area between the two phases. For the investigation of the experimental absorption-desorption rate two of the paraments required are the solubility and diffusivity of the acid gas in the liquid phase, the use of overall mass transfer coefficient is due to the difficulty to measure those parameters.

EXPERIMENTAL SETUP

Schematic and a photo of the test rig are given in Fig.2. Columns consist of two Pyrex glass, each with an outer diameter of 65 mm, an inner diameter of 60 mm, and a height of 400 mm. The columns were filled with 330 ml of Reagent grade MEA 30% (w/w) with an assay of 99.0% obtained from Merck. Connecting tubes and reactors were purged with N_2 from a nitrogen tank. The system was heated and cooled in a cycle using a heating element and an ice bath respectively, for two hours to reduce any traces of other gases. Mass flow controllers (MFC) ensure a fixed gas ratio of CO_2/N_2 (Tylan 2900 series) ranges from 0-500 sccm, with an accuracy of 1% of full scale. Inlet gas is inserted in the bottom of the column and affected by the behaviour of the solution. CO_2 concentrations at the stripper and absorber outlet were measured using NDIR (Nondispersive infra-red) CO_2 sensors (SPRINTIR WF-20, SPRINTIR WF-100) ranges of the sensors is 0-20% and 0-100% of CO_2 by volume respectively both with an accuracy of 5% of reading. Two 12-watt liquid pump (TFP) with five centrifugal impellers, Fig.3, and a maximum speed of 2000 rpm connected to the bottom of the columns. Pulse Width Modulation of the control signal to pumps driver kept speed control at ±1%. Due to low concentration of amine solution, no significant raise in temperature was observed during absorption process, and the column temperature is considered constant after cooling to 40 °C. During the experiments, the temperature of the solution was measured at the top of the columns using special k type thermocouples with an accuracy of ±0.6 ˚C. Each measurement was taken after ensuring steady state behaviour of the process i.e., no fluctuations in CO_2 reading and constant temperature reading in the columns.

a)

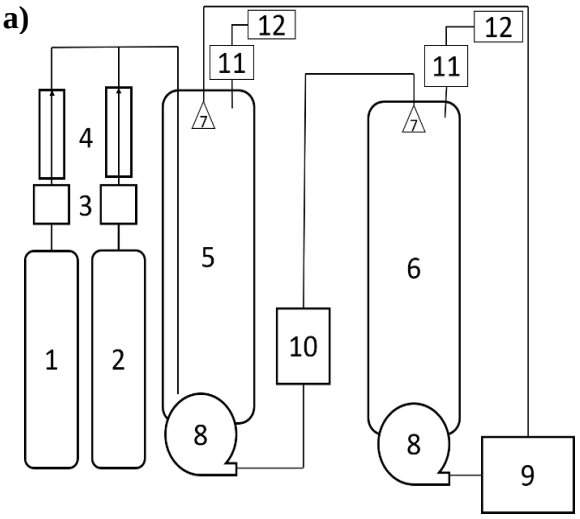

b)

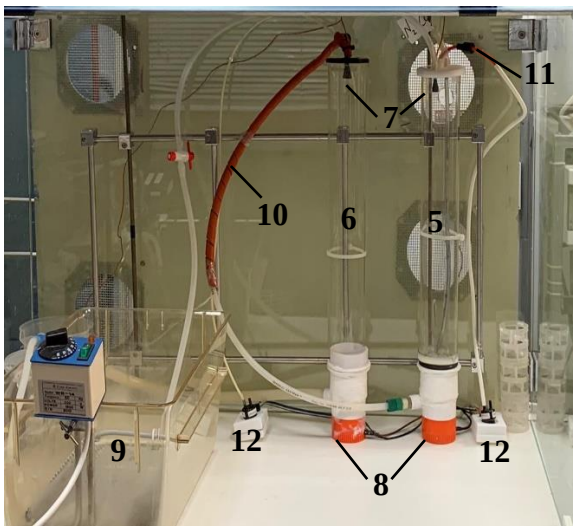

Fig.2. a) Schematic of the experimental setup. b) A photo of the test rig placed in a fume hood: 1- CO_2 tank, 2- N_2 tank, 3- mass flow controller, 4- check valve, 5- absorption column, 6- desorption column, 7- spray nozzle, 8- TFP, 9- cooling bath, 10- heating element, 11- desiccant, 12 – NDIR CO_2 sensor.

In this experiment, the use of TFPs enhanced the effect of a smooth gas-liquid interface, which who is advantageous in preserving the contact area for the reaction. The diameters of the spray nozzles and TFP set the maximum flow rate of the solution in the system for each reactor. TFPs power set the amount of liquid that accumulates at the bottom of the stripper and the turbulency flow of both gas and liquid phases. Turbulent flow allows both gas and liquid phases to remain homogeneous at the bottom of the reactors during CO_2 mass transfer and reduce film thickness.

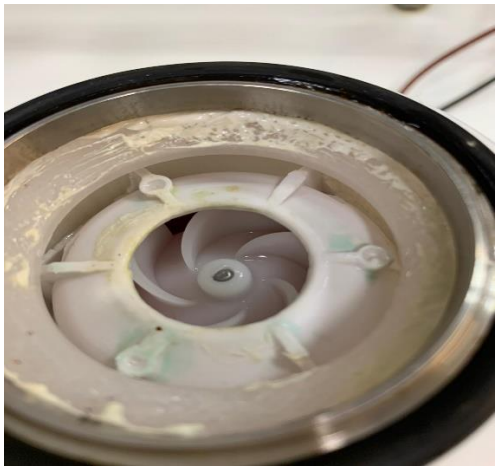

Fig.3. TFP impeller

RESULTS AND DISCUSSION

The process variables listed in Tab.1 were maintained constant, except that for each set of experiments one variable was varied to measure the effect of that variable on the CO_2 concentration vented out from the absorption column. All measurements were performed after the system is considered in steady state operation, to ensure the changes in CO_2 concentration is due to the regulated variable and not transition on other parameters.

Table 1. List of experiment variables

Variable	value	Units
Absorption temperature	35	$°C$
Desorption temperature	90	$°C$
Total flow rate	200	ml/min
Inlet CO2 concentration	11	% VOL
TFP Power	12	W
Pressure	114	kPa

Changes of CO_2 concentration

While changing the CO_2 concentration using the mass flow controllers, reading from the NDIR sensor gives the CO_2 concentration in the outlet of the absorption tower was recorded. The results in Fig.4 show the overall mass transfer coefficient decreases as CO_2 concentration increases. The expression of driving force increases with the increase in CO_2 concentration, resulting in a

decrease of the overall mass transfer coefficient. The relationship between CO_2 inlet concentration and the mass transfer coefficient, per the results in Fig.4, was observed to be exponential, which show a significant drop off in the mass transfer coefficient as the carbon dioxide concentration increases from 10% to 20% and high decline at higher concentrations. This behaviour is expected, due to CO_2 solubility decrease with reduced active MEA molecules. The liquid phase rates become significant in the process, and thus, a linear relation is not agreed.

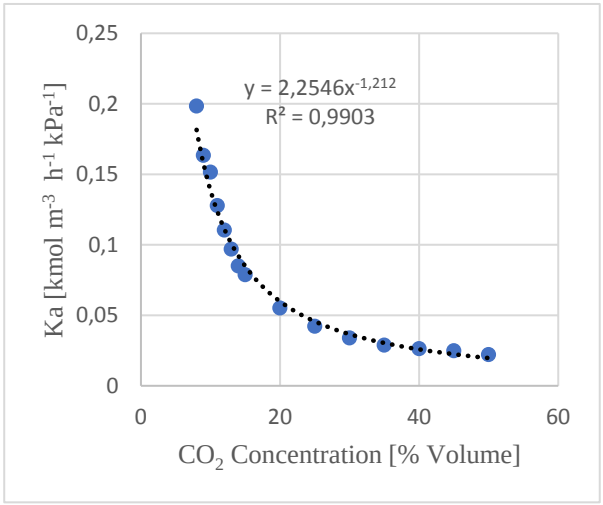

Fig.4. Impact of inlet gas CO_2 Concentration on mass transfer coefficient

For low CO_2 concentrated inlet gas, the results shown in Fig.5, suggests that as for low concentrations of CO_2, the linear behaviour is according to the reduction in driving force on Eq.1.

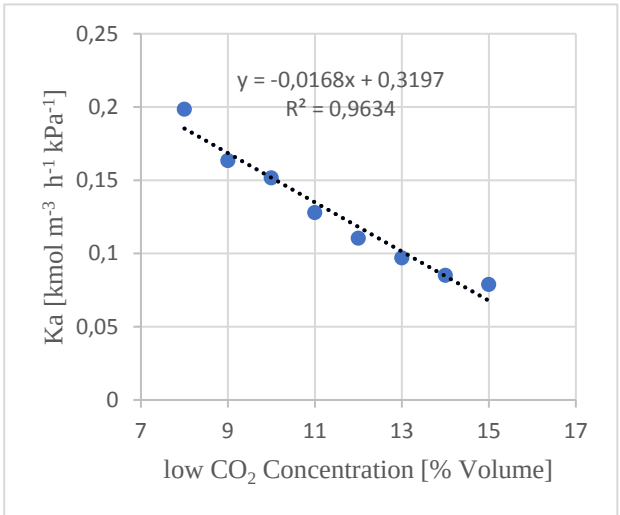

Fig.5. Impact of low concentrated CO_2 on mass transfer coefficient

Changes of inlet gas flow rate

The results shown in Fig.6 are consistent with thin film mass transfer theory the overall mass transfer coefficient is proportional to the gas flow rate. Since no packing used in the columns, no flooding consideration was needed when varying the gas flow rate. The trending observed was expected given high flow rate causes increased points of contact between the solvent and the mixed gas.

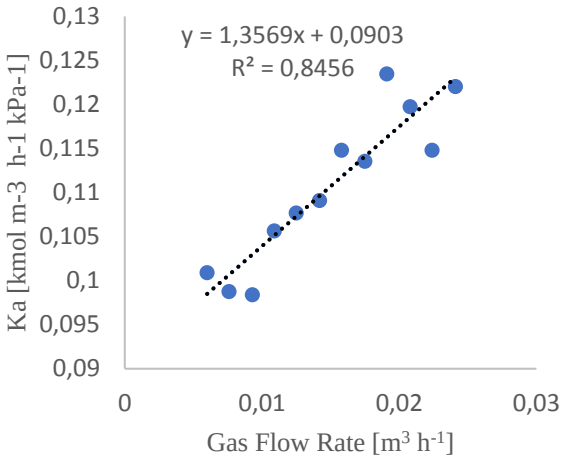

Fig.6. Impact of inlet gas flow rate on Mass Transfer Coefficient

Changes of TFP Power

TFP Power was set within the range of 4-13 watt. Results shown in Fig.7 show a clear tendency of the behaviour of the overall mass transfer coefficient when increasing the TFP power. Constrained in flow rate by the spray nozzle, the excess power of the TFP is related to the liquid stirring and creation of vortexes in accumulated solution at the bottom of the column. Below 6 watt no change in the liquid surface due to turbulence flow was observed, and under 4 watt there was not enough power to run the system. The range of operation 4-6 watt considered as laminar flow in the liquid phase. It is deduced that the turbulence flow of the solution and gas in the reactor decreases the boundary layer between the liquid and gas phase and therefore increases both gas phase and liquid phase mass transport. The laminar flow region starts with no difference in mass transfer measurement, and an increasing tendency is observed as the transition to turbulent flow occurs. The relationship between the pump power and mass transfer was linear and can be explained as the small increase in liquid phase mass transfer can

raise the equivalent overall gas phase mass transfer linearly Eq.4. This behaviour expected to increase both gas phase transfer and reaction rates enables the eddies to move into the boundary layer due to a decrease in laminar film thickness.

$$K_G \cong k_G \cdot \Delta k_L \quad (4)$$

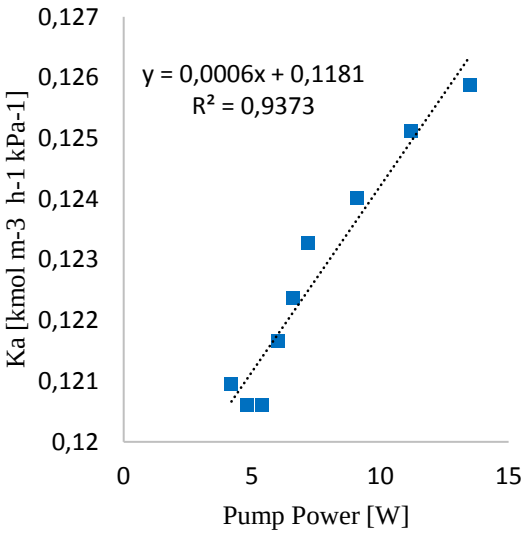

Fig.7. TFP power on overall mass transfer coefficient

REGREATION MODEL

Regression models have been applied according to Tab.2. The regression models explain the expected behaviour of the system.

Table 2. Regression models for experimental results

Parameter	Effect	Model
CO_2 partial pressure	Change in driving force	Power,
Gas Flow rate	Increase in gas phase molecule transfer	Linear,
TFP power	Increase in packing volume	Linear,

CONCLUSIONS

A study on the gas-liquid mass transfer enhanced using a TFP was proposed to improve the process efficiency. The use of a TFP both simplifies mass transfer calculation due to solution turbulence stirring and increases mass transfer coefficient in compare to laminar flow. Using TFP integrated absorption desorption cycles, the mass transfer coefficient was measured to determine the effect of different variables on the process efficiency. The increase in CO_2 concentration reduces the overall mass transfer coefficient. A nonlinear trend was observed for high concentrated inlet gas streams as the mass transfer linear model is no longer valid. An increase observed when increasing the inlet gas flow rate and TFP Power. Integration of the TFP in laboratory scale model found to be beneficial for use in CO_2 removal process to reduce columns size. However, the results presented only indicate the behaviour of the system, and for scale-up purposes, a larger scale laboratory experiment is needed.

ACKNOWLEDGEMENTS

We thank the Israel Ministry of Energy and Livolt Ltd. for funding our work.

NOMENCLATURE

$Y_{CO_2,G}$ - CO_2 mole ratio in gas phase, mol%;
$y^*_{CO_2,G}$ - CO_2 equilibrium mole ratio in gas, mol%;
$y_{CO_2,B}$- CO_2 mole ratio in liquid bulk, mol%;
$y_{CO_2,i}$ - CO_2 mole ratio in liquid-gas interface, mol%;
P - pressure, kPa;
G_I - inert gas molar flux, $\frac{\text{kmol}}{\text{m}^2\cdot\text{h}}$;
k_G – gas phase mass transfer coefficient, $\frac{m}{h}$;
k_L – liquid phase mass transfer coefficient, $\frac{m}{h}$;
K_G- overall gas phase mass transfer coefficient, $\frac{m}{h}$;
η – CO_2 removal efficiency;
a_e – interface effective contacting area, $\frac{\text{m}^2}{\text{m}^3}$;
Z – column height, m;
T - temperature, K;
TFP – turbulent flow pump;
MEA - monoethanolamine;

REFERENCES

[1] R. Schlögl, Put the Sun in the Tank: Future Developments in Sustainable Energy Systems, *Angewandte Chemie International Edition* **58**, 343-348 (2019).

[2] M. R. Radzuan, N. A. Syarina, W. M. Rosdi, A. H. Hussin and M. F. Adnan, Sustainable Optimization of Natural Gas Sweetening Using A Process Simulation Approach and Sustainability Evaluator, *Materials Today: Proceedings* **19**, 1628-1637 (2019).

[3] C. Saiwan, T. Supap, R. O. Idem and P. Tontiwachwuthikul, Part 3: Corrosion and prevention in post-combustion CO2 capture

systems, *Carbon Management* **2**, 659-675 (2011).

[4] B. Lu, X. Wang, Y. Xia, N. Liu, S. Li and W. Li, Kinetics of Carbon Dioxide Absorption into Mixed Aqueous Solutions of MEA + [Bmim]BF4 Using a Double Stirred Cell, *Energy & Fuels* **27**, 6002–6009 (2013).

[5] J. Kuntz and A. Aroonwilas, Performance of Spray Column for CO2 Capture Application, *Industrial & Engineering Chemistry Research* **47**, 145-153 (2008).

[6] A. Dimiccoli, M. D. Serio and E. Santacesaria, Mass Transfer and Kinetics in Spray-Tower-Loop Absorbers and Reactors, *Industrial & Engineering Chemistry Research* **39** (2000).

[7] H. Karlsson and H. Svensson, Rate of Absorption for CO2 Absorption Systems Using a Wetted Wall Column, *Energy Procedia* **114**, 2009-2023 (2017).

[8] W. K. Lewis and W. G. Whitman, Principles of Gas Absorption, *Industrial and Ingineering chemistry*, 1215-1220 (1924).

[9] X. Wu, M. He, Y. Yu, Z. Qin and Z. Zhang, Overall Mass Transfer Coefficient of CO2 Absorption in a Diameter-varying Spray Tower, *Energy Procedia* **114**, 1665-1670 (2017).

[10] M. Heydarifard, H. Pashaei, A. Ghaemi and M. Nasiri, Reactive absorption of CO2 into Piperazine aqueous solution in a stirrer bubble column: Modeling and experimental, *International Journal of Greenhouse Gas Control* **79**, 91-116 (2018).

Bulgarian Chemical Communications, Volume 52, Special Issue C (pp. 85-90) 2020 DOI: 10.34049/bcc.52.C.0045

Open Top Seeding Crystal Growth Control System

S. Zerbib, G. Orr, G. Golan*

Ariel University, Science Park, Ariel 40700, Israel

The majority of crystal growth systems require overcoming problems related to process monitoring and continuous electronic control. In order to monitor and control such systems, high quality industrial equipment has to be used, due to its high reliability, requiring minimum long-term maintenance. In particular, reliable temperature controllers, are prevalent components which are devoted to thermal control of high temperature profiles in crystal growth systems. The following paper describes an inexpensive top seeding crystal growth system, using open-source software and low-cost electronics. This system was built in order to control and monitor the entire growth process in a Bridgman method growth system at our laboratories in Ariel University, Israel.

Keywords: crystal growth, seed growth, high temperature thermal control, top seeding method, motion control, Bridgman.

INTRODUCTION

By using inexpensive microcontrollers and electric components, coupled with rapid 3-D printing and wide Open-Source applications, the Crystal Growth community can drastically reduce the time and resources needed to manufacture such crystal growth systems. The use of industrial Single Loop Temperature Controller (SLTC) makes the whole interface with the instrument, via open-source software, both reliable and independent of the manufacturer closed source operation system. The benefits of using SLTC with accessible detailed memory addresses are associated with better supervision over the instruments via open source supervisory and control software. There is a diverse of available information on the internet about open-source supervisory systems based on PLC's, and several Arduino based SCADA systems [1, 2], however, these systems still lack reliability and errors are still found and reported in libraries or code lines [2]. The supervisory and data storage therefore is implemented using the more reliable open-source platform – the Raspberry-Pi. Crystals possess a high degree of perfection and purity, [3] these crystals play key roles in the modern science and technology whether in their natural, synthetic or engineered form. The main problem of crystal quality control is the thermal boundary conditions [6], Thermal boundary conditions dictate the interface shape between the solid and liquid regions of the material.

Most of the time, a set of variables defines the quality of the crystal, according to its unique desired properties, and it is not always accessible, or hard to predict during the growth process. Compositional homogeneity and reduced chemical stresses were reported by [7], using a rotation of the seed or melt. To control the desired variables in these complicated systems, an accurate motion and temperature control is needed. In this article, we describe an open hardware and software design resulting in a high-performance Top Seeded Solution or Bridgman control system. The resulting system can control crystal growth in the range of room to high temperatures (limited only by refractory materials and heating elements). As proof of concept, we built and characterized the Bridgman method furnace's temperature profile and demonstrated its usefulness by growing aluminium crystals with a melting point at 660^{O}C. The requirements from this growth are a high thermal mass, low heat loss due to conduction and radiation while reaching the temperature of 750 ˚C in separated zones, with T_H, T_C that refer to the hot and cold zones temperatures, respectively. During the growth process, the molten charge is lowered in an ampoule inside the furnace temperature gradient. In the specific implementation of the Bridgman method, a crystalline oriented seed is placed right below the molten charge with its temperature slightly below the melting point of the charge. The crucible with the molten charge slowly translates from the high temperature to the solidification temperature where it obtains a crystalline structure (single crystal) oriented in the

* *To whom all correspondence should be sent:*
gadygo@ariel.ac.il

seeds direction. The upper zone is required to be slightly above the melting point, and the lower zone below melting. The importance of temperature profile and precise control over the process are key features of the crystal growth process.

MATERIALS AND METHODS

Temperature control

All temperatures were measured using a Watlow K24-2-505 special type K thermocouples with an accuracy of 0.4% up to 1096 ^{O}C, and Schneider Electric's Eurotherm 3216 temperature controllers. An industrial temperature controller and low limit of error thermocouple were used to ensure stable and precise control on the growth spot in the furnace. The controllers (Fig.1) switch the power supply using two Fotek SSR-25 DA Solid state relays capable of switching up to 16 [A] of heating element current [4], connected in series to a residual current device to turn off the furnace in case of an alarm or short circuit. The power was taken from the power grid via an UPS. All connections were done via [5] a supervisory unit, using RS232-to-USB converters.

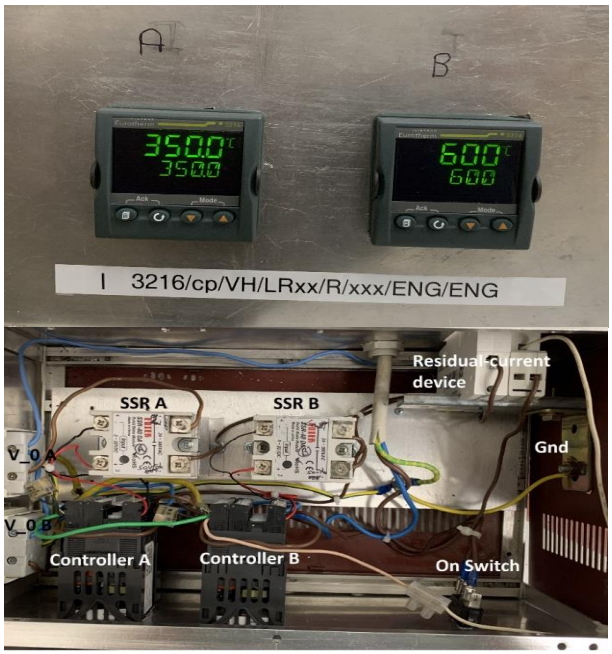

Fig.1. Temperature control box front panel and internal components

Motion control

Temperature control is handled according to the temperature profile of the furnace and stable melting zone temperatures, as the motion of the sample along the furnace is handled using a stepper motor. A NEMA 17 stepper motor is used characterized by 1.8˚ per step. Pulse Width Modulation of the control signal to the motor driver is applied resulting in smooth rotation of the motor and consistent translational or rotational movement to the charge and grown crystal. The load determines the number of steps per revolution as the torque to the crystal decreases with the increase in the number of steps. Speed of growth in the typical range of mm/hour depends on the move of the temperature gradient [6]. The Arduino platform continually moves the motors according to the last instruction (rate) stored in the microcontroller memory. The interaction between the Arduino and the actual movement of the system is done by the Raspberry-pi's Top Seeding software. The key objective of the control algorithm is to move the sample with precise accuracy through the crystallization zone to optimize the growth conditions and prevent undesired defects [3]. The flowchart described in Fig.2 illustrates the control decisions that manage the Arduino software.

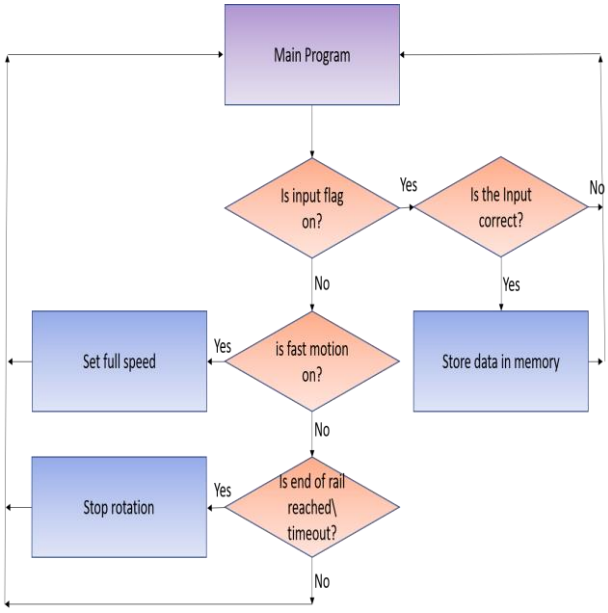

Fig.2. Flowchart of the algorithm to control the motion of the crystal inside the furnace

The Arduino board and the motor driver have been placed in a costume-built box using Open Scad and a 3-D printer is shown in Figs.3 and 4. The control over the growth variables is done semi-automatically as the vertical motion can be controlled manually to move across the rail using a switch.

An Arduino is using embedded RS232 to USB converter and is connected to the Raspberry-pi using a USB cable. A design choice was made, in which each motor has a different Arduino as a controller. This increases the robustness and reliability of the growth system, simplifying on site repairs should one of the controllers fail. The cost of this redundancy is negligible.

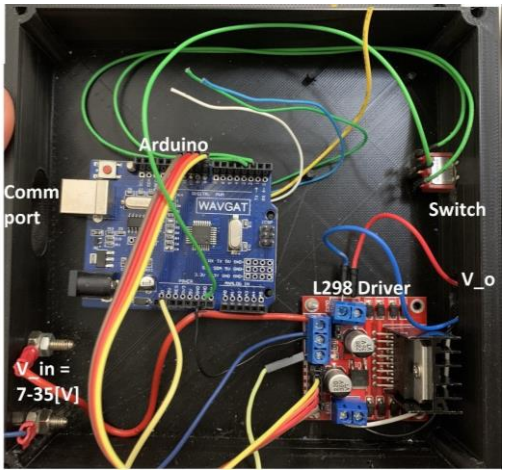

Fig.3. Arduino box and schematics drawn with Fritzing [8]

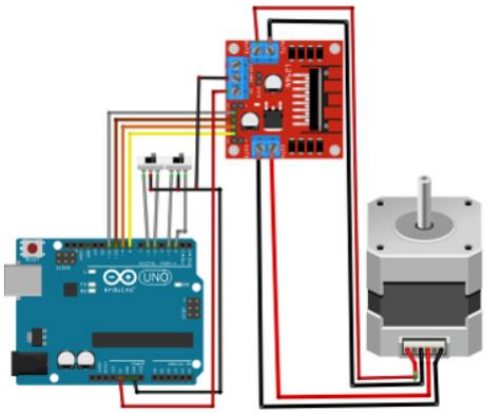

Fig..3 Electronic wiring of the Arduino Uno to L298 driver and switches used to control the stepper motor motion. A power supply of at least 7-35[V DC] and 0.8-1.5[A] is needed

Bridgeman furnace assembly

High thermal mass can be achieved using thick insolation around the heating element, and sufficient power per square centimeter of the heating element. The heating element was prepared from 2.5cm O.D ceramic tube made by extrusion to ensure even wall thickness and high tube concentricity. These features prevent thermal strains and ensure uniform isolation profile [9]. The heating coil was wrapped around a ceramic tube in different spaces to set the furnace with its unique temperature profiles of hot and cold zones. The furnace was designed with a total heating power of 1130 [W] separated for the hotter zone and the cooler zone. The two zones were connected in parallel to the power supply. The difference between these zones was achieved using different length of heating wires. The hotter zone benefits longer wire and therefore higher power per surface area, making it favourite for higher temperatures. The resulting resistances are R_C = 120 [Ω], R_C = 100 [Ω], with R_H, R_C referring to the hot and cold zones, respectively. The heating wires were covered with an alumina isolating blanket. Another ceramic tube was attached in parallel to the main tube for the measurements of the temperature along the furnace. The heating wires were connected to the power supply fitting box (Fig.5).

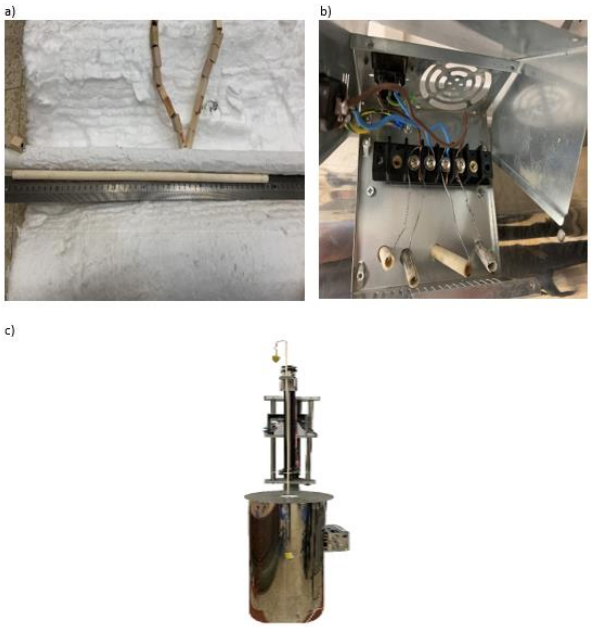

Fig.4. Assembly of Bridgman method furnace. a) Heating wired wrapped around 2.5 [mm] X 70 [cm] ceramic tube. b) The heating wires connection to the power box. c) The fully assembled system, the furnace at the bottom and translation stage above it

The motion module was attached to the entrance of the furnace with thermocouple connecting the motor's rail for temperature measurements along with the furnace. A meter was attached next to the rail to indicate the motor movement.

Open-source user interface

An open-source software called Top Seeding, based on Python programming language [10] [11], Remote terminal Unit (RTU) Modbus

communication protocol [12], and matplotlib for visualization was designed to gather data from the process, generate commands and send these commands to the process. To communicate with the Raspberry-pi, SLTCs, and Arduino, an asynchronous serial communication was set via RS232 connectors for each RTU with the ability to convert signals obtained from the sensors to digital data and sending them to the supervisory system. According to [13], using asynchronous communication "silent period" of 3.5 bytes in the message limits the maximal baud rate optional, using RTU Modbus protocol (Fig.6). The User Interface was designed using Object Oriented Programming (OOP) architecture. Number of libraries were used in this software and they are all listed in Tab.1. Following the OOP architecture, the devices features, connected to the Top Seeding software, were defined as specific modules for each instrument in the system and described the access to the instrument's memory addresses.

Table 1. List of libraries and fields corresponding to the Top Seeding software

Name of Python Library	Field of attributes
Tkinter	GUI
OS	Operation system
Matplotlib	Graphics
Minimalmodbus	Modbus protocol
Pyserial	Serial communication

The object oriented nature of the software, gives the desired agility adding the flexibility of inverting objects and applying the programming paradigm to a variety of instruments and future additions.

Fig.5. The Raspberry-Pi is connected to instruments via USB ports and stored in a 3-D printed box (designed using Open-Scad)

Cautiousion was taken by blocking the operators ability of writing to non-volatile flash memory. Although the system cannot change configuration settings on the PLC's memory and initial conditions on motion control modules, this setting has been considered preferable to prevent memory failures.

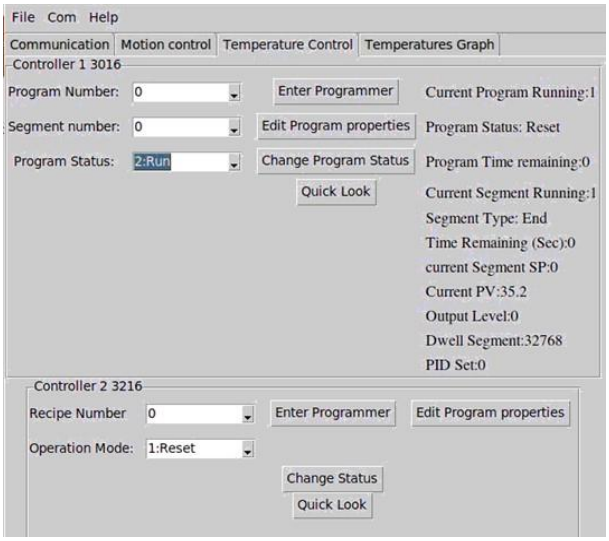

Fig.6. Top seeding software, Temperature control tab communicates with Eurotherm controllers using Modbus protocol

RESULTS

The furnace was heated up to $T_H = 600\ [°C]$, $T_L = 350[°C]$, motion control was set to gradually rotate downward the furnace at a constant velocity of two revolutions per minute i.e. 4 mm/min. At the end of the translation stage, a microswitch was set to stop the motor and the profile was tested again while the TC moving upwards the furnace. To reflect the effective operation of the approach, Fig.7 shows the screen of Top Seeding software temperature control tab under working conditions. The variables from the Arduino and SLTC are displayed in real-time for the user, separated to different informative tabs demonstrating the current process. In many automated infrastructures, the system also preforms active control tasks. In the present case, the growth time of a typical crystal makes it more reasonable to handle the process semi-automatically. It means that the control algorithm carried out by the motion control module and SLTC, can be intervened with at any time, using the Top Seeding software. As can be observed in Fig.7, a graphic chart illustrates the measured temperature along the furnace axis. The tab named

Temperature Control on the Top Seeding software GUI, displays its numeric value together with other variables related to the SLTC; including the type of operation, target value, output level etc. Additionally, an output logger records the entire process corresponding to UTC date and time for desired interval of seconds on the Raspberry-pi memory.

The resulting average temperature profile is shown in Fig.8. This temperature profile indicates that the growth interface should be at approximately at a depth of 35 cm from the upper opening of the furnace, yet a more detailed profile of the hottest spot in the furnace had to be taken in order to place the crystal seed exactly in the right position, where it can benefit the best growth conditions. The temperature profile indicates that placing the seed below 35cm, lowering it at a constant velocity will commence crystal growth. Once the entire ampoule passes the melting point, the higher zone is slowly cooled to the same temperature of the lower zone and annealing take place at a constant temperature of 350 ˚C.

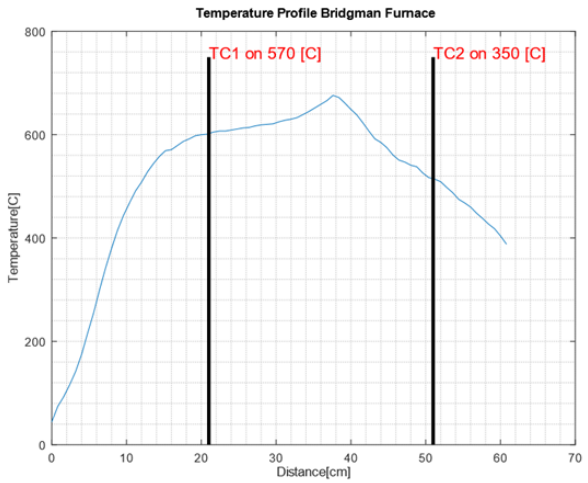

Fig.7. Measured temperature profile along the furnace axis

The temperature measured outside the ceramic tube, indicated on the efficiency of the measurements and the SLTC. It is indicated by the vertical lines on the chart. Despite the obtained results, some disadvantages characterize this system in comparison to other industrial systems. Open hardware-based setups can be unreliable due to the use of jumper wires that might disconnect. Raspberry-Pi does not meet the required system safety due to its multitasking nature and thus results long delays depending on the CPU load. This delay is unacceptable in case of high power and temperatures. Therefore, alarm commands are all handled by the industrial SLTP. Although full open hardware system is not considered suitable for hard real application, this system provides a proper behaviour on the so-called semi-automatic approach.

CONCLUSIONS

Open hardware and software became a viable option for lab control systems. They cost less than industrial devices and are supported with a wide range of literature. This article has presented a system for half open-source electronics hardware (Arduino and SLTC) and open-source software (Top Seeding) for crystal growth systems based on the Top Seeding method. The open-source device is responsible for sensing, control, and data acquisition tasks. The proposed technique represents the versatile open-source approach to the crystal growth control systems. A Bridgman furnace was built and characterized for use as a benchmark to analyse and validate the proposed solution by means of temperature profile test under real operating conditions. The experimental results reflect on the effectiveness of the system display, data exchange, and process logging.

ACKNOWLEDGEMENTS

This work has been supported financially by the Nofar research project 1.07.2019 of Ariel University, Ariel, Israel, which is gratefully acknowledged by the author.

REFERENCES

[1] A. J. C. Isasiac Gonzalez. Integration of open source hardware Arduino platform in automation systems applied to Smart Grids/Micro-Grids. *Sustainable Energy Technologies and Assessments* **36**, (2019).

[2] Z. Z. D. D. B. S. Akram Sted Ali. Open Source Building Science Sensors (OSBSS): A low-cost Arduino-based platform for long-term indoor environmental data collection. *Building and Environment* **100**, 114-126 (2016).

[3] J. R. B. M. N. Ye. Functional Crystals. *Modern Inorganic Synthetic Chemistry*, 575-611 (2017).

[4] Fotek SSR Series, Fotek. https://cdn.sparkfun.com/datasheets/Components/General/SSR40DA.pdf. (Accessed 03 10 2019).

[5] Eurotherm, 3216, 3116 PID Temperature Controllers Engineering Handbook HA027986, (2004).

[6] A. S. W. M. B. D. a. N. B. S. C. Batur. Control of Crystal Growth In Brigdman Furnace. *Prog. Crystal Growth and Charact*, **30**, 217-236 (1995).

[7] A. O. P. S. Dutta. Melt Growth in Quasi-binary (GaSb)1-x(InAs)x crystals. *Journal of Crystal Growth*, **198-199**, 384-389 (1999).

[8] Fritzing Home Page, fritzing, https://fritzing.org/. (Accessed 04 10 2019).

[9] R. C. R. I. B. R. James L. Eucker. Process for manufacturing ceramic tubes. US Patent 524,264, (1990).

[10] B. M. Meier, Python GUI Programming Coockbook, Packt Publishing Ltd., 2015.

[11] S. Nagar, Object-Oriented Programming, Apress, 2018.

[12] The Modbus Organization, www.modbus.org.

[13] P. S. S. K. S. B. H. L. K. Dutta. Growth of Gallium Antimonide by Vertical Bridgman Technique with Planar Crystal-Melt Interface. *Journal of Crystal Growth* **141**, 44-50 (1994).

Bulgarian Chemical Communications, Volume 52, Special Issue C (pp. 91-95) 2020 DOI: 10.34049/bcc.52.C.0035

Integrated combustion flue gas separation and Methanation

S. Zerbib[1*], N. Shahar[2*], G. Golan[1]

[1] *Ariel University, Science Park, Ariel 40700, Israel*
[2]*Livolt Ltd., 54/6 Moshe Dayan Blvd, Jerusalem 9757025, Israel*

Chemical energy storage is a potential process for balancing supply and demand in energy production based on renewable energy. The objective of this paper is firstly to review characteristics of conventional exhaust treatments and methane formation and secondly to propose a combustion flue gas methanation model that will be able to achieve an alternative energy storage solution. An initial description and technical analysis of its key features are presented. This research demonstrates a scalable process that integrates the abundance of renewable energy and the dispatchability of fossil fuels by using wind/Solar electricity to convert carbon dioxide into methane. As a result, an existing fossil-fuel-fired combustion appliance may be turned into a 100% carbon neutral system that maintains a closed-loop on carbon. The process includes the following critical steps: Capture of combustion exhaust, separation of water from the exhaust, Separation of nitrogen from the exhaust, a distillation of the water produced, electrolysis of the water to produce hydrogen, mixing of carbon dioxide and hydrogen in a Sabatier reactor to produce methane.

Keywords: Methanation, CO_2 capture, power to methane

INTRODUCTION

Reducing CO_2 emissions produced via combustion is an essential goal to achieve the economical and climate change objectives defined by the COP-21 in Paris in 2015, when 194 states and the European Union signed the Paris Agreement, in order to reduce global emissions and limit the temperature increase to 1.5 $°C$ above pre- industrial levels [1]. The fact that these goals have significant economic implications created difficulties resulting in the USA announcement to withdraw from the Paris agreement [2]. Chemical energy generated from renewable sources such as PV solar and wind can meet the gap created between economic and climate goals and thus enable detractor of the Paris Climate Agreement such as the USA to rejoin the accord. The primary challenge is fluctuations of wind and sunlight. Development economic baseload renewable electricity production requires the implementation of energy storage technologies to address overproduction periods and distribute it during underproduction periods. Based on the Power To Gas (PtG) concept [3], The suggested system will capture the CO_2 from combustion exhaust gas and use PV solar energy to convert it to natural gas which has already existing infrastructure for storage and distribution. This innovative system integrates within a single device all of the core processes required to seamlessly convert the combustion exhaust of any system into renewable natural gas. These processes include but are not limited to the following: CO_2 post-combustion capture, electrolysis of water entrained in both the combustion and methanation exhaust to generate hydrogen, and a methanation (Sabatier) reaction for the desired conversion of CO_2 to methane. The combustion reaction can be described according to Eq.(1):

$$C_aH_b + \epsilon\left(a+\frac{b}{4}\right)\cdot(O_2+3.76N_2) \rightarrow aCO_2 + \frac{b}{4}H_2O + (\epsilon-1)\left(a+\frac{b}{4}\right)O_2 + (a+\frac{b}{4})3.76N_2 \quad (1)$$

where *a* and *b* are defined as C_aH_b, and ϵ represents the added amount of air to the burner system which is more than the amount required for perfect stoichiometric combustion and is defined as Eq.(2).

$$\epsilon = 1 + \frac{\%\ Excess\ Air}{100} \quad (2)$$

The two key reactions of methane production are:

$$CO_2 + 4H_2 \leftrightarrow CH_4 + 2H_2O \quad (\Delta H = -165\ \frac{kJ}{mol_{CO_2}}) \quad (3)$$

$$CO + 3H_2 \leftrightarrow CH_4 + H_2O \quad (\Delta H = -206\ \frac{kJ}{mol_{CO}}) \quad (4)$$

* To whom all correspondence should be sent:
Shlomizar13@gmail.com
natan@livolt.net

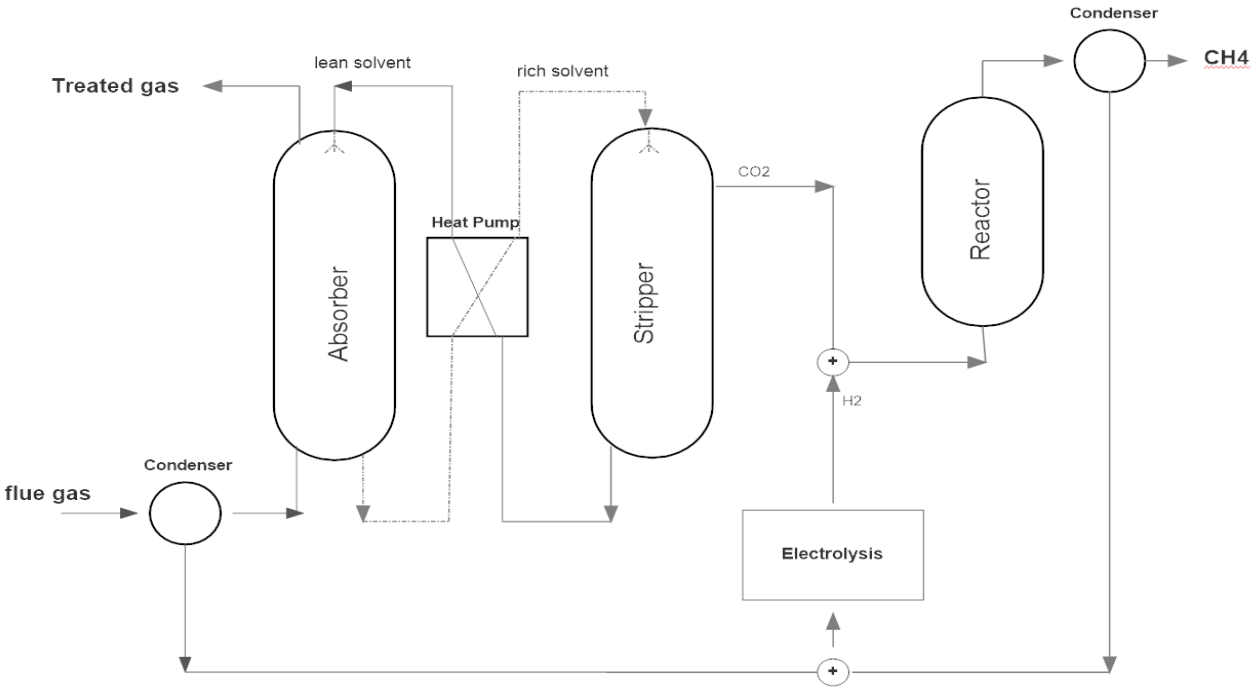

Fig 1. Process flow diagram for CO_2 capture and methanation reaction

The exhaust gas characteristics in the simulation of the processes is shown in Tab.1, as in ideal combustion with 20% excess air.

Table 1. Typical characteristics of flue gas

Flue Gas Specification	Composition
CO_2 (mol %)	6.7
N_2 (mol %)	75.8
O_2 (mol %)	4.1
H_2O (mol %)	13.4

Methanation reactions are thermodynamically favorable, yet a catalyst is necessary to obtain an appropriate conversion rate, with reported efficiencies of up to 80% CO_2 due to the high-water content produced in the process, and up to 89% in three phase reactors [3]. However, all research is done on pure gases without contaminants and therefore lower values are to be expected. The main effect on CO_2 conversion is reaction temperature, catalyst activity, and H_2/CO_2 ratio. It has been reported that a molar ratio of 4 which is higher than the stoichiometric ratio is favored for this reaction as well as a temperature range of 300-350 $°C$, as for catalysts, research is still being done on the field of methanation. Ni-based catalysts are reported to produce good results, and 80% CO_2 conversion is expected to be achievable. The scope of our study is to demonstrate the integration of combustion exhaust gas capture, treatment, and conversion into a single system that may economically be deployed on existing appliances. The threefold research aims include a) separation of CO_2 from generator exhaust, b) ensure negligible emissions of greenhouse gases to the atmosphere c) to demonstrate high CO_2 conversion (>70%) with the proposed system.

SYSTEM DESCRIPTION

The model in Fig.1, consists of two spray towers, a heat pump, a tubular reactor, an electrolysis machine, and gas supply lines of O_2, N_2, CO_2, and water. The system consists of four sections: feed, absorption, desorption and methanation. The approach adopted in this study Fig.1 is to remove the water before capturing the CO_2 and flue with the cyclic aqueous amine absorber, heating the rich solvent to release the desired CO_2 on the stripper column and adding hydrogen from electrolysis machine to satisfy high H_2/CO_2 ratio in the reactor. All water produced in this process (exhaust gas and reaction products condensation) is to be distilled to prevent electrolyte contaminations [4], and feed the electrolysis machine.

Condenser

Condensation is made using two tanks and the same principle is considered on both exhaust water and reaction product, the first tank is held at room

temperature to cool the gases and condense the water, the second contains silica gel to fully condense the vapor formed in the exhaust and the reaction to prevent it from reaching the system sensors, analyzers and dilute the liquid amine absorber. Silica gel has recorded adsorption capacity towards both CO_2 and H_2O but favors the second [5]. Note the condenser will produce water not suitable for electrolysis due to sulfur solubility in water and absorption of other gases in it, therefore distillation is required before feeding the excess water to the electrolysis process. The amount of water produced in the process varies at about four moles as both exhaust feed and Sabatier reaction products contains two moles of H_2O.

Absorption

Aqueous solutions of Alkanolamines are frequently used for the removal of acid gases from a variety of gas streams. Acid gas absorption-desorption cycle of the acid gas is presented in Fig.1, the CO_2 contents of the exhaust gas are chemically absorbed by the basic liquid absorbent and are released at elevated temperatures or low-pressure conditions. The absorber is designed to capture 90% of CO_2 emitted from the generator. The desired temperatures for the operation of the absorber are room temperature for the acid gas capture and elevated temperature (about 120 $°C$) on the stripper. The temperature regime and amine transfer between the two tanks are made using a heat pump. The gas and liquid are moving in opposite direction both on absorber and stripper, the flue gas is injected at the bottom and removed as exhaust at the top while the solvent is injected at the top and removed at the bottom. In this flow consideration [6] the concentration of the CO_2 in the flue gas will decrease as a function of the height in the column. The concentration of CO_2 in the solvent is the lowest at the top and highest on the bottom of the absorber tank making it easier for the acid gas to be absorbed due to the high difference between actual concentration and the equilibrium concentration and opposite for the stripper. This approach ensures high mass transfer efficiency. The application of a spray tower promises substantial advantages in comparison with a packed dry adsorption tower, due to expensive packing, insignificant pressure drop, and the ability to use precipitating solvents. in the stripper. The consequent reduction in operating costs and investment is are expected to also reduce the size for the facility as the absorber height depends on amine concentration. Absorber efficiency can be determined as η_{abs} and equals the amount of CO_2 moles exiting the stripper exhaust times moles of CO_2 in the absorber flue gas as shown in Eq.(5). High power efficiency is expected on the absorption-desorption section since the absorber vents the majority of the flue gases to the atmosphere without requiring additional electricity investment in the process. The desorption temperature serves as Sabatier reactor pre-heater. The amine solution is determined according to its selectivity towards CO_2 according to its partial pressure. Absorber efficiency sets the amount of hydrogen needed to be produced as well as the amount of excess water accumulated in the condensers. The efficiency of the absorber is defined based on the solvent temperature and flow rate.

$$\eta_{abs} = \frac{y_{CO_2\,inlet} - y_{CO_2\,outlet}}{y_{CO_2\,inlet}} \cdot 100\% \quad (5)$$

The absorber efficiency in turn determines the tower dimensions [7]. The minimum energy required to separate the CO_2 from flue gas can be easily calculated relative to the gas mixture entropy [8] and is dependent on the acid gas concentration, the lower the initial concentration of the CO_2 in the flue gas, and the higher the minimum work required to separate it. Thus, high concentrations of CO_2 in flue gas are preferred and will produce more methane as well as reduce separation costs.

Electrolysis

Electrolysis demands relatively high amounts of energy for separation of water molecules at ambient temperature and is, the highest power consumer in the system. The equilibrium voltage of a water molecule is approximately 1.23V, which and is needed to break the water molecules into hydrogen and oxygen as noted in Eq.(6). The hydrogen production rate depends on the stable CO_2 flow out of the stripper on maintaining a high CO_2/H_2 ratio.

$$2H_{2O} \rightarrow 2H_2 + O_2 \quad (6)$$

Sabatier Reaction

Synthesis of hydrocarbons from H_2/CO_2 mixtures via thermos catalystic processes are favored over group VIII metals (Fe, Co, Ni, Ru, Rh, Pd, Ir, Pt) dispersed on metal oxide supports. Preferred catalysts for the methanation reaction are Nickel and Ruthenium [9] due to their high catalytic activity and selectivity, while Ni is more efficient on the temperature range of 300-350 $°C$ and Ru can produce

methane on a lower temperature. There still exist some problems, such as carbon deposition, and sulfur poisoning during SNG production [10] [11]. Sulfur deactivatesd carbon dioxide absorption. Carbon deposition mainly affects the activity, reducing the performance and impacts the amount of catalyst needed in the reactor.

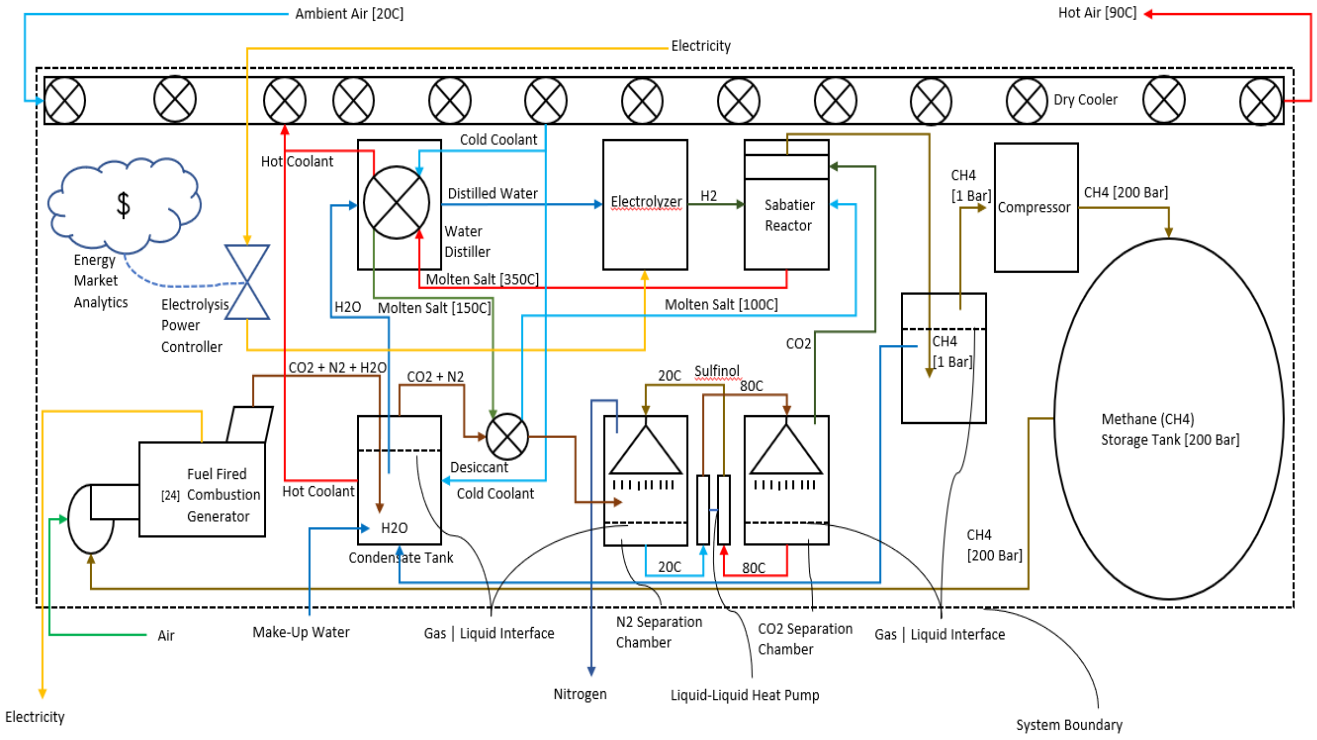

Fig.2. Proposed process for shipping container scale CH_4 production and storage of exhaust gas

Reaction efficiency can be determined as:

$$\eta_{reactor} = \frac{y_{CO_2\,inlet} - y_{CO_2\,inlet}}{y_{CO_2\,inlet}} \cdot 100\% \quad (7)$$

And therefore, overall methane yield in the process is:

$$\Re = \eta_{abs} \cdot \eta_{reactor} \quad (8)$$

$\Re$ is the CH_4 yield and is depends on both absorber and reaction efficiencies. The desired CO_2 capture and solvent flow rate determines the spray tower dimensions. The Sabatier reaction is a highly exothermic reaction, and thus harvesting heat generated during the reaction can be used to reduce cost. Fig.2 is a suggested model for the integration of all four sections. Real time analysis of electricity prices triggers the electrolysis process, which in turn feeds hydrogen to the methanation reactor. Electrolysis is the system's highest power consumer. Distillation is used to purify the condensed water and feed the electrolysis machine. Molten salt transferrers additional heat from the reactor to boil pre-electrolysis distilled water. At the process end, the resultant CH_4 is compressed to pressure at which it can be stored. All pressures and temperatures noted were designed around achieving a minimum power consumption, amine solvents (sulfinol – manufactured by Shell), and a ($NiAlO_3$) reaction catalyst.

Gas Impurities

The combustion reaction described in Eq.(1) is somewhat idealized. For typical gaseous fuel, N forms NO_x and S forms SO_x with traces metals. The major pollutants resulting from combustion are carbon monoxide (CO) and Nitrogen dioxide (NO_x), generally including nitrogen monoxide also known as nitric oxide (NO) and nitrogen dioxide (NO_2), the majority of the NO_x exiting the exhaust stack is in the form of NO. According to Eq.(4) CO reacts as carbon dioxide to produce methane and does not require pretreatments. Sulfur on the other hand is poisonous and reduces the catalyst activity drastically [12] by switching the reaction mechanism at the

Catalysts surface to produce Hydrogen-Sulfide, which adsorbs strongly and reduces its active sites.

$$H_2S + Ni \leftrightarrow Ni - S + H_2 \quad (9)$$

Sulfur containing components must be cleaned ahead a time to ppb levels [12]. Impurities in the exhaust gas set the requirments for the system with respect to impurity removal. Selection of the ideal amine absorbant should be based on its selectivity towards Sulfur, in order to reduce the sulfur content and prevent catalyast poisioning. The linear dependency between catalyst lifetime, and S,H_2 adsorption capacities descibed in detail in [12] predicted a lifetime for $NiAlO$ catalyst on constant flow of 20 ppb Sulfur of 350 days.

CONCLUSIONS

Producing synthetic renewable methane from combustion exhaust gas and feeding it into the existing natural gas distribution infrastructure will reduce greenhouse gases and will allow for the establishment of energy storage to overcome the disadvantages of intermittent renewable energies (e.g., solar or wind). The proposed system will overcome current challenges making the methanation technology truly commercially viable. The main characteristics of this system will be as follows:

- Power Quality – in terms of supporting the electric grid for voltage stability, availability, and resiliency.
- Energy Storage - the ability to store energy on the grid on a varied timescale from hours to months
- Energy Sink – the ability to capture overproduction of renewable energy through the generation of methane.

The main disadvantage of such a system is periodic replacement/ regeneration of the catalyst after the activity is reduced.

ACKNOWLEDGEMENT

We thank the Israel Ministry of science and technology for funding our work.

NOMENCLATURE

η_{abs} - absorption efficiency, %;
$y_{CO_2\,inlet}$ - CO_2 inlet mole ratio, mol%;
$y_{CO_2\,outlet}$ - CO_2 outlet mole ratio, mol%;
$\eta_{reactor}$ – reactor efficiency, %;
$\Re$ - overall methane yield, %;

REFERENCES

[1] U. Nations, UNFCCC Paris agreement, (2015).
[2] Q. Chai, S. Fu, H. Xu, W. Li, Y. Zhong. The gap report of global climate change mitigation, finance, and governance after the United States declared its withdrawal from the Paris Agreement. *Chinese Journal of Population Resources and Environment* **15**, 196-208 (2017).
[3] M. V. Landau, R. Vidruk, M. Herskowitz. Sustainable Production of Green Feed from Carbon Dioxide and Hydrogen. *ChemSusChem* **7**, 785-794 (2014).
[4] S. K. Mazloomi, N. Sulaiman. Influencing factors of water electrolysis electrical efficiency. *Renewable and Sustainable Energy Reviews* **16**, 4257-4263 (2012).
[5] M. Aresta, Ed. Carbon Dioxide Recovery and Utilization, Springer Netherlands, 2003.
[6] S. Berend, A. R. J., M. O. C., C. B.I. Introduction To Carbon Capture And Sequestration, World Scientific Publishing Company, 2014.
[7] W.H. Chen, M.-H. Tsai, C.-I. Hung. Numerical prediction of CO2 capture process by a single droplet in alkaline spray. *Applied Energy* **109**, 125-134 (2013).
[8] H. K. Zenz, A. C. Baclig, R. Manya, van Nierop Ernst A, W. Jennifer, J. Herzog Howard. Economic and energetic analysis of capturing CO_2 from ambient air. *PNAS* **108**(51), 20428- 20433 (2011).
[9] J. Gao, Q. Liu, F. Gu, B. Liu, Z. Zhong, F. Su. Recent advances in methanation catalysts for the production of synthetic natural gas. *RSC Adv.* **5**, 22759-22776 (2015).
[10] C. H. Bartholomew. Carbon Deposition in Steam Reforming and Methanation. *Catalysis Reviews* **24**, 67-112 (1982).
[11] J. Sehested. Four challenges for nickel steam-reforming catalysts. *Catalysis Today* **111**, 103-110, (2006).
[12] U. E. P. Agency. Nitrogen oxide control for stationary combustion sources. U. S. EPA report EPA/625/5-86/020, (1986).

Bulgarian Chemical Communications, Volume 52, Special Issue C (pp. 96-102) 2020 DOI: 10.34049/bcc.52.C.0058

Numerical simulation of paraffin heat storage process in concentric tubes

Y. Li*, G.Y. You, Q.Z. Zhu*, M.L. Di, G. Yue

College of Energy and Mechanical Engineering, Shanghai University of Electric Power, Shanghai 200090, China

Energy storage is an important means to solve the problem of space-time energy mismatch and has become a current research hotspot. The rate of heat absorption and release will affect the application range of heat storage materials, which is worthy of further study. This paper studies the phase change heat storage law of the concentric double-pipe heat exchanger at different fluid inlet temperatures and inlet velocities. The research results show that the influence of inlet velocity is much smaller than that of inlet temperature. The fluid inlet temperature has a great influence on the heat transfer effect, but when the fluid inlet temperature reaches a certain temperature range, further changing fluid inlet temperature to increase the melting rate is no longer effective.

Keywords: Energy storage, phase change heat storage, inlet temperature, inlet velocity

INTRODUCTION

The development of heat storage technology plays an important role in improving energy efficiency [1]. The phase change material is approximately isothermal in the process of phase change and some phase change materials have high heat storage density, which is beneficial to reduce the volume of the device [2]. Therefore, it has wide application prospects in the use of solar energy, the recovery of industrial waste heat, the "peak shifting valley filling" of the power industry, and phase change material composite walls, etc. [3, 4]. It has become a research hotspot worldwide [5-7].

The solid-liquid phase change material has a broad application prospect due to its small volume change during the phase change process. The phase change material can absorb/release a large amount of energy during the melting/solidification process, which is called the latent heat of phase change, and the corresponding melting or solidification temperature is called the phase change temperature. There are many kinds of phase change heat storage materials, which are mainly divided into organic phase change heat storage materials (such as paraffin [8, 9], fatty acid [10], etc.), inorganic phase change heat storage materials (such as hydrated salts [11], metals, etc.) and mixed phase change heat storage materials [12]. Among the organic phase change heat storage materials, paraffin have received widespread attention because of its high heat storage density, safety and stability, no phase separation and low cost [13-15].

* To whom all correspondence should be sent:
yli@shiep.edu.cn
zhuqunzhi@shiep.edu.cn

This paper simulates the phase change heat storage process of paraffin in concentric tubes. Compare the influence of different inlet temperatures and inlet velocities on phase change heat storage, so as to point out the way to improve the phase change heat transfer.

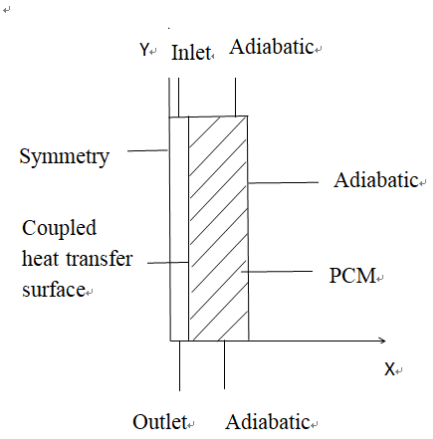

Fig.1. Physical model of paraffin heat storage process in concentric circular tube

PHYSICAL MODEL AND MATHEMATICAL MODEL

The dimensions of the concentric circular tube phase change heat exchanger are as follows: the outer tube has a diameter of 47 mm and a height of 400 mm, and the inner tube has a diameter of 6 mm and a height of 400 mm. The phase change material paraffin is filled in the outer ring. The physical properties of paraffin are shown in Tab.1. The hot water flows longitudinally from top to bottom in the inner tube. When the temperature of hot water is higher than the phase change temperature of paraffin, the phase change material absorbs heat and undergoes a phase change from solid to liquid,

thereby completing the heat storage process. 1/2 area of the heat storage unit along the flow direction is selected as the calculation area, and the center line of the inner tube is a symmetric boundary to establish a two-dimensional model, as shown in Fig.1.

Basic equation

For the convenience of analysis, simplify the physical model and make the following assumptions.

(1) The solid-liquid two-phase phase change material has uniform and isotropic physical properties.

(2) The liquid phase region is Newton's incompressible fluid.

(3) The natural convection in the liquid phase region is a two-dimensional laminar flow.

(4) Only consider the change of phase change density with temperature when the buoyancy force acts.

(5) The thickness and thermal resistance of the pipeline are negligible.

Based on the above assumptions, the governing equation is as follows:

Mass equation:

$$\nabla\left(\rho\vec{\upsilon}\right)=0 \tag{1}$$

where:

$\underline{\rho}$ – density, kg/m^3;

υ –velocity vector, m/s.

Momentum equation:

$$\frac{\partial\left(\rho\vec{\upsilon}\right)}{\partial t}+\nabla\left(\rho\vec{\upsilon}\vec{\upsilon}\right)=-\nabla\rho+\nabla\left(\mu\vec{\upsilon}\right)+S \tag{2}$$

where:

t– time, s;

μ–dynamic viscosity, kg/(m·s);

S– source term.

Energy equation:

$$\rho\frac{\partial H}{\partial t}=\lambda\nabla^2 T \tag{3}$$

where:

H – the specific enthalpy at any time, J/kg;

λ – thermal conductivity, W/(m·K);

T – temperature, K.

$$H=\mathrm{h}+\Delta H \tag{4}$$

$$h=h_{ref}+\int_{T_{ref}}^{T}c_p dT \tag{5}$$

$$\Delta H=\beta L \tag{6}$$

where:

h – specific enthalpy of sensible heat, J/kg;

h_{ref} – specific enthalpy at reference temperature, J/kg;

T_{ref} – reference temperature, K;

C_p – specific heat at constant pressure, J/(kg·K);

β – liquid fraction;

L – latent heat, J/kg.

Table1. The thermal properties of paraffin

Name	Density	C_p	Thermal conductivity
	kg/m^3	kJ/(kg·K)	W/(m·K)
paraffin	760	2100	0.25
viscosity	Latent heat	Freezing point	Melting point
kg/(m·s)	kJ/kg	K	K
0.00324	170	324.15	330.15

Boundary conditions and parameters

Considering the axial symmetry of the physical model, a two-dimensional axisymmetric transient numerical model is established to study the heat transfer of phase transition. SIMPLE algorithm is used to couple the pressure-velocity term. Meanwhile, the energy and momentum equations are discretized by adopting second order upwind schemes, and PRESTO! approach is selected to discretize the pressure equation. Considering the natural convection in the liquid region, the phase change material density term selects Boussinesq model, and the thermal expansion coefficient is 0.0006 K^{-1} [16]. At the boundary inlet, the velocity-inlet boundary condition is selected. At the boundary outlet, the outflow boundary condition is defined. The external boundaries of the phase change material are considered adiabatic. In the simulation, the change of the liquid phase volume fraction of the phase change material with time is monitored.

RESULTS AND ANALYSIS

Model validation

In order to verify the correctness of the model, the numerical simulation results are compared with

Jin's [17] experimental results under the same working conditions (the initial temperature of paraffin is 301.15 K, the inlet temperature of hot fluid is 336.15 K, and the inlet velocity of hot fluid is 0.028 m/s). Fig.2 shows the curve of outlet temperature with time. It can be found that the trend of the numerical simulation results is basically consistent with the experimental results, and the error is very small.

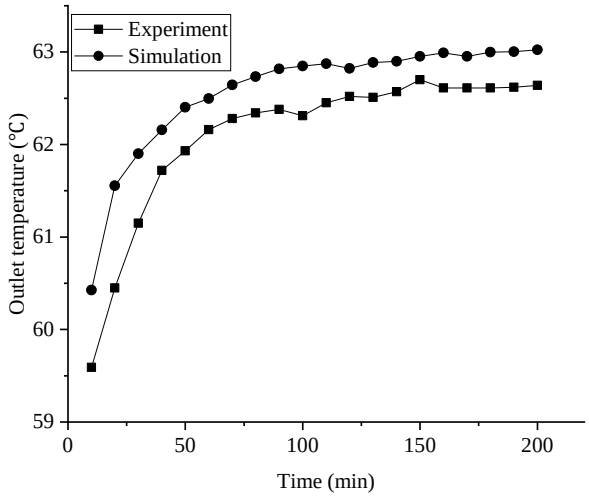

Fig.2. Variation curve of outlet temperature with time

Grid independence validation

The models with 8260, 16300 and 28740 grids are selected for numerical simulation, and the outlet temperatures of thermal fluid with time under different grid sizes are compared as shown in Fig.3. When the number of grid increases, the calculation is more accurate, but the calculation time will also increase. Under comprehensive consideration, the model with 16300 grids is selected.

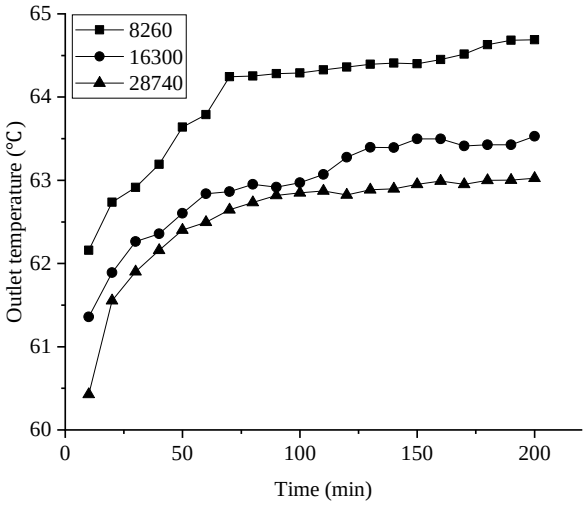

Fig.3. The curve of outlet temperature with time under different grid sizes

Simulation results

1. Influence of inlet velocity

The paraffin melting process is simulated with an initial temperature of 298.15 K, a thermal fluid inlet temperature of 360.15 K, and a thermal fluid inlet velocity of 0.035 m/s, 0.045 m/s and 0.055 m/s. The simulation results are as follows.

Fig.4 shows the curve of the liquid phase volume fraction of paraffin with time at different inlet velocities. It can be seen from Fig.4 that the liquid phase volume fraction of paraffin increases with time, showing a tendency that the melting velocity is faster at the beginning and slower afterwards. This is mainly because at the beginning of melting, the temperature difference between the phase change material and the thermal fluid is large, and the heat transfer is fast. As the heating time increases, the content of liquid paraffin is more and more, and the amount of liquid paraffin near the wall also increases. After the liquid near the wall is heated, the temperature increases and the density decreases. As a result, under the driving force of the density difference, the high-temperature liquid near the wall surface and the low-temperature liquid near the phase interface appear natural convection.

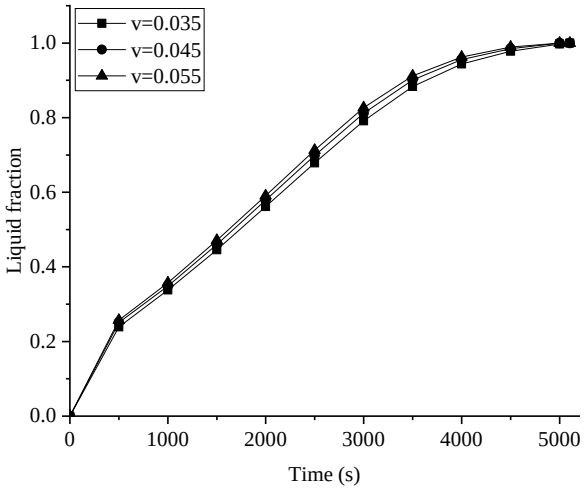

Fig.4. Variation curve of liquid phase volume fraction of paraffin with time

Fig.5 shows the velocity field distribution of paraffin when the fluid inlet velocity is 0.045 m/s and the inlet temperature is 360.15 K. It can be seen that due to the relatively large ratio of length to diameter of the concentric circular tube, natural convection disappears after a period of time along the radial direction, and then develops downward along the length direction. As the heat transfer

progresses, the temperature difference between the phase change materials becomes smaller and smaller, and the natural convection will weaken until it disappears. Due to the disappearance of natural convection, the heat transfer becomes weaker and the melting rate of the phase change material becomes slower. The three curves in Fig.4 have very little difference, which shows that the inlet velocity has little effect on the melting process of paraffin.

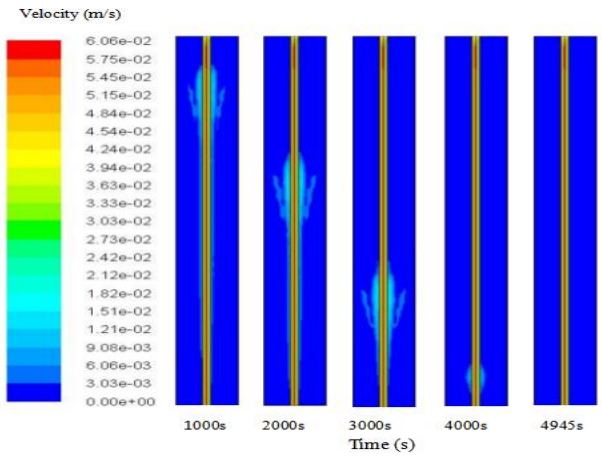

Fig.5. Velocity field distribution at the fluid inlet temperature of 360.15 K

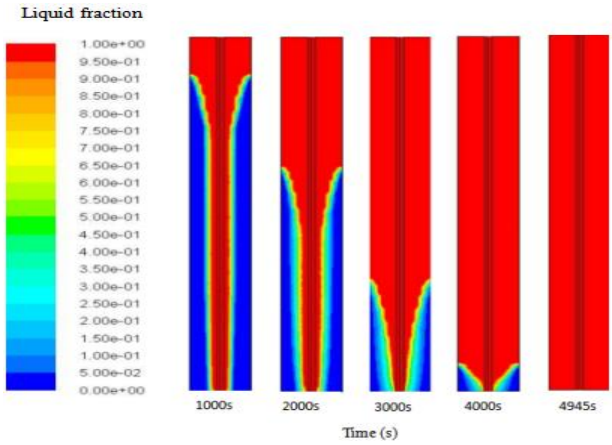

Fig.6. Liquid fraction distribution at the fluid inlet temperature of 360.15 K

Fig.6 and Fig.7 are the cloud pictures of the liquid phase volume fraction and temperature field distribution of paraffin at different time when the fluid inlet velocity is 0.045 m/s and the inlet temperature is 360.15 K. When the melting time reaches 1000 s, the temperature of the phase change material first rises near the inner tube and near the entrance, and the phase change material near the inlet begins to melt. As the melting progresses, the heating zone gradually expands downward, and the liquid phase volume fraction becomes larger and larger. As the melting time increases, the natural convection in the lower region weakens until it disappears, and the heat conduction is dominated. The melting time of the phase change material near the fluid outlet is longer. According to the cloud chart of the liquid phase volume fraction and the temperature field distribution, it can be seen that the area near the fluid outlet is the most difficult to melt.

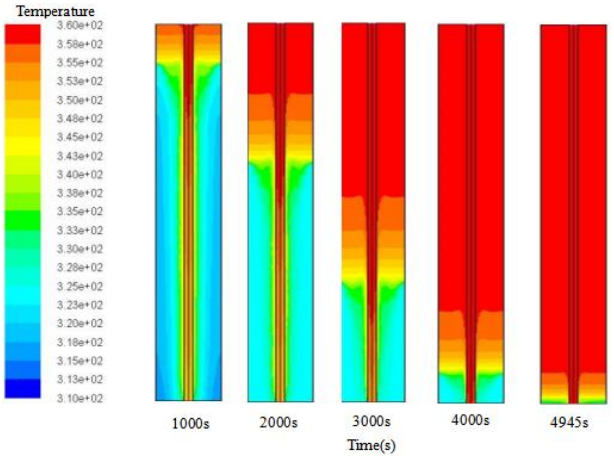

Fig.7. Temperature field distribution at the fluid inlet temperature of 360.15 K

2. Influence of inlet temperature

The paraffin melting process with an initial temperature of 298.15 K, a thermal fluid inlet velocity of 0.045 m/s, and a thermal fluid inlet temperature of 350.15 K, 360.15 K and 370.15 K are simulated.

It can be seen from Fig.8 that when liquid phase ratio is between 0 and 0.8, the slopes of the three curves are relatively large and basically unchanged. When the ratio is between 0.8 and 1, the slopes of the curves gradually decrease. This is because as the proportion of paraffin increases, natural convection occurs and the heat transfer rate is relatively fast. In the late melting stage, the heat transfer effect of natural convection is weakened and the heat transfer is mainly heat conduction, which causes the melting rate to decrease and the curve slope becomes smaller. It can also be found from Fig.8 that at three different fluid inlet temperatures, when the fluid inlet temperature is 370.15 K, the slope of the curve is the largest. That is, increasing the fluid inlet temperature will increase the melting rate of paraffin and shorten the melting time. Comparing Fig.5, Fig.9 and Fig.10, it can be found that as the temperature increases, the downward development of natural convection accelerates, and the radial development does not change much.

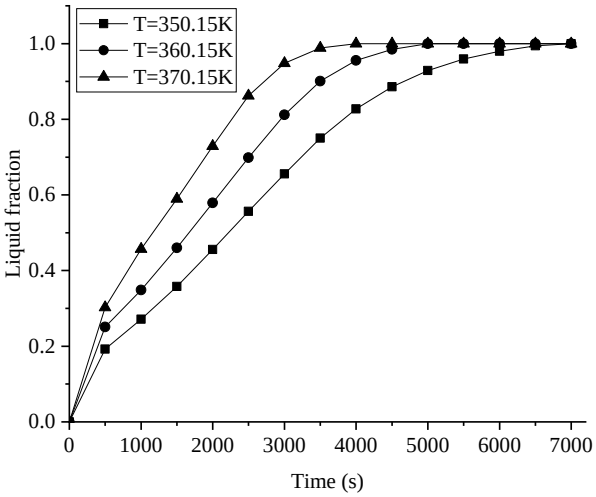

Fig.8. Variation curve of liquid phase volume fraction of paraffin with time

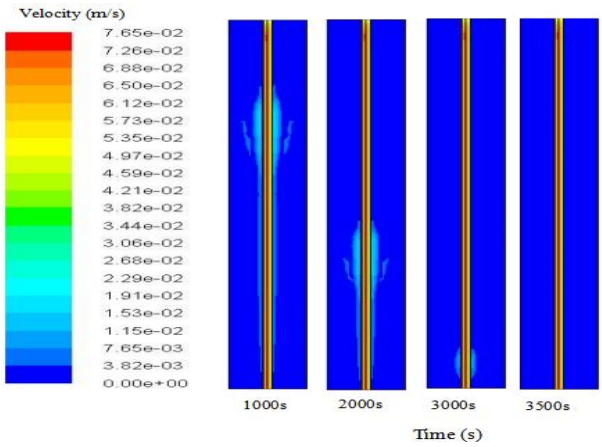

Fig.9. Velocity field distribution at the fluid inlet temperature of 370.15 K

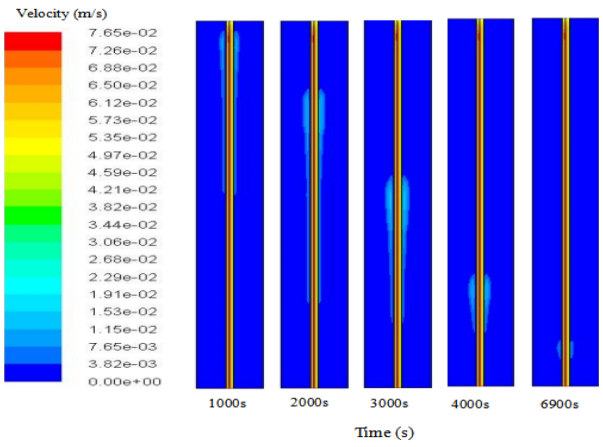

Fig.10. Velocity field distribution at the fluid inlet temperature of 350.15 K

It can be seen from Fig.6, Fig.11 and Fig.12 that when the thermal fluid inlet temperature is 350.15 K, 360.15 K, 370.15 K, the paraffin is completely melted at 6900 s, 4945 s and 3800 s, respectively. When the hot fluid inlet temperature increases from 350.15 K to 360.15 K and from 360.15 K to 370.15 K, the complete melting time is shortened by 1955 s and 1145 s, respectively. The corresponding reduction rates are 28.3% and 23.1%. As the temperature increases, under the same temperature difference, the shortening of the melting time will decrease. Therefore, when the inlet temperature of the thermal fluid rises to a certain range, the effect of continuously increasing the temperature on shortening the complete melting time of the phase change material will be weakened.

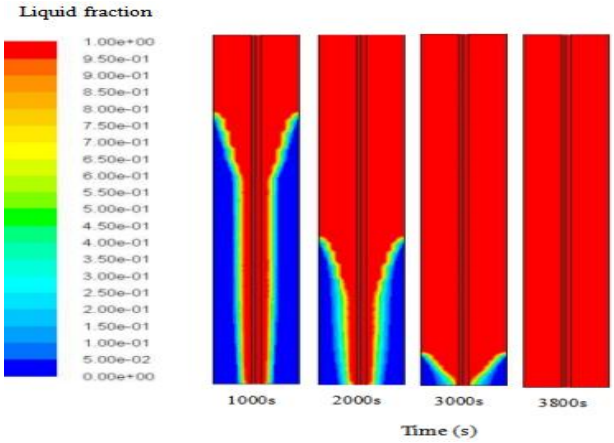

Fig.11. Liquid fraction distribution at the fluid inlet temperature of 370.15 K

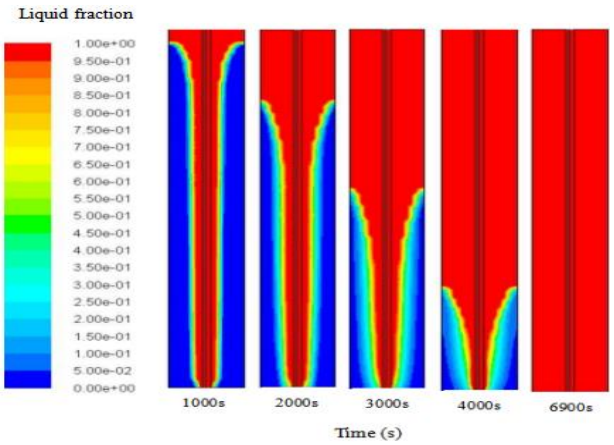

Fig.12. Liquid fraction distribution at the fluid inlet temperature of 350.15 K

Fig.13 and Fig.14 show the temperature field distribution at different fluid inlet temperatures. It can be seen from Fig.7, Fig.13 and Fig.14 that as the inlet temperature of the thermal fluid increases, the temperature change of the phase change

material accelerates, and the isotherm becomes more irregular. Since the ratio of length to diameter of the heat exchanger is relatively large, the radial heat transfer ends quickly, so the upper high-temperature liquid paraffin can quickly exchange heat with the paraffin in the lower mushy area, thereby speeding up the heat transfer. When the paraffin has completely melted, the heat transfer of the tail is still going on.

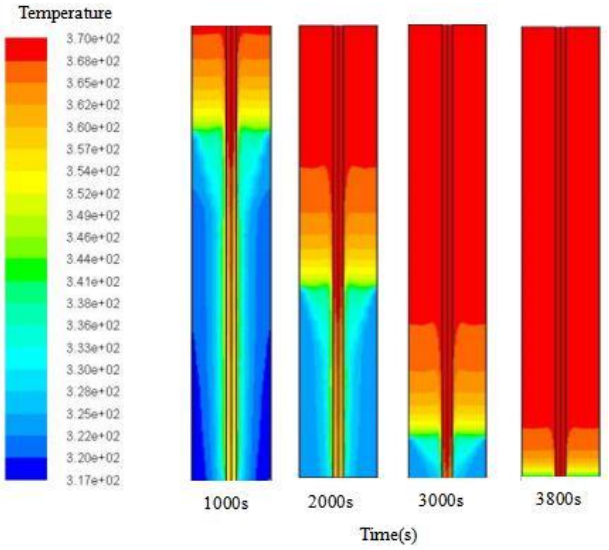

Fig.13. Temperature field distribution at the fluid inlet temperature of 370.15 K

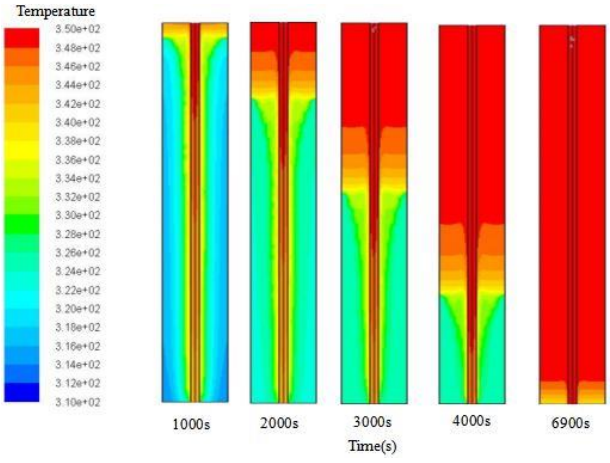

Fig.14. Temperature field distribution at the fluid inlet temperature of 350.15 K

CONCLUSIONS

(1) As the melting progresses, natural convection appears on the near wall side. Due to the relatively large ratio of length to diameter, natural convection disappears after a period of time along the radial direction, and then develops downward along the length direction.

(2) Compared with the inlet temperature, the inlet velocity has less influence on the phase change heat transfer process.

(3) When the inlet temperature of the hot fluid increases from 350.15 K to 360.15 K and from 360.15 K to 370.15 K, the decrease rates of the complete melting time are 28.3% and 23.1% respectively. With the increase of inlet temperature, the effect of increasing the inlet temperature on shortening the complete melting time of the phase change materials decreases.

(4) At different inlet temperatures of the thermal fluid, when the liquid fraction of paraffin is between 0 and 0.8, the curve slope of the liquid volume fraction of paraffin over time is relatively large and basically remains unchanged. When the liquid fraction of paraffin is between 0.8 and 1.0, the curve slope gradually becomes smaller. The curve slope increases with the increase of the fluid inlet temperature.

ACKNOWLEDGEMENTS

This research is supported by the National Natural Science Foundation of China under the contract No. 51576119 and the Science and Technology Commission of Shanghai Municipality under the contract No. 20dz1205208, which are gratefully acknowledged by the authors.

REFERENCES

[1] H. L. Zhang, J. Baeyens, G. Cáceres, J. Degreve, Y.Q. Lv. Thermal energy storage: Recent developments and practical aspects. Progress in Energy & Combustion Science 53, 1-40 (2016).

[2] Y. P. Yuan, N. Zhang, W. Q. Tao, X. L. Cao, Y. L. He. Fatty acids as phase change materials: a review. Renewable and Sustainable Energy Reviews 29, 482-498 (2014).

[3] T. Ma, H. Yang, Y. Zhang, L. Lu, X. Wang. Using phase change materials in photovoltaic systems for thermal regulation and electrical efficiency improvement: A review and outlook. Renewable and Sustainable Energy Reviews 43, 1273–1284 (2015).

[4] J. Yang, Y. L. Jia, N. C. Bing, L. L. Wang, H. Q. Xie, W. Yu. Reduced graphene oxide and zirconium carbide co-modified melamine sponge/paraffin wax composites as new form-stable phase change materials for photothermal energy conversion and storage. Applied thermal engineering 163, 114412 (2019).

[5] M. Medrano, M. O. Yilmaz, M. Nogues, I. Martorell, J. Roca. Experimental evaluation of commercial heat exchangers for use as PCM thermal storage systems. Applied Energy 86(10), 2047-2055 (2009).

[6] Z. G. Luo. Z. W. Huang, N. Xie, X. N. Gao, T. Xu, Y. T. Fang, Z. G. Zhang. Numerical and experimental study on temperature control of solar panels with form-stable paraffin/expanded graphite composite PCM. Energy conversion and management 149, 416-423 (2017).

[7] E. Assis, L. Katsman, G. Ziskind, R. Letan. Numerical and experimental study of melting in a spherical shell. International Journal of Heat and Mass Transfer 50(9-10), 1790-1804 (2007).

[8] B. Q. Ma, J. Q. LI, Z. J. Peng, Y. L. Ding. Thermal conductivity of paraffin based composite phase change thermal storage materials. Energy Storage Science and Techology 1(2), 131-138 (2012) (in Chinese).

[9] Z. G. Zhang, N. Zhang, J. Peng, X.M. Fang, X. N. Gao. Preparation and thermal energy storage properties of paraffin/expanded graphite composite phase change material. Applied Energy 91(1), 426-431 (2012).

[10] S. Wu, T. X. Li, T. Yan, Y. J. Dai, R. Z. Wang. Preparation and thermal properties of high performance shape stabilized composite phase change energy storage materials. CIESC Journal 66(12), 5127-5134 (2015) (in Chinese).

[11] D. L. Wu, T. X. Li, F. He, R. Z. Wang. Modified preparation and thermal storage / exothermic properties of sodium acetate trihydrate phase change energy storage Composites. CIESC Journal 69(7), 2860-2868 (2018) (in Chinese).

[12] K. Pielichowaka, K. Pielichowaki. Phase change materials or thermal energy storage. Progress in Materials Science 65(10), 67-123 (2014).

[13] P. Zhang, X. Xiao, Z. W. Ma. A review of the composite phase change materials: Fabrication, characterization, mathematical modeling and application to performance enhancement. Applied Energy 165, 472-510 (2016).

[14] M. Kenisarin, K. Mahkamov. Salt hydrates as latent heat storage materials: Thermophysical properties and costs. Solar Energy Materials & Solar Cells 145, 255-286 (2016).

[15] C. Veerakumar, A. Sreekumar. Phase change material based cold thermal energy storage: materials, techniques and applications - A review. International Journal of Refrigeration 67, 271-289 (2016).

[16] T. Tabassum, M. Hasan, L. Begum. Transient melting of an impure paraffin wax in a double-pipe heat exchanger: Effect of forced convective flow of the heat transfer fluid. Solar Energy 159, 197-211 (2018).

[17] R. F. Jin. Experimental and simulation research on heat storage performance of solar phase change heat storage device. Shanghai: Donghua University, 2009 (in Chinese).

BULGARIAN CHEMICAL COMMUNICATIONS

Instructions about Preparation of Manuscripts

General remarks: Manuscripts are submitted in English by e-mail or by mail (in duplicate). The text must be typed double-spaced, on A4 format paper using Times New Roman font size 12, normal character spacing. The manuscript should not exceed 15 pages (about 3500 words), including photographs, tables, drawings, formulae, etc. Authors are requested to use margins of 3 cm on all sides. For mail submission hard copies, made by a clearly legible duplication process, are requested. Manuscripts should be subdivided into labelled sections, e.g. **Introduction, Experimental, Results and Discussion**, *etc*.

The title page comprises headline, author's names and affiliations, abstract and key words.

Attention is drawn to the following:

a) **The title** of the manuscript should reflect concisely the purpose and findings of the work. Abbreviations, symbols, chemical formulas, references and footnotes should be avoided. If indispensable, abbreviations and formulas should be given in parentheses immediately after the respective full form.

b) **The author**'s first and middle name initials, and family name in full should be given, followed by the address (or addresses) of the contributing laboratory (laboratories). **The affiliation** of the author(s) should be listed in detail (no abbreviations!). The author to whom correspondence and/or inquiries should be sent should be indicated by asterisk (*).

The abstract should be self-explanatory and intelligible without any references to the text and containing not more than 250 words. It should be followed by key words (not more than six).

References should be numbered sequentially in the order, in which they are cited in the text. The numbers in the text should be enclosed in brackets [2], [5, 6], [9–12], etc., set on the text line. References, typed with double spacing, are to be listed in numerical order on a separate sheet. All references are to be given in Latin letters. The names of the authors are given without inversion. Titles of journals must be abbreviated according to Chemical Abstracts and given in italics, the volume is typed in bold, the initial page is given and the year in parentheses. Attention is drawn to the following conventions:

a) The names of all authors of a certain publications should be given. The use of "*et al*." in the list of references is not acceptable.

b) Only the initials of the first and middle names should be given.

In the manuscripts, the reference to author(s) of cited works should be made without giving initials, e.g. "Bush and Smith [7] pioneered...". If the reference carries the names of three or more authors it should be quoted as "Bush *et al*. [7]", if Bush is the first author, or as "Bush and co-workers [7]", if Bush is the senior author.

Footnotes should be reduced to a minimum. Each footnote should be typed double-spaced at the bottom of the page, on which its subject is first mentioned.

Tables are numbered with Arabic numerals on the left-hand top. Each table should be referred to in the text. Column headings should be as short as possible but they must define units unambiguously. The units are to be separated from the preceding symbols by a comma or brackets.

Note: The following format should be used when figures, equations, *etc*. are referred to the text (followed by the respective numbers): Fig., Eqns., Table, Scheme.

Schemes and figures. Each manuscript (hard copy) should contain or be accompanied by the respective illustrative material as well as by the respective figure captions in a separate file (sheet). As far as presentation of units is concerned, SI units are to be used. However, some non-SI units are also acceptable, such as °C, ml, l, etc.

The author(s) name(s), the title of the manuscript, the number of drawings, photographs, diagrams, etc., should be written in black pencil on the back of the illustrative material (hard copies) in accordance with the list enclosed. Avoid using more than 6 (12 for reviews, respectively) figures in the manuscript. Since most of the illustrative materials are to be presented as 8-cm wide pictures, attention should be paid that all axis titles, numerals, legend(s) and texts are legible.

The authors are asked to submit **the final text** (after the manuscript has been accepted for publication) in electronic form either by e-mail or mail on a 3.5'' diskette (CD) using a PC Word-processor. The main text, list of references, tables and figure captions should be saved in separate files (as *.rtf or *.doc) with clearly identifiable file names. It is essential that the name and version of the word-processing program and the format of the

text files is clearly indicated. It is recommended that the pictures are presented in *.tif, *.jpg, *.cdr or *.bmp format, the equations are written using "Equation Editor" and chemical reaction schemes are written using ISIS Draw or ChemDraw programme.

The authors are required to submit the final text with a list of three individuals and their e-mail addresses that can be considered by the Editors as potential reviewers. Please, note that the reviewers should be outside the authors' own institution or organization. The Editorial Board of the journal is not obliged to accept these proposals.

EXAMPLES FOR PRESENTATION OF REFERENCES

REFERENCES

1. D. S. Newsome, *Catal. Rev.–Sci. Eng*., **21**, 275 (1980).
2. C.-H. Lin, C.-Y. Hsu, *J. Chem. Soc. Chem. Commun*., 1479 (1992).
3. R. G. Parr, W. Yang, Density Functional Theory of Atoms and Molecules, Oxford Univ. Press, New York, 1989.
4. V. Ponec, G. C. Bond, Catalysis by Metals and Alloys (Stud. Surf. Sci. Catal., vol. 95), Elsevier, Amsterdam, 1995.
5. G. Kadinov, S. Todorova, A. Palazov, in: New Frontiers in Catalysis (Proc. 10th Int. Congr. Catal., Budapest, 1992), L. Guczi, F. Solymosi, P. Tetenyi (eds.), Akademiai Kiado, Budapest, 1993, Part C, p. 2817.
6. G. L. C. Maire, F. Garin, in: Catalysis. Science and Technology, J. R. Anderson, M. Boudart (eds), vol. 6, Springer-Verlag, Berlin, 1984, p. 161.
7. D. Pocknell, *GB Patent* 2 207 355 (1949).
8. G. Angelov, PhD Thesis, UCTM, Sofia, 2001.
9. JCPDS International Center for Diffraction Data, Power Diffraction File, Swarthmore, PA, 1991.
10. CA **127**, 184 762q (1998).
11. P. Hou, H. Wise, *J. Catal.*, in press.
12. M. Sinev, private communication.
13. http://www.chemweb.com/alchem/articles/1051611477211.html.

CONTENTS